Toward Spin-LED and Spin-VECSEL operations at magnetic remanence

Julien Frougier

Julien Frougier. Toward Spin-LED and Spin-VECSEL operations at magnetic remanence. Other [cond-mat.other]. Université Paris Sud - Paris XI, 2014. English. NNT : 2014PA112175 . tel-01127040

HAL Id: tel-01127040
https://theses.hal.science/tel-01127040
Submitted on 6 Mar 2015

UNIVERSITÉ PARIS-SUD

ECOLE DOCTORALE 564:
PHYSIQUE EN ÎLE-DE-FRANCE

LABORATOIRE: UNITÉ MIXTE DE PHYSIQUE CNRS/THALES

DISCIPLINE : PHYSIQUE

THÈSE DE DOCTORAT

Soutenue le 29 Septembre 2014

par

Julien FROUGIER

Towards Spin-LED and Spin-VECSEL operation at magnetic remanence

Composition du Jury :

Directeur de thèse :	Jean-Marie GEORGE	Chargé de Recherche (UMφ CNRS/Thales)
Rapporteurs :	Angélique RISSONS	Chargé de Recherche (ISAE)
	Michael OESTREICH	Professeur (University of Hannover)
Examinateurs :	Ghaya BAILI	Ingénieur (Thales Research & Technology)
	Fabien BRETENAKER	Directeur de Recherche (Laboratoire Aimé Cotton)
	Stéphane MANGIN	Chargé de Recherche (Institut Jean Lamour)

Acknowledgements

I would like to start by sincerely thanking the Prof. Angélique Rissons and the Prof. Michael Oestreich for reviewing this thesis manuscript as well as Prof. Fabien Bretenaker and Dr. Stéphane Mangin for accepting to be members of my evaluation jury.

Thank you very much Yong Chang Lau, my friend and fellow *INSA Toulouse* graduate, for introducing me to the *UM*φ staff as a candidate on this Ph.D Thesis.

Next, I would like to give a special thank to Dr. Jean-Marie George, Dr. Ghaya Baili and Dr. Henri Jaffrès for trusting me and recruiting me on this Ph.D position. Thank you Jean-Marie for your supervision and your good humor throughout those three years. I appreciated the work freedom that you let to your students; this way of functioning was the right one for me. Being able to learn without pressure is always enjoyable. Thank you also for dealing so well with my "control freak syndrome" and helping me in my Post-Doctoral Job search. I learned a lot at your contact and I leave your team feeling ready to climb the next rung on the ladder: mission accomplished. Thank you Ghaya for introducing me to the optics community but also for teaching and sharing with me your experimental expertise on VECSEL. Good job on managing me when I was freaking out on deadlines and intense workloads. And of course, congratulations again on your new "Young and Dynamic Mom" status! Thank you Henri for your scientific and human support throughout this Thesis. You have always been available when I needed it, ready to deliver your precious advices. Be sure that you stand out as a major participant in the success of this Thesis. Thank you also for helping me in my Post-Doctoral Job search.

Many thanks to Dr. Daniel Dolfi who initiated the Spin-VESCEL project and whose amazing human and management qualities lead to a fruitful partnership between the *Unité Mixte de Physique CNRS/Thales* and *Thales Research & Technology.* Thank you Daniel for always behind available when I needed advices and for helping me in my Post-Doctoral job search.

I also want to thanks the Dr. Pascale Nouchi for actively participating in my recruitment and introducing me to the optics division of *Thales Research & Technology.* Thanks for your advices and for all the pleasant discussions about California, Florida and your US experience in general.

Many thanks to the project partners Dr. Mehdi Alouini (*IPR*), Dr. Isabelle Sagnes (*LPN*) and Dr. Arnaud Garnache (*IES*) for their tremendous work on the theoretical and experimental development of Spin-VECSEL. Thank you Mehdi for applying your talent to the benefit of the project and for being a continual source of brilliant ideas and scientific intuition. Thank you Isabelle and Arnaud for the amazing structures emerging from your partnership and for your availability throughout the

project.

I would like to thanks all the members of the *LPCNO*'s Quantum Optoelectronic team for their contribution to both the Spin-LED and the Spin-VECSEL projects. Thank you Prof. Pierre Renucci and Prof. Xavier Marie for inspiring me when I was still a student at the *INSA Toulouse*. Thank you Pierre for taking the time to correct part of this manuscript, I really appreciated it.

Thank you to all the members of Dr. Yuan Lu's team (*Institut Jean-Lamour*) for their contribution to both the Spin-LED and the Spin-VECSEL projects. Thank you Yuan for your help, advices and legendary efficiency throughout those three years. Your outstanding management skills combined with your scientific passion lead to remarkable developments on both the *SISTER* and the *INSPIRE* projects.

Thanks to the Lab's managing trinity: the Prof. Dr. and 2007 Nobel Laureate Albert Fert for his kindness, modesty, scientific inspiration and support in my Post-Doctoral job search, Dr. Frédéric Nguyen Van Dau for his scientific advices and knowledge, and Dr. Frédéric Petroff for running the Lab like clockwork.

Another special thanks to Dr. Nicolas Reyren, the man whose knowledge is only equaled by his unshakeable good mood. Your passion for science, extraordinary sense of Physics and human qualities always makes it enjoyable to work by your side. Do not change anything you got the winning recipe! Thank you for correcting part of this manuscript and for helping with the corrections of my first paper. Thank you also for all the little helps and advices given here and there that made a huge difference all the time. I hope that I will get the opportunity to work with you again in a near future.

Thanks to Dr. Michael Tran and Dr. Julian Peiro, two official JMG-Boys Club members, for helping me on my arrival, introducing me to the lab and making me feel home. Thank you Michael for your precious cleanroom training and for your amazing joy of living. Thank you Julian for all your advices, countless helps and priceless discussions about your already legendary optimism.

I also would like to thanks the team of the III-V lab for letting me access their cleanroom during these three years and use their lithography equipment. Many thanks to Bouzid Simourad, Marco Lamponi and Dr. Gregory Maisons for their help, advices and impressive problem solving skills. You made me feel home in the III-V cleanroom and I really appreciated it. Don't change anything, you guys rock!

Thank you Dr. Gilles Feugnet for your help, expertise and advices during the long hours I spent struggling on the extended laser cavity. I really appreciated your sense of humor and your capacity to always minimize the seriousness of the problems faced.

Special thanks to "CEO" Cyrile Deranlot, the man who rubs shoulders with success on a daily basis. An uncompromised professionalism and exemplary human values, I am really happy I got to know you during these three years at the *UMφ*. Good luck in your new adventure. "Work seriously without taking yourself seriously!"

BACK IN THE GYM!!! With Edouard Lesne and Ryan Cherifi, a.k.a Lord Ed and Lord Ryan, a.k.a Trapzilla and Quadzilla,...a.k.a Bishop Gains and Bishop Shreds! Thank you guys for the awesome training sessions we spent making ALL KINDS OF GAINS! All kinds$\cdots$ But also for the priceless moments we spent optimizing the anabolic window by eating tons and tons of food. I am really glad I got to meet you guys during my stay at the *UMφ*. Let's keep it clean brahs: Go Hard or Go Home, Curls for the girls and of course one more rep' for the Sparta!

Thank you Dr. Nicolas Locatelli for your brilliant advices throughout these three years, both on the scientific and administrative sides. I really enjoyed interacting with you and hope that I will continue seeing you around.

Merci à Eric Jacquet, l'homme ayant détrôné George Abitbol au titre de l'homme le plus classe du monde. Je prends l'initiative d'écrire ces remerciements en français car je sais que l'anglais n'est pas (encore) ta langue favorite. Merci pour tes coups de mains, tes dépannages de matériels et tes discussions sportives. Toujours un plaisir de te croiser dans un couloir ou de t'entendre tailler un costard (toujours sur mesure) à une victime innocente! Ne change rien, tu es royal!

Je souhaite également sincèrement remercier Christine Marchand-Goudroye et Anne Dussart, véritable travailleuses de l'ombre à l'efficacité inégalable, pour leur remarquable assistance quotidienne tout au long de ces trois années. Votre gentillesse et vos sourires amicaux n'ont jamais manqué d'illuminer mes journées. Merci Mesdames!

I also would like to thank the rest of the lab: Ph.D Students, Ph.Ds and Engineers who might not be mentioned above but whose daily assistance, support and friendship helped me to successfully complete this Thesis.

Je remercie très sincèrement ma famille pour avoir cru en moi, supporté et encouragé depuis le début de ces longues études. Merci à mes parents, Michel et Annette, de toujours avoir fait votre maximum pour assurer la réussite de votre progéniture. Merci à ma soeur Claire pour son soutien, pour avoir brillamment supporté mon caractère pas toujours évident et pour m'avoir fait redescendre sur terre quand le besoin s'en faisait sentir.

Of course, I also would like to thanks my close friends Victor, Val, Emilien, Jeremy, Sylvain, Aurélien, Pierre and Chloé for their unconditional support since we met in High School or over the years.

Finally, I will conclude by thanking a very special lady, Jennifer Castiblanco, who has always been there for me during the past four years. 5 feet 2 of highly concentrated awesomeness always mentally by my side despite the geographical remoteness. Thank you so much for your unconditional support and daily encouragements. Now that this chapter is over, I can't wait to start the next one with you, in the US and physically present by your side. Thank you for your patience, mental strength and kindness. You are the best.

Contents

List of Acronyms

A.

- **AO-HDS:** All Optical-Heliticity Dependent Switching
- **ASE:** Amplified Spontaneous Emission

B.

- **BAP:** Bir-Aronov-Pikus

C.

- **CB:** Conduction Band
- **CESR:** Conduction Electron Spin Resonance
- **CIP:** Current-In-Plane
- **CMOS:** Complementary Metal-Oxide Semiconductor
- **CNT:** Carbon Nano-Tube
- **CPO:** Coherent Population Oscillation
- **CPP:** Current Perpendicular to the Plane
- **CPT:** Coherent Population Trapping
- **CW:** Continuous Wave

D.

- **DBR:** Distributed Bragg Reflector
- **DFT:** Density Functional Theory
- **DMS:** Diluted Magnetic Semiconductor
- **DoCP:** Degree of Circular Polarization (Also identified as P_c or P_{circ})
- **DOS:** Density Of State
- **DP:** Dyakonov-Perel (Spin relaxation mechanism)

E.

- **EL:** Electro-Luminescence
- **ESA:** Electrical Spectrum Analyzer
- **EY:** Elliot-Yafet (Spin relaxation mechanism)

F.

- **FFT images:** Fast Fourier Transform images
- **F/N:** Ferromagnetic/Non-magnetic metal
- **F/SC:** Ferromagnetic/Semiconductor
- **F/I/SC:** Ferromagnetic/Insulator/Semiconductor
- **F/T/SC:** Ferromagnetic/Tunnel/Semiconductor
- **FP:** Fabry-Perot (Interferometer)
- **FSR:** Free Spectral Range

G.

- **GCD:** Gain Circular Dichroism
- **GMR:** Giant Magneto-Resistance

H.

- **HEMFET:** High-Electron-Mobility-Field-Effect-Transistor
- **HEMT:** High-Electron-Mobility-Transistor
- **HH:** Heavy Hole (Valence Band)
- **HMF:** Half-Metallic Ferromagnet
- **HR-TEM:** High Resolved-Transmission Electron Microscopy

I.

- **ISHE:** Inverse Spin-Hall Effect
- **ITRS:** International Technology Roadmap for Semiconductors

J.

K.

L.

- **LASER:** Light Amplification by Stimulated Emission Radiation
- **LED:** Light Emitting Diode
- **LH:** Light Hole (Valence Band)
- **LIDAR:** LIght Detection and Ranging

M.

- **MA:** Magnetic Anisotropy
- **MBE:** Molecular Beam Epitaxy
- **MCD:** Magnetic Circular Dichroism
- **MOCVD:** Metal-Organic Chemical Vapor Deposition
- **MQW:** Multiple Quantum Wells
- **MRAM:** Magnetic Random Access Memory
- **MTJ:** Magnetic-Tunnel-Junction

N.

O.

P.

- **PD:** Photo-Diode
- **PL:** Photo-Luminescence
- **PMA:** Perpendicular Magnetic Anisotropy

Q.

- **QW:** Quantum Well

R.

- **RGB light source:** Red-Green-Blue light source
- **RHEED:** Reflection High Energy Electron Diffraction
- **RT:** Room Temperature
- **RTA:** Rapid Thermal Annealing

S.

- **SFM:** Spin-Flip Model
- **SHE:** Spin-Hall Effect
- **SO:** Spin-Orbit
- **SQUID:** Superconducting Quantum Interference Device Magnetometer
- **SSE:** Spin-Seebeck Effect
- **STT:** Spin-Transfer-Torque
- **STT-MRAM:** Spin Transfer Torque-Magnetic Random Access Memory

T.

- **TE:** Transverse Electric (Polarization mode)
- **TEGFET:** Two-dimensional-Electron-Gas-Field-Effect-Transistor
- **TM:** Transverse Magnetic (Polarization mode)
- **TMR:** Tunnel Magneto-Resistance
- **TRPL:** Time Resolved Photo-Luminescence

U.

V.

- **VB:** Valence Band
- **VCSEL:** Vertical Cavity Surface Emitting Laser
- **VECSEL:** Vertical External Cavity Surface Emitting Laser

W.

X.

- **XH:** Heavy Exciton

Y.

- **YAG:** Yttrium Aluminum Garnet

Z.

Chapter 1

Introduction: The Rise of Semiconductor Spintronics

Contents

Spintronics describes a paradigm where the information is carried by the electron spin instead of its charge like in mainstream electronics. This offers opportunities for a new generation of devices combining standard microelectronics with spin-dependent effects arising from the interaction between the electrons' spin and the magnetic properties of the material.

The discovery of the Giant Magneto-Resistance (GMR) by Albert Fert [1] and Peter Grunberg [2] in 1988, both awarded the Nobel Prize in 2007, revealed the tremendous potential of spintronics for technological applications. In the consecutive years important research efforts toward the control and manipulation of the electron spin in various systems have been displayed. Fields of studies such as Tunnel Magneto-Resistance (TMR) [3, 4, 5], Spin Transfer Torque oscillators [6] and spin injection in metals [7], semiconductors [8], graphene [9, 10], Carbon Nano-Tubes (CNT) [11] and other organic materials emerged [12, 13, 14] . Impressive R&D achievements enabled to rapidly reach a high technological maturity for the first spintronic based hardware devices [15] leading to the commercialization of hard drives using GMR (IBM, 1997) and TMR (Seagate, 2006), GMR-based galvanic isolators, Magnetic Random Access Memories (MRAM) and in a near future the Spin Transfer Torque Random Access Memories (STT-RAM).
Nevertheless, spintronics present the paradox of being one of the best non-volatile storage technology available while in the meantime the spin information is highly volatile when transported. Even if the science and technology behind passive spintronic devices is well mastered today, the realization of active devices such as Spin-Transistors or Spin-Lasers remains a great challenge. The intense research towards the creation of such components are motivated by the potentiality of combining magnetic storage of information with electronic readout in a single device. In the case of Spin-Lasers for instance, one could envisage to propagate the information contained in a magnetic bit over kilo-metric distances after converting the spin-

information onto the polarization of the emitted light. On the other hand, Spin-Transistors could lead to computers in which the distinction between active and passive memory has been removed and in which the data is processed in the same part of memory in which it is stored [16]. Therefore, this field of condensed matter physics represents one of the great potential alternative to overcome the predicted limits of conventional electronics in a near future.

1.1 Context and motivations

Spin-polarized electron injection into semiconductors has been a field of growing interest for the past two decades. From a technological transfer point of view, it is probably the most promising path to explore regardless of the existing micro-electronic industry dynamic. The injection, transport, manipulation and detection of spins in such materials are the four key points to master in the future to create an active spin-based device. The Spin-High Electron Mobility Field Effect Transistor (HEMFET) proposed by Datta et Das [17] is a great conceptual illustration of what could be achieved with this technology (Figure 1.1).

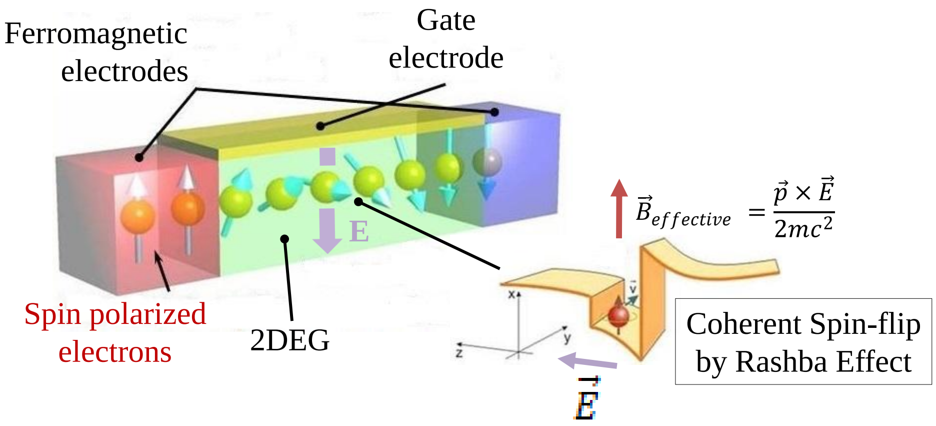

Figure 1.1: Conceptual illustration of Datta et Das Spin-HEMFET [17]. In a spin-FET, spin-polarized electrons are injected from a ferromagnetic source into a semiconductor and detected using a ferromagnetic drain electrode. The coherent spin-flip of the 2D-Electron Gas (2DEG) in the channel can be controlled by the Rashba Effect emerging from the Spin-Orbit interaction [18].

Spin-Transistors, classified by the ITRS as "Non-Conventional Charge-based Extended CMOS Devices", are one of the considered options for the post-CMOS era. Spin-based transistors that do not strictly rely on the raising or lowering of electrostatic barriers can overcome scaling limits in charge-based transistors [19, 20]. Spin transport in semiconductors might also lead to dissipation-less information transfer with pure spin currents [21]. Adding the spin degree of freedom to conventional semiconductor charge-based electronics will add substantially more capability and performance to electronic products [15]. The advantages of these new devices would be non-volatility, increased data processing speed, decreased electric power consumption and increased integration densities compared with conventional semiconductor devices [15]. Different compounds such as IV-IV semiconductors (Si, Ge) [22, 23, 24, 25] and III-V semiconductors (GaAs, InAs) [26] have already been strongly investigated. When thinking about minimizing technological transfer challenges, one probably envisages using Si as transport medium. Indeed it would be very interesting to get conclusive results with this material and take advantage, for future R&D, of the unmatched technological maturity developed by the multi-billion dollars microelectronic industry built around silicon. The first electrical measurements in Si showed a high potential for spin transport with a relatively long spin lifetime and a non-local spin signal detectable up to 500 K [27].

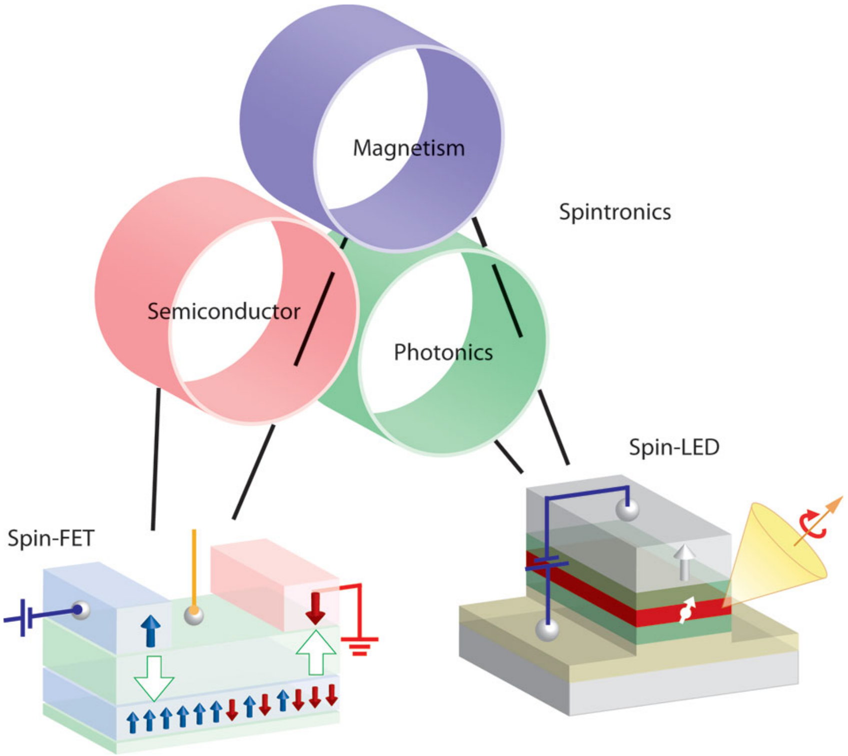

Figure 1.2: General overview of spin-based electronic devices. As opposition with the Spin-FET, in a spin-LED the spin injection efficiency is probed by measuring circularly polarized light emission occurring under spin injection. Figure adapted from reference [28]

Nevertheless, when it comes to the study of spin-injection in semiconductors, III-V compounds also provides really interesting and attractive properties. Binary (GaAs, InP, GaN) and Ternary (InGaAs, GaAsP) III-V semiconductors are already widely used in optoelectronics as base materials for light sources and detectors. Their direct gap enables radiative recombination of the injected carriers. Moreover, the mastering of III-V epitaxy lead to competitive development of high electron mobility transistors (HEMT, HEMFET, TEGFET) which are massively used in hyper-frequency data treatment (cellphones, satellite telecommunications). In the past decade, a continuous interest and a research effort have been dedicated to the study of spin-injection into III-V semiconductor based Light Emitting Device such as Spin-Light Emitting Diodes (Spin-LEDs). The first functional Spin-LED was proposed by Fiederling *et al.* in 1999 [29]. This experimental demonstration opened the door to a new field of study: the opto-spintronics.

In Spin-LEDs (Figure 1.2), the spin information of the injected electrons can be converted into circular polarization information carried by the emitted photons. This information transfer happens through the optical quantum selection rules for dipole radiation associated with the conservation of angular momentum z-projections m_z occurring in confined strained active medium or Quantum Wells (QWs) [30]. This results in an emission of right- or left-circularly polarized photons depending on the electrons' spin orientation. Encouraging results were already obtained with electrically injected Spin-LEDs in applied magnetic field at cryogenic temperatures. Nevertheless, such spin-optoelectronic devices will be competitive for realistic applications only if the spin-injection can be performed electrically at room temperature without an applied magnetic field. Additionally, the device must provide a coherent light emission with switchable polarization state and an output polarization degree (P_c) as high as possible in order for instance to robustly encode a bit of information.

In recent years, Spin-LASERs came out as a potential solution by proposing higher and promising performances in terms of emission coherence (spatially and temporally), output Degree of Circular Polarization (DoCP) and room temperature operation as compared to Spin-LEDs. The amplification effects induced by the combination of a gain medium and a resonant optical cavity give a unique opportunity to maximize the conversion efficiency of the carrier spin-information into light polarization information. Such Spin-LASERs would provide a number of advantages over conventional VCSELs for future optical communication systems such as spin driven reconfigurable optical interconnects [31, 32, 33], fast modulation dynamics [34, 35], polarization control [36, 37] as well as higher performances such as laser threshold reduction [37, 38, 39], improved laser intensity, and polarization stability. The ideas emerging from Spin-LASERs and polarization switching may also motivate other device concepts like, for example, cryptography, coherent detection systems or magneto-optical recording [40].

In terms of device implementation, III-V semiconductor based Vertical Cavity Surface Emitting Lasers (VCSEL) emerged as perfect candidates for a Spin-Laser implementation thank to their vertical geometry (Figure 1.3(a)). Additionally, they exhibit a polarization emission much more isotropic than the conventional side-emitting laser diodes. Outstanding optical [36, 41, 42, 43] and electrical [37, 44] spin-injection results were already achieved in monolithic VCSEL structures in the past few years. However, VCSEL also exhibit intrinsic limitations in terms of noise

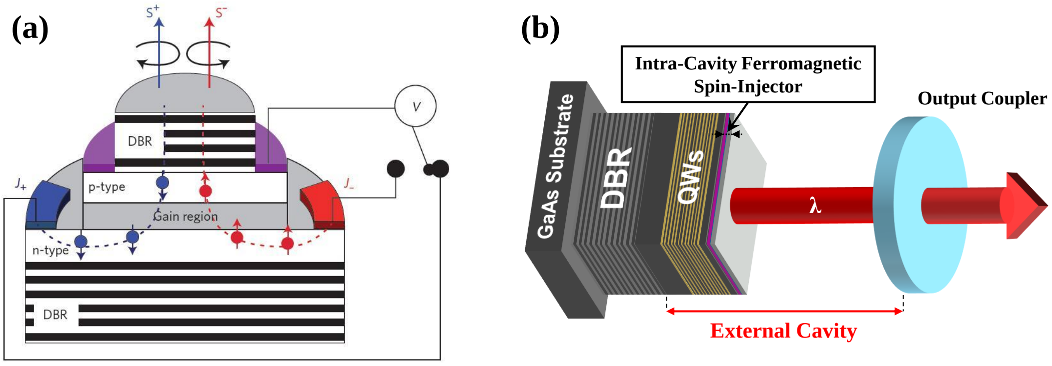

Figure 1.3: Comparison between a monolithic-VCSEL and a VECSEL: (a) Conceptual scheme of a Spin-injected Vertical Cavity Surface Emitting Laser. Figure reprinted from [45]. **(b)** Illustration of a Vertical External Cavity Surface Emitting Laser based on a $\frac{1}{2}$-VCSEL chip. The ferromagnetic spin-injector is deposited inside the external cavity on top of the structure.

performances due to their Class-B behavior, output power and also device flexibility. Indeed, from a fundamental study viewpoint, their compact monolithic design usually standing as a major asset when it comes to application becomes a hindrance for the exploratory approach of spin-injection in lasers with vertical geometries. In particular, when considering electrical spin-injection, the classic VCSEL architecture with the annular top electrode deposited on the top Distributed Bragg Reflector (DBR) far from the active medium is not optimal. To maximize the spin-injection efficiency in optoelectronics devices, a general rule is to minimize the distance between the spin-injector and the active medium of the structures; where radiative recombinations occur in order to minimize the spin-relaxation during electronic transport. Fortunately, Vertical External Cavity Surface Emitting Lasers (VECSEL) based on $\frac{1}{2}$-VCSEL offer effective solutions to overcome these problems.

1.2 The Manuscript

This Ph.D thesis proposes to explore this new paradigm of spin-information propagation over very long distances after encoding on coherent light polarization. This recent multidisciplinary theme, at the interface of Semiconductors, Magnetism and Photonics (Figure 1.2), still present to this day great understanding and technological challenges. While so far all the Spin-Laser experiments have been performed using monolithic VCSEL, we decided during this Ph.D to explore an alternative path by focusing on the study of optical and electrical spin-injection in VECSEL (Figure 1.3(b)). Hereinafter, the term $\frac{1}{2}$-VCSEL describes a monolithic VCSEL where the top DBR has been taken off and characterizes the semiconductor chip itself. However, the term VECSEL defines the whole laser itself where the $\frac{1}{2}$-VCSEL has been completed with a conventional mirror to create an external cavity (Figure 1.3(b)).

VECSEL devices combine wavelength versatility and potential for high output power with a high beam quality. Moreover, they stand out as a perfect tool for the investigation of fundamental physics by allowing the insertion of additional intra-cavity optical components to modify the laser's behavior. They already demonstrated ultrashort pulses generation with modelocking using semiconductor saturable absorber mirrors (SESAM) [46, 47, 48, 49, 50, 51] and also intracavity frequency doubling by inserting a nonlinear crystal into the laser resonator. VECSEL are of great interest for Thales which needs to acquire increasingly sophisticated technologies. In particular for detection, analysis and decision-making technology, in order to design and develop critical information systems. Dual-frequency VECSEL could stand out as innovative solutions in the fields of secure military communications, space systems, air traffic control but also on-board electronics and government information networks. They emit two orthogonally-polarized coherent beams with a frequency detuning between the modes that can be precisely adjusted from few MHz to few THz [52]. Optical sources with low noise-level are also required for applications such as optical-fiber sensing, cryptography and microwave photonics [53]. In terms of electrical spin-injection, the elimination of top DBR in $\frac{1}{2}$-VCSEL offers the unique advantage to deposit a spin-injector on top of the structure as close as possible to the QWs (Figure 1.3(b)). Using this technique maximizes the spin polarization degree reaching the active medium by taking advantage of a spin diffusion length l_{sf} longer than the distance between the injector and the QWs.

Many challenges and interrogations emerged from this ambitious and innovative project which among these: What major physical parameters control the spin-injection in VECSEL? Can the injection of spin-polarized carriers overpower the linear birefringence and set the device polarization? How can we evaluate the conversion efficiency of the spin-information onto the emitted light polarization? For the electrical spin-injection, is it possible to develop a spin-injector with Perpendicular Magnetic Anisotropy at magnetic remanence for room temperature operation free of any applied magnetic field? Also, will the VECSEL tolerate the important losses induced by a highly absorbent ferromagnetic spin-injector deposited intra-cavity?

All these challenges will be addressed in this manuscript. The investigation will be divided into three major chapters. The subject of this thesis being at the interface of Spintronics, Photonics, Semiconductor Physics and Material Science, this manuscipt is addressed to a wide range of readers having completely or partially different backgrounds. Consequently, I made the personal choice to develop an exhaustive State-of-the-art (second chapter) where most of the informations required to fully appreciate this highly multi-disciplinary subject can be found. Additionally, as the *Spin-VECSEL project* started with my Ph.D thesis, one of the manuscript's first vocation is to lay a solid foundation for the good continuation of the project. Consequently, depending on the reader background and knowledge, one should feel free to skip some sections in the first part if the need arises. The presentation of the experimental work performed during this Ph.D thesis starts page 101 and is fully described in the second and the third and fourth chapters of this manuscript.

The second chapter regroups a state-of-the-art of spin-injection into III-V semiconductors optoelectronics devices and focuses on the physical phenomena engaged in the conversion of a spin accumulation into light polarization information. As a preliminary, we start by discussing spin-injection and spin-transport into III-V semiconductor structures. Then, we develop the reference models on spin-injection as well as the state-of-the-art methods to generate a spin accumulation. Following, we detail the several spin relaxation mechanisms originating from spin-orbit interaction. Then, a more device-oriented review is conducted by focusing on spin-injection in Light Emitting Diodes (LEDs) and Vertical Cavity Surface Emitting Lasers (VCSELs). A special attention is given to the understanding of Spin-VCSELs by introducing an analytical analysis and a polarization dynamic model of such systems.

The third chapter is articulated around our experimental work on the development and the optimization on III-V semiconductors LEDs of an ultra-thin MgO/CoFeB/Ta spin-injector with perpendicular magnetization at magnetic remanence. The fundamental comprehension and the material mastering that emerged from this work stood out as a prerequisite for our work on Spin-LASERs. We first start with a general discussion on Spin-LEDs and their fabrication by photolithography process. Then we focus on the optimization of the MgO tunnel barrier for maximizing the spin-injection efficiency. Next, we will detailed the development and the characterization of a MgO(2.5nm)/CoFeB(1.2nm)/Ta(5nm) spin-injector with perpendicular magnetization at remanence. Finally, we conclude on the results and the limits brought to light by this research and further introduce spin-injection in lasers as a potential solution for overcoming the intrinsic limitation of Spin-LEDs.
In this highly collaborative project, the LED structures were grown by Molecular Beam Epitaxy (MBE) at the *Key Laboratory of Semiconductor Materials Science* (Beijing, CHINA) by Prof. B. Xu's team. The ferromagnetic Metal-Tunnel-

Junction (MTJ) spin-injector were deposited and annealed at the *Institut Jean-Lamour* (Nancy, FRANCE) by Dr. Y. Lu's team. The devices characterization by Time Resolved Photo-Luminescence (TRPL) were performed at the *Laboratoire de Physique et de Chimie des Nano-Objet* (Toulouse, FRANCE) by Dr. P. Barate in the team of Prof. Pierre Renucci and Prof. Xavier Marie. I had the luck to be cordially invited by the LPCNO's team to familiarize myself with the experimental setup and participate to some of the TRPL measurements. For this project, I was in charge of the Spin-LEDs fabrication by photolithography process at *Thales Research & Technology* (Palaiseau, FRANCE) and I also took part to the analyze and interpretation of the data.

The forth chapter contains the main part of this thesis work. It is fully dedicated to our experimental work on spin-injection in Vertical External Cavity Surface Emitting Laser structures. Following a general introduction on VECSEL devices, we walk through a vectorial analysis allowing the theoretical understanding of polarization selection in spin-injected VECSELs. Next, we report birefringence measurements of a VECSEL designed for optical pumping using an original frequency detuning measurement between the two orthogonal TE- and TM-modes. Afterward, we present, analyze and commente our observations and results on optical spin injection in VECSELs. The study is farther extended to the characterization of the ratio between the carriers spin-lifetime τ_s and the carriers recombination time τ using TRPL measurements in order to evaluate the spin-information conversion efficiency. Finally, we discuss the preliminary results of our experiments on electrical spin-injection.
This project also involves a lot of partnerships. All the $\frac{1}{2}$-VCSEL structures used during this Ph.D thesis are the result of a fruitful collaboration between Dr. A. Garnache from the *Institut d' électronique du Sud* (Montpellier, FRANCE) and Dr. I. Sagnes from *Laboratoire de Photonique et Nanostructures* (Marcoussis, FRANCE). The designs and simulations of the structures are first performed by the Dr. A. Garnache and the growths are realized using Metal-Organic Chemical Vapor Deposition (MOCVD) by the Dr. I. Sagnes and the Dr. G. Beaudoin. The vectorial model has been developed by the Dr. M. Alouini from the *Insitut de Physique de Rennes* (Rennes, FRANCE). The measurement of the VECSEL's spin-lifetime and carrier-lifetime by TRPL are performed at the *Laboratoire de Physique et de Chimie des Nano-Objet* (Toulouse, FRANCE) by Dr. P. Barate while the *k.p* simulations of the $\frac{1}{2}$-VCSEL structure presented in Chapter 13 are realized by Prof. X. Marie. At *Thales Research Technology*, under the co-supervision of Dr. G. Baili and Dr. J. -M. George, I performed all the experimental investigations related to the optical and electrical spin-injection in VECSEL structures.

CHAPTER 2

Conversion of a magnetic information into light polarization information using spin-injected III-V semiconductors

---

Contents

Introduction

In this first chapter we introduce the state-of-the-art knowledge related to spin-injection into semiconductor Light Emitting Diodes (Spin-LEDs) and Vertical (External) Cavity Surface Emitting Lasers (Spin-V(E)CSELs). The goal is to put in place a granite foundation in order to better understand the challenges around these problematics. It will also outline the experimental work discuss in the third and fourth chapters of the manuscript. As the considered thematic is at the interface between the fields of spintronics and optoelectronics, this investigation will be divided into two main sections respectively devoted to: **(i)** the general study of spin-injection in semiconductors and **(ii)** the relation between injected-carriers/emitted-photons in III-V optoelectronic devices.

For the theoretical study of spin-injection into semiconductors we start by introducing the concept of spin accumulation at a Ferromagnetic/Non-magnetic interface (F/N). We then extend it to Ferromagnetic/Non-Magnetic metallic multilayer systems $\big((F/N)_m \big)$ and further to Ferromagnetic/Semiconductor interface (F/SC). We pursue through the examination of the different way to generate a spin-polarized current in a semiconductor using ferromagnetic tunnel contacts but also pure spin-current thanks to indirect injection mechanism. Finally we complete the section by focusing on the different spin relaxation mechanisms responsible for the loss of current spin-polarization. In other words, we examine the several terms driving the spin lifetime in a semiconductors system: τ_{sf}.

The next section is dedicated to the conversion of a spin accumulation into light polarization information using spin-injected optoelectronic devices. We expose how an optical detection of a spin-polarized current can be performed using the optical quantum selection rules for dipole radiation occuring in confined potentials. We also address the considerations related to the design of spin-polarized light sources and the precautions related to measurement technics. We conclude the state-of-the-art by a device-oriented discussion on Spin-LEDs and show that the limitations of their principal of operation require to go toward spin injection into Spin-V(E)CSELs for cutting edge applications.

2.1 Spin injection into semiconductors

In 1925, Uhlenbeck & Goudsmit introduced the concept of electronic spin to fit the experimental observations of Stern & Gerlach made in 1922. Historically, this new paradigm stood out as a kick-off for a new contemporary vision of electronic transport properties.

Ten years later, Mott first proposed that in a ferromagnetic metal the electrical transport properties can be express as a two-current model [54, 55]. He introduced a model based on the hypothesis that, in a ferromagnet below its Curie Temperature ($T < T_c$) most scattering events will conserve the electron spin direction. Hence, spin-up and spin-down electrons can be considered independent. This means that the electronic current flowing through the ferromagnet can be conceptually visualized as a two-spin channels current. The experimental demonstration was made by Fert & Campbell in 1968 using Nickel systems doped with magnetic impurities [56]. They showed that the conduction process can be considered as two non-equivalent channels where the physical properties in each one of them depends on the electron spin orientation. These two channels are coupled through spin-flip mechanisms.
In 1975, Jullière published the first demonstration of Tunnel Magneto-Resistance (TMR) at low temperature using a Ferromagnetic (F)/Insulator (I)/Ferromagnetic (F) junction [3]. He showed that two resistance states are accessible by the system depending on the relative magnetization orientation of the ferromagnetic layers (Figure 2.1 (b)). It will be several years before Moodera *et al.* demonstrated a 12% TMR effect at room temperature using $CoFeB/Al_2O_3/Co$ junctions [4].

In the mean time, the idea that a spin-current may come with a charge current was theorized by Aronov & Pikus [58]. They observed that the electric current flux originating from a ferromagnetic displayed a spin polarization due to the spin-polarized Density Of State (DOS) of the material. They extrapolated that if this spin-polarized current can be transfer in a non magnetic medium, a transfer of magnetization flux might also operate: the concept of spin injection was born. The first experimental studies in 1985 focused on spin-injection in metals using Conduction Electron Spin Resonance (CESR) methods. It showed a magnetization disequilibrium in the non-magnetic metal induced by spin-injection from the ferromagnetic [59].
In 1988, the discovery of the CIP-GMR[2] by Fert [1] and Gr*ü*nberg [2] placed the spintronic in orbit. The effect is based on the difference of diffusive 4s-3d interaction between majority and minority electrons in a multilayer system. This discovery opened the door to the all-metallic spin-valve device which was patented by Gr*ü*nberg the same year (Figure 2.1 (a)). The GMR stood out as a revolutionary concept as it offers to encode bits of information at room temperature on two resistance level associated with the relative orientation of both magnetizations.

---

[2] CIP: Current In Plane, the current flows parallel to the layers

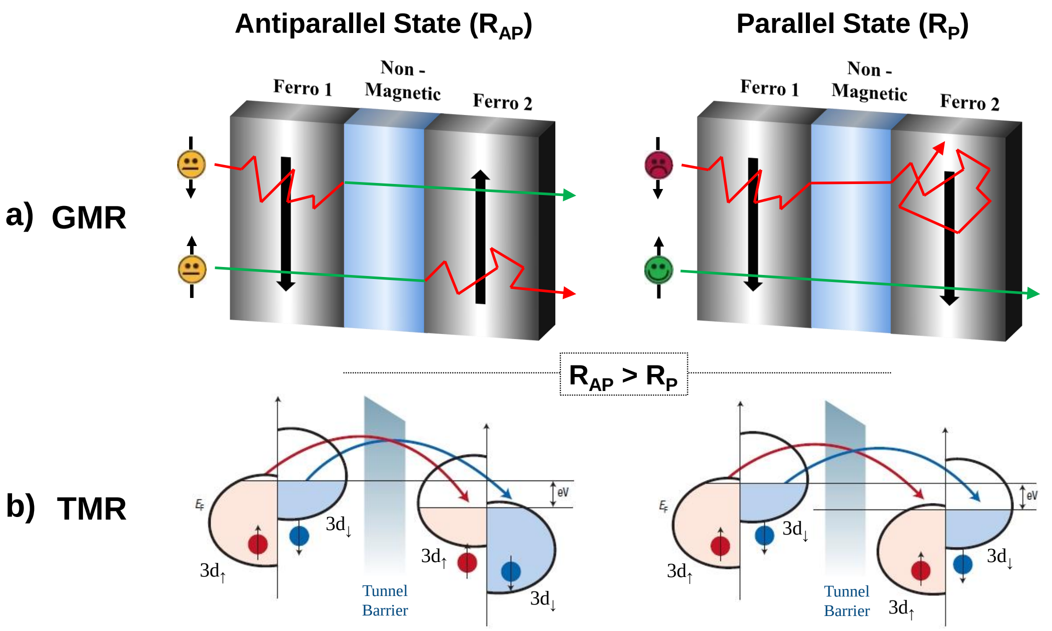

Figure 2.1: Schematic representation of (a) the CPP-GMR[1] and (b) the TMR for both relative magnetization orientations. Even if the output responses are the same: $R_{AP} > R_P$, the physical mechanisms engaged in both effects are different. **(a)** For the GMR, the difference of resistive states originates from the difference of spin-dependent collision probability in the ferromagnetic electrodes for both spin orientation. **(b)** The TMR effect depends on the difference of tunneling probability between the ferromagnetic electrodes 3d-bands for both spin orientations. The output responses measured for the GMR and the TMR can differ by several orders of magnitude. Adapted from [57].

Identifying the tremendous potential of this technological node, IBM bought the patent for the trifling amount of 40 Millions USD and invested an important R&D effort. The efforts of Stuart Parkin and his team lead to the first commercial spin-valve in 1991 [60]. Then in 1997, the first hardrive with a GMR read head was sent on the market by IBM rapidly followed by the first TMR hard-drive in 2006 (Seagate). Today the hard-drive market weight more than 40 Billions USD yearly [61].

Heir to this rich legacy, this section provides the necessary tools required for the fundamental understanding of spin injection in semiconductors.

2.1.1 Theoretical study of spin injection

We are going to historically and logically introduce the most remarkable and relevant models to expose and understand the physical processes controlling the mechanism of injection. To present the electronic transport, the Boltzmann model offers a perfectly adapted general framework to describe mesoscopic system such as thin films used on our devices as spin-injectors. It has been extended by Valet and Fert [62] to describe spin injection through single and multiple Ferromagnetic/Non-Magnetic metallic multilayer systems $\left((F/N)_m \right)$. Once armed with the right toolbox, the study of the Fert-Jaffrès model [63] is going to display the most complete and accurate description of spin-injection phenomenon in semiconductors. From a general point of view, a transport theory is usually built on a reversible dynamic equation (Newton or Schrodinger for instance) combined with one or several irreversibility sources which materialize the irreversibility and the dissipative characteristic of the transport mechanism. Hereinafter, the studied system is considered non-dissipative and in contact with a carrier reservoir in thermal equilibrium.

2.1.1.1 Electronic transport: Boltzmann Model

The Boltzmann formalism enables a modeling of mesoscopic electronic transport by combining a semi-classical definition of the carriers with a probabilist description of dissipative phenomenon. As opposed to the Landauer method which spatially separates the conductive system and the carrier reservoir, it stands as a powerful tool for analyzing transport phenomena within dissipative systems. The strength of the Boltzmann model lies in its capacity to describe mesoscopic conductive systems with the intrinsic dissipative processes regardless of the ratios between the carriers mean free path λ, the spin diffusion length l_{sf} and the system dimensions. In the Boltzmann formalism, electrons are described by a Fermi-Dirac statistic and considered in a parabolic conduction band.

The demonstration of the general Boltzmann equation being unessential to the global understanding of this section, we directly give its expression below. I invite the curious reader to refer to Appendix 1, section A.1 for the formal demonstration of the equation.

$$\boxed{\frac{\partial f}{\partial t} + \vec{v}\frac{\partial f}{\partial \vec{r}} - \frac{e}{\hbar}\left[\vec{E} + \vec{v} \times \vec{H}\right]\frac{\partial f}{\partial \vec{k}} = -\frac{f - f^0}{\tau}} \tag{2.1}$$

where $f(\vec{k}, \vec{r}, t)$ is the carriers Fermi-Dirac distribution function, $f^0(\vec{k})$ the non-perturbed Fermi-Dirac distribution function, $\tau(\vec{k})$ the characteristic scattering time, $\vec{v}(\vec{k})$ the speed of the electronic wave packet and $\vec{F} = -e\left[\vec{E} + \vec{v}(\vec{k}) \times \vec{H}\right]$ is the Lorentz force induced by the applied electromagnetic field. This fundamental equation stands out as the starting point of the Valet-Fert model. In further, solutions are discussed in the particular cases of spin transport through a single Ferromagnetic/Non-Magnetic (F/N) interface and multiple $(F/N)_m$ interfaces.

2.1.1.2 Concept of spin accumulation at a single F/N interface

Preliminary remark: In the following section, we keep the Valet-Fert notation convention where the index $s = \pm$ correspond to the absolute spin direction ($s_x = \pm 1/2$) while ↑,↓ correspond to the majority and minority spin directions in the given conductor.

The Boltzmann model describes the electronic transport properties of a conductor in the most general case. In order to push further our investigation, we have to consider a system closer to Spin-LEDs and Spin-Lasers. These devices are both constituted of an active semi-conductive optoelectronic structure with magnetic contacts playing the role of spin injectors. In first approximation, the spin injection area can simply be describe as a ferromagnetic conductor in contact with a non-magnetic conductor. In this section, we consider the simplest system composed of a ferromagnetic metal (F) in contact with a non-magnetic metal (N) (Figure 2.2). Their conduction bands are described in the "Effective Mass" model. In further, the reader will notice the focalization on the use of ferromagnetic metals (Co, Fe, Ni) as spin injector. Indeed, unlike other ferromagnetic materials (Diluted Magnetic Semiconductors, Half-Metals), they still exhibit a significant spin polarized conduction at room temperature, making them particularly attractive for applications.

In 1936, Mott first introduced the concept of two spin-dependent conduction channels. He considered the conductivities of spin-up and spin-down channels not equal $\sigma_+ \neq \sigma_-$ as the band structure of spin-up and spin-down are distinct in ferromagnets below their Curie Temperature ($T < T_c$). In 1987, van Son *et al.* [64] and Johnson *et al.* [65] independently presented a macroscopic approach describing the electron transport through an interface between ferromagnetic and non-magnetic metals in "Current Perpendicular to the Plane" (CPP) configuration. They introduced the concepts of spin accumulation generated by conductivity splitting $\sigma_+ \neq \sigma_-$ around the interface. If a current is spin-polarized in a ferromagnet, the application of an electrical potential on the F/N bilayer is going to create a spin disequilibrium proportional to the current density J around the interface called spin accumulation $\Delta\mu$. It translates into an additional potential drop historically called "spin-induced interface resistance".

We consider the 1D F/N system under an applied tension $V(z)$ where F occupies the half-space $z < 0$, N the half-space $z > 0$ and where an electronic current flows in the positive z-direction with a density J (A.m^{-2}) perpendicularly to the interface. The two electrochemical potential associated for spin-up and spin-down are defined in any point by $\bar{\mu}_+(z) = \mu_+(z) - eV(z)$ and $\bar{\mu}_-(z) = \mu_-(z) - eV(z)$ respectively, $\mu_\pm$ being the chemical potentials for spin-$\pm$ and e the electron charge. For each

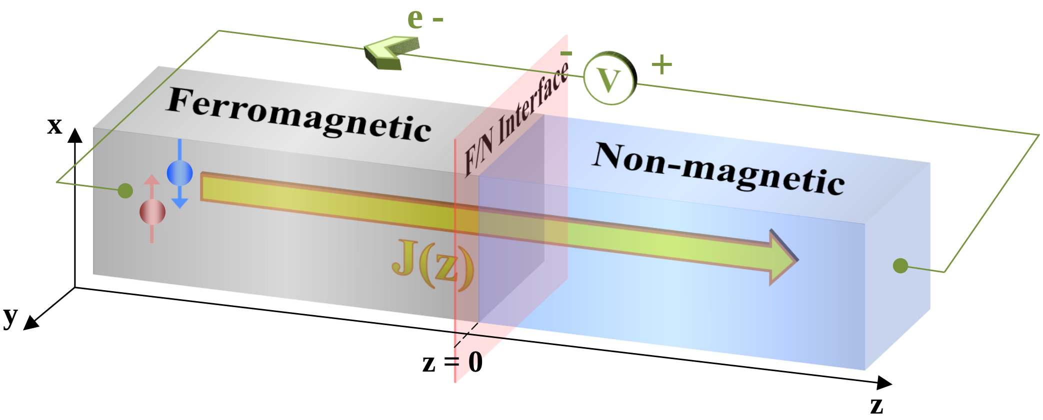

Figure 2.2: Illustration of a 1D Ferromagnetic/Non-magnetic system: The junction is reverse biased and spins are injected from F (grey) into N (blue) through the F/N interface (red).

spin channels, the current determines the spatial variation of the electrochemical potential:

$$\frac{\partial \bar{\mu}_s}{\partial z} = \frac{e}{\sigma_s} J_s \tag{2.2}$$

$$\frac{e}{\sigma_s} \frac{\partial J_s}{\partial z} = \frac{\bar{\mu}_s - \bar{\mu}_{-s}}{l_s^2} \tag{2.3}$$

where σ_s is the conductivity, J_s the current density, $\bar{\mu}_s$ the electrochemical potential and $l_s = \sqrt{D_s \tau_s}$ the spin diffusion length for each spin channel. Equations (2.2) and (2.3) are the macroscopic transport equations in 1D including spin relaxation. Equation (2.2) is an Ohm law while equation (2.3) translates that in a steady-state regime the spin polarized current generates a spin accumulation weighted by spin-flip mechanism.

Far from the interface, spin-up and spin-down are in equilibrium: $\partial(\bar{\mu}_s - \bar{\mu}_{-s})/\partial z = 0$. At the interface the conductivity between F and N changes abruptly while the spin-currents have to be continuous $J_s(z = z_0^-) = J_s(z = z_0^+)$. The potential difference $(\bar{\mu}_s - \bar{\mu}_{-s})$ becomes the driving force of the electrical current. The spin dependent electrochemical potentials can be re-expressed as a function of the spin accumulation $\Delta\mu$ at the interface: $\bar{\mu}_\pm = \bar{\mu} \pm \Delta\mu$. The potential difference $(\bar{\mu}_\pm - \bar{\mu}_\mp) = \pm 2\Delta\mu$ obeys to the following second order diffusion equation deducted by substituting equation (2.2) in (2.3):

$$\boxed{\frac{\partial^2 \Delta\mu}{\partial z^2} = \frac{\Delta\mu}{l_{sf}^2}} \tag{2.4}$$

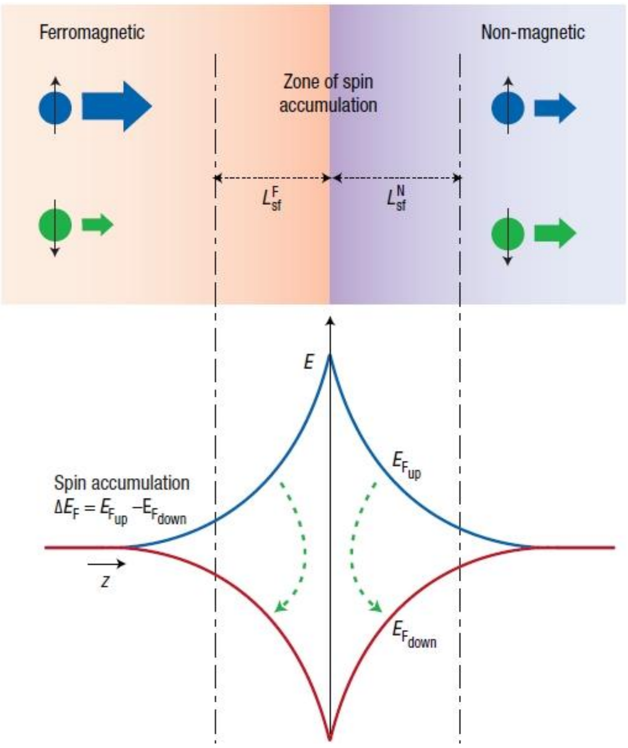

Figure 2.3: Schematic representation of the spin accumulation at an interface between a ferromagnetic metal and a non-magnetic layer generated by a splitting of the Fermi levels E_F^{up} and E_F^{down} at the interface. The dashed green arrows symbolize the transfer of current between the two channels by the unbalanced spin flips caused by the out-of-equilibrium spin-split distribution. Figure reprinted from [57].

where $\left(\frac{1}{l_{sf}}\right)^2 = \left(\frac{1}{l_\uparrow}\right)^2 + \left(\frac{1}{l_\downarrow}\right)^2$, l_{sf} being the average spin diffusion length for both spin channels.

The solution of (2.4) can then be expressed has:

$$\Delta\mu(z) = A \cdot exp\left(\frac{z}{l_{sf}}\right) + B \cdot exp\left(-\frac{z}{l_{sf}}\right) \tag{2.5}$$

where A and B are the exponential pre-factors. They characterize the increase or decrease of spin accumulation as one goes further from the interface across length of the order of l_{sf}. This solution translates the splitting of electrochemical potential between the two spin population occurring at a F/N interface (Figure 2.3). The magnitude of the spin accumulation is determined by the ease with which the current conversion takes place when passing from the ferromagnetic to the non-magnetic material. In the presence of interface scattering, the current conversion process takes place both in the ferromagnetic and the non-magnetic. We extract using the boundary condition:

$$r_s = -\frac{\bar{\mu}_s(z = z_0^+) - \bar{\mu}_s(z = z_0^-)}{|e|\, J_s(z = z_0)} \tag{2.6}$$

where r_s is the interface spin-dependent ”Resistance-Area” (RA) product.

Comments:

- We assumed that the rate of scattering events without spin-flip is greater than the spin-flip rate $\frac{1}{\tau_{sf}}$ for both F and N, where τ_{sf} is the characteristic spin-flip time.

- The continuity condition for the current density J at the F/N interface $J(z = z_0^-) = J(z = z_0^+)$ stays valid as long as the spin relaxation at the interface is negligible [66].

- In the free electron model, the potential drop created by the spin accumulation $\Delta\mu$ can be interpreted as a non-equilibrium magnetization ΔM around the F/N interface [58]:

  $$|\Delta\mu| = \frac{2}{3}\frac{\mu_0|\Delta M|}{n_{E_F}\mu_B} \tag{2.7}$$

  where n_{E_F} is the electronic density at the fermi level and μ_B the Bohr magneton.

2.1.1.3 Extension to multilayers problems $(F/N)_m$: Valet-Fert Model

In 1993, five years after the discovery of the GMR, Valet and Fert proposed a powerful model to solve the problem of magnetic multilayers in CPP-GMR for the most general situation [62]. The Valet-Fert model shows that the macroscopic equations already used by Johnson *et al.* and van Son *et al.* are particular cases of the more general Boltzmann model. They simply considered that the average spin diffusion length is much greater than the electron mean free path $l_{sf} >> \lambda$, even for individual layer thickness of the order of λ.

We consider here a multilayer structure $(F/N)_m$ where signle-domain ferromagnetic metals layers (F) alternate with non-magnetic metal (N) layers. A charge current density J flows through the structure perpendicularly to the interface along the z-axis. The "up" or "down" magnetization of the Ferromagnetic layers is along the x-axis taken as the spin quantification axis.

We investigate the Boltzmann equation model to assess more precisely the validity domain of the macroscopic approach. As all the magnetization of the F layers are collinear it is possible to define a distribution function $f_s(z, \vec{k})$ of the conduction electron for the spin direction s. The general Boltzmann equation (2.1) can be linearized as follow regardless of the considered parameters of the problem:

$$v_z \frac{\partial f_s}{z}(z, \vec{k}) - e\vec{E}(z) v_z \frac{\partial f^0}{\partial \varepsilon}(v) = \frac{\partial f(\vec{k})}{\partial t}\Big(W_s(z,\varepsilon), W_{sf}(z,\varepsilon)\Big)\Big|_{\text{scattering}} \tag{2.8}$$

where $\varepsilon(v) = \frac{1}{2}mv^2$ is the electron energy, $\vec{E}(z) = -\frac{\partial \vec{V}(z)}{z}$ the local electric field and $f^0(v)$ the equilibrium Fermi-Dirac distribution. The collision integral depends on $W_s(z,\varepsilon)$ and $W_{sf}(z,\varepsilon)$ standing for the spin conserving and the spin-flip transition probabilities respectively. These collision integral can be expressed using the Fermi golden rule (see Appendix 1, section A.1).

The velocity distribution function $f_s(z,\vec{k})$ of the considered Boltzmann equation is searched under the following form:

$$f_s(z,\vec{k}) = f^0(v) + \frac{\partial f^0}{\varepsilon}\left\{\left[\mu^0 - \mu_s(z)\right] + g_s(z,\vec{k})\right\} \tag{2.9}$$

where $g_s(z,\vec{k})$ shows the electronic distribution anisotropy and $\mu_s(z)$ is still the spin chemical potential.

By substituting the solution (2.9) in (2.8), one can show that in the CPP geometry the resulting equation is reducible to the system:

$$\begin{cases} \dfrac{e}{\sigma_s}\dfrac{\partial J_s}{\partial z} = \dfrac{\bar{\mu}_s - \bar{\mu}_{-s}}{l_s^2} \\ \dfrac{\partial \bar{\mu}_s}{\partial z}(z) = \dfrac{e}{\sigma_s}\Big[J_s(z) + B\big(\lambda_s(z), J_s(\tilde{z})\big)\Big] \end{cases} \tag{2.10}$$

with: $$B\big(\lambda_s(z), J_s(\tilde{z})\big) = -\tfrac{4}{15}\lambda_s(z)\tfrac{\partial}{\partial z}\int_{-\infty}^{\infty} G_s^{(2)}(z,\tilde{z})\left(\lambda_s(\tilde{z})\frac{\partial J_s}{\partial \tilde{z}}(\tilde{z})\right) \mathrm{d}\tilde{z}$$

where $G_s^{(2)}(z,\tilde{z})$ is a Green function and λ_s the electron mean free path for the spin s. We find the system of macroscopic equations already introduced by van Son *et al.* [64] and Johnson *et al.* [65] without the Boltzmann correction $B\big(\lambda_s(z), J_s(\tilde{z})\big)$. B breaks the linear response between $\frac{\partial \bar{\mu}_s}{\partial z}$ and $J_s(z)$. It shows that, at a given point, the variation of the spin electrochemical potential no longer depends only on the spin current but also on the current divergence $\frac{\partial J_s}{\partial \tilde{z}}$ around this point. The physical origins of this current divergence are the spin relaxation mechanisms occurring on the length scale of the spin diffusion length l_s.

It is demonstrable that the Boltzmann correction term $B\big(\lambda_s(z), J_s(\tilde{z})\big)$ is proportional to $\frac{\lambda_s}{l_{sf}}$ [62]. Accordingly, in the limit case where $l_{sf} \gg \lambda_s$, the Boltzmann correction becomes negligible. This is true when the spin-flip probability during scattering is relatively small: $W_{sf} \simeq \frac{\lambda_s}{l_{sf}} \simeq \sqrt{\frac{\tau_{sf}}{\tau_s}} < 0.1$. This condition is verified in metal with strong spin-orbit coupling as well as in IV and III-V semiconductors. This directly implies that the problem of spin injection through F/N interface reduces to the system of macroscopic equations introduced in the previous section:

$$\left\{\begin{array}{r} \frac{\partial^2 \Delta\mu}{\partial z^2} = \frac{\Delta\mu}{l_{sf}^2} \\ \frac{\partial^2}{\partial z^2}(\sigma_+ \bar{\mu}_+ + \sigma_- \bar{\mu}_-) = 0 \end{array}\right. \tag{2.11}$$

with the two boundary condition at the interface:

$$\left\{\begin{array}{r} J_s(z = z_0^+) - J_s(z = z_0^-) = 0 \\ \bar{\mu}_s(z = z_0^+) - \bar{\mu}_s(z = z_0^-) = -\left|e\right| r_s J_s(z = z_0) \end{array}\right. \tag{2.12}$$

We can straightaway define some useful physical variables to help characterize the system [62]:

- For the considered material (F or N), the Spin-RA product represents the resistivity of a spin-coherent volume:

$$\left\{\begin{array}{l} r_F = \rho_F^* \times l_{sf}^F \\ r_N = \rho_N^* \times l_{sf}^N \end{array}\right. \tag{2.13}$$

- We introduce a bulk spin asymmetry coefficient β for the ferromagnetic layers ($\beta = 0$ for the non-magnetic layers). The resistivity $\rho_{\uparrow(\downarrow)}$ for the majority and minority electrons are given by:

$$\left\{\begin{array}{rl} \rho_{\uparrow(\downarrow)} = \frac{1}{\sigma_{\uparrow(\downarrow)}} = 2\rho_F^*\big(1 - (+)\beta\big) & \text{,for the ferromagnetic layers} \\ \rho_{\uparrow(\downarrow)} = \frac{1}{\sigma_{\uparrow(\downarrow)}} = 2\rho_N^* & \text{,for the non-magnetic layers} \end{array}\right. \tag{2.14}$$

- In a same way than in the bulk, we introduce an interfacial spin asymmetry γ taking into account the spin-dependent interface resistance r_b^*:

$$r_{\uparrow(\downarrow)} = 2r_b^*\big(1 - (+)\gamma\big) \tag{2.15}$$

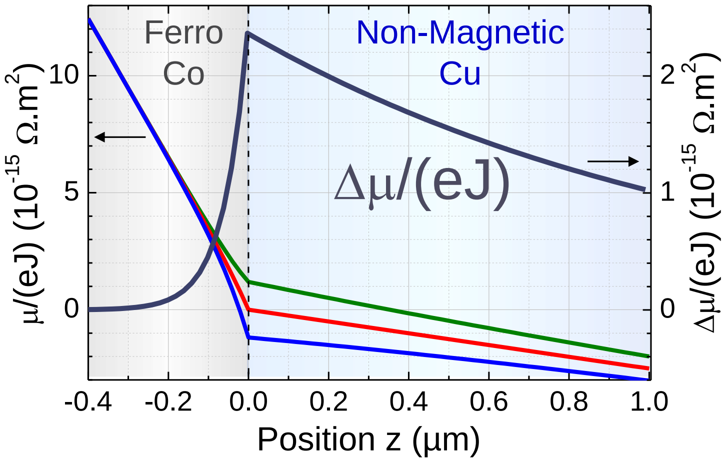

Figure 2.4: Electrochemical potentials profiles for spin-up (green), spin-down (blue)and the average spin population $\frac{\mu_\uparrow+\mu_\downarrow}{2}$ (red) for a Co/Cu junction. The right scales shows the accumulation profile associated with the splitting of electrochemical potential for both spin populations at the interface. It also illustrates the spin diffusion length asymmetry between the ferromagnetic and the non-magnetic. The physical values used for the simulation can be found in reference [63]. Figure adapted from [67].

From the four equations (2.11) and (2.12) it is possible to calculate all the spin-polarized electronic transport parameters relative to a F/N bilayer system. The general solutions obtained from the Valet-Fert theory give the expression of the electrochemical potentials and the associated currents. These detailed solutions can be found in Appendix 1, section A.2. The evolution of the electrochemical potentials at the interface Co/Cu is illustrated in figure 2.4.

In conclusion, by using the general solutions (Appendix 1, section A.2) and taking into account the boundary conditions (2.12) at each interfaces, we can now calculate any physical parameter of interest in any $(F/N)_m$ multilayer structures. In the following, as the studied spin-optoelectronic device are semiconductor-based, we are going to place much interest in the specific case of a single F/N interface where the non-magnetic layer is a semiconductor (SC). In the next section, we will demonstrate and discuss some specific interface issues resulting of a F/SC system. Then we will see what strategies allows to overcome these problems and efficiently control the spin injection in a semiconductor.

Comments:

- The analysis is limited to zero temperature where the electron-magnon spin-flip scattering is frozen out. Thus the spin-flip scattering events occur through spin-orbit interactions on defects or impurities.
- The displayed equations are valid under low applied electric field in the flat-band hypothesis. In the case of a semiconductor for instance, the spin accumu-

lation generates a spin-dependance of the carriers number in the semiconductor as soon as the band curvature has to be considered [68, 69].

2.1.1.4 Efficient spin injection in a semiconductor: Fert-Jaffrès Model

The Valet-Fert model is a formidable tool to understand the spin mechanisms engaged when spin injection is performed in a ferromagnetic/non-magnetic metallic multilayer structures. However, additional issues emerge when the considered non magnetic material is a semiconductor.

In 1999, the first spin injection experiments from a ferromagnetic metal (F) into a semiconductor (SC) showed interface current polarizations of noly few percents [70, 71]. In 2000, Schmidt *et al.* solved the macroscopic spin transport equation in the diffusive regime at a F/SC interface. They revealed that the fundamental obstacle for an efficient injection originates from the conductivity mismatch between the ferromagnetic metal and semiconductor [72]. The problem is rooted in the large DOS difference between F and SC (Figure 2.5).

In 2001, Fert and Jaffrès confronted the Valet-Fert model to the issue of spin injection from a ferromagnetic metal (F) into a semiconductor (SC). They described the perpendicular spin-polarized electronic transport through F/SC and $F/Tunnel/SC$ interfaces [63]. They extended the Valet-Fert model by including a spin-dependent interface resistance r_b^*. It demonstrates an enhancement of the spin polarization of the injected current in the CPP geometry when the interface resistance stands above a threshold value related to the resistivity ρ_{SC}^* and the spin diffusion length l_{sf}^{SC} of the semiconductor. Emmanuel Rashba simultaneously demonstrated theoretically how the use of tunnel contacts can dramatically increase spin injection in a semiconductor by solving the impedance mismatch problem [73]. Nev-

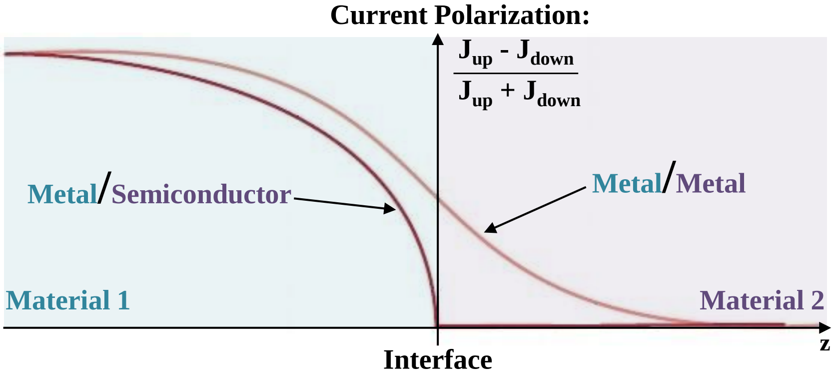

Figure 2.5: Variation of current spin polarization: (i) when there is an approximate balance between the spin flips on both sides (metal/metal) and (ii) when the spin flips on the left side are predominant (metal/semiconductor, for example). Figure reprinted from [57].

ertheless, by neglecting the spin relaxation in the non-magnetic canal, the Rashba approach is not entirely accurate. Indeed, it has been showed experimentally that the detection conditions are essential for the spin information preservation [11, 9, 74]. Consequently, I chose to develop in this section the Fert-Jaffrès model which is from a general point of view more complete, rigorous and in line with the experimental observations.

The objective here is to understand the physical phenomena behind the impedance mismatch issue conducive to the experimental implementation of a functional semiconductor-based spin-injected optoelectronic device.

We consider the system made of a semi-infinite single domain ferromagnetic metal F $]-\infty; z < z_0]$ in contact at z_0 with a semi-infinite semiconductor SC $[z > z_0; +\infty[$. The interface F/SC is parallel to the (x,y)-plan and a charge current density J flows through the structure along the z-axis (Figure 2.6).

We consider the particular case where the spin diffusion length is much greater than the mean free path of the carriers: $l_{sf} >> \lambda$. As a direct consequence, $\lim_{l_{sf}>>\lambda} B\big(\lambda_s(z), J_s(\tilde{z})\big) \longmapsto 0$ and the macroscopic drift diffusion equations (2.10) are still valid for the F/SC system without having to take into account the Boltzmann correction term. In a given layer, the equation system (2.10) can be rewritten as a function of the resistivity ρ_s for spin s, the spin lifetime τ_{sf}, the spin accumulation $\Delta\mu = \bar{\mu}_+ - \bar{\mu}_-$ and the variation of the total number of carrier at the Fermi Level $\frac{\partial n}{\partial E_F}$:

$$\begin{cases} J = J_s + J_{-s} \\ J_s = \dfrac{1}{|e|\rho_s}\dfrac{\partial \bar{\mu}_s}{\partial z} \\ \dfrac{\partial (J_s - J_{-s})}{\partial z}(z) = \dfrac{2e}{\tau_{sf}}\dfrac{\partial n}{\partial E_F}\Delta\mu \end{cases} \tag{2.16}$$

We find the variation of electrochemical potential:

$$\frac{\partial^2 \Delta\mu}{\partial z^2} = \frac{\Delta\mu}{l_{sf}^2} \tag{2.17}$$

where $l_{sf}^{F(SC)}$ is the spin diffusion length of the considered material. Contrary to metals, transport properties of semiconductors strongly depend on the position of the Fermi level in the band structure. We can identify two situations depending on the nature of the semiconductor conduction regime:

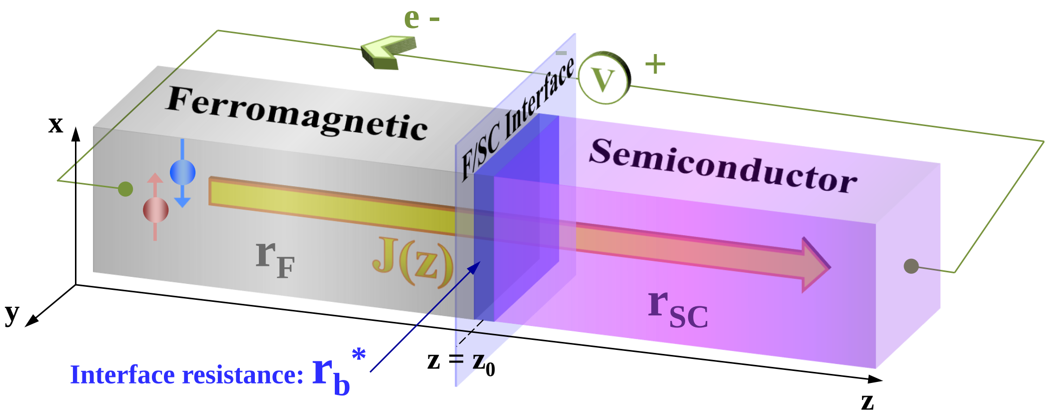

Figure 2.6: Illustration of a ferromagnetic metal (F) is in contact with a Semiconductor (SC) in $z = z_0$. We consider an interfacial resistance r_b^* as a characteristic parameter of the F/SC contact, as well as the RA-products r_F and r_{SC} for the ferromagnetic and the semiconductor respectively.

- If SC is a non-degenerate semiconductor:

$$\frac{\partial n}{\partial E_F} = \frac{n}{2k_BT} \qquad \Longrightarrow \qquad l_{sf}^{SC} = \sqrt{\frac{k_BT\tau_{sf}}{2ne^2\rho_{SC}^*}}$$

- If SC is identified as a degenerate Fermi gas semiconductor ($\Longleftrightarrow$ metal):

$$\frac{\partial n}{\partial E_F} = N(E_F) \qquad \Longrightarrow \qquad l_{sf}^{SC} = \sqrt{\frac{\tau_{sf}}{4e^2N(E_F)\rho_{SC}^*}}$$

The expression of the electrochemical potentials and the associated currents for the considered F/SC structure can be derived from the general solutions of the Valet-Fert model (Appendix 1, section A.2). This new set of solution specific to spin-injection into semiconductors can be found in Appendix 1, section A.3.

Comments:

► For the ferromagnetic metal, we kept the assumption of the Valet-Fert Model: $N_+(E_F) = N_-(E_F) = N(E_F)$. But, as F presents different densities of states for spin-up ($N_+(E_F)$) and spin-down ($N_-(E_F)$), if one wants to be perfectly accurate in the calculations it is necessary to replace $N(E_F)$ by $\bar{N}(E_F) = \frac{1}{N_+(E_F)} + \frac{1}{N_-(E_F)}$

Impact of the interface resistance on spin injection:

In order to pull the blinds on the physics mechanisms ruling the spin injection in semiconductors, it is interesting to pay close attention to the variation of current spin polarization at the F/SC boundary: P_S^b. Using the expressions of the electrochemical potentials and the associated currents for the considered F/SC structure (Appendix 1, section A.3), P_S^b can be expressed as a function of the interface resistance r_b^* and the spin-RA products r_F and r_{SC} of the ferromagnetic and the semiconductor respectively:

$$\boxed{P_S^b = \left(\frac{J_+ - J_-}{J}\right)_b = \frac{\beta r_F + \gamma r_b^*}{r_F + r_{SC} + r_b^*}} \tag{2.18}$$

We use this expression of the current spin-polarization at the F/SC boundary to discriminate different situations depending on the presence or not of interface resistance between F and SC. We also need to consider the relative ratio between r_b^* and the spin-RA products (r_F, r_{SC}).

A) **If there is no interface resistance: $r_b^* = 0$:**
The variations of current spin-polarization reduces to:

$$P_S^b = \frac{\beta r_F}{r_F + r_{SC}} = \frac{\beta}{1 + \frac{r_{SC}}{r_F}}$$

As previously discussed, the expression of the spin diffusion length and so r_{SC} depends on the semiconductor regime. Thus, we can distinguish two sub-cases:

1. $r_b^* = 0$ **and SC is a non-degenerate semiconductor:**

We already defined in (2.13) that $r_F = \rho_F^* \times l_{sf}^F$ and $r_{SC} = \rho_{SC}^* \times l_{sf}^{SC}$. As in the Drude model (diffusive regime) $\rho = \frac{m}{ne^2\tau}$ and using the expression of l_{sf} extracted from (2.29), it is possible to express the Spin-RA products as a function of the carrier densities n_F and n_{SC} in the materials:

$$\begin{cases} r_F = \dfrac{\hbar\pi}{(3\pi^2)^{\frac{1}{6}} e^2} \sqrt{\dfrac{\tau_{sf}^{SC}}{2\tau}} n_{SC}^{-\frac{2}{3}} \\ r_{SC} = \sqrt{2mk_bT \dfrac{\tau_{sf}^F}{\tau} e^2 n_F^{-1}} \end{cases}$$

Despite the difference of τ_{sf} values between the ferromagnetic metal and the semiconductor ($\tau_{sf}^{F} \approx 1\ ns << \tau_{sf}^{SC} \approx 100\ ns$ [75, 76]), the behavior of r_F and r_{SC} is driven by the evolution of the carrier density n. As the semiconductor is non-degenerated, we can affirm that $n_F >> n_{SC}$ directly implying: $r_F << r_{SC}$. This means:

$$\lim_{\substack{r_F << r_{SC} \\ r_b^* = 0}} \left(P_S^b = \frac{\beta}{1 + \frac{r_{SC}}{r_F}} \right) \longmapsto 0$$

We understand here the weak spin injection rates witnessed during the first spin injection experiments in semiconductors. This strong reduction of injected spin polarization had already been pointed out by Schimdt *et al.* [72]

2. **$r_b^* = 0$ and SC is identify as a degenerate Fermi gas semiconductor ($\Longleftrightarrow$ metal):**

In this case $n_F \approx n_{SC} \implies r_F \approx r_{SC}$ and:

$$\lim_{\substack{r_F \approx r_{SC} \\ r_b^* = 0}} \left(P_S^b = \frac{\beta}{1 + \frac{r_{SC}}{r_F}} \right) \longmapsto \frac{\beta}{2}$$

The spin polarization of the current penetrating the semiconductor is reduced by half from the value of the ferromagnetic bulk spin asymmetry coefficient β. This situation holds when a ferromagnetic metal is in contact with a non-magnetic metal (Valet-Fert F/N case) such as the Co/Cu system for instance.

B) **When an interface resistance is introduced: $r_b^* \neq 0$:**

Even in the presence of an interface resistance, the spin polarization injected in the semiconductor will be significant only if the spin dependent interface resistance is at least of the order of magnitude of the semiconductor resistance: $r_b^* \geq \{r_F, r_{SC}\}$.

1. **If the interface resistance is high enough to fully control the injection at interface: $r_b^* >> \{r_F, r_{SC}\}$**

It is not of importance here to separate the two cases of the degenerate ($r_F \approx r_{SC}$) and non-degenerate ($r_F << r_{SC}$) semiconductor because for both situations the interface resistance controls the behavior of the spin-injection. We have:

$$\lim_{\substack{r_b^* >> \{r_F, r_{SC}\} \\ r_b^* \neq 0}} \left(P_S^b = \frac{\beta r_F + \gamma r_b^*}{r_F + r_{SC} + r_b^*} \right) \longmapsto \frac{\gamma r_b^*}{r_b^*} = \gamma$$

When the interface resistance drives the injection at the interface and fully overcome the impedance mismatch, the current spin polarization is given by the interfacial spin asymmetry γ.

2. **If SC is non degenerated and $r_b^* \approx r_{SC} > r_F$:**

$$\lim_{\substack{r_b^* \approx r_{SC} > r_F \\ r_b^* \neq 0}} \left(P_S^b \right) \longmapsto \frac{\gamma}{2}$$

In practice, this intermediate regime is quite representative of ferromagnetic contacts on semiconductors. The spin accumulation is limited by the spin relaxation in F (spin back-flow) induced by the coupling with the ferromagnetic metal. Although it is still a manifestation of the impedance mismatch, it is usually classified as the "Back flow regime".

3. **If SC is identify as a degenerate Fermi gas semiconductor ($\Longleftrightarrow$ metal) and $r_b^* \approx r_{SC} \approx r_F$:**

$$\lim_{\substack{r_b^* \approx r_{SC} \approx r_F \\ r_b^* \neq 0}} \left(P_S^b \right) \longmapsto \frac{\beta + \gamma}{3}$$

The spin polarized current injected in the degenerate semiconductor has a double dependance on the spin asymmetry occurring in the bulk of the ferromagnetic injector and at the interface.

Conclusions: Theoretical conditions for an efficient experimental spin injection in semiconductors:

As a first thought, I would like to thanks and congratulate the reader for following me through this bestiary of 18 equations in the name of the spin injection understandings. Beyond all this mathematical formalism, the one fundamental concept to remember here for the successful implementation of a spin-optoelectronic device is that: a spin-dependent interface resistance r_b^*, greater than the threshold value r_{SC}, needs to be inserted between the ferromagnetic metal spin injector and the semiconductor.

In the absence of interface resistance, the Fermi energy splitting due to spin accumulation $\Delta\mu$ has the same value $\Delta\mu_b$ on both side of the interface. When one goes away from the interface, this spin accumulation decreases exponentially with decays lengths l_{sf}^F and l_{sf}^{SC}. The variations of current spin polarization in F and SC are proportional to the respective spin-flip probabilities in F and SC. It is demonstrable that with the same $\Delta\mu_b$ in F and SC these total spin-flip rates are respectively proportional to $\frac{1}{r_F}$ and $\frac{1}{r_{SC}}$. When the semiconductor is non-degenerate $r_F << r_{SC}$, the spin-flip rate and so the spin-depolarization of the current are more important in F than in SC. To summarize, without interface resistance ($r_b^* = 0$), the current is already completely depolarized when it crosses the interface ($P_S^b \longmapsto 0$). The addition of an interface resistance introduces a spin dependent discontinuity of $\Delta\mu$ at the interface and generate a much higher $\Delta\mu$ in the semiconductor than in the ferromagnetic metal. This leads to a more balanced spin-flip ratio between F and SC thus restoring the spin polarization at the interface and in the semiconductor.

The resistance and the depolarization at an interface can be measured experimentally [77]. Most of the time in the literature, the F/SC junctions are characterized by the tension variation ΔV associated with their Resistance-Area (RA) product independent of the junction dimensions:

$$\boxed{R_S A = \frac{\Delta V}{I} A = \frac{\gamma \Delta\mu}{2eJ} = \gamma r_{SC} \left(\frac{\beta r_F + \gamma r_b^*}{r_F + r_{SC} + r_b^*} \right) \underset{r_F << \{r_{SC}, r_b^*\}}{\longmapsto} \frac{\gamma^2 r_b^* r_{SC}}{r_b^* + r_{SC}}} \qquad (2.19)$$

Ideally, from the experimental perspective, one wants to prepare a system that fits the case *B)1)*. The very high resistance required by the condition $r_{SC} << r_b^*$ combines with the need of a significant spin asymmetry γ can be delivered by tunnel junctions. These Magnetic-Tunnel-Junction (MTJ) are achieved by inserting an ultra-thin insulating layer between the ferromagnetic metal and the semiconductor. Because of the excellent results they display in metallic systems, the two most used barrier materials are the aluminum oxide (AlO_x) and the magnesium oxide (MgO) [100, 103, 99, 97].

Another way is to use Schottky barriers by putting the ferromagnetic injector directly in contact with the semiconductor over-doped on a small thickness at the

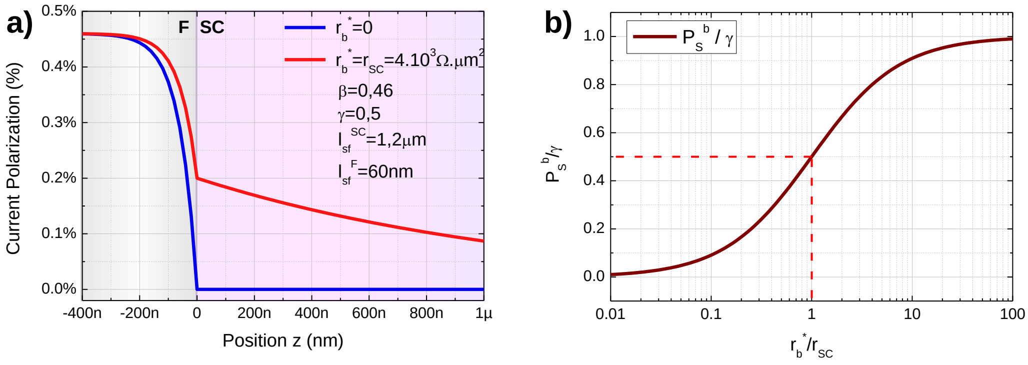

Figure 2.7: **(a) Evolution of the current spin polarization at a Ferromagnetic/Semiconductor interface for different values interface resistance.** We considered the case where the interface resistance is non-existant (blue) and the case where the interface resistance is of the order-of-magnitude of the semiconductor resistance (red). **(b) Evolution of the normalized current spin polarization at the interface** as a function of the ratio between the interface resistance and the semiconductor resistance. Figure adapted from [67].

interface. The spin-polarized electrons are injected by tunnel effect through the potential barrier created by the Schottky contact. These Schottky injectors also display large interface resistances but it requires most of the time an important band engineering development to control the height and the thickness of the potential barrier in order to get an efficient electrons tunneling.

The reader should be aware that, despite the fundamental understandings it provides, the above-introduced study remains a simplified approach of spin-injection into semiconductors. The reality tends to be more complex as the nature of the F/SC or $F/T/SC$ contacts modifies the pinning of the Fermi level in the band structure. Such structure and interfaces can also tune the carrier population and trigger electric field variations near the interface(s).

In the next section, we will walk through the different ways to generate a spin-polarized current in a semiconductor structure. In terms of direct injection, as they gave and still give the most impressive results in the literature, we will pay a particular attention to the MTJ and Schottky barrier injectors. We can already reveal that we are also working with MTJ spin-injectors based on $MgO/CoFeB/Ta$ multilayers for our experiments with Spin-LED and Spin-VECSEL. Their optimization and the experimental results they provided during this Ph.D will be precisely detailed in the third chapter of the manuscript.

2.1.2 Generation of a spin-polarized carriers in a semiconductor

When it comes to generating a spin-current in a semiconductor, several methods can be explored. Obviously, what first comes to mind is the use of a ferromagnetic materials directly in contact with the semiconductor to be used as a spin-polarizer. But, in well designed devices, one has also the possibility to take advantages of some physical mechanisms link to light/matter interaction, heat diffusion or whether electronic diffusion to indirectly engender a spin accumulation. This second section is fully devoted to the introduction and the description of these state-of-the-art mechanisms.

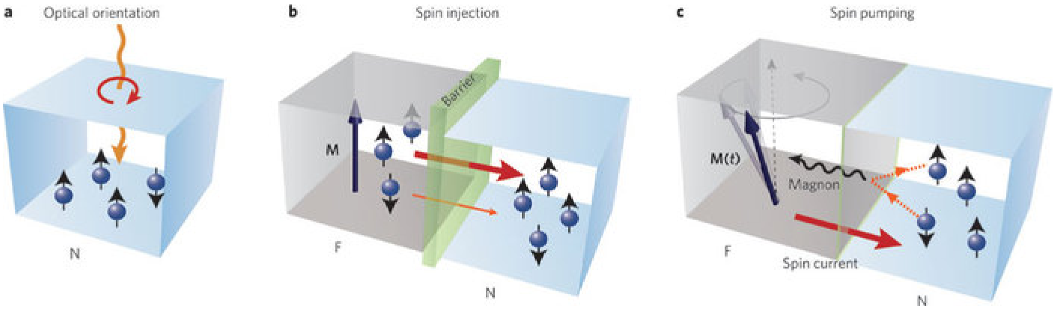

Figure 2.8: Illustration of three physical mechanism generator of spin imbalance in a non-magnetic material. Figure reprinted from [78].

2.1.2.1 Electrical spin-injection from a ferromagnetic metals

Here we discuss the generation of a spin polarized current in a semiconductor using "direct spin-injection" through ferromagnetic metals. The generation of a spin-current, in the two-spin channels conduction model, is directly associated with a disequilibrium between the spin-up electrons and the spin-down electrons populations. It is useful to emphasize the important distinction between the spin polarization of the injected electron current and the spin polarization of the electron density. Indeed, even if an injected current is highly polarized, it can result in small changes in the spin population of conduction electrons if the electron gas into which the injection occurs has a high density or if the injection current magnitude is small [79].

The use of ferromagnetic metals as spin-injector on non-magnetic metallic and semiconductors structures was first theoretically predicted by Aronov & Pikus in 1976. Their research were stimulated by the early work of Tedrow & Meservey on spin injection in superconductors using Ferromagnetic (F)/Insulator (I)/Superconductor (S) junctions [80]. In 1971, they succeeded in measuring the spin polarization at the FM/I interface using Andreev reflexion experiment.[3]

---

[3] The Andreev reflection (Andreev 1964) is a scattering process responsible for a conversion between a dissipative quasi-particle current and a dissipation-less super-current.

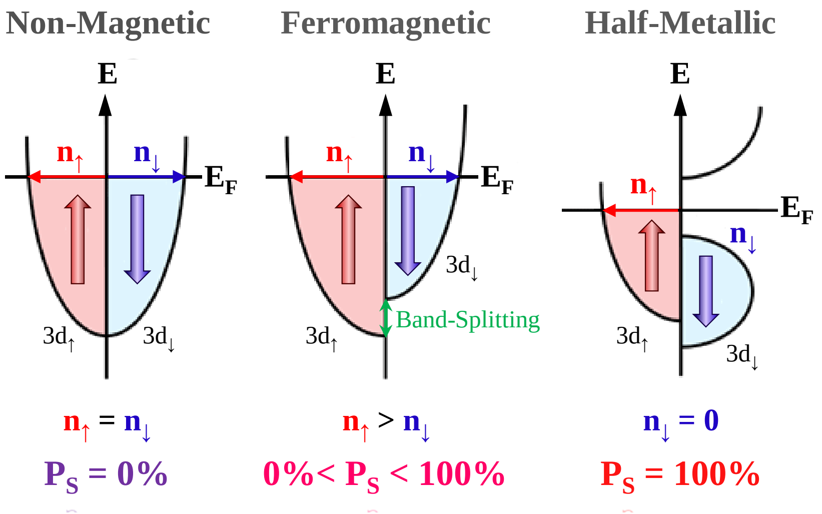

Figure 2.9: Scheme of the 3d-band structures for a non-magnetic metal, a ferromagnetic metal and a Half-Metal. It illustrates how the spin-polarization P_S directly depends on the difference of DOS for the two spin populations at the Fermi level generated by the spin-splitting of the d-states

The use of ferromagnetic metals (Fe, Co, Ni) and their alloys ($CoFe$, $CoFeB$, $NiFe$) for spin-injection experiments is motivated by their high Curie temperature T_c. This property makes them particularly suitable for room temperature applications and potential future spintronics devices (Table 2.1). In a ferromagnetic metal, the DOS at the Fermi level has both s- and d- components. The exchange interaction in the ferromagnet leads to a spin-splitting of the d-states and therefore to different DOS for the two spin populations at the Fermi level (Figure 2.9) [81]. The current flowing in the metal is carried by the s-electrons since s-electrons have significantly smaller effective mass compared to d-electrons. However, due to the splitting of the d-like DOS, spin-up and spin-down electrons have different probabilities of scattering into the d-states. This result in different mobilities for spin-up and spin-down s-electrons [82]. Consequently, the current flow will be dominated by s-electrons in the spin-state with the less d-like DOS at the Fermi level. The spin polarization of the ferromagnetic at the Fermi level is given by:

$$P_S^F = \frac{n_\uparrow^F - n_\downarrow^F}{n_\uparrow^F + n_\downarrow^F} \tag{2.20}$$

where $n_\uparrow^F$ and $n_\downarrow^F$ are the DOS at the Fermi level for spin-up and spin-down in the ferromagnet respectively. It describes the degree to which one spin sub-band is occupied relative to the other. Experimental values of spin-polarization for commonly used ferromagnetic metals and alloys are given in Table 2.1 [83][4].

---

[4] These experimental results were measured using $Ferromagnetic/Al_2O_3/Superconductor$ tun-

	P_S	M	B_s	H_c	μ_{max}	T_c	ρ
Metal	$\%$	$10^3 kg \cdot m^{-3}$	T	$A \cdot m^{-1}$	-	K	$10^{-8}\Omega \cdot m$
Fe	44	7.8	2.15	4	180000	1043	10
Co	45	8.9	1.79	1600	-	1400	6.24
Ni	33	8.9	0.615	800	1000	631	6.84
$Co_{50}Fe_{50}$	51	-	-	-	-	1388	-
$Ni_{80}Fe_{20}$	48	-	0.75	-	300000	723	-

Table 2.1: Intrinsic spin polarization and datasheet of the ferromagnetic metals and alloys commonly used as spin-injectors

The spin-polarization of the current injected into the non-magnetic semiconductor P_S^{SC} is typically used to characterize the spin injection efficiency of the ferromagnet/semiconductor structure. The injected spin-polarization and spin-injection efficiency η are defined as [84]:

$$\begin{cases} P_S^{SC} = \dfrac{n_\uparrow^{SC} - n_\downarrow^{SC}}{n_\uparrow^{SC} + n_\downarrow^{SC}} \\ \eta = \dfrac{P_S^{SC}}{P_S^F} \end{cases} \tag{2.21}$$

where $n_\uparrow^{SC}$ and $n_\downarrow^{SC}$ represent the DOS at the Fermi level for majority and minority spins in the non-magnetic semiconductor respectively. While the choice of P_S^F requires careful considerations [85, 86], η provides a figure of merit for the comparison of various spin injection structures. To this day, the spin injection efficiency is experimentally always inferior to 100% due to limitations factors such as interface quality, defect/impurity densities, band structures but also by the limited intrinsic spin polarization of ferromagnet P_S^F (up to 50% for the best ferromagnetic metals). Studies revealed that interface defects such as stacking faults, poorly matched band symmetries and the formation of "magnetically dead" interfacial layers during epitaxial growth all result in reduced spin injection efficiencies [84, 87].

As introduced in the previous section, with a normal ohmic contact between a ferromagnetic and a semiconductor, the large conductivity mismatch [72] leads to nearly negligible spin injection efficiency. The interfacial resistance r_b^* necessary to reach an efficient spin injection regime can be experimentally implemented by the use of a tunnel contact. There are different ways to implement a tunnel barrier in semiconductors. Theoretically, Fermi electrons cannot enter the conduction band of most semiconductors from a metallic contact without undergoing a tunneling through the native Schottky barrier [88]. An efficient tunnel contact can be

---

nel junctions. The values of the conduction electrons spin-polarization P_S depend of the measurement technique.

engineered by inserting a thin and heavily doped semiconductor layer at the interface with the metal. A second possibility is to introduce an artificial magnetic or non-magnetic tunnel barrier between the metal and the semiconductor. In further, both mechanisms are detailed based on the comparison studies made by Van Roy *et al.* in the review entitled "Spin injection in LEDs and in unipolar devices" [89] and by Gregg *et al.* in the review "Spin electronics" [81]. We remind that, as an electron approaches a tunnel barrier, it satisfies the following Schrodinger equation and solution:

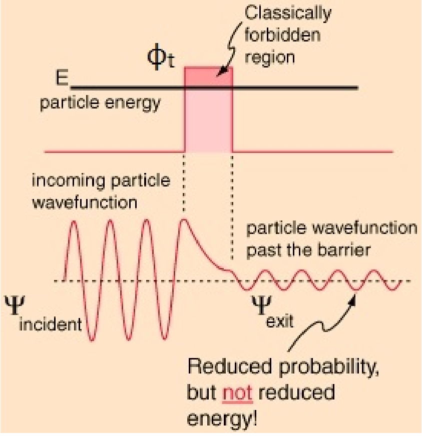

Figure 2.10: $\frac{-\hbar^2}{2m}\frac{\partial^2\Psi(z)}{\partial z^2} = (E-\Phi_t)\,\Psi(z)$

The associated solution is given by:

$\Psi(z) = A \cdot exp\,(-\alpha z)$ with $\alpha = \sqrt{\frac{2m(E-\Phi_t)}{\hbar^2}}$,

where m is the electron mass, Φ_t the barrier height, A an exponential pre-factor and α the evanescent decay of the wave function.

Figure extracted from [90].

In tunnel contacts, the tunnelling rate of the electrons is proportional to the DOS of the materials on both sides of the tunnel barriers. This property enables a robust spin injection from the metal into the semiconductor due to the spin splitting of the d-states in the ferromagnetic metals.

Schottky tunnel injectors

The first glaring result of electrical spin injection from a ferromagnetic metal into a semiconductor at RT was realized using a Fe/GaAs Schottky contact [91]. A Schottky barrier provides a natural tunnel barrier between a metal contact and a semiconductor. It is already a routine ingredient in semiconductor device technology [92]. Surface states in semiconductors usually cause the Fermi level of a metal contact to be pinned in the middle of the semiconductor band gap. This results in a Schottky barrier with a width depending on the subsurface doping level of the semiconductor. When the doping level is sufficiently high ($\approx 10^{19} cm^{-3}$), the Schottky barrier is narrow enough to allow tunneling. This results in an original way of creating a tunnel barrier on semiconductors [93, 88, 92, 94]. The highly doped subsurface layer needs to be carefully tailored such that it is fully depleted and the drop of built-in voltage is exactly large enough to accommodate the full height of the Schottky barrier. If the subsurface layer is under-dimensioned (insufficient thickness and/or insufficient doping level) the rectifying behavior remains as part of the energy offset. On the contrary, if the subsurface layer is over-dimensioned (layer too thick and/or doping level too high) an undepleted n^{++} region will remain which

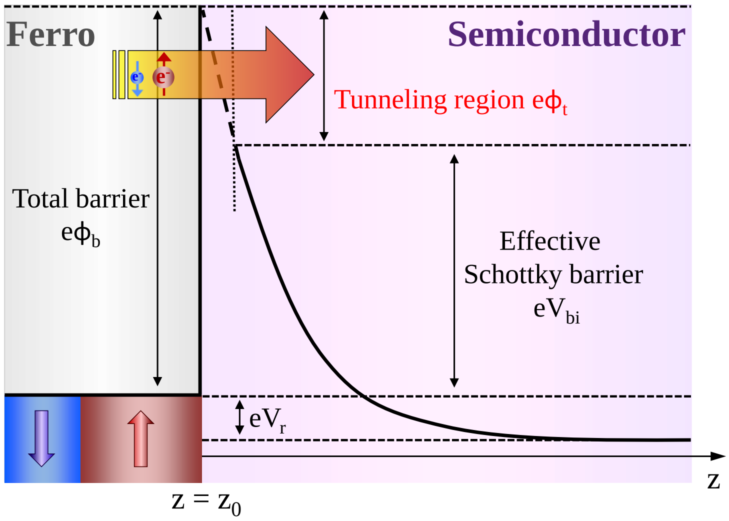

Figure 2.11: Energy diagram of a Schottky contact including the possibility of a narrow tunneling region near the interface. The highly doped region near the interface, through which electrons tunnel, is indicated by the dashed portion of the conduction band profile. Adapted from [79].

will dilute the injected electron spins.

The heavily doped region reduces the effective energy barrier that determines the properties of the depletion region (Figure 2.11). The total barrier $e\phi_b$ is divided into two parts: (i) a tunneling region with a barrier height $e\phi_t$ and (ii) an effective Schottky barrier with a barrier height eV_{bi}. The potential drop in the depletion region consists of the height of the effective Schottky barrier added to the applied reverse bias eV_R. The tunneling resistance and the reduction of the effective Schottky barrier can be separately controlled by the doping profile: for example, the height and width of the heavily doped region [79].

Just as the oxide-based tunnel injectors, Schottky tunnel injectors show little intrinsic bias dependence of the injected spin-polarization. The doping of the active region has a similar influence on the thermalization of hot carriers. In addition, overdoping the Schottky tunnel barrier may add a new contribution to the spin injection bias dependence. At low bias, the overdoped subsurface layer is not fully depleted and generates a retarding-electrical field that slows down the passage of the electrons through this region. The transit time is reduced when the bias voltage increases as the depletion of the subsurface layer increases. This mechanism holds until the flat-band regime is reached.

One has to note that even for a perfectly designed Schottky barrier, the injected spin polarization degree achievable in the semiconductor is limited by the tunneling spin polarization of the injected electrons. As the evanescent decays for spin up $(\alpha_\uparrow)$ and spin down $(\alpha_\downarrow)$ are identical $\alpha_\uparrow = \alpha_\downarrow$, the device will exhibit $P_S^{SC} = P_S^F$ at the very best.

Oxide-based tunnel injectors

The first experiment of spin injection in a semiconductor using a tunnel barrier were done by Alvarado and Renaud at IBM Zurich in 1992. They used a Scanning Tunneling Microscope (STM) mounted with an Ni probe and successfully demonstrated spin-injection in GaAs(110) at room temperature [95].

With the use of an oxide as tunnel barrier, issues related to Schottky barrier interface states and differential material resistivities are not called into play. The insulator/semiconductor combination affords a high degree of flexibility to chose the point on the semiconductor band structure where spin injection occurs.

Non-magnetic tunnel barriers: The insertion of a non-magnetic tunnel barrier at the F/SC interface creates a very large voltage drop compared to the electrochemical potential divergences. Hence, it totally controls the injected current and its spin polarization. Indeed, the relative signs of the electrochemical potential of the two spin sub-bands in F and SC can even become inverted (figure 2.12 (a)). Spin-depolarization still occurs in the F but is now of no consequences since the injected polarization is now independent of DOS for spin-up and DOS for spin-down. In oxide-based tunneling system, the spin polarization is fully determined by $\rho_d^{\uparrow}$ and $\rho_d^{\downarrow}$ via tunnel process. Its magnitude thus directly reflects the ferromagnet DOS asymmetry for d-electrons and hence approaches unity [81]. Contrary to Schottky barriers, non-magnetic tunnel barriers are spin-selective along preferential crystalline symmetries. However, the evanescent decays of the wave function for spin-up and spin-down are also identical: $\alpha_{\uparrow} = \alpha_{\downarrow}$. As a direct consequence, the maximum spin polarization injected in the SC will be at best equal to the intrinsic spin polarization of the FM and so less than a 100%. Non-magnetic tunnel barriers can be classified in two categories depending on their crystallinity:

- **Amorphous** tunnel barriers such as Al_2O_3 or MgO already demonstrated significant spin injection in semiconductors [96, 97, 98].
- **Crystalline** tunnel barriers such as ZnSe or MgO demonstrated much higher spin polarization for certain crystalline F/I combinations due to strongly spin-polarized evanescent decay of particular wave functions through the tunnel barrier [99, 100, 101, 102, 103, 104]. As an example, the spin filtering capacity of MgO (001) is much higher than the one of MgO (111). To this day, crystalline MgO (001) stand out as the most competitive insulator for the implementation of a high efficiency MTJ-based spin-injector on semiconductors at room temperature.

Generally, non-magnetic tunnel barrier exhibit strong bias dependence.

Magnetic tunnel barriers: With Schottky barriers and non-magnetic tunnel barriers, the injected spin polarization is limited by the tunneling spin polarization

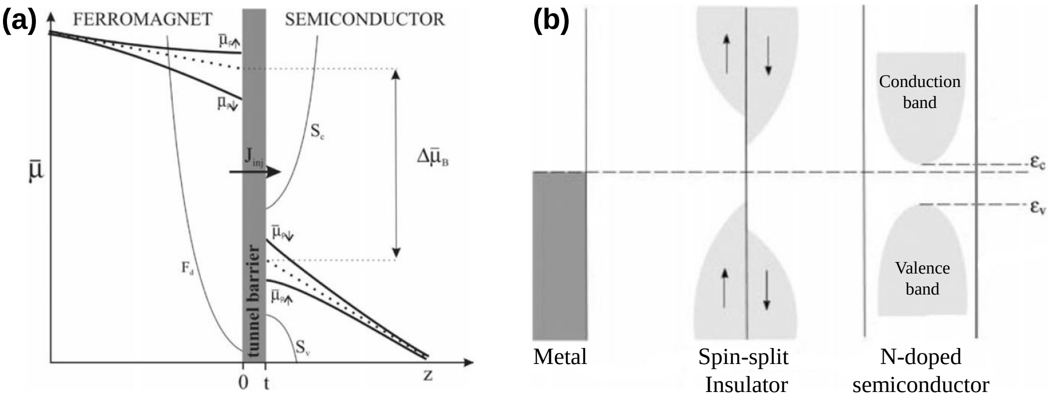

Figure 2.12: **(a)** Evolution of the electrochemical potentials at an interface F/I/SC. **(b)** Unbiased spin-split insulator band structure. Figures reprinted from [81].

of the injected electrons ($\alpha_{\uparrow} = \alpha_{\downarrow}$). The alternative solution to theoretically approach an injected spin polarization of 100% is to perform tunnel injection from a ferromagnetic metal into a semiconductor through a spin-split magnetic insulator (figure 2.12 (b)). Contrary to non-magnetic insulator, the spin-filtering effect is driven by the spin splitting of the insulator bandgap. Consequently, a tunneling electron with its energy in the bandgap sees different heights of tunnel barrier depending on its spin. The band splitting of insulator means that the two spin channels exhibit different evanescent decay rates. The injected spin polarization into the semiconductor is then given as $P_S^{SC} = 1 - exp(t\Delta\alpha)$ where t is the barrier thickness and $\Delta\alpha$ is the difference in decay rates $\alpha_{\uparrow} - \alpha_{\downarrow}$ with $\alpha_{\uparrow,\downarrow} = \sqrt{\frac{2m(E_{\uparrow,\downarrow})}{\hbar^2}}$ [81]. For incident electrons already significantly spin-polarized, this leads to reinforcement of the spin asymmetry for the tunnel current with a potential spin-injection polarization in the SC higher than the intrinsic spin-polarization of the F. Therefore, by potentially enhancing the spin injection and exhibiting a weaker bias dependance, spin-split magnetic insulators such as EuO stand out as interesting candidates for the realization of high efficiency MTJ spin-injectors.

Schottky vs. Oxide-based Tunnel Injectors

For electrical spin injection, beyond the properties of the chosen tunnel barriers (Schottky, non-magnetic oxide or magnetic oxide), interfaces qualities and properties have been shown to be of critical importance in spin-dependent tunnel experiments [105, 106]. Hence, the value of the injected spin polarization reached in the semiconductor does not only depends on the materials choice but also and mainly on the materials crystalline qualities (MBE vs. Sputtering), the lattice mismatches and the matching of the materials band structures.

In term of growth method and in contrast with the oxide tunnel barriers, the ferromagnetic Schottky contact needs to be deposited in-situ since oxidation of the top part would damage the careful design of the n^{++} doped layer. In-situ deposition on a crystalline semiconductor surface has the advantage to allow the growth of epitaxial, single crystalline, magnetic contacts. It provides a control over the magnetic properties than layers deposited on amorphous oxide such as AlO_x or MgO. Experiments showed that epitaxial Fe contacts result in injected spin polarizations that are very similar to those obtained with Fe/AlO_x and CoFeB/AlO_x spin injectors [107]. Generally, tunneling through reverse-biased Schottky diodes formed with ferromagnetic metals have been experimentally proven to result in high spin-injection efficiencies [92].

Also, a comparative study between a F/SC Schottky tunnel junction and F/Al_2O_3/SC non-magnetic oxide-based tunnel junction grown on LED showed a higher operating efficiency by a factor of 10 for the Schottky barrier. This difference was attributed to a combination of factors linked to the higher surface recombination velocities in the case of the oxide barrier, the scattering at the Al_2O_3/SC interface and/or differences in tunnel electron energies [107].

On the other hand, the use of an oxide tunnel barrier prevents any intermixing of the ferromagnetic metal and the semiconductor. Thus, this type a barrier leads to a much better thermal stability compared to the Schottky barriers [108]. Generally, the introduction of an oxide layer allows the fabrication of more stable and robust spin-injectors.

Using a Spin-LED configuration[5], typical injected spin-polarization degree measured with Schottky tunnel barriers are around 30%, but only at low temperatures [92]. Typical values reached with AlO_x barriers on GaAs are around 25-40% at low temperature (4.2 - 77 K) [109, 98, 107] and up to 16% at 300 K while with epitaxial MgO(001)/CoFeB on GaAs spin polarization degrees up to 52% at 100 K [100, 101] and 32% at 300 K [99] are obtained. The highest spin-selectivity of the epitaxial MgO(001)/CoFeB lead to an increase of the spin-injection efficiency.

Conclusion: Choice of electrical spin-injector

We can conclude from this analysis and the state-of-the-art experimental work that the most attractive multilayer structure to efficiently spin-inject a semiconductor at room temperature is a Magnetic-Tunnel-Junction based on the combination of: 1) the high intrinsic spin-polarization ferromagnetic metal: CoFeB with 2) the crystalline MgO(001) tunnel barrier. Additionally, under careful structural engineering, a MgO(001)/CoFeB/Ta MTJ offers the possibility to display Perpendicular Mag-

---

[5] For more informations, injectors efficiency comparisons and detection geometries in Spin-LED systems, please refer to the comparison table in section 2.2.2.2: State-of-the-Art

netic Anisotropy at room temperature. This colossal advantage over Schottky barrier injectors motivated the important optimization work achieved during this Ph.D on MgO(001)/CoFeB/Ta injectors using Spin-LEDs to ideally reach device operation with Perpendicular Magnetic remanence at room temperature. The combination of the Ta capping with a Rapid Thermal Annealing (RTA) (≈ 250°C during 3 minuts) leads to a re-crystallization of the amorphous CoFeB layer thanks to the pumping of B by the Ta layer and the restructuration of the CoFe from the interface with the crystalline MgO(001).

Beyond these standard methods inherited from spintronics with metal systems, it is interesting to mention that other type of injectors offers really attractive spin-injection performances:

- **Diluted Magnetic Semiconductors:** Magnetic semiconductors were the first successful sources for spin injection into a non-magnetic semiconductor. By combining two domains of condensed matter physics: semiconductors and magnetism, they generated a strong interest. A DMS is built on two distinct elements: a semiconductive matrix where magnetic impurities are introduced. The spin exchange interaction between the magnetic impurities (and so the macroscopic behavior of the DMS magnetization) depends on the semiconductive matrix surrounding the impurities as well as their nature, spatial distribution and concentration. The percentage of incorporated magnetic impurities is relatively low, usually less than 10%. All these parameters make the growth of a DMS quite challenging. To this day, the international community deployed a special effort on the study of III-V based DMS and especially (Ga,Mn)As [110, 111, 112, 113]. It was shown that with an optimized doping design and high-quality (Ga,Mn)As films, injected electron spin polarizations of 80% at 4.2 K and 25% at 80 K can be achieved [89, 113, 84][6].

- **Half-Metallic Ferromagnets:** In the ideal limit where only one spin direction remains at the Fermi level, the spin polarization of the conduction electrons is maximal: $P_S = 100\%$. The materials exhibiting this unique property are named Half-metals. A half-metallic ferromagnet (HMF) behaves like a metal for one spin direction and like an insulator for the other spin direction [115, 116, 117, 115, 118]. Generally, half-metallic compounds stand out as really attractive candidates to play the role of high spin-polarized current sources to perform spin injection into semiconductors. They come out as a potential solution to overcome the intrinsic spin polarization limitation at the Fermi level of common transition metals Fe, Co, Ni ($P_S \approx 30$ to 40%) created by the s-d band hybridization. The spin-flip loss is canceled by the complete absence of final states for spin flipping.
  Nevertheless, so far only pioneering investigations have been conducted on the

---

[6] For complementary information on Diluted Magnetic Semiconductors, please refer to reference [114]

growth of Heusler HMF/SC hybrid structures [119, 120, 121, 122]. The highest injected spin-polarization degree reached was around 13% at 5 K using off-stoichiometric $Co_{1.6}Mn_{2.4}Ga$ on InGaAs [121]. An injected spin polarization of 27% at 2K was reported for the system Co_2MnGe/GaAs [123], contrasting with the value of 40% reached with a standard Fe injectors. Since spin injection experiments probe the spin polarization at the interface, a realistic theory does not only need to consider the electronic structure of the interface, but also the presence of atomic disorder as well as the effects of non-zero temperature. Indeed, these factors play an essential role in interpreting spin injection measurements on new materials [117]. From a pragmatic view point, as the interface is controlling the spin injection, the real challenge is to develop a half-metallic interface.

In terms of realistic application for spin-injection, the hunt for a half-metallic ferromagnet exhibiting a high T_C, a control of the atomic disorder and a control of the interface structure is still on[7].

2.1.2.2 Generation of spin accumulation: Beyond direct spin injection

We highlighted that the impedance mismatch issue at a F/SC interface arises from the injection of a spin polarized current across the interface between two materials with highly different conductivities. Thus, it seems reasonable to consider that this problem vanishes if spins are injected into the semiconductor using pure spin current without charge transport [124].

In recent years, new sources of pure spin currents have been demonstrated [125, 126, 127, 128] and applied [7, 8, 25]. A pure spin current correspond to the transport of spin angular momentum without net charge currents. In this section we present state-of-the-art methods for generating pure spin current in semiconductors.

Spin-Hall Effect and Inverse Spin-Hall Effect

The Spin Hall Effect was predicted in 1971 [129] and stands for a collection of phenomena resulting from spin-orbit coupling. An electrical current flowing through a sample can lead to spin transport in a perpendicular direction as well as a spin accumulation at lateral boundaries [130]. These purely electrical mechanisms do not require applied magnetic field nor feromagnets and are consequently application "friendly". These effects can be observed in materials with strong Spin-Orbit (SO) as the SO coupling acts like an effective magnetic field H_{SO} on the spin of the moving electrons.

The Spin-Hall Effect: The spin-hall effect (SHE) originates from the spin-orbit interaction (SOI) that couples the electron spin to the orbital motion of the elec-

---

[7] For complementary information on Half-Metallic Ferromagnets and Heusler Alloys, please refer to reference [117]

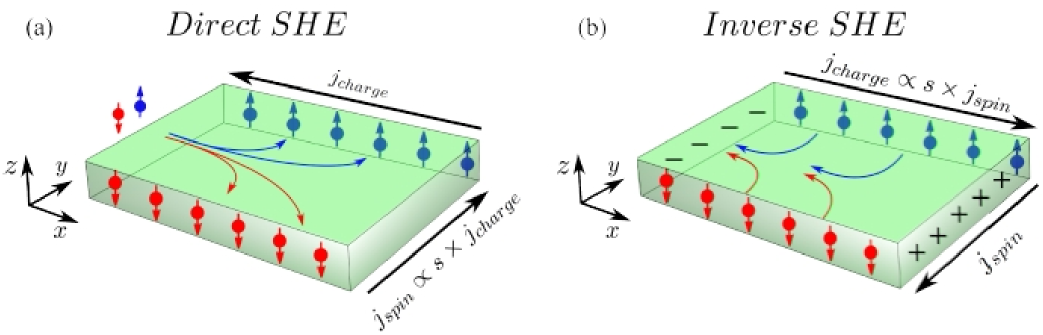

Figure 2.13: **(a) Schematic mechanism of the Spin Hall Effect** converting a charge current into a spin current. **(b) Schematic mechanism of the Inverse Spin Hall Effect**, reciprocal mechanism converting a pure spin current into a charge current. Figure reprinted from [130].

tron [131]. The origin of the SHE is classified as: (i) intrinsic if SO effects on the wave functions of conduction band are predominant or (ii) extrinsic if SO effects occur on the scattering potential of impurities or defects. In a non-magnetic conductor the SOI generates a pure spin current J_{spin} orthogonal to the charge current J_{charge} (Figure 2.13 (a)). If the lateral dimension of the sample is larger than the spin diffusion length, a spin accumulation is induced on the edges of the sample and can directly be measured electrically [132, 133, 130]. The first observation of SHE in semiconductors was detected and imaged with the use of Kerr rotation microscopy in 2004 by Kato *et al.* [134].

The conversion efficiency of the charge current density into spin current density is characterized by the Spin Hall Angle (SHA) given by:

$$\theta_{SHE} = \frac{J_{spin}}{J_{charge}} \tag{2.22}$$

where J_{spin} and J_{charge} are the pure spin current and the charge current respectively. Promising application could be foreseen if the conversion efficiency of charge current into spin current becomes competitive with the values reached using F/N interfaces [135]. The use of SHE lead to the developpement of experiments and concept involving the spin-torque switching of ferro-magnets [136], spin-torque ferromagnetic resonance [137] and the SHE-Transistors [138].

The Inverse Spin-Hall Effect: The Inverse Spin-Hall Effect (ISHE) qualifies the SHE reciprocal mechanism in which a pure spin current can be converted into a charge current and a charge accumulation. The ISHE is caused by the bending of electron orbits of up and down spins into opposite directions normal to their group velocity, owing to the spin-orbit interaction [139, 140, 126, 141] (Figure 2.13 (b)). It generates relatively large voltage for heavy metals such as Pt and has the advantage to scale linearly with the device lentgh.

Spin-Caloritronics

The new-born research field of Spin-Caloritronics focuses on non-equilibrium phenomena related to spin, charge and heat transport in magnetic structures and devices [139, 142]. This recently invigorated field is of high interest for creating spin-currents and pure spin-currents in systems hosting important temperature gradient. The Spin Seebeck Effect (SSE) is observed when a thermal gradient applied to a spin-polarized material in conact with a non spin-polarized material. It leads to a spatially varying transverse spin current in an adjacent non-spin-polarized material. Then, this spin-current usualy gets converted into a measurable voltage using ISHE (Figure 2.14 (a)) [143]. Its efficiency is characterized by the spin Seebeck coefficient $S = (\sigma_\uparrow S_\uparrow + \sigma_\downarrow S_\downarrow) / (\sigma_\uparrow + \sigma_\downarrow)$. It corresponds to the ratio of measured voltage per unit of length to the temperature gradient. In a metallic magnet spin-↑ and spin-↓ conduction electrons notably have have different scattering rates and densities. It directly implyes that the two spin channels have different Seebeck coefficients ($S_\uparrow \neq S_\downarrow$) [144]. When a temperature gradient is applied, a spin accumulation $\mu_\uparrow - \mu_\downarrow$ proportional to the temperature difference appears. Therefore, in the spin sector, a magnet works in the same way as a thermocouple [128]. In a ferromagnet, the SSE results from the interaction between phonons and magnons (excitations of magnetic moments), which creates a gradient in the magnetization across the sample [145, 146, 147, 142, 148, 149, 150, 144]. The dissipation of angular momentum generates a spin current flowing into the adjacent non-magnetic material. This effect is interpreted in terms of a spin current injected into the non-magnetic material from the ferromagnet [128]. The thermally induced spin voltage persists even at distances far from the sample ends (several millimeters) and spins can be extracted from any position on the magnet by simply contacting a metal. The conversion of the pure spin-current generated by the thermal gradient into a measurable voltage ocurs through Inverse-Spin-Hall-Effect (ISHE).

The Spin Seebeck Effect has been discovered first in $Ni_{81}Fe_{19}/Pt$ systems by Uchida *et al* in 2008 [128] and later in other magnetically ordered materials such as the electrically insulating Yttrium Iron Garnet (YIG = $LaY_2Fe_5O_{12}$) [151], the Diluted Magnetic Semiconductor GaMnAs [19], Heusler alloys (Co_2MnSi) [152] with a magnitude of microvolts per Kelvin. Lately, SSE has also been demonstrated in the intrinsically non-magnetic Te-doped n-type III-V semiconductors InSb [143]. The SSE could be directly applicable to the construction of thermo-power generators to drive spintronics devices [153] or devices such as Spin Seebeck-assisted magnetic random access memories [154]. Combined with the ISHE it could also lead to temperature gradient sensors as well as thermoelectric generators, allowing new approaches towards the improvement of thermoelectric generation efficiency. Nevertheless in terms of realistic applications, it remains to be seen whether a magnetic

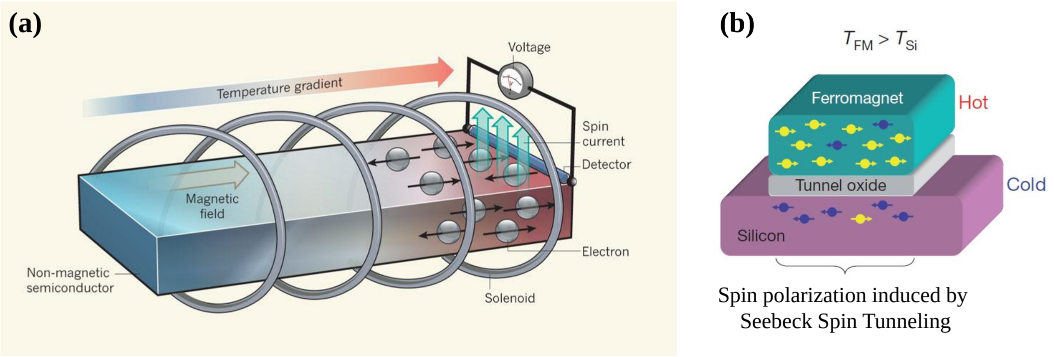

Figure 2.14: (a) Transverse experimental configuration use for the observation of SSE: The system is composed of a ferromagnetic material subjected to a temperature gradient ∇T in contact with a non-magnetic Pt wire orthogonal to ∇T. The whole system is placed in a large magnetic field that has a direction parallel to ∇T. Owing to the large field, more electrons have spins (black arrows) that align parallel with the field than antiparallel to it. This strong spin polarization and the temperature gradient generates a pure spin current in the ferromagnet detected as a voltage thanks to a Platinum (Pt) wire. The ISHE voltage generated can be amplified by increasing the length of the Pt wire. Figure reprinted from [155]. **(b) Basic concept of Seebeck spin tunneling:** In a tunnel contact between a F electrode and a N electrode, a temperature difference between the electrodes causes a transfer of spin angular momentum from the F to N. The thermal spin current requires no tunnel charge current. Figure reprinted from [156].

field is needed at all to observe SSE at room temperature.

Interestingly, efficient spin injection using Spin-Dependent Seebeck Effect (SDSE) has recently been demonstrated in lateral $F/N/F$ spin-valve structures [144]. But also in a dedicated perpendicular spin-valve nanostructure consisting of two ferromagnetic layers (15 nm $Ni_{80}Fe_{20}$) separated by a non-ferromagnetic metal (15 nm Cu) [157]. Amazingly, Le Breton *et al.* also reported the demonstration of Seebeck Spin Tunneling (SST) generated in a Ferromagnet-Oxide-Silicon tunnel junction (Figure 2.14 (b)) [156]. The mechanisms involved are different as the thermal spin flow is of purely interfacial nature.

The SST stands out as a very interesting effect to use in optical experiments where significant thermal gradient are usually engaged due to the use of lasers. A laser beam well focused on the ferromagnet can be use to generate a temperature gradient in TMR junctions [158] or in a $F/T/SC$ structures. It could trigger spin-injection in the devices without the need for circularly polarized light and optical orientation. The total spin-injection yield in the QWs of Spin-LEDs and Spin-VCSELs could then be optimized by assisting the injection of the conventional spin-polarized charge current with pure spin-currents generated by SST. For semiconductor lasers especially, SST could be used to : (i) increase the global efficiency of the system by functionalizing the significant heat losses and (ii) combine the pure spin current with the non-linear amplification effects of the optical cavity to control the laser modes polarization. Fairly large SST effect has already been observed and carries the promise of useful applications.

Spin-Pumping and Ferromagnetic Resonance

In 2011, Ando *et al.* proposed with a new approach to overcome the impedence mismatch at a Ferromagnetic/Semiconductor interface: the Spin Pumping [124]. Contrary to spin-injection by carrier transport through the F/SC interface, here a pure spin current is injected in the SC by Ferromagnetic Resonance (FMR) from the F layer (Figure 2.15 (a)) [127, 159, 160, 161].

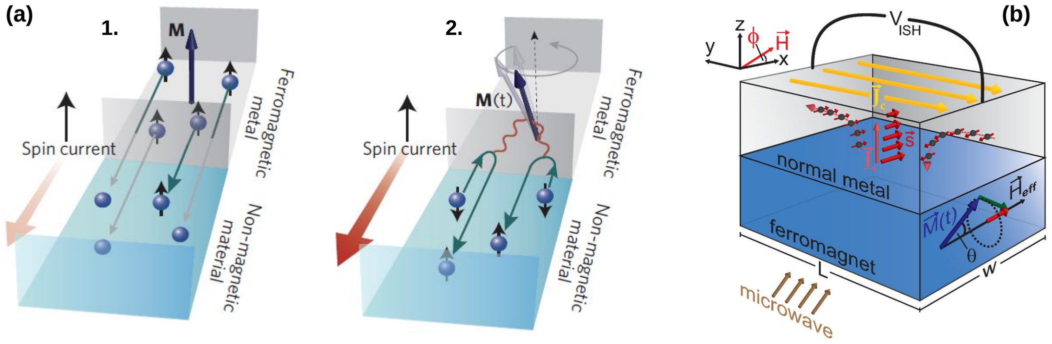

Figure 2.15: (a) Comparison between spin injection through carrier transport and dynamical exchange: 1. Scheme of the conventional electrical spin injection by carrier transport through the F/N interface **2.** Scheme of the spin pumping mechanism. A pure spin current is injected in the non-magnetic material by induced Ferromagnetic Resonance of the F layer. Figure Reprinted from [124]. **(b) Detection configuration:** the injected pure spin current is detected as a spin voltage on the sample edges using ISHE.

The concept is based on the use of a F/N-bilayer placed in a radiofrequency field in the GHz range. These microwaves engage a Ferromagnetic Resonance (FMR) of the FM layer magnetization under a specific external magnetic field. The magnetization's precession associated with a change of the longitudinal component of the magnetization is transfered to the electronic bath at the F/N interface through dynamical exchange interaction and generate a vertical pure spin current in the non-magnetic metal. As for the Spin Seebeck Effect, the spin accumulation induced by spin-pumping in the non-magnetic metal is detected as a voltage using ISHE (Figure 2.15 (b)). Additionally, the spin pumping can be tuned by applying a bias voltage at the F/N interface and controlling the level exchange interaction.

Tunable spin injection from $Ni_{81}Fe_{19}$ into both p- and n-doped GaAs through both Ohmic and Schottky contacts has been demonstrated with an ISHE detection at room temperature [124]. The spin pumping is a powerful and versatil method with potential spin injection capability into a wide range of material free from the impedence mismatch issue. As it only requires a precession of the F layer magnetization, this method can be integrated on a wide range of systems such as spin-torque oscillators or semiconductor spin-laser [162]. The spin-pumping is also a very practical tool to characterize and measure the Spin Hall Angle in a material using the ISHE [137, 163, 164, 165, 166].

2.1.3 Spin-Orbit interaction and Spin relaxation mechanisms

To conclude this section treating the general question of spin injection in semiconductors, I propose to focus on the different spin relaxation mechanisms responsible for the depolarization of the current. In other words, we are going to examine the several terms driving the spin life time τ_{sf} in a system. In IV and III-V semiconductors, we can expect four principal mechanisms: three are directly attributed to the Spin-Orbit (SO) interaction (Dyakonov-Perel, Elliot-Yafet and Bir-Aronov-Pikus) and one is induced by the interaction between the electrons' spin and nuclear magnetic moments of the crystalline network (Hyperfine Interaction).

2.1.3.1 Dyakonov-Perel

The Dyakonov-Perel (DP) mechanism [167] is a particularity of the non centrosymmetric materials such as GaAs or interfaces between different materials. In these materials, the SO coupling generates a splitting between the two conduction spin sub-bands ($E_{\vec{k}\uparrow} \neq E_{\vec{k}\downarrow}$). This splitting can be calculated by introducing the effective magnetic field induced by the SO coupling $\vec{H}_{SO}(\vec{k})$. The Hamiltonian term describing the spin precession of the conduction electrons around this effective magnetic field at the Larmor fequency $\vec{\Omega}(\vec{k}) = \frac{e}{m}\vec{H}_{SO}(\vec{k})$ (Average value: $\bar{\Omega}$) is given by:

$$H_{DP}(\vec{k}) = \frac{1}{2}\hbar\hat{\sigma} \cdot \Omega(\vec{k}) \tag{2.23}$$

where $\hat{\sigma}$ are the Pauli matrices. The $\vec{k}$ dependent spin precession $\Omega(\vec{k})$ combined with the collisions (which trigger the moment relaxation) are responsible for the spin dephasing. We define $\tau_p(E_{\vec{k}})$ as the characteristic moment relaxation time at the energy $E_{\vec{k}}$ and we identify two regimes:

1. **If $\bar{\Omega} \geqslant \frac{1}{\tau_p}$:** the spin of the electron has enough time to realize a whole precession before the moment relaxes by diffusion from the state $\vec{k}$ to the state $\vec{k}'$. In this regime, the spin dephasing rate depends on the Larmor fequency values $\vec{\Omega}(\vec{k})$ and is in general proportional to the bandwidth given by the Larmor frequencies $\Delta\Omega$ such that: $\frac{1}{\tau_{sf}} \approx \Delta\Omega \Longrightarrow \tau_{sf} \propto \tau_p$.

2. **If $\bar{\Omega} \leq \frac{1}{\tau_p}$, the Dyakonov-Perel regime:** the spin of the electron rotates from an angle $\delta\phi = \tau_p\bar{\Omega}$ before the moment relaxes and undergoes another effective spin-orbit magnetic field. Physically, this mechanism corresponds to a spin precession around fluctuating magnetic fields which amplitude and direction randomly change with a characteristic average time τ_p (Figure 2.16 (a)).
   Consequently, the spin phase variations of the electrons are randomized and after a time t the spin's dispersion angle is given by the standard deviation

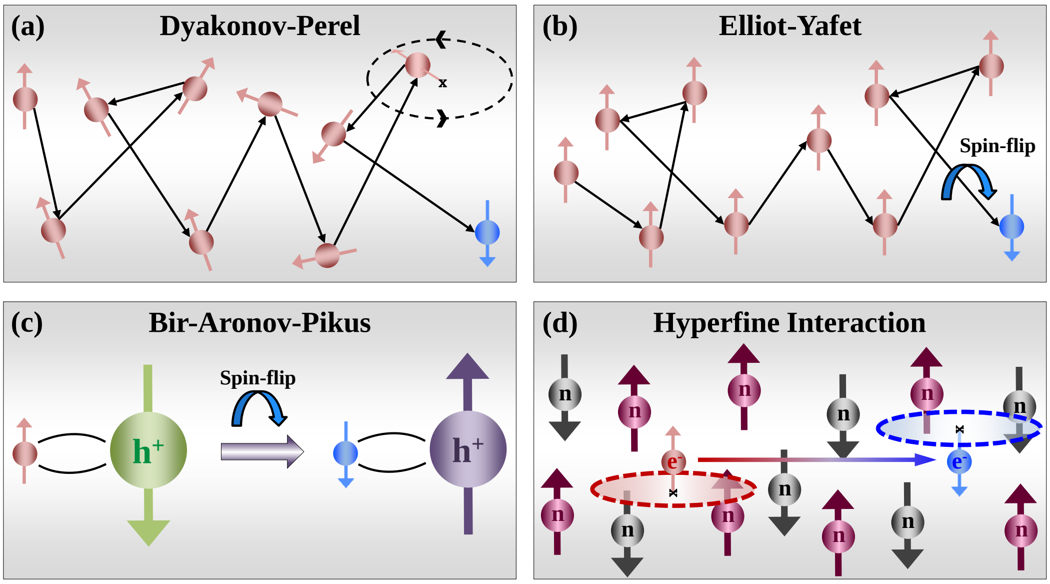

Figure 2.16: Illustration of the four principles mechanisms responsible for spin relaxation in semiconductors. (a) Dyakonov-Perel: Relaxation by spin precession around the effective $\vec{k}$ dependent SO magnetic field, and so by diffusion on the crystalline network. **(b) Elliot-Yafet:** Relaxation by diffusion on impurities or phonons. **(c) Bir-Aronov-Pikus:** Electron-Hole exchange interaction leading to fast spin relaxation through Elliot-Yafet mechanism. **(d) Hyperfine Interaction:** Electron-Nucleus exchange interaction.

angle $\phi(t) \approx \delta\phi\sqrt{\frac{t}{\tau_p}}$. τ_{sf}^{DP} is define as the time such that $\phi(t) = 1$. This mechanism is qualified as "motional narrowing" and is described by: $\frac{1}{\tau_{sf}^{DP}} = \bar{\Omega}^2\tau_p$. Under this form, one clearly sees that the spin lifetime is inversely proportionate to the moment relaxation time τ_p.
For GaAs in the Dyakonov-Perel regime, the exact expression of τ_{sf}^{DP} is given by [168]:

$$\frac{1}{\tau_{sf}^{DP}\left(E_{\vec{k}}\right)} = \frac{32}{105}\gamma_3^{-1}\tau_p E_{\vec{k}}\alpha^2\frac{E_{\vec{k}}^3}{\hbar^2 E_g} \tag{2.24}$$

where α is the Spin-Orbit interaction parameter ($\alpha \approx 0.07$ in $GaAs$ [169]) and γ_3 is a parameter representing the efficiency of the moment diffusion to randomize the Larmor Frequencies.

In GaAs, the Dyakonov-Perel mechanism is by far the dominant mechanism [170].

2.1.3.2 Elliot-Yafet

The Elliot-Yafet (EY) mechanism treats the spin relaxation of the electrons by diffusion in the crystalline network (Figure 2.16 (b)). It requires a SO interaction to couple the electron spin wave function with the lattice wave function. The SO coupling Hamiltonian is given by:

$$H_{EY} = \frac{\hbar}{4m^2c^2} \nabla V_{SC} \times \hat{p} \cdot \hat{\sigma} \tag{2.25}$$

where V_{SC} is the spin-independent scalar periodical potential of the lattice, $\hat{p} = -i\hbar\nabla$ is the linear moment operator and $\hat{\sigma}$ is the Pauli matrix. The Bloch wave functions are not described by one eigen state of $\hat{\sigma}_z$ but by a combination of spin-up $|\uparrow\rangle$ and spin-down $|\downarrow\rangle$ states. Accordingly, each time a collision between an electron and a network impurity, a default, a phonon, etc... occurs, the spin-flip probability is non-zero. In the case of III-V semiconductors, this spin-flip probability is characterized by a spin lifetime τ_{sf}^{EY} given by [171]:

$$\frac{1}{\tau_{sf}^{EY}\left(E_{\vec{k}}\right)} = A \left(\frac{\Delta_{SO}}{E_g + \Delta_{SO}}\right)^2 \left(\frac{E_{\vec{k}}}{E_g}\right)^2 \frac{1}{\tau_p\left(E_{\vec{k}}\right)} \tag{2.26}$$

where $A \approx 1$ is a numerical factor traducing the type of diffusion mechanism involved (charged impurity, neutral impurity, phonon, $e^- - h^+$ recombination, etc$\cdots$), $\tau_p(E_{\vec{k}})$ is the characteristic moment relaxation time at the energy $E_{\vec{k}}$, E_g is the energy band gap of the semiconductor and Δ_{SO} is the valence band splitting parameter induce by the SO coupling. Equation (2.26) highlights how the increase of the semiconductor gap and the SO coupling reinforce the impact of the EY mechanism. For a degenerate semiconductor: $E_{\vec{k}} = E_F$ while for a non degenerate semiconductor: $E_{\vec{k}} \approx k_B T$. But in both cases: $\tau_{sf}^{EY} \propto \tau_p$.

For degenerate SC, the temperature evolution of τ_{sf}^{EY} and τ_p are similar. For a non-degenerate SC, the temperature evolution of τ_{sf}^{EY} is given by: $\frac{1}{\tau_{sf}^{EY}(T)} \propto \frac{T^2}{\tau_p(T)}$ except in the case of diffusion on charged impurities where: $\frac{1}{\tau_{sf}^{EY}(T)} \propto T^{1/2}$.

2.1.3.3 Bir-Aronov-Pikus

The Bir-Aronov-Pikus (BAP) mechanism describes the spin relaxation of conduction electrons in p-type semiconductors [172]. The exchange interaction creates a coupling between the wave functions of a spin-up electron $\left(+\frac{1}{2}\right)$ and a spin-down hole $\left(-\frac{3}{2}\right)$. It acts as an effective magnetic field which stimulates electrons spin precession and results in spin relaxation (Figure 2.16 (c)). The BAP relaxation rates increases with the degree of spatial overlap between electron and hole. Th spatial overlap increases at low temperatures and for larg confining potentials such as QWs and QDs [84].

2.1.3.4 Hyperfine interaction

The hyperfine interaction rises from the exchange interaction between the spin of electrons and nuclear spin of atoms in the crystalline lattice (Figure 2.16 (d)). It naturally requires for the total nuclear spin to be non-zero $S_n \neq 0$ which is the case in GaAs where $S_n^{GaAs} = \frac{3}{2}$ per atom. The effective magnetic field generated by the hyperfine interaction is given by:

$$\vec{B}_n = \frac{2\mu_0}{3}\frac{g_0}{g}\mu_B \sum_i \hbar\gamma_{n,i}\vec{S}\cdot\vec{I}_i\delta\left(\vec{r}-\vec{R}_i\right) \tag{2.27}$$

where μ_0 is the vacuum permeability, $g_0 = 2.0023$ and g are the free and effective electron Landé factor respectively, μ_B is the Bohr magneton and $\gamma_{n,i}$ is nuclear gyromagnetic factor. i identifies the considered nucleus in position $\vec{R}_i$ while $\vec{S}$ and $\vec{I}_i$ are the spin operators of the electron and the nucleus respectively.

Generally in semiconductors, the influence of the hyperfine interaction on the global spin relaxation is negligible compared to the impact of mechanisms originating from SO (DP, EY). Indeed, its leverage is highly diminished by the motional narrowing phenomenons [173]. Nevertheless its contribution can become significant when the nucleus polarization increases in case of optical pumping for example [174, 175, 176].

2.1.3.5 Spin relaxation in confined potentials: QW and QD

This Ph.D project focuses on the study of spin injection in LED and VECSELs with AlGaAs/GaAs and InGaAs/GaAs QW active mediums. Consequently, it is necessary to pay closer attention to the spin relaxation mechanisms occuring in the particular case of confined potentials. Indeed, as the three relaxation mechanisms induced by SO (DP, EY and BAP) are influenced by factor such as mobility, charge localization or the band-structure, the spin dynamics of the electrons significantly changes in confined potentials compared to bulk material [84].

It has been shown that heterovalent QW displays spin relaxation times orders of magnitude lower than homovalent QW. Additionally, reduced spin-relaxation rates have been observed in QW structures where spatial separation of electrons and holes is achieve using modulation-doped double heterostructures [177] or bias [178]. This increase of the spin relaxation time can be associated with the inhibition of the BAP mechanism.

More specifically, studies on the AlGaAs/GaAs QW revealed that the spin relaxation time of the electrons depends weakly on the temperature for narrow wells ($< 10nm$). In the case of wider wells, the temperature dependance of the spin relaxation approaches the bulk GaAs which follow a $\frac{1}{T^2}$ law [179]. Likewise experiments conducted at room temperature with AlGaAs/GaAs QW showed that the quantum confinement strongly enhances the spin relaxation with variations as function of the confinement energy of the form $E_{conf.}^{-2}$ [179, 180]. This observation is counter intuitive as one would expect the spin lifetime to increase with the quantum confinement. Indeed a restriction of the electron's motion in the lattice reduces the impact of the dominant DP mechanism. In the case of QD Spin-LED [181] for example, this can even lead to temperature-independent spin-polarization unlike QW Spin-LED where the temperature dependence has clearly been demonstrated [93].

Finally, in low-dimensional semiconductor structures the hyperfine interaction becomes relevant by depolarizing the localized electrons. The spin dynamics of an electron confined in a QD is almost not influenced by DP, EY and BAP mechanisms. The only spin depolarizing mechanisms remaining are the electron-hole exchange interaction and the Hyperfine interaction. In these systems, spin lifetime up to the milli-second have been observed [182].

2.2 From matter to light: Conversion of spin accumulation into light polarization information

We described in the previous secion different methods to creat a spin-accumulation in a semiconductor. Now we focus on ways to efficiently convert the spin-bit generated by the spin accumulation into light polarization information. Historically, research on the optical detection of a spin signal were motivated by the necessity to by-pass the impedance mismatch issue faced for an electrical detection through at a SC/F interface. Adjusting the RA product on both the injection and the detection interfaces to match the electrical spin injection and detection conditions is quite challenging. Replacing the electrical detection by an optical detection remove the constraint on the detection and enable to measure an unbiased value of the spin injection in the SC. Additionally, the optical detection condition $\tau_r \ << \ \tau_s$ is easier to fulfill than the electrical detection condition $\tau_d \ << \ \tau_s$, where τ_r is the recombination time in the active medium, τ_d the spin dwell time in the semiconductor canal and τ_s the spin-lifetime.

In this section the conversion of a spin accumulation into light polarization information is investigated. After describing the mechanisms engaged behind the optical detection of a spin-polarized current in a III-V semiconductor, a device oriented study is conducted on Spin-LEDs and Spin-LASERs.

2.2.1 Optical detection of a spin-polarized current in a III-V semiconductor

In spin-polarized light sources, a transfer of a spin-polarized electrons (e^-) operates from a magnetic contact into a non-magnetic n-i-p semiconductor structure through drift and diffusion mechanisms. After thermalization, they recombines radiatively with unpolarized holes (h^+) injected from a non-magnetic contact in the active medium of the structure (Bulk, QWs or QDs). If the carriers spin lifetime τ_s is greater than the recombination time τ_r in the active medium of the n-i-p diode, the resulting electroluminescence (EL) will exhibit a net circular polarization according to the optical quantum selection rules. Then, the degree of circular polarization (DoCP) of the emitted light can be analyzed and used as a probe for the characterization of the spin polarized carriers population.

In this sub-section we discuss the operation principles and the general considerations for the design of spin-polarized light sources. I would like to acknowledge the brilliant review written by M. Holub and P. Bhattacharya's on "Spin-polarized light-emitting diodes and lasers" that stands out as a reference paper on the subject. Most of the fundamental informations displayed further are extracted from this reference [84].

2.2.1.1 General properties of III-V semiconductors

Energy bands of semiconductors

In a semiconductor, the energy bands of the crystal are either accessible (conduction band, valence band) or non accessible (band gap). One can rebuild the energy diagram of the semiconductor by determining some key parameters, such as the band gap energy and the eigen states associated with high symmetries $\vec{k}$ wave vectors, thanks to optical measurements (Figure 2.17 (a)).

An intrinsic (pure crystal) semiconductor is characterized by having its Fermi level in the middle of the energy band gap. Generally, only the first few bands above and below the Fermi level matters when studying the conduction properties of the material. Theoretically at 0 K, the lowest energy bands do not participate to the electronic conduction and are filled according to the Pauli exclusion rule while the upper energy bands stay empty. This framework of electronic distribution can be tuned by adding doping impurities in the semiconductor to manipulate the crystal's electrons concentration. Adding a sufficient concentration of ”electron-acceptor” impurities in the semiconductive matrix will decrease the band filling and enable the Fermi level to enter the Valence Band (VB) where electrical conduction is enabled by holes. Oppositely, introducing "electron-donor" impurities will drive the Fermi level into the Conduction Band (CB) where the electrical current is ran by conduction electrons. For classical semiconductors, the band gap energy is usually around 1 eV: $E_g^{GaAs} = 1.5\ eV$, $E_g^{InP} = 1.34\ eV$, $E_g^{Si} = 1.1\ eV$ and $E_g^{Ge} = 0.7\ eV$ (Figure 3.2).

Taking into account the Spin-Orbit interaction, an electron traveling in the semiconductor crystal is characterized by the following Hamiltonian:

$$\vec{H} = \frac{\vec{p}^2}{2m_0} - qV(\vec{r}) - \frac{q\hbar}{4m_0c^2}(\nabla V \times \vec{p}) \cdot \sigma \tag{2.28}$$

where $V(\vec{r})$ is the crystalline potential, $\vec{p}$ is the electron momentum quantity vector and σ the Pauli matrix. The solution of the Schrodinger equation associated with this Hamiltonian can be find applying the "$\vec{k} \cdot \vec{p}$-method". This approach is particularly powerful for the calculation of the excited states at the center of the Brillouin zone (Figure 2.17 (a)).

Notion of effective mass

In semiconductors the number of free carriers, either electrons in the CB or holes in the VB, are generated by thermal agitation or by adding doping impurities. The carriers concentration never exceeds $10^{20}\ cm^{-3}$ while the DOS available in a given band is around $10^{22}\ cm^{-3}$ (like in metals). Thus, the electrons and holes occupy a small percentage of the CB and the VB respectively and are concentrated on low

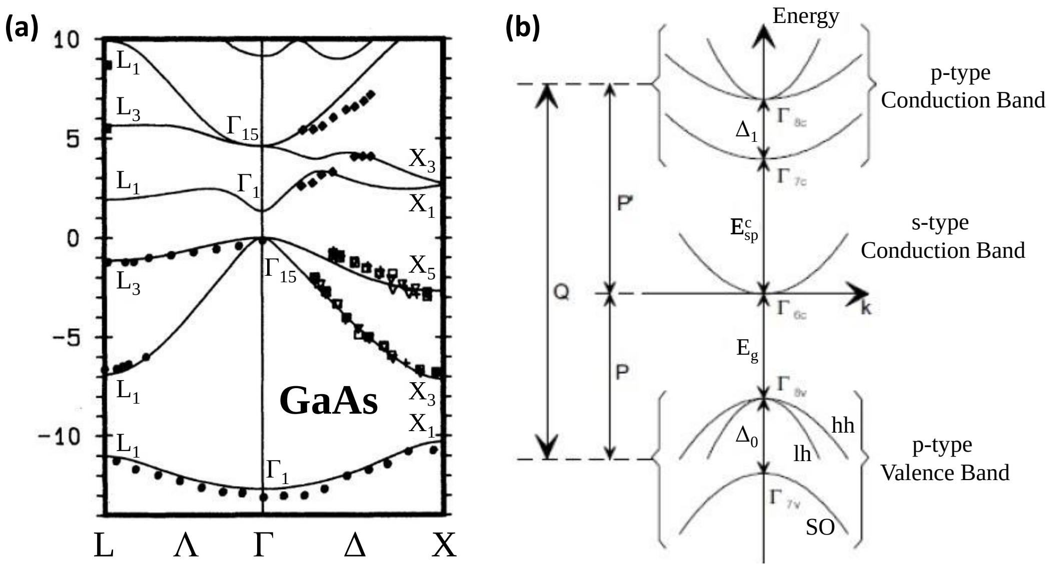

Figure 2.17: **(a)** Schematic band structure of direct gap III-V semiconductors near k=0. Figure adapted from [67] **(b)** Ab-initio calculations of the electronic band structure of GaAs along lines of symmetry in the first Brillouin zone. Figure reprinted from [183].

energy states. Consequently, the study of semiconductors properties usually focuses on the energy spectra close to the CB minimum and the VB maximum. If these two local extrema are energetically aligned in $k = 0$ (Γ-point) at the center of the Brillouin zone, the semiconductor has a direct gap (GaAs, InP,...) and offers interesting radiative e^- - h^+ properties for optoelectronic applications (Figure 2.17 (b)).

In the approximation of the "effective mass", the CB and VB around these extrema can be considered parabolic and the dispersion relation associated are given by:

$$\begin{cases} E_c(p) = \dfrac{p^2}{2m_c} & \text{,for the CB} \\ E_v(p) = \dfrac{p^2}{2m_v} & \text{,for the VB} \end{cases} \tag{2.29}$$

where m_c and m_v are electrons effective mass in the CB and the VB respectively.

The periodical crystalline potential can be neglect if: (i) the spatial variations of external forces induced by an applied electric or magnetic field are small compared to the spatial variations created by the periodical crystalline potential and (ii) if the carriers energy stays relatively small compared the gap energy E_g of the semiconductor. In this case, the carriers are considered as free particles with an effective

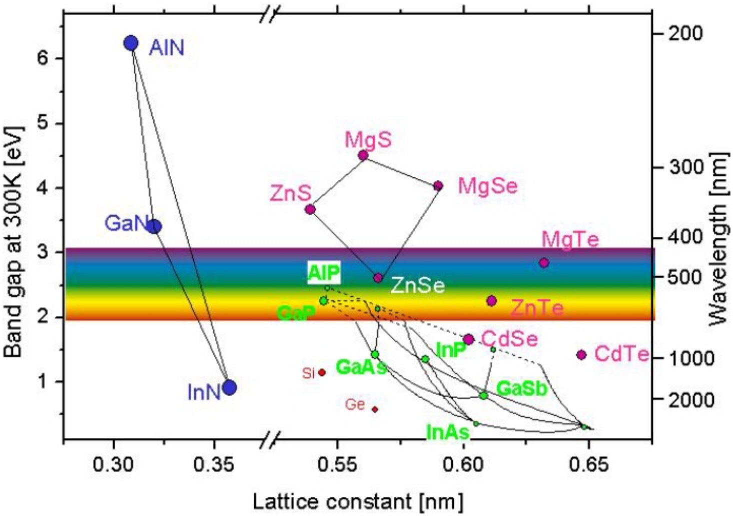

Figure 2.18: Map of the main III-V semiconductors according to the lattice parameter and the band gap energy.

mass slightly different from their free particle mass. For GaAs $m_c = 0.067m_0$ but the value is anisotropic according to crystalline symmetries and strains.

Band Structure of III-V semiconductors

Most of III-V semiconductors such as GaAs and InP display a Zinc-Blende structure with a direct gap (Figure 2.17 (b)). The VB is divided into three valleys energetically close (Heavy Holes - HH, Light Holes - LH and Split-Off - SO) while the CB is splitted into two groups of valleys with a significant energy difference. At the Γ-point ($k = 0$), in the CB the lower energy band states respond to s-type orbitals ($l = 0$) while the corresponding states in the VB are p-type orbitals ($l = 1$) triply-degenerated (m_l = -1, 0, +1). For the VB:

$$\left\{\begin{array}{l} E_{HH}(k) = \hbar^2(A+B)k^2 \text{ for } L_z = \pm 1 \quad \text{and} \quad E_{LH}(k) = \hbar^2 A k^2 \text{ for } L_z = 0 \\ \qquad \dfrac{\partial^2 E_{HH}}{\partial k^2} = \dfrac{1}{m_{HH}} \quad < \quad \dfrac{\partial^2 E_{LH}}{\partial k^2} = \dfrac{1}{m_{LH}} \quad \Longleftrightarrow \quad m_{LH} < m_{HH} \end{array}\right. \tag{2.30}$$

with A and B Hamiltonian constants verifying $B < 0$ and $A + B > 0$. The band with the highest effective mass ($L_z = \pm 1$) is called the Heavy Hole Band (HH) while the one with the lowest effective mass is called the Light Hole Band (LH).

However, the consideration of the Spin-Orbit interaction modifies the band diagram. Indeed $\vec{L}$ and $\vec{S}$ are no more conserved separately and one has to consider the vectorial sum $\vec{J} = \vec{L} + \vec{S}$ and the eigen values of $\vec{J}^2$: $j(j+1)$ with $|l - s| \leq j \leq |l + s|$. The lowest s-type ($l = 0$) energy band of the CB stays independent from the SO interaction contrary to the p-type VB ($l = 1$) that is directly affected and divides into sub-bands $j = \frac{1}{2}$ and $j = \frac{3}{2}$ in $k = 0$. The band associated with $j = \frac{3}{2}$ is

Semi-conducteur	Gap 0K/300K (eV)	Mobility e^- 300K $(cm^2/V.S)$	Mobility h^+ 300K $(cm^2/V.S)$	m^*/m_0 e^-	m^*/m_0 h^+	$\varepsilon_s/\varepsilon_0$
GaAs	(D) $1,52/1,42$	8500	400	$0,067$	$0,082$	$13,1$
InP	(D) $1,42/1,35$	4600	150	$0,077$	$0,64$	$12,4$
Si	(I) $1,17/1,12$	1500	450	$\|0,98$ $\perp 0,19$	$0,16lh$ $0,49hh$	$11,9$
Ge	(I) $0,74/0,66$	3900	1900	$\|1,64$ $\perp 0,082$	$0,04lh$ $0,28hh$	16

Table 2.2: Transport datas for electrons and holes in four semiconductors typically used to study spin injection. Table extracted from [67]

four time degenerated $j_z = -\frac{3}{2},\ -\frac{1}{2},\ \frac{1}{2},\ \frac{3}{2}$ (LH-band + HH-band for both spin orientation). The HH-band and the LH-band can be assimilated to parabols for $k \neq 0$ and are described by:

$$\begin{cases} E_{HH}(p) = \dfrac{p^2}{2m_{HH}} \text{ for } J_z = \pm\frac{3}{2} \\ E_{LH}(p) = \dfrac{p^2}{2m_{LH}} \text{ for } J_z = \pm\frac{1}{2} \end{cases} \tag{2.31}$$

The band of lower energy $j = \frac{1}{2}$ is two time degenerate $j_z = -\frac{1}{2},\ \frac{1}{2}$ and is called the Split-Off band (Figure 2.17 (b)). In $k = 0$, it is separated from the HH-band and the LH-band by an energy included 0.1 to 1 eV depending on the atomic number of the III-V semiconductor's cation. In GaAs $\Delta_0 = 0.34$ eV while in InP $\Delta_0 = 0.11$ eV.

2.2.1.2 Spin information conversion through quantum opto-electrical mechanism

In Spin-LEDs and Spin-LASERs emission of circularly polarized light originates from radiative recombinations of spin polarized electrons with unpolarized hole in active mediums such as QWs. The spin polarization is directly related to the optical polarization through the optical quantum selection rules governing radiative recombination. There is a proportionality relation between the spin polarization of the injected current P_s and the DoCP of the emitted light P_{circ} when the ferromagnetic layer magnetization and the optical measurement direction are parallel to the QWs quantification axis (growth direction) [29, 184, 92, 99, 98]. The annihilation of an e^- - h^+ pair during the inter-band recombination process triggers a transfer of the total electron-hole angular momentum to the emitted photon. In $\hbar$ units, polarized photons have an angular momentum projection on the wave vector direction equal to +1 or 1 respectively. Thus the radiation resulting from the recombination of the spin-polarized carriers will be partially circularly polarized if the spin orientation

Band	$\lvert J, m_j\rangle$	Wavefunction
Conduction	$\left\lvert\frac{1}{2}, +\frac{1}{2}\right\rangle$	$\lvert s\rangle\uparrow$
	$\left\lvert\frac{1}{2}, -\frac{1}{2}\right\rangle$	$\lvert s\rangle\downarrow$
Heavy Hole	$\left\lvert\frac{3}{2}, +\frac{3}{2}\right\rangle$	$-\frac{1}{\sqrt{2}}\left(\lvert p_x\rangle + i\lvert p_y\rangle\right)\uparrow$
	$\left\lvert\frac{3}{2}, -\frac{3}{2}\right\rangle$	$+\frac{1}{\sqrt{2}}\left(\lvert p_x\rangle - i\lvert p_y\rangle\right)\downarrow$
Light Hole	$\left\lvert\frac{3}{2}, +\frac{1}{2}\right\rangle$	$-\frac{1}{\sqrt{6}}\left(\lvert p_x\rangle + i\lvert p_y\rangle\right)\downarrow -2\lvert p_z\rangle\uparrow$
	$\left\lvert\frac{3}{2}, -\frac{1}{2}\right\rangle$	$+\frac{1}{\sqrt{6}}\left(\lvert p_x\rangle - i\lvert p_y\rangle\right)\downarrow +2\lvert p_z\rangle\downarrow$

Table 2.3: Wavefunctions describing the CB and the VB states near the Γ-point. Table reprinted from [84].

has not entirely relaxed by the time of recombination. Thereupon, the DoCP of the radiation serves as a useful and direct measure of the carrier density spin state as well as its change under the influence of external factors and relaxation processes.

The spin polarization can be quantified from optical polarization measurements by examining the optical quantum selection rules. In a direct gap semiconductor the interband transition rate W_{if} from an initial state Φ_i to a final state Φ_f is given by the Fermi's golden rule [84]:

$$W_{if} = \frac{2\pi}{\hbar}\left\lvert\langle\Phi_f\rvert H_I\lvert\Phi_i\rangle\right\rvert^2 N \tag{2.32}$$

$$\text{with:}\qquad \langle\Phi_f\rvert H_I\lvert\Phi_i\rangle = M_{if} = \int \Phi_f^*(\vec{r})H_I\Phi_i(\vec{r})d^3r$$

where H_I is the interaction Hamiltonian and N is the density of final states representing the number of ways in which the transition can occur. The matrix element $\langle\Phi_f\rvert H_I\lvert\Phi_i\rangle$ given by the overlap integral quantifies the coupling strength between the initial state and the final state. For electronic state close to the Γ-point, the electron wavefunctions in the CB and VB can be described by Bloch wavefunctions with associated Bloch states $\lvert J, m_j\rangle$ denoted according to the total angular momentum J and its projection onto the quantification axis m_j. In this notation, the wavefunctions describing the CB and the VB states near Γ can be expressed in terms of wavefunctions with s, p_x, p_y and p_z orbital character (See table 2.3).

The interaction Hamiltonian H_I is the operator materializing the physical interaction coupling the initial and final states. In the present case, the interaction is between an electric dipole and an external field such that the interaction operator is given by:

$$H_I = \vec{\mu} \cdot \vec{E} = \mu_x E_x + \mu_y E_y + \mu_z E_z \tag{2.33}$$

where $\vec{\mu}$ is the dipole moment and $\vec{E}$ is the electric field of the light wave. The components of the electric field E_x, E_y and E_z are considered constant as the electric field variations are small compare to the periodical variation of the lattice potential. When the vector operator $\vec{\mu}$ is expressed as a spherical tensor $\mu^1_{\pm 1}$ for $\sigma^{\pm}$ optical transition, the Wigner-Eckart theorem enunciate that the non-zero matrix element ($\langle \Phi_f | H_I | \Phi_i \rangle \neq 0$) are the terms verifying the relation $\Delta m_j = \pm 1$ [84]. Then in surface emitting devices, the conservation of angular momentum for $m_j = \pm 1$ radiative transition imposes the generation of $\sigma^{\mp}$-polarized photon. The transition probabilities for allowed transitions are given in table 2.4. The orientation convention is to consider a photon right circularly polarized σ^+ (respectively left circularly polarized σ^-) when emitted from a $\Delta m_j = -1$ transition and propagating toward the surface (respectively toward the backside). The optical selection rule are only strictly valid at the Γ-point. By moving away from Γ the HH and LH band mixture results in a non-ideal optical polarization.

At Γ, the CB → HH transition are three times more probable than the CB → LH transition regardless to the active medium nature (Table 2.4 & Figure 2.19 (b)). In a bulk semiconductor the HH-band and the LH-band are degenerate in Γ which intrinsically limit the DoCP to half the value of the spin polarization degree injected in the device (Figure 2.19 (a)). Thus, the maximum value theoretically reachable for P_{circ} with a bulk active medium will be limited to 50% for a carrier's spin polarization of 100% [84]:

$$P_{circ} = \frac{I(\sigma^+) - I(\sigma^-)}{I(\sigma^+) + I(\sigma^-)} = \frac{(3n_\downarrow + n_\uparrow) - (3n_\uparrow + n_\downarrow)}{(3n_\downarrow + n_\uparrow) + (3n_\uparrow + n_\downarrow)} = \frac{n_\downarrow - n_\uparrow}{2(n_\uparrow - n_\downarrow)} = -\frac{P_s}{2} \tag{2.34}$$

where $I(\sigma^+)$ and $I(\sigma^-)$ are the intensities for σ^+- and σ^--polarized light respectively. $n_\uparrow$ and $n_\downarrow$ stands for the DOS of spin-up and spin-down electrons respectively.

The case of QWs is much more appealing as the quantum confinement and potential epitaxial strain lift the degeneracy between the HH-band and the LH-band in Γ. For $\mathrm{Al}_x\mathrm{Ga}_{1-x}\mathrm{As}$ and $\mathrm{In}_x\mathrm{Ga}_{1-x}\mathrm{As}$, that we extensively used in the active medium of Spin-LEDs and Spin-VECSELs, the HH-band is energetically higher than the LH-band. Consequently the LH states can be ignored, especially since the CB → HH transitions are three times more probable than the CB → LH transitions. It is then theoretically possible to reach 100% DoCP for an injected spin polarization of 100% [84]:

$$P_{circ} = \frac{I(\sigma^+) - I(\sigma^-)}{I(\sigma^+) + I(\sigma^-)} \cong \frac{3n_\downarrow - 3n_\uparrow}{3n_\downarrow + 3n_\uparrow} = \frac{n_\downarrow - n_\uparrow}{n_\downarrow + n_\uparrow} = -P_s \tag{2.35}$$

Interband Transition	Matrix element M_{ij}	Δm_j	Emission Polarization	Transition Probability $\|M_{ij}\|^2$
CB↑ ⟶ HH↑	$\langle \frac{3}{2}, +\frac{3}{2} \| \mu_x \| \frac{1}{2}, +\frac{1}{2} \rangle$	-1	σ^+	$\frac{1}{2} \| \langle p_x \| \mu_x \| s \rangle \|^2$
CB↓ ⟶ HH↓	$\langle \frac{3}{2}, -\frac{3}{2} \| \mu_x \| \frac{1}{2}, -\frac{1}{2} \rangle$	+1	σ^-	$\frac{1}{2} \| \langle p_x \| \mu_x \| s \rangle \|^2$
CB↑ ⟶ LH↓	$\langle \frac{3}{2}, -\frac{1}{2} \| \mu_x \| \frac{1}{2}, +\frac{1}{2} \rangle$	+1	σ^-	$\frac{1}{6} \| \langle p_x \| \mu_x \| s \rangle \|^2$
CB↓ ⟶ LH↑	$\langle \frac{3}{2}, +\frac{1}{2} \| \mu_x \| \frac{1}{2}, -\frac{1}{2} \rangle$	-1	σ^+	$\frac{1}{6} \| \langle p_x \| \mu_x \| s \rangle \|^2$

Table 2.4: Interband transitions probabilities and related polarization of the emitted photon. Table reprinted from [84].

Nevertheless, in the permanent regime, the spin polarization in the active medium is not immediately converted into optical circular polarization. The conversion process is governed by a recombination time τ characteristic of the active region with $\frac{1}{\tau} = \frac{1}{\tau_r} + \frac{1}{\tau_{nr}}$ where τ_r and τ_{nr} are the radiative and non-radiative recombination rate respectively. In the case where the spin relaxation time τ_s is shorter than the recombination time: $\tau_s << \tau$, the spin information will be lost through relaxation mechanisms before the carriers recombine. Thus, when trying to extract the spin polarization degree of the injected carriers from the emitted light DoCP, it is necessary to introduce a renormalization factor $F = \frac{1}{1+\frac{\tau}{\tau_s}}$ taking into account the relative variation of the characteristic life times:

$$\boxed{P_s = \frac{1}{F} \cdot P_{circ} = \left(1 + \frac{\tau}{\tau_s}\right) \cdot P_{circ}} \tag{2.36}$$

This relation enables us to directly use the emitted light DoCP as a probe for the measurement of the injected carriers spin polarization degree and is used to characterize the injection efficiency of the ferromagnetic spin injectors. Nevertheless, as the depolarization mechanisms occurring during transport from the injector the the active medium are not taken into account, this only provides us an inferior limit value of the spin injection efficiency (see section 2.2.1.4).

2.2.1.3 Circularly-Polarized Optical Pumping

Circularly-polarized optical pumping stands out as a corner stone of the spin injection in III-V optoelectronic devices. This mechanism enables the generation of spin polarized carrier by engaging light/matter interactions. We used it extensively during our experiments and it deserve a particular attention.

Under optical pumping, the electron gas of a semiconductor medium is photoexcited between different energy levels by absorption of the incident light. The technique was developed by 1966 Nobel Laureate Alfred Kastler in the early 1950s [185, 186, 187].

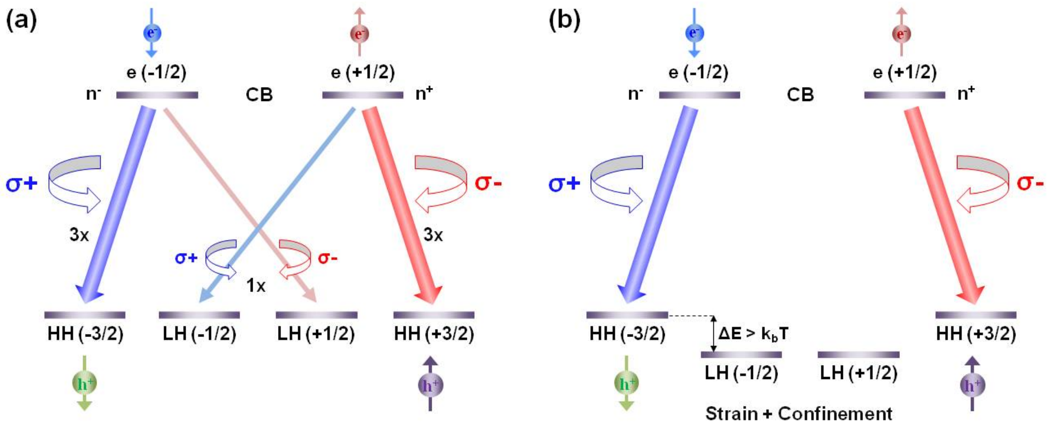

Figure 2.19: Optical Quantum selection rules for dipole radiation: (a) In the case of a bulk active medium, the HH-band and LH-Band are degenerated and a CB→HH recombination is three times more probable than a CB→LH recombination. (b) In QWs, the epitaxial strain and quantum confinement lift the degeneracy between the HH-band and LH-Band. The energetically favored transition becomes CB→HH and if the bands are separated by an energy at least several times the thermal energy: $P_{circ} = P_s$

The influence of the light polarization on the spin generation in the active medium was highlighted by Lampel in 1968 [188]. In the context of lasers, the goal is to achieve a population inversion in the gain medium to obtain optical amplification via stimulated emission for some range of optical frequencies. The width of that range is called the gain bandwidth.

In case of Spin-LEDs and Spin-VECSELs, optical pumping is used to cyclically pump electrons bound within a well-defined quantum state. Generally, the quantum confinement is ensured by quantum well structures based on binary ($GaAs$, GaN, InP, $InAs$, $ZnSe$, ...) or ternary ($\mathrm{Al}_x\mathrm{Ga}_{1-x}\mathrm{As}$, $\mathrm{In}_x\mathrm{G}_{1-x}\mathrm{As}$, $\mathrm{Al}_x\mathrm{Ga}_{1-x}\mathrm{P}$, GaAsP, ...) direct gap semiconductors. For the simplest case of coherent two-level optical pumping in a semiconductor band structure, this means that the electron is coherently pumped from the valence band (VB) to the conduction band (CB). Due to the cyclic nature of optical pumping the bound electron will actually be undergoing repeated excitation and decay between VB and CB.

As light absorption is the exact reverse mechanism of radiative recombination, the generation of spin-polarized carriers by absorption of circularly polarized light follows the same functioning pattern and obey to the same quantum selection rules. Consequently the reader can relate to the previous section for more details on the mechanism involved. The key for an efficient optical spin-injection in a semiconductor relies on the optical quantum selection rules for dipole radiation associated with the conservation of angular momentum z-projections m_z occurring in confined

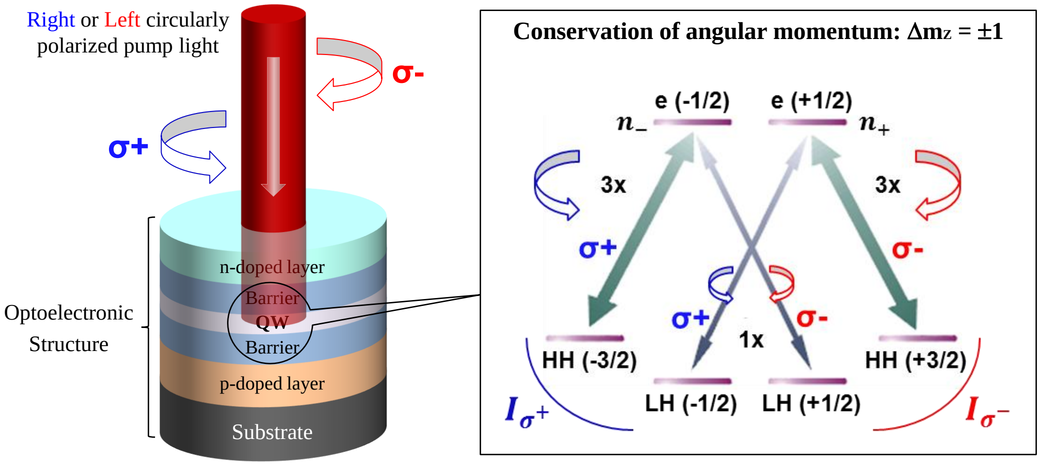

Figure 2.20: Scheme of the circularly polarized optical pumping mechanism: Spin generation happens through preferential transition driven by the optical quantum selection rule in the active medium (QW) of the optoelectronic device.

strained active medium or Quantum Wells (QWs) [30]. The allowed transitions are quantified by $\Delta m_z = \pm 1$. In QWs, the lift of degeneracy between the Heavy Hole (HH) band and the Light Hole band (LH) leads to preferential spin-polarized carriers generation by absorption of circularly polarized photons between the HH-band and the Conduction Band (CB). The absorption of left circularly polarized light σ^- of intensity I_{σ^-} (respectively right circularly polarized light σ^+ of intensity I_{σ^+}) results in the generation of spin-$\uparrow$ electrons with an associated DOS at the Fermi level $n_\uparrow$ (respectively spin-$\downarrow$ with an associated DOS at the Fermi level $n_\downarrow$) for the $HH(+3/2) \to CB(+1/2)$ transition (respectively $HH(-3/2) \to CB(-1/2)$ transition). The spin polarization degree of the optically injected electrons can be then defined by $P_s^{opt} = (n_\uparrow - n_\downarrow)/(n_\uparrow + n_\downarrow)$ (Figure 2.20). While in bulk GaAs a 50% spin polarization can be induced at best, a P_s^{opt} close to a 100% can theoretically be achieved in QWs. Thus, on a pure spin injection efficiency point of view, spin injection using circularly polarized optical pumping offers an interesting solution to overcome the limitations faced with direct injection where the efficiency is limited by the intrinsic spin polarization of the ferromagnetic P_s^F and the interface resistance r_b^*.

It is important to note that the quantum selection rules are strictly valid at the Γ-point of the band structure. Additionally, to prevent the spin mixing and maximize P_s^{opt} the incident photons energy needs to be higher than the band gap energy but not high enough to excite carriers from the split-off band. The absorption coefficient $\alpha = A^* \sqrt{h\nu - E_g}$ of the material at the wavelength $\lambda = \frac{v}{\nu}$ also plays a fundamental role in the conversion efficiency of the angular momentum. Finally, the incidence of the pump beam should be normal to the devices active medium in order to prevent any elliptical projection of the circular polarization ("end pumping") which would significantly reduce the mechanism performances.

Even though semiconductor optoelectronic devices are commonly electrically pumped for application requirement, optical pumping offers certain advantages. For example in the case of VECSELs, it allows for a laser output with very high brightness (high power combined with high beam quality). In other cases, optical pumping is sometimes used for testing purposes, e.g. when new semiconductor compositions are investigated. Optically pumped semiconductor gain media generally have a simpler structure than their electrically pumped counterparts.

2.2.1.4 Design of spin-polarized light sources

General considerations

The first parameter to address is the distance between the spin injector and the active medium of the device.

The travel time between the ferromagnetic spin polarizer and the QWs needs to be as short as possible to maximize the spin collection and minimize the spin depolarization through relaxation mechanisms. The dependency of spacer thickness on the spin injection efficiency was experimentally witnessed in a study investigating anisotropic spin injection in an InGaAs QW Spin-LED with GaMnAs spin-injector. A monotonic increase from 0.5% to 7% in the polarization was measured as the spacer thickness decreased from 420 nm to 20 nm [189]. This results clearly highlights that the spacer thickness should be minimized in order to maximize the spin conversion. However, in practice a compromise has to be found between minimizing the spin transport length and limiting the interdiffusion of magnetic impurities into the active region. The contamination of the recombination area can potentially result in unwanted parasitic polarization which could bias the measurement of the emitted light DoCP or even mask the evidence of spin injection [84].

The second significant criterion to consider is the emitting geometry of the device:

Surface-emitting geometry: This geometry has been applied for the architecture of every Spin-LEDs and Spin-VECSELs used during this Ph.D thesis. It offers at least two advantages over an edge-emitting geometry. The major one concern the optical quantum selection rules: heart of the conversion mechanism, they are much more straightforward in the Faraday geometry due to considerations on the projection of the angular momentum. In QWs the quantum confinement and reduced symmetries pull the angular momentum of the HH-states along the quantification axis (along the surface direction). Thus, the spin orientation of the injected electrons should also be parallel to the quantification axis and the conservation of the angular momentum has to be analyzed along the z-axis. Secondly, a surface-emitting geometry offers a short escape distance (≈ 100 nm) for the photons stemming from the radiative recombinations which significantly reduces photon reabsorption and recycling. The down side of using a surface-emitting geometry lies in the passage of the circularly polarized emitted photons through the ferromagnetic spin aligner. The differential absorption of right (σ^+) and left (σ^-) circularly polarized light in the ferromagnetic layer introduces an artificial polarization which has the potential to distort the light DoCP measurements. This phenomenon is called Magnetic Circular Dichroism (MCD) (see section 2.2.1.5). Moreover, a relatively strong applied magnetic field is usually required to overcome the shape anisotropy of the ferromagnetic thin layer and drive the magnetization out-of-plane in order to polarize the injected carriers along the z-axis. In the second part of the manuscript, we will see that this issue can be overcome by implementing of spin-injector exhibiting intrinsic Perpendicular Magnetic Anisotropy (PMA).

Edge-emitting geometry: Prima facie this configuration seems to be the most suitable for applications as only modest applied magnetic field are required for spin manipulation. Indeed, the shape anisotropy of the ferromagnetic thin film restricts the easy magnetization axis in-plane. The device can operate in a remanent state and easily switched with a weak magnetic field (induced by a command electrical line for instance). Nevertheless, the main handicap of this architecture is the orthogonal orientation between the confinement axis and the spin polarization of the injected carriers. This geometry considerably reduces the spin conversion efficiency through the optical quantum selection rules. Additionally, the light has to travel distances that can potentially exceeds several 100 μm to escape the structure. This opens the door to strong photons reabsorption and complicate the precise quantification of spin polarization from optical polarization measurements [84]. Nonetheless, despite the reduced efficiency of the quantum selection rules in edge-emitting geometry, spin injection performances competitive with the values obtained in surface-emitting geometry were experimentally demonstrated in AlGaAs/GaAs QW Spin-LEDs [190].

Active region - Spin detection medium

One can instinctively understand that the structure and composition of the active medium of the spin-polarized light source considerably influence the operating characteristics of the device. The ideal active medium would display an almost infinite spin lifetime τ_s compare to the radiative recombination time τ_r to reach a 100% information conversion efficiency. As explain in section 2.1.3.5, τ_s tends to significantly increase with the carrier confinement due to the inversely related impact of the spin relaxation mechanism. Naturally, when walking through the state-of-the-art of spin-polarized light sources, QWs and QDs clearly stands out the dominant choice for active mediums. They combine: (i) a strong carrier spatial localization (depth resolution) and (ii) the generation of photons easily distinguishable from other spectroscopic features arising from emission in other region of the heterostructure thanks to the smaller band gap of the QWs compare with the bulk material. This also has the advantage to limit the photons interactions with the heterostructure and minimizing the MCD re-absorption.

The trend goes preferentially to the use of lattice-matched AlGaAs/GaAs or InGaAs/GaAs QW wherein optical quantum selection rules can immediately apply. The strains active medium should be avoid as recombination dynamics can deviate significantly from the textbook case and reduce the spin conversion efficiency [191, 192]. It was theoretically predicted that for 100% spin-polarized injected electron a maximum proportionality factor $\frac{P_s}{P_{circ}}$ is achievable even at low temperatures [191]. The QWs growth direction ((100) or (110)) also plays a key role in the spin relaxation time. Spin lifetimes of the nanosecond order at room temperature were experimentally measured in (110)-GaAs QWs Spin-LEDs as a consequence of the inhibition of the DP relaxation mechanism. This is more than an order of magnitude longer than that of the (100) counterparts [193]. In QWs the increase of τ_r and the decrease τ_s associated with the increase of temperature and bias tend to decrease the $\frac{\tau_r}{\tau_s}$ ratio. For a considered carrier initially spin polarized, the condition $\tau_r \geq \tau_s$ leads to a loss of the spin information before the radiative recombination occurs and so to an average decrease of P_{circ}. At constant bias the variations of τ_r and τ_s relative to one another with the temperature fix the global dynamics evolution of P_{circ}. Consequently, it is necessary to take into account the $\frac{\tau_r}{\tau_s}$ ratio to accurately quantify the injected spin polarization from optical measurements (eq. 2.36). It is also observe that as either the temperature or bias increases, P_{circ} further decreases. Particularly since thermal spreading of the carrier distribution results in the occupation of the QW light-hole bands and the occupation of non-zero quasi-momentum states were band maxing arises [84].

The active medium of the devices used during the thesis were based on: (i) $Al_xGa_{1-x}As$/GaAs and $In_xGa_{1-x}As$/GaAs QWs for the Spin-LED and (ii) strained $In_{22\%}Ga_{78\%}As$/$GaAs_{95\%}P_{5\%}$ QWs for the VECSEL. The use of strained-balanced QWs in the case of lasers enables to stack more QWs in the active medium without adding any strains which would induce dislocations and thus reduce the carrier lifetime. But as we will see in the fourth chapter, circularly polarized mode stabilization issues arise from the lattice strains.

2.2.1.5 Measurements considerations

Detection geometries

Three measurement geometries are typically employed for the characterization of spin-polarized light sources: Faraday, Voigt and oblique Hanle effect. The best configuration for a particular experiment is determined by the details of the heterostructure and device design.

Faraday geometry: This geometry was used for all the measurement performed during the Ph.D. project. It is commonly the most used geometry as the optical selection rules are straightforward in this configuration allowing a direct readout of the spin injection efficiency (Figure 2.21 (a)). In most cases, this configuration is associated with the need to apply an external magnetic field to overcome the spin injector shape anisotropy and align the magnetization out-of-plane parallel to the quantification axis. A field of few Tesla can easily create a sizable Zeeman splitting of the CB and the VB states in the QWs and induce a parasitic contribution to the emitted DoCP. This problem is instantly overcome if the injector naturally displays perpendicular magnetic anisotropy.

Voigt geometry: This geometry is applied to characterize the rarely used edge-emitting Spin-LEDs (Figure 2.21 (b)). The selection rules applied in the Faraday geometry with QWs active medium are no longer valid as the injected carriers are spin polarized in the direction perpendicular to the quantification axis. In-plane spin-polarized electrons may be conceived as a coherent superposition of an equal number of spin-up and spin-down electrons; thus the resulting optical polarization will not attain a net CP when measuring along the z-axis [84].The active mediums usable for this geometry are either QD or bulk medium and the relation between P_s and P_{circ} is no longer direct. In most cases, the performances exhibited by Voigt geometry devices are always below the results achieved with surface-emitting devices. P_{circ} levels hardly flirting with 2% at low temperature (see table 2.5). The only advantage lies in the possibility of operation at magnetic remanence as most thin film ferromagnets easy axis is in-plane. It also avoids any magnetic field-dependent artifacts and MCD contribution as the emission is collected through a cleaved facet and does not have to pass through a ferromagnetic spin aligner.

Oblique Hanle geometry: This detection method was first implemented on Spin-LEDs by Motsnyi *et al.* [109, 98]. It involves the application of an oblique magnetic field $\vec{B}$ making an angle of roughly 45° with respect to the horizontal axis (Figure 3.5 (c)). $\vec{B}$ induces a precession of the carrier's spin with the Larmor frequency $\vec{\Omega}$ and assigns a perpendicular component to the spin vector detectable through the emitted light DoCP. This configuration is a clever way to effectively detect spin injection from an in-plane ferromagnetic contact. The application of a small oblique $\vec{B}$ manipulates spins during transport sufficiently enough to obtain a component along the z-axis. In OHE geometry where the applied $\vec{B}$ make an angle θ with the horizontal axis, P_{circ} is related to P_s through the following equation [194]:

$$P_{circ} = \frac{I(\sigma^+) - I(\sigma^-)}{I(\sigma^+) + I(\sigma^-)} = \frac{1}{4} \cdot \frac{T_s}{\tau} \left[\frac{(\Omega T_s)^2}{1 + (\Omega T_s)^2} \cdot cos(\theta) + \frac{1 + \frac{(\Omega T_s)^2}{2}}{1 + (\Omega T_s)^2} \cdot sin(\theta) \right] \cdot P_s \tag{2.37}$$

where the ratio $\frac{T_s}{\tau}$ is the spin detection efficiency of the active medium, T_s being the spin life time with $\frac{1}{T_s} = \frac{1}{\tau} + \frac{1}{\tau_s}$, τ the e^- - h^+ recombination time and τ_s the spin-relaxation time. This technique provides additional insights not immediately available in the other measurement geometries. It offers the advantage

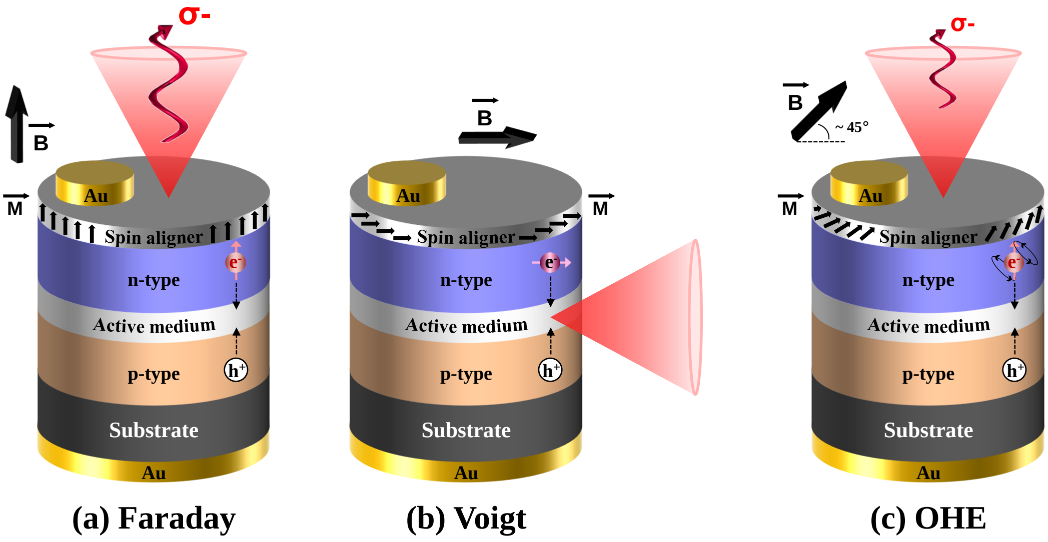

Figure 2.21: Schematic representation of the three detection geometries for Spin-LEDS: (a) Faraday geometry: Injection of carriers spin-polarized along the QWs confinement axis combined with a vertical emission. **(b)** Voigt geometry: Injection of carriers spin-polarized in-plane (bulk active medium) combined with a side emission. **(c)** Oblique Hanle Effect: Injection of carriers spin-polarized with a 45° angle regarding to the QWs confinement axis combined with a vertical emission.

to discriminate the actual spin injection from bias contributions such as MCD and Zeeman effect [84].

Determination of the Spin Polarization Degree

When measuring the spin polarization degree of the injected carriers P_s using optical technics, it is important to remember that the DoCP emitted by the device reflects a multi-step process. The steady-state optical polarization is typically less than the spin polarization of the carriers injected at the F/SC interface [84]. The measured DoCP only reflects the spin polarization of the carrier density in the active region and not the spin polarization at the F/SC interface. During transport from the injection interface towards the active medium, the spin polarization is reduced due to spin scattering processes linked to hot electrons thermalization.
However, the spin depolarization rate associated with transport from the F/SC interface towards the QWs have a negligible impact on the average carrier spin lifetime compare to the spin depolarization rate in the QWs before radiative recombinations. Indeed, the transport drift time is smaller (τ_{drift} <ps) than the "waiting" time in the active medium ($\tau_r \approx$ 100ps in $GaAs$ QW at 10 K. Consequently, we consider the normalized value of P_s in the QWs calculated from P_{circ} using the renormalization factor F gives a good estimation of the actual spin injection efficiency under the injector. Assuming that there is no re-polarization mechanisms such as magnetic impurities in the active medium, this calculated spin polarization value (equations

2.34, 2.35, 2.36) stands as an inferior limit of the spin injection efficiency at the F/SC interface.

Additionally, only the free exciton's and free carrier's components of the optical polarization provide a quantitative measure of the spin polarization of the carriers involved in the quantum selection rule [195]. Thus, a reliable measure of the spin injection efficiency can be obtained only if one takes care to spectroscopically resolve and accurately identify the free exciton and free carrier components. Other spectral features such as donor- and acceptor-bound excitons, phonon replicas, recombinations mediated by various impurity levels or complexes (CB → Acceptor, Donor → Acceptor, etc...), exhibit polarization characteristics which do not reflect spin polarization. These processes do not have well defined angular momentum [196]. The relative intensity of these spectral components can be minimized with careful control of the heterostructure doping profile and material quality.

Spurious contribution to the Degree of Circular Polarization

When probing the spin injection efficiency in a spin-polarized light source, separating real DoCP from artifacts contribution is of primary importance. Induced circular polarization (CP) can arise from the three main parasite mechanisms: the diffusion of magnetic impurities, Magnetic Circular Dichroism (MCD) and Zeeman effect.

Even a small diffusion of magnetic impurities from the ferromagnetic spin injector into the active medium of the device can induce a significant CP of the emitted light by sporadic spin polarization or re-polarization of the electrically injected carriers. In practice, a non-magnetic spacer of at least several tens of angstroms thick should be introduced in between the ferromagnetic thin layer and the active region considering the typical interdiffusion lengths for MBE-grown structures [84]. This condition is usually easily verified since the thickness of the multilayer stack (with a doping gradient) inserted in between the ferromagnet and the QWs is commonly around 100 nm.

In surface emitting devices, the emitted light passes trough the ferromagnetic layer used as a spin polarizer before reaching the measurement setup. The differential absorption between σ^+ and σ^- polarized light by the ferromagnetic material induces Magnetic Circular Dichroism (MCD) that modifies the total DoCP of the emitted light. In Spin-LEDs the MCD artefact depends on the emission angle and is rarely above 3%. The MCD contribution can be directly quantify by pumping the device with linearly polarized light and analyzing the Photoluminescence (PL) ellipticity. Otherwise it can be bypassed using QWs with different energy gap to generate photons transparent to the rest of the device and detect the EL in a back-side configuration. In the case of Spin-VECSELs, the impact of the intra-cavities injectors is suspected to be much more significant as the number of light round trip in the resonant cavity is considerably higher.

In most experiments, an apply magnetic field is required to drive and switch the magnetization of the ferromagnetic spin injector. Spurious Zeeman effect can arise from the lift of degeneracy of the spin sub-bands within the active medium. Since carriers thermalize to fill the lowest energy states, the carrier density in the active region will attain a net spin polarization resulting in a slight CP for the emission not related to direct injection from the magnetic contact. Thankfully, this artifact can be easily identify by looking at the measured DoCP when reversing the magnetic field.

2.2.2 The Spin-LED concept

A Spin-LED is a Light Emitting Diode structure caped with a ferromagnetic spin injector used to spin polarized the carriers before injection in the active medium of the LED structure. The LED structure is typically a semiconductor heterostructure including an electron reservoir (n-doped region) and a hole reservoir (p-doped region) separated by a lightly doped "near" intrinsic semiconductor region. The first significant demonstration of spin injection in a LED structure was achieved by Fiederling *et al.* with a II-VI DMS ferromagnetic injector on top of an AlGaAS/GaAS QW LED structure [29].

2.2.2.1 n-i-p band structure

A n-i-p semiconductor structure is a diode with a wide, lightly doped "near" intrinsic semiconductor region between a p-type semiconductor and an n-type semiconductor region. The p-type and n-type regions are typically heavily doped as they are used for ohmic contacts. The addition of an intrinsic layer changes properties of the p-n junction.

When reverse biased, a n-i-p diode enable the emission of light from the intrinsic region. By energetically concentrating the radiative recombinations, the i-region reduces the spectral enlargement emerging from the layers inhomogeneities. Compared to conventional p-n diodes, the emitted wavelength is not submitted to a commonly observed redshift when emission happens from a doped region. It is also possible to introduce a confined potential such as QWs or QDs in the intrinsic region (Figure 2.22). In addition of increasing the radiative recombination efficiency, this gives an additional degree of freedom to modulate the emitted wavelentgh according to the dimensions and strains of the QWs/QDs. When the diode is forward biased, the injected carrier concentration is typically several orders of magnitude higher than the intrinsic level carrier concentration. Due to this high injection level (favored by the depletion process) the electric field extends deeply (almost the entire length) into the region. This electric field helps to speed up the transport of charge carriers from the P region to the N region. This process results in faster operation of the diode making it a suitable device for high frequency operations.

When reversed biased, a n-i-p diode can be use as an ultra-fast photo-detector with a bandwidth of several GHz. Indeed, the small carrier density in the intrinsic region provides a relatively long lifetime to the photo-generated e^{-} - h^{+} pairs by the reason of a low recombination probability. This translates in a highly efficient photo-generation.

Compare to conventional p-n diodes, the wide intrinsic region makes the n-i-p diode an inferior rectifier (one typical function of a diode). But, on the other hand, it makes the n-i-p diode suitable for attenuators, fast switches, photo-detectors, and high voltage power electronics applications.

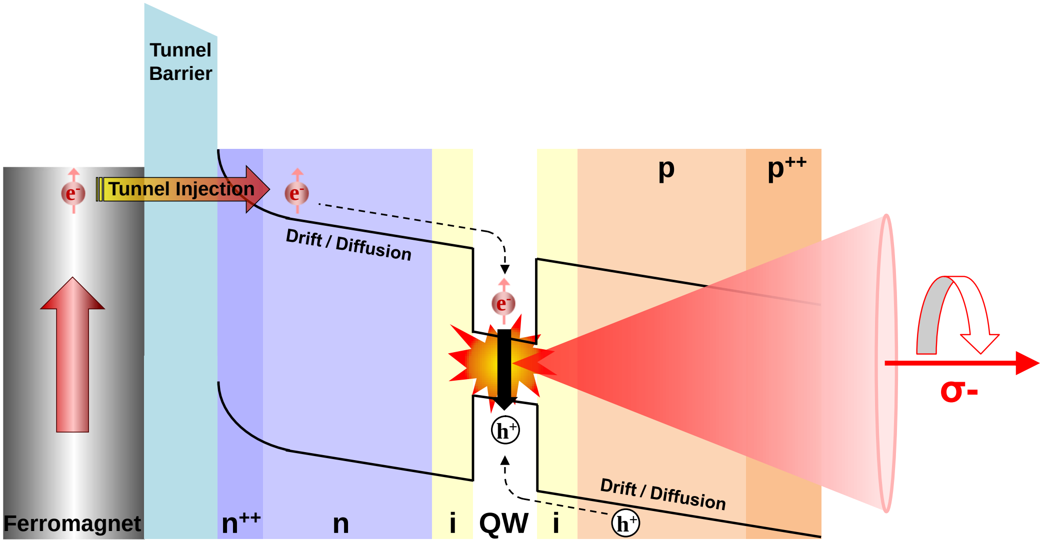

Figure 2.22: **Schematic band structure of a n-i-p Spin-LED**

2.2.2.2 State-of-the-art

The very first two Spin-LEDs were reported simultaneously by Fiederling *et al.* [29] and Ohno *et al.* [197] in 1999.

Outstanding results were already obtained with electrically injected Spin-LEDs using different type of spin-injectors polarized in an applied magnetic field on different active mediums. As displayed in table 3.5, a degree of circular polarization P_{circ} as high as 86% at 1.5 K was reached by Fiederling *et al.* using a BeZnMnSe Diluted Magnetic Semiconductor (DMS) on top of a GaAs-bulk LED in the Faraday geometry [29]. Jiang *et al.* demonstrated a $P_{circ} = 47\%$ at 290 K using a CoFe/MgO(100) Metal Tunnel Junction (MTJ) deposited on a AlGaAs/GaAs QW Spin-LED in a Faraday configuration with a 5 T perpendicular applied magnetic field [99]. With Fe/(Al)GaAs Schottky barrier, Hanbicki *et al.* showed a $P_{circ} = 30\%$ at 240 K also in a vertical configuration with a 3 T magnetic field [93].

To this day, the record for highest EL DoCP at room temperature is still held by Jiang *et al.* with the CoFe/MgO(100) MTJ injector. This same group also highlighted the weaker temperature dependence of the efficiency compared to the EL DoCP using this injector. They showed a stable $P_s \approx 70\%$ from 10 K to 300 K [198]. Unfortunately, the magnetization of most thin film ferromagnets resides in-plane due to the shape anisotropy. All these experiments required an applied $\vec{B}(T)$ to drive the magnetization out-of-plane to match the operation conditions (for Faraday configurations). This stays a strong limitation for potential applications.

So far, only a few groups have reported ferromagnetic spin injectors exhibiting Perpendicular Magnetic Anisotropy (PMA) [218, 219, 220]. Using a PMA MnGa

Spin Injector FM|DMS|Heusler	Active Region	Spin Polarization (%) / Temperature (K)	Geometry	Reference
$CoFe/MgO$	GaAs QW	52%/100 K; 32%/290 K	Faraday	[99]
	GaAs QW	70%/10-300 K	Faraday	[198]
	GaAs QW	32%/100 K	Faraday	[199]
$CoFe/AlO_x$	GaAs Bulk	21%/80 K; 16%/300 K	OHE	[98]
	GaAs Bulk	9%/80 K	OHE	[109]
Co/Al_2O_3	GaAs QW	2%/300 K	Faraday	[200]
Fe/AlO_x	InGaAs QW	15%/5 K (Switchable)	Voigt	[201]
Fe/GaO	GaAs QW	20%/2	Faraday	[202]
$NiFe\text{-}CoFe/AlO_x$	GaAs bulk	24%/80 K; 12%/300 K	OHE	[194]
$Ni_{80}Fe_{20}/Al_2O_3$	GaAs QW	0.2%/300 K	Faraday	[200]
Fe Schotttky	InGaAs QW	78%/2 K (BB Tans.)	Faraday	[203]
	GaAs QW	32%/4.5 K; 30%/240 K	Faraday	[93]
	GaAs QW	30%/20 K	Voigt	[190]
	InAs/GaAs QD	7.5%/15 K	OHE	[205]
	InAs QD	5%/80-300 K	Faraday	[181]
Fe_3Si *Schotttky*	InGaAs QW	3.5%/25 K; 2%/300 K	Faraday	[206]
MnAs	InGaAs QW	6%/80 K; <6%/300 K	Faraday	[207]
	GaAs QW	26%/300 K	Faraday	[208]
MnGa w/ PMA	GaAs QW	5%/2 K	Faraday	[209]
MnSb Schottky	GaAs Bulk	20%/80 K	OHE	[88]
(Fe/Tb) w/ PMA	InGaAs QW	0.75%/90 K	Faraday	[210]
	GaAs QW	3%/300 K	Faraday	[306]
GaMnAs (holes)	InGaAs QW	18%/5.1 K	Faraday	[212]
	InGaAs QW	1%/6 K	Voigt	[197]
	InAs QD	1%/4.5 K	Voigt	[213]
GaMnAs Zener	GaAs Bulk	82%/4.6 K	OHE	[113]
	InGaAs QW	6.5%/6 K	Faraday	[112]
	InGaAs QW	0.82%/5 K	Faraday	[214]
	InAs QD	1.2%/5 K; 0.2%/60 K	Voigt	[213]
ZnMnSe	GaAs Bulk	86%/1.5 K; 24%/33 K	Faraday	[29]
	GaAs QW	83%/4.5 K	Faraday	[195]
	CdSe QD	70%/2 K	Faraday	[215]
	InGaAs QD	21%/5 K	Faraday	[216]
$CdCr_2Se_4$	GaAs QW	4-6%/5 K	Faraday	[217]
Co_2MnGe	GaAs QW	27%/2 K; 2%/280 K	OHE	[123]
$Co_{2.4}Mn_{1.6}Ga$	InGaAs QW	13%/5 K	OHE	[121]

Table 2.5: Comparison of state-of-the-art spin injection efficiencies from various ferromagnetic contacts into Spin-LEDs with different active mediums. Table completed from [84].

ferromagnetic layer for spin injection, Adelmann *et al.* showed $P_{circ} = 5\%$ at 2 K in a remanent state [209]. Hovel *et al.* reported $P_{circ} = 3\%$ at room temperature using a rare earth based Cr/(Fe/Tb)$_{10}$ spin-injector in both Schottky and Tunnel configuration at magnetic remanence [306]. During this Ph.D, we succeeded in setting a new world record for PMA Spin-LED operating at magnetic remanence and at room temperature. A DoCP $P_{circ} = 8\%$ at room temperature was demonstrated using a $MgO/CoFeB/Ta$ MTJ spin-injector on an InGaAs/GaAs QW LED structure in Faraday configuration [312] (see Chapter III).

Table 3.5 overviews the state-of-the-art of spin injection in Spin-LEDs using spin-polarized electrical injection. Nevertheless one as to be careful when comparing the reported spin-injection efficiencies. In some cases the spin polarization stem from equations (2.32)-(2.33) while in other cases additional calculations accounting for spin relaxation are applied to ascertain the spin injection efficiency. If so, the reported spin-injection efficiency is systematically greater than that inferred directly from the EL polarization ($P_s > P_{circ}$).

2.2.2.3 Application limits: Towards spin injection in LASER systems

Despite the tremendous results obtained so far with Spin-LEDs, such spin optoelectronic devices will be competitive for realistic applications only if the spin-injection can be performed electrically, at room temperature and without applied magnetic field. Moreover the device must provide a switchable polarization state with an output P_c of nearly 100% in order for instance to robustly encode a bit of information.

Unfortunately, Spin-LEDs operate in a spontaneous emission regime. Their ability to efficiently convert the spin information into light polarization information is intrinsically limited by the ratio between the carriers recombination time τ_r and spin-life time τ_s in the active medium. This is particularly true when the temperature increases as the impact of the spin relaxation mechanisms (especially Dyakonov-Perel) becomes more significant in the structure and reduce the spin lifetime. Therefore, even if one could experimentally achieved an absolute spin polarization of 100% at the interface F/SC (Half-Metallic Ferromagnets), the carriers spin polarization at the time of radiative recombination would be notably inferior to 100%. Consequently, the DoCP of the emitted light is greatly restrained at room temperature due to the spin relaxation mechanisms occurring during the carriers drift towards QWs and inside the active region before radiative recombination. Additionally, when thinking of potentials applications, the spatially unfocused (4π-steradians emission) and non-coherent light emission is a great handicap. Finally, recent simulations also clearly highlights that the measured the emitted light DoCP depends on the measurement angle regarding to the z-axis [221].

All these limitations complicates the usability the Spin-LEDs for realistic applications. However, from a fundamental study viewpoint, the system remains a wonderful tools for the optimization of spin injectors as they offer a fairly direct readout of the spin injection efficiency. We extensively used the concept as an optimization platform for the development of III-V SC//MgO/CoFeB/Ta MTJ spin injector with remanent Perpendicular Magnetic Anisotropy (see Chapter III).

Fortunately, Lasers can overcome most of the limitation factors exhibited by LEDs just by their intrinsic nature of operation. Spin-LASERs provide higher performances as compared to Spin-LEDs in terms of beam properties and output P_c due to the amplification effect induced by the combination of a gain medium and a resonant optical cavity. An output P_c close to 100% can hence be achieved even by injecting a relatively low polarized spin-current in the active medium. Semiconductor based Vertical-Cavity-Surface-Emitting-Lasers (VCSELs) and Vertical-External-Cavity-Surface-Emitting-Lasers (VECSELs) stand out as perfect candidates for the implementation of spin-polarized laser sources. In the next section we will introduce VCSELs in details and their theoretical behavior under spin injection as well as the state-of-the-art on spin injection in such structures.

2.2.3 Spin injection into semiconductor laser structures

2.2.3.1 Description and properties of VCSELs

Vertical-Cavity Surface-Emitting Laser (VCSEL) qualifies a type of semiconductor laser where the monolithic resonator and the laser beam emission are oriented perpendicularly to the surface. By comparison, conventional edge-emitting semiconductor lasers emit from side surfaces formed by cleaving the individual chip out of the wafer [222, 223] (Figure 2.23 (a)).

The resonator (cavity) is constituted of two semiconductor Distributed Bragg Reflector (DBR). Each DBR is formed by multiple layers of alternating materials exhibiting different refractive index. Each layer has a thickness of $\frac{\lambda}{4}$ and the total reflectivity of the DBR can be finely tuned by choosing the number of layers stacked (Figure 2.23 (b)). Between those stands an active region (gain medium) with typically several quantum wells and a total thickness of only a few micrometers. High reflectivity mirrors are required in VCSEL to balance the short axial length of the gain region. For applications, the active region can be electrically pumped with a few tens of milliwatts and generates output powers in the range of 0.5 to 5 mW. Higher output powers are reachable in multimode emission. In the case of lab investigations, the active region of VCSEL may be pumped by an external light source with a shorter wavelength using another laser (optical pumping). This allows the demonstration of laser operation without the additional requirement of good electrical performance. The implementation of a mixed optical/electrical pumping is also possible [224].

VCSEL exhibit many attractive properties such as on-chip testing, long lifetime and low power consumption as the high reflectivity mirrors significantly reduce the threshold current compared to their edge-emitting counterparts. This low threshold current also enable to reach high intrinsic modulation bandwidths. They exhibit good beam quality for fairly small mode areas (diameters of a few microns) and the short resonator makes it easy to achieve single-frequency operation. VCSEL can even combined wavelength tunability by adjusting the gain band of the active region by adjusting the thickness of the reflector layers. A wide range of wavelength is also achievable with appropriate band engineering by tuning the active medium materials. The most common emission wavelengths of VCSELs are in the range of 750-980 nm (GaAs/AlGaAs QWs). Longer wavelengths of 1.3 μm, 1.55 μm (Telecom) or even beyond 2 μm (gas sensing) can be obtained with dilute nitrides (GaInNAs/GaAs QWs) and from devices based on indium phosphide (InAlGaAsP/InP QWs). In addition, VCSEL display low output beam divergence angle compared to edge-emitting laser diodes thanks to a larger aperture and a symmetric beam profile. Consequently, the output beam can be easily collimated using a simple lens with a small numerical aperture and makes possible high coupling efficiency with optical fibers. Combined with their potentiality of high frequencies modulation, VCSEL make perfect candidates for optical fiber communications.

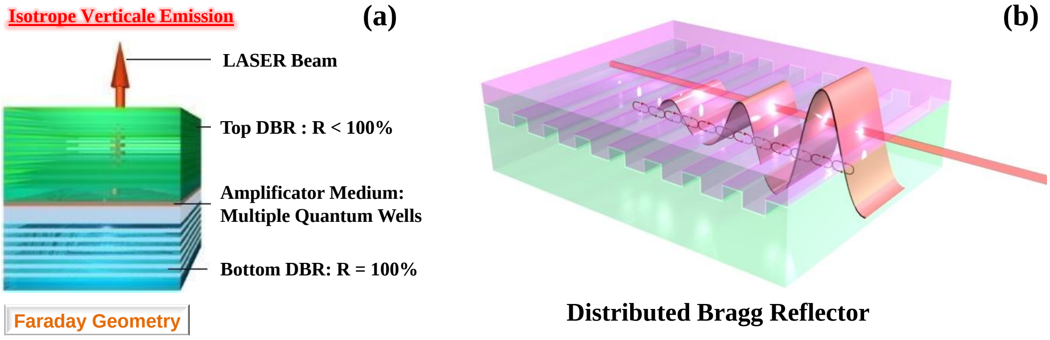

Figure 2.23: (a) Schematic representation of a VCSEL device. (b) Distributed Bragg Reflector: Formed from multiple layers of alternating materials with varying refractive index resulting in periodic variation of the effective refractive index. Each layer boundary causes a partial reflection of an optical wave. For waves whose wavelength is close to four time the optical thickness of the layers, the many reflections combine with constructive interference and the multilayer act as a high-quality reflector.

VCSEL make perfect candidates for a Spin-laser implementation thanks to the efficiency of the optical selection rules in the Faraday geometry (see section 2.2.1.3). Furthermore, VCSEL system provide a relatively isotropic polarization emission as there is no preferential guiding for TE or TM modes like in classic laser diodes [225]. VCSEL are quasi-symmetric devices exhibiting extremely small polarization selectivity. Accordingly, it is difficult to predict, stabilize or control their polarization characteristics. In general, the linearly polarized emission of the fundamental transverse mode in VCSEL is randomly oriented in-plane, and the orientation can vary from device to device and with changes in injection current or temperature [226, 227]. Polarization stability and control can be built into VCSEL through the introduction of geometric asymmetry or various anisotropy mechanisms to select a preferred polarization [84].

2.2.3.2 Spin-VCSEL: Operation Principal and Analytical Model

Spin-lasers can be described as a generalization of conventional lasers. A spin-unpolarized injection reduces Spin-lasers to conventional laser operation [228, 39, 229, 34]. As detailed in section 2.2.1.2, the polarization characteristics of semiconductor lasers are determined by the polarization properties of the gain medium and optical cavity. In QW V(E)CSEL the injection of spin-polarized carriers leads to circular polarization of the emitted light according to the optical quantum selection rules: **(i)** spin-up electrons recombine with spin-up HH resulting in the emission of a σ^--polarized photon or **(ii)** spin-down electrons recombine with spin-down HH resulting in the emission of a σ^+-polarized photon. Thus, spin-polarized electrons couple selectively to one of the two lasing modes, emitting either left- or right-circularly polarized light. Consequently, spin manipulation in a VCSEL provides a means for optical polarization control. As for Spin-LEDs, the spin-polarized carriers are injected by circularly polarized light or by electrical injection using ferromagnetic contacts. However, contrary to Spin-LEDs, we will show that a purely circularly polarized emission along with threshold reduction can result under certain bias conditions for small spin polarizations.

An intuitive picture depicting the differences in operation principal between conventional and spin polarized lasers was introduced by Zutic *et al.* using the image of a bucket filled with water [230]. The bucket model illustrates the changes arising from the injection of spin-polarized carrier in conventional lasers (figure 2.24 (a)):

- **Conventional lasers:** A simple analogy with the pumped bucket illustrates the on and off regimes, where the outgoing water represents the emitted light. At low injection or pumping J, the laser operates in a spontaneous emission regime similar to a LED and the output light generated by the spontaneous recombination is only negligible. At higher injection, when the injection current J reaches the injection threshold J_T, the water starts to gush out of the large slit. For $J > J_T$ stimulated emission starts and the emitted light intensity increases significantly. This regime corresponds to lasing operation in which the stimulated recombination is the dominant mechanism of light emission (Figure 2.24 (a) ①). A sufficiently high injection leads to the onset of lasing when the optical gain can overcome losses in the resonant cavity. As the injection or pumping of the lasers is increased, there is a transition from incoherent to coherent emitted light that can be described by the Landau theory of second-order phase transitions [230]. In summary, a conventional lasers exhibit two operating regime (ON and OFF) with one threshold separating the two modes of operation. When pumped with an unpolarized spin current, the gain spectra for the left- and right-circularly polarized modes overlap since they are fed with an equal number of spin-up and spin-down carriers (Figure 2.24 (b) ①). Consequently, for a perfectly isotropic V(E)CSEL, the emitted-light will be linearly polarized.

- **Spin-lasers:** To model different projections of carriers' spin or helicities of light, it is convenient to think of an analogy with hot and cold water (Figure 2.24 (a) ②). The bucket is partitioned into two halves, representing two spin populations,which are separately filled with hot and cold water, respectively. The openings in the partition allow mixing of hot and cold water, intended to model the spin relaxation. With an unequal injection of hot and cold water, injection spin polarization is defined as [230]:

$$P_J = \frac{(J_+ - J_-)}{J} \tag{2.38}$$

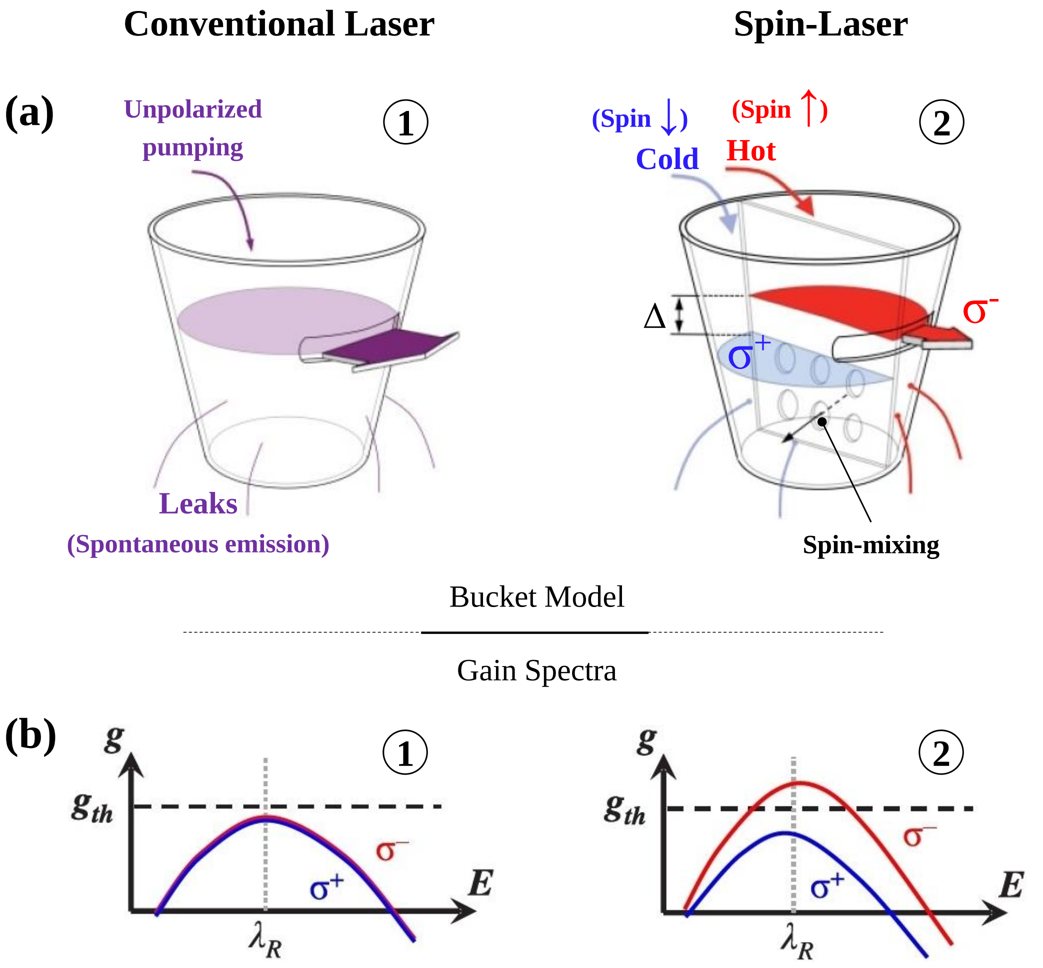

Figure 2.24: Comparison of operation principal between Conventional-Lasers and Spin-Lasers. (a) Lasers bucket model: 1. Conventional Laser: The water (unpolarized injection) fills the bucket until the threshold is reached and the water starts to gush out (Stimulated emission). Only two operatin regimes are displayed: either OFF or ON. **2. Spin-Laser:** Two halves of the bucket, representing two spin populations (hot and cold water) are separately filled. Here, in addition to the ON and OFF regimes, one can infer a regime where only hot water will gush out. This represents the spin-filtering regime between two different lasing thresholds: even a modest polarization of injection leads to complete polarization of emission. Figures adapted from [230]. **(b) Gain spectra: 1. Conventional Laser:** When pumped with an equal number of spin-up and spin-down, the gain spectra for σ^+- and σ^--polarized modes overlap. **2. Spin-Laser:** If the laser is pumped with a spin-polarized current, a gain anisotropy favoring the majority carriers immediately appears. Figures adapted from [84].

where J_+ and J_- are the injection/pumping of the spin-up and spin-down populations respectively which together comprise the total injection/pumping $J = J_+ + J_-$. Compared to conventional lasers, the spin imbalance Δ between

the spin-up and spin-down populations (difference in the hot and cold water levels) leads to three different lasing regimes and two different lasing threshold J_{T1} and J_{T2} for the majority and minority spins respectively (Figure 2.25). At low pumping, when the laser is biased below thresholds (both hot and cold water levels are below the large slit, both circularly polarized lasing modes are subcritical and only negligible spontaneous emission is produced (Spin-LED regime). Then, if the pumping increases preferentially for one spin orientation, the associated circularly polarized lasing mode will be fed preferentially causing this favored mode to rise above the threshold gain level at the expense of the other mode, whose peak subsequently falls further below the threshold gain level. Thus, the spin anisotropy introduced from spin-polarized current injection results in a gain anisotropy for the two orthogonal circularly polarized lasing modes (Figure 2.24 (b) ②). Under these pumping conditions, the hot water reaches the large slit and gushes out while the amount of cold water coming out is still negligible. Such a scenario represents a regime in which the majority spin is lasing, while the minority spin is still in the LED regime. Thus the stimulated emission exclusively originates from recombination of majority spin carriers.
Two important consequences of this regime are already confirmed experimentally:

1. A spin-laser will start lasing for a smaller total injection compared to its conventional counterpart (only one side of the bucket needs to be filled). This represents the threshold reduction in spin lasers [228, 37, 39, 231, 232, 233] which can be parametrized as [230]:

   $$r = 1 - \frac{J_{T1}}{J_T} \tag{2.39}$$

   with $J_{T1} < J_T$.
2. Even a modest injection polarization $P_J << 1$ can lead to highly circularly polarized light [34, 234]. When biased near threshold, a small difference in spin polarization can result in a large difference between right- and left-circular polarization intensities if the gain coefficient for one mode is above the threshold gain while the other is sub-threshold. The relative width of this "spin-filtering regime" can be expressed as the interval [229, 230]:

   $$d = \frac{J_{T2} - J_{T1}}{J_T} \tag{2.40}$$

   with $J_{T1} < J_T < J_{T2}$. The threshold difference d between the two circularly polarized mode linked to the two spin-populations increases with spin polarization of the injection.

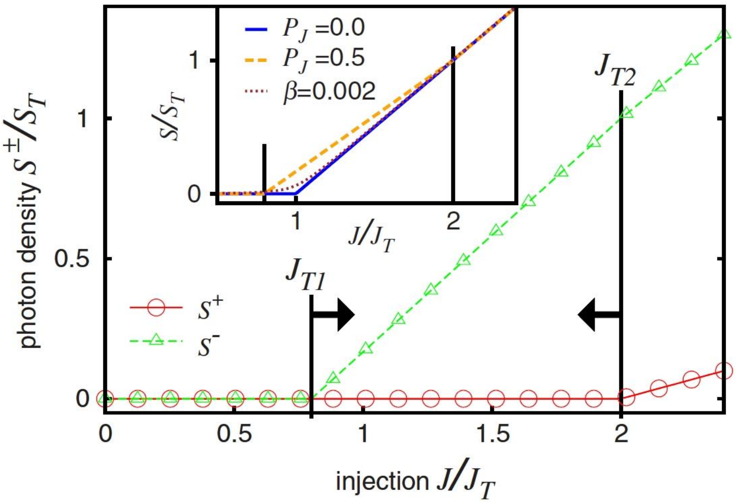

Figure 2.25: Photon densities of the left- (S^-) and right- (S^+) circularly polarized light as a function of the current density J for a spin-polarization of P_J=0.5 and an infinite electron spin-relaxation time $\tau_s \to \infty$. J is normalized to the unpolarized threshold current $J_T = \frac{N_T}{\tau_r}$ with N_T denoting the total electron density at (an above) threshold. The photon densities S^+ and S^- are normalized to $S_T = J_T \Gamma \tau_{ph}$. The vertical lines indicate the majority (J_{T1}) and minority (J_{T2}) carrier threholds while the arrows show their change when P_J decreases. The inset exhibit the total photon density ($S = S^+ + S^-$) for a conventional laser (P_J=0) and two spontaneous-emission coefficients (β=0 and β=0.002), as well as a Spin-laser with P_J=0.5 and β=0. The theoretical results showcased in this figure were obtained by Gothgen *et al.* using a simplified rate equation system deducted from equations (2.42)-(2.44) [39]. Figure reprinted from [39].

The carrier-photon dynamics of a Spin-V(E)CSEL may be modeled using a spin-dependent rate equation analysis which have already been successfully used to describe both conventional and spin lasers [230, 228, 38, 37, 39, 235, 44, 234, 236, 237, 238, 239, 35, 240, 241]. An advantage of this approach is its relative simplicity. When simplified according to some experimental conditions, the rate equations can provide a direct relation between material characteristics and device parameters [237]. They also allow to derive analytical solutions [39] and are an effective method to elucidate many trends in the operation of lasers [39, 34].

We consider a Multi-Quantum Wells (MQW) structure as the active region of the laser. The rate equation analysis accounts for the spin-up and spin-down carrier densities in the barriers $n_b^{\pm}$, the spin-up and spin-down carrier densities in the active region $n^{\pm}$ and the photon density for right- and left-circularly polarized light $S^{\pm}$. The total carrier densities are $n_b = n_b^+ + n_b^-$ and $n = n^+ + n^-$. As the spin relaxation time of holes is much shorter than the spin relaxation time of electrons $\tau_s^p << \tau_s^n$ [162], the holes are here considered unpolarized with $p^{\pm} = \frac{p}{2}$. The total photon density is given by $S = S^+ + S^-$. Electrically or optically injected pumped spin-polarized electrons into the MQW are represented by the current density $J = J_+ + J_-$ associated with the pump current I. The spin polarization of the electrically/optically pumped current density is introduced by $P_J = \frac{(J_+ - J_-)}{J}$ as well as of electron and photon densities $P_n = \frac{(n^+ - n^-)}{n}$ and $P_S = \frac{(S^+ - S^-)}{S}$. In the case of spin-polarized laser, the gain in the laser cavity is generalized as [39, 84]:

$$g^{\pm}(n^{\pm}, S^{\mp}) = \frac{dg}{dn}\left(\frac{n^{\pm} - n_{trans}}{1 - \varepsilon S^{\mp}}\right) \tag{2.41}$$

where $\frac{dn}{dg}$ is the differential gain, n_{trans} is the transparency carrier density and ε is the phenomenological gain compression factor accounting for the non-linear photon density dependence of the optical gain (g saturates at high photon density levels). This gain compression term is an approximate description of the spectral hole burning and carrier heating [39, 242].
The system of six coupled rate equations is given by [228, 38, 243, 84]:

$$\frac{\partial n_b^{\pm}}{\partial t} = -\frac{n_b^{\pm}}{\tau_{cap}} + \frac{1 \pm P_J}{2}\frac{I}{qV_b} \mp \frac{n_b^{+} - n_b^{-}}{\tau_s^{barrier}} \tag{2.42}$$

$$\frac{\partial n^{\pm}}{\partial t} = \frac{V_b}{V_{MQW}}\frac{\partial n_b^{\pm}}{\tau_{cap}} - \upsilon_g g^{\pm}(n^{\pm}, S^{\mp})S^{\mp} \mp \frac{n^{+} - n^{-}}{\tau_s} - C\frac{n^{\pm}(n^{+} + n^{-})^2}{2} - B_{sp}\frac{n^{\pm}(n^{+} + n^{-})}{2} \tag{2.43}$$

$$\frac{\partial S^{\pm}}{\partial t} = \Gamma \upsilon_g g^{\mp}(n^{\mp}, S^{\pm})S^{\pm} + \Gamma\beta B_{sp}\frac{n^{\pm}(n^{+} + n^{-})}{2} - \frac{S^{\pm}}{\tau_{ph}} \tag{2.44}$$

where υ_g is the light group velocity, Γ is the optical confinement coefficient, β is the spontaneous emission factor and τ_{ph} is the photon lifetime in the cavity. B_{sp} and C are the bimolecular radiative recombination and Auger recombination coefficient respectively. The carrier capture time τ_{cap} includes the two sequential steps of carriers transport from the barriers to the QW and relaxation time within the well. The spin-flip time in the barrier and in the QWs are represented by $\tau_s^{barrier}$ and τ_s respectively. Finally, $\frac{V_b}{V_{MQW}}$ stands for the volume ratio between the barriers and the active region. $n_b^{\pm}$ and $n^{\pm}$ are normalized with respect to these two volumes.

An example of simulation using these rates equations was proposed by Holub & Bhattacharya to model a AlGaAs/GaAs MQW VCSEL operating at room temperature [84]. The results are illustrated in figure 2.26. For a 100% spin-polarized pump current, the first simulation clearly highlight that the threshold reduction increases significantly when the spin relaxation time ramps up from 10 ps to 2 ns. The second simulation shows that for a spin relaxation time long enough ($\tau_s > 10$ ps) the

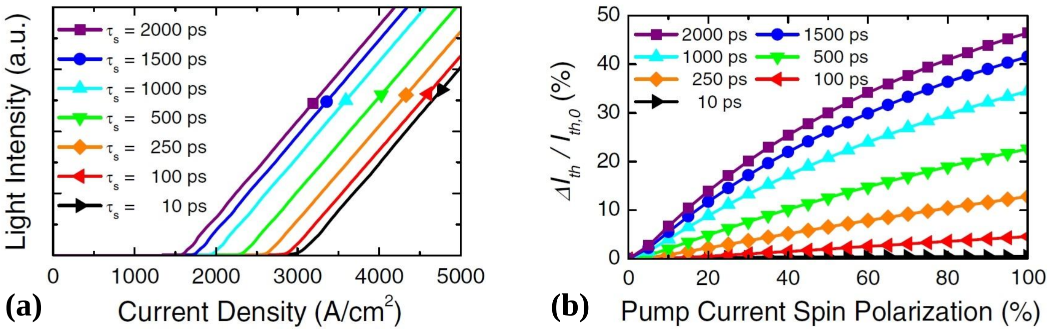

Figure 2.26: Light vs. Current characteristics of a AlGaAs/GaAs MQW VCSEL driven with a spin-polarized pump current at room temperature: **(a)** Threshold evolution of the majority carriers (J_{T1}) as a function of the spin relaxation time τ_s for a 100% spin-polarized pump current. **(b)** Threshold current reduction as a function of the pump spin polarization for different spin lifetime. Simulations were performed using the following parameters: $\tau_{ph} = 1$ ps, $\tau_{cap} = 20$ ps, $n_{trans} = 2 \times 10^{17}$ cm^{-3}, $\frac{dg}{dn} = 7.5 \times 10^{-16}$ cm^2, $\varepsilon = 1.5 \times 10^{-17}$ cm^3, $\upsilon_g = 0.86 \times 10^{10}$ cm.s^{-1}, $\Gamma = 0.03$, $\beta = 1.7 \times 10^{-4}$, $B_{sp} = 1.0 \times 10^{-10}$ cm^3.s^{-1} and $C = 3.5 \times 10^{-30}$ cm^6.s^{-1}. Figures reprinted from [84].

relative width of this "spin-filtering regime" d (threshold reduction) increases with the spin-polarization of the pump current. For a $\tau_s > 1$ ns the threshold reduction approaches the theoretical limit of 50% when the laser is pumped with 100% spin-polarized pump current.

2.2.3.3 Polarization dynamics of VCSEL: The Spin Flip Model

This section introduces the Spin Flip Model (SFM) developed by San Miguel *et al.*. The model provides a theoretical understanding of the polarization dynamics in VCSEL [236]. Compared to conventional edge emitting laser diodes, the light polarization of such devices is not well stabilized due to their cylindrical symmetry. This becomes a problem for applications requiring a well stabilized polarization and numerous solutions were proposed to fix or control the polarization state of the emitted light. These methods include the introduction of polarization sensitive DBR [244], geometrical or stress-induced anisotropies [245], or engineering of the semiconductor material or the growth process [246, 247] to preferentially favor the gain of one polarization. Another paradigm would be to learn how to control and use the degree of freedom of the polarization vector and use it for applications based on the control of the polarization state such as optical switching [248, 249], information processing or storage, etc.

Phenomenology of Polarization selection in VCSEL:

The light emitted by VCSEL is typically linearly polarized with the electrical field vector either: (i) randomly oriented in the (x,y)-plane transverse to the light emission (z-direction) or (ii) with a preferred orientation along one of two orthogonal crystal axis in the (x,y)-plane. Close to threshold VCSEL generally emits in the fundamental transverse mode. Transverse modes of different order are clearly separated in frequency (100-200 GHz) while transverse modes of the same order are separated in frequency by the birefringence γ_p in the structure. This separation can vary from smaller than 1 GHz up to tens of GHz. The birefringence is believed to have two main origins: 1) there is a main and systematic contribution of the electro-optic effect during laser operation for electrically pumped VCSEL [250] and 2) a random contribution of the elasto-optic effect [251]. The second contribution is due to residual strain in the fabrication process or in the electrical contacts.

Thermal effects are another important aspect influencing polarization properties of VCSEL. The self-heating of the device during operation, mostly induced by the DBR mirrors, leads to a reversible extinction of the output light. For electrically pumped VCSEL, this is explained by the parabolic dependence of the threshold current with the temperature. The resonant frequency selected by the short optical cavity and the gain profile red-shift at different rates. Consequently, the resonance frequency is eventually expelled outside the frequencies range for which there is a positive gain. The minimum threshold current corresponds to the alignment of the cavity resonance and the gain peak frequencies. Additionally, the heating of the device can give rise to thermal lensing that produces an effective index guiding effect.

What determines the light polarization state? :

The polarization state of light emitted by a laser depends on two main factors. The first one is the angular momentum of the quantum states involved in the optical transitions (emission or absorption). As explained in the section 2.2.1.2, the emission of a right- (left-) circularly polarized photon corresponds to an allowed optical transition in which the projection of the total angular momentum of the gain medium on the direction of light propagation changes by +1 (-1). This mechanism reflects the nonlinear dynamics of the gain medium. The second factor is associated with the linear effects of the laser cavity. The cavity anisotropies (birefringence, dichroism), geometry, detuning and waveguiding effects lead to preferential polarization state selection. These two ingredients can compete or be complementary to one another. The emitted linear polarization is either randomly oriented in the plane of the active region or along two orthogonal directions associated with crystalline orientation. If the gain medium selects linearly polarized light, the birefringence will fix the preferred orientations. Then potential polarization switching between these preferred orientations can be explained by phase-amplitude coupling due to the combined effect of birefringence and detuning. The coexistence of orthogonal polarizations (bistability) and polarization switching can both be observed [226, 252, 227, 253]. For conventional edge emitting lasers, cavity effects associated with thegeometry are usually predominant: light is polarized in the plane of the active region since the orthogonal direction displays much larger cavity losses. For VCSEL, the cylindrical symmetry combined with the isotropy of III-V compounds grown on the [001] direction, make the nonlinear gain dynamics much more important. In addition, the semiconductors linewidth enhancement factor (α) gives the same type of amplitude-phase coupling than detuning in a gas laser, but its magnitude is considerably larger. It is expected that the effect of the saturable dispersion combined with the α-factor and birefringence also plays an important role as a polarization selection mechanism. The α factor of semiconductor lasers [254, 255] is a common way of summarizing in a parameter many microscopic processes and in particular the inhomogeneous broadened character of the lasing transition. A main effect of the α factor is to produce phase-sensitive dynamics. This sensitivity is analogous to the effect of cavity detuning in two-level models.

The Spin-flip Model

The Spin-Flip Model (SFM) enables to describe the polarization dynamics of semiconductor lasers by extending the rate equations model based on a two-level model approximation. The rate equations model is not appropriate to describe the polarization properties of the electric field on very short time scales. However, the SFM can overcome this limitation as it does not take a fix polarization for granted. The SFM is a four level model taking into account the electric field polarization by including the CB and VB spin sub-levels of the semiconductor. Consequently, it allows to consider the light polarization as a degree of freedom of the laser emission. The two distinct carrier densities $n_\uparrow$ and $n_\downarrow$, associated with the spin-up and spin-down populations respectively, cause two lasing transitions associated with right- or left-circularly polarized emission. If there is no disequilibrium between the two transitions, the two circularly-polarized emissions combined to generate linearly polarized light. The two transitions are coupled by spin-flip processes characterized by the so-called spin relaxation rate γ_{sf} $\left(= \frac{1}{\tau_{sf}}\right)$. The four-level SFM model accounts for the vectorial nature of the light's electric field by allowing both circular polarization states through dipole transitions between independent pairs of energy levels [168, 256, 257, 258, 259].

We consider a surface-emitting quantum-well laser with the 2D active medium oriented perpendicularly to the direction of laser emission (z-axis). The quantization axis is also oriented along the z-direction (Figure 2.27 (c)). In this geometry, and for a gain-guided broad area laser, the electric field is in the x-y plane, so that two independent TE and TM polarization modes are available for the laser field. The linear components (E_x, E_y) and the circularly (E_+, E_-) polarized components satisfy the relation [236]:

$$E_\pm = \frac{1}{\sqrt{2}}\left(E_x \pm iE_y\right) \tag{2.45}$$

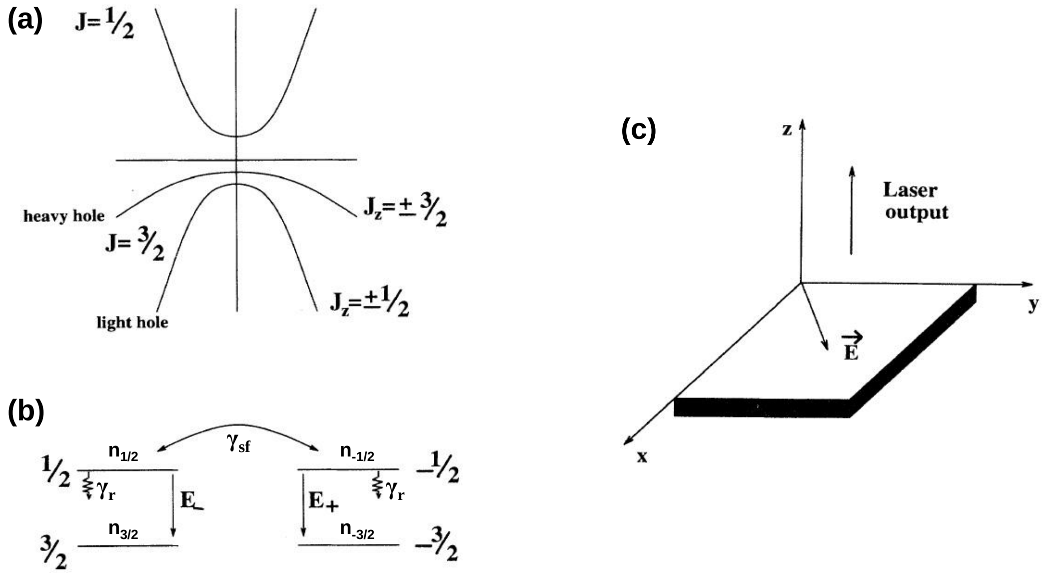

Figure 2.27: **(a)** Schematic band structure of the QW. **(b)** Schematic representation of the four level SFM model. **(c)** Geometry of the surface-emitting laser considered.

A first important effect of the optical cavity is the selection of a longitudinal mode K with an associated resonant cavity frequency ν. The high reflectivity of each DBR enable the construction of a vectorial standing wave with a forward and backward propagating components. In a mean field approximation, one can average out the longitudinal z dependence of these amplitudes and write the electric field for a single longitudinal laser mode as [236]:

$$\mathbf{E} = [F_x(x,y,t) + F_y(x,y,t)] \cdot exp\,[i(K \cdot z - \nu \cdot t)] + c.c. \tag{2.46}$$

where $\mathbf{F}(x,y,t)$ is the amplitude of the selected longitudinal mode. From Maxwell's equations, one can identify that F originates from the slowly varying amplitude of the the dipole polarizations associated with inter-band transitions: $P(x,y,t)$. The linear cavity effects amount to a linear cavity susceptibility matrix M. The basic equation for the field is then:

$$\partial_t \vec{F} = \frac{ic^2}{2\nu n_e^2} \nabla_\perp^2 \vec{F} + \vec{P} - M\vec{F} \tag{2.47}$$

where $\frac{ic^2}{2\nu n_e^2} \nabla_\perp^2 \vec{F}$ represents the diffraction in the transverse plane, n_e being the background refraction index. The gain medium polarization $\vec{P}$ and the optical cavity contribution $M\vec{F}$ are the two main ingredients contributing to the polarization selection. The cavity susceptibility M can be written as:

$$M = \kappa I - \Gamma \qquad ,with:\ \ \Gamma = -(\gamma_a + i\gamma_p)\begin{pmatrix} 1 & 0 \\ 0 & -1 \end{pmatrix} \tag{2.48}$$

where κ is the stimulated emission coefficient ($\Longleftrightarrow$ represents the cavity losses), proportional to the stimulated emission cross-section and is the inverse of the photon lifetime. Γ is the cavity anisotropy matrix [260] expressed in the linear basis in the simplest case where: 1) the circular anisotropies are neglected and 2) the amplitude and phase anisotropies are along the same directions.

- The hermitian part of Γ is associated with the amplitude anisotropies of the electric field components, most commonly named: Dichroism γ_a. In the cavity, the two orthogonally polarized modes might have a slightly different Gain-to-Loss ratio emerging from: (i) the intrinsic gain anisotropies of the crystal [246, 262], (ii) a slightly different position of the modes frequencies with respect to the gain versus frequency curve [263, 264], and/or (iii) different cavity geometries for the differently polarized modes [265, 266]. All these potential effects are regrouped and modeled by the amplitude anisotropy represented by the parameter γ_a. Experimentally γ_a is going to select which of the two linear polarizations has the lower threshold.

- The antihermitian part of Γ is associated with phase anisotropies, also called: Birefringence γ_p. For VCSEL, it is known that there are often two preferred linearly-polarized modes that coincide with the crystal axes. These two modes have a frequency splitting (detunning) associated with the birefringence of the medium. Physically, this linear birefringence γ_p represents the effect of different refraction indexes viewed by each polarization modes. An experimental measurement of the mode detuning is a way to quantify the cavity birefringence. γ_p is typically two orders of magnitude greater than γ_a [267].

In the VCSEL's QWs, the optical quantum selection rules and the lift of degeneracy between the HH-band and the LH-band in Γ ($k = 0$) restrain the allowed dipole transitions to CB(-1/2) → HH(-3/2) and CB(1/2) → HH(3/2) associated with the emission of right and left circularly polarized light respectively (see section 2.2.1.2). In first approximation, these transitions can be modeled by a four-level model. The picture emerging is a two two-level lasing transitions (two "channels" of light emission) with different circular polarizations (Figure 2.27 (b)). The spin-flip mechanism coupling the two spin-sublevels is modelized by the spin-flip rate γ_{sf}.

The dynamics of the radiation-matter interaction in the four-level model follows from a standard density matrix calculation [268]. This analysis leads to a set of equations forming with equation (2.47) the closed set of Maxwell-Bloch equations of the SFM model. The slowly varying amplitudes (F_x, F_y) satisfy the Maxwell-Bloch equations and are conveniently written in terms of right- and left-circularly polarized components $F_\pm = \frac{1}{\sqrt{2}}(F_x \pm F_y)$ associated with the transitions CB(-1/2) →

HH(-3/2) and CB(1/2) → HH(3/2) respectively. The four Maxwell-Bloch equations are given by [236]:

$$\partial_t F_\pm = -\kappa F_\pm - i g_0^* P_\pm + i \frac{c^2}{2\nu n_e^2} \nabla_\perp^2 F_\pm \tag{2.49}$$

$$\partial_t P_\pm = -\left[\gamma_\perp + i(\omega_g - \nu)\right] P_\pm + i g_0 F_\pm (D \pm d) \tag{2.50}$$

$$\partial_t D = -\gamma_r (D - \sigma) + \left[i g_0^* \left(F_+^* P_+ + F_-^* P_-\right) + c.c.\right] + D_f \nabla_\perp^2 D \tag{2.51}$$

$$\partial_t d = -\gamma_s d + \left[i g_0^* \left(F_+^* P_+ - F_-^* P_-\right) + c.c.\right] + D_f \nabla_\perp^2 d \tag{2.52}$$

where ω_g is the band gap frequency, g_0 the coupling constant, σ is an incoherent pumping parameter associated with the injection current, D_f a carrier diffusion coefficient and $\gamma_\perp$ is the decay rate of the dipole polarization. The model also includes a transverse diffraction term and carrier diffusion $[\nabla_\perp = (\partial_x, \partial_y)]$. These equations are written for the two circularly polarized components of $\vec{F}$ and $\vec{P}$ which naturally correspond to each of the two coupled two-level systems (Figure 2.27 (b)). The population differences D and d are defined as [236]:

$$D = \frac{1}{2}\left[(n_{1/2} + n_{-1/2}) - (n_{3/2} + n_{-3/2})\right] \tag{2.53}$$

$$d = \frac{1}{2}\left[(n_{-1/2} - n_{-3/2}) - (n_{1/2} + n_{3/2})\right] \tag{2.54}$$

where $n_{i/2}$ stands for the spin population on the sublevel i. Each component of the material polarization $P_\pm$ is directly coupled to the carrier density $D_\pm$ of the corresponding two-level system with a differential gain parameter a. Physically, $D = D_+ + D_-$ associated with the total population difference between the CB and the VB represents the total carrier density referred to its transparency value D_0. $d = D_+ - D_-$ represents the difference in population inversions associated with σ^+- and σ^--polarized emissions. The coupling between the two lasing transitions occurs through nonzero values of d. Decay rates are also included to characterize the evolution the two populations differences D and d. The population difference D has an associated decay rate γ_r $\left(= \frac{1}{\tau_r}\right)$ accounting for the electron-hole recombination while the decay rate associated with d is defined by [236]:

$$\gamma_s = \gamma_r + 2\gamma_{sf} \tag{2.55}$$

The phenomenological constant $\gamma_s \left(= \frac{1}{\tau_s}\right)$ is introduced to model spin-flip in the CB and the VB and take into account the spin relaxation processes mixing the carriers population with opposite J_z values. In QWs, experimental measurements of spin relaxation times have estimated that [259, 269, 236]:

$$\gamma_r \ \leq \ \gamma_{sf} \ \leq \ 10^2 \cdot \gamma_r \quad \Longleftrightarrow \quad 10^{-2} \cdot \tau_r \ \leq \ \tau_{sf} \ \leq \ \tau_r \tag{2.56}$$

with $\frac{1}{\gamma_r} = \tau_r \approx 1$ ns. Typically for monolithic VCSEL, the spin mixing occurs on larger time scales than the photon lifetime: $\tau_p \left(= \frac{1}{\kappa}\right) \approx 1\, ns \ \ll \ \tau_{sf} \ \in \ [10ps - 1ns]$.

Case of a single mode emission

For fundamental understandings, we treat here the most simple case of a VCSEL operating on the fundamental transverse mode with two polarization modes shifted in frequency.

Equations (2.49) to (2.52) can be simplified when the reasoning is restricted to the polarization dynamics of a single longitudinal mode with neglected transverse effects. The fastest time scale included in equations (2.49)-(2.52) is the decay rate of the dipole polarization: $\gamma_\perp \ \gg \ \gamma_r, \gamma_s, \kappa$. Therefore, in time scales relevant to VCSEL operation, the dipole polarization variables ($\vec{P}$) follows the dynamics of the other variables and can thus be adiabatically eliminated. Note however, that d typically evolves in an intermediate dynamical scale between D and $F_\pm$. Within this model, it plays a crucial role in the nonlinear dynamical properties of the VCSEL. The elimination of P defines, through equation (2.50), a susceptibility matrix $\chi_\pm$ [236]:

$$P_\pm = \chi_\pm \cdot F_\pm = \frac{g_0(\Omega + i\gamma_\perp)}{\Omega^2 + \gamma_\perp^2}(D \pm d) \cdot F_\pm \tag{2.57}$$

where $\Omega = \omega_g - \nu$ stands for the detuning parameter which characterize the difference between the mode frequency (= band gap frequency) ω_g and the cavity resonant frequency ν. The linewidth enhancement factor of the semiconductors laser α (normalized detuning) can be expressed as a function of the susceptibility matrix $\chi_\pm$:

$$\alpha = \frac{Re(\chi_\pm)}{Im(\chi_\pm)} = \frac{\Omega}{\gamma_\perp} = \frac{\omega_g - \nu}{\gamma_\perp} \tag{2.58}$$

A reduction of equations (2.49)-(2.52) with an apropriate choice of unit so that: $E_\pm \sim F_\pm$, $N \sim (D - D_0)$, $n \sim d$, lead to the following Maxwell-Bloch equation system [270]:

$$\frac{dE_\pm}{dt} = -\kappa E_\pm - i\omega_0 E_\pm + \kappa(1 + i\alpha)(N \pm n)E_\pm \tag{2.59}$$

$$\frac{dN}{dt} = -\gamma_r(N - \mu) - \gamma_r(N + n)|E_+|^2 - \gamma_r(N - n)|E_-|^2 \tag{2.60}$$

$$\frac{dn}{dt} = -\gamma_s n - \gamma_r(N + n)|E_+|^2 + \gamma_r(N - n)|E_-|^2 \tag{2.61}$$

This equation system describes a VCSEL operating in the fundamental transverse mode with two polarization modes with different frequencies. $N = N_+ + N_-$ represents the total population inversion (total carrier number in excess of its value at transparency normalized to the value of that excess at the lasing threshold) where N_+ and N_- are the population inversion for the transition amplifying σ^+- and σ^--polarized light respectively. $n = N_+ - N_-$ is the population inversion between the transitions between the magnetic sublevelss, i. e. the difference between the population inversions for the σ^+ and σ^- transitions. We also define N_0 as the unsaturated population inversion proportional to the pumping rate. N, n and N_0 are dimensionless quantities, i. e. numbers of atoms or differences between numbers of atoms on the different levels [271].

In this model, the spin flip rate γ_s has to be considered as an effective parameter describing a variety of microscopic processes. In a VCSEL in operating conditions there is a dense plasma of electron and holes with no significant exciton contribution. Since holes in QWs are known to relax much faster than electrons, the important spin relaxation processes are those of the electrons at RT. The spin lifetime is found to be a non-monotonic function of carrier density. For a lower n-doping level of bulk GaAs semiconductor materials, lifetimes larger than 100 ns have been observed at a temperature of 5 K [75]. These lifetimes are far longer than the electron-hole relaxation time and in these cases the spin lifetime becomes the slow time scale of the system.

In an operating VCSEL, very little is known about the relative importance of the different spin relaxation mechanisms and the spin relaxation time of the electrons under the high-density, room temperature conditions. However, some proposals and experiments have been made to determine γ_s (τ_s) on the basis of the SFM model introduced above. One is based on measuring the effect of a longitudinal magnetic field on the emitted light ellipticity due to the Zeeman splitting of the magnetic sublevels [272, 273]. Another technique is based on fitting the values of injection current associated with polarization switches at constant temperature [274, 275]. Other measurements [276] are based on the fluctuations of the ellipticity and the polarization direction as well as on properties of the optical spectrum [277, 278]. A final proposal is based on the analog of the Hanle effect for an optically pumped VCSEL [267]. These studies give an estimation of the characteristic spin relaxation time in the range of 1-15 ps. Given the fact that they are indirect measurements, the actual value of the electron spin relaxation time and of the effective parameter γ_s (τ_s) determined from them is rather uncertain. However, it will be seen that polarization selection and switching is very sensitive to its precise value. Generally, one should remember that an excess in the decay rate γ_s over γ_r accounts for the mixing of the carriers with opposite value of J_z.

The predictions of this limit case concerning polarization selection and polarization switching are summarized in further [270]. As compared with the most general equations (2.49)-(2.52), these equations do not contain a frequency dependent gain and dispersion as there values are fixed by the single operating frequency of the laser. Consequently, the two polarization modes splitted in frequency by the birefringence γ_p are seeing the same gain. However, small differences in gain associated with the birefringence can be taken into account through an amplitude anisotropy parameter γ_a. While in (2.49)-(2.52) this parameter only models intrinsic cavity anisotropies, it can be used in this particular case to account for the gain differences. It can also eventually depends on the injection current and/or the temperature.

Incorporating the linear phase anisotropy γ_p (birefringence) and the amplitude anisotropy γ_a into equation (2.52) leads to:

$$\frac{dE_\pm}{dt} = \kappa(1+i\alpha)(N \pm n - 1)E_\pm - i\gamma_p E_\mp - \gamma_a E_\mp \tag{2.62}$$

The model given either by the set of equations (2.49)-(2.52) or the set (2.59)-(2.61) includes five fundamental physical processes shown to control the polarization state to a large extent: the Henry phase-amplitude coupling factor α [254], the linear amplitude anisotropy γ_a, the linear birefringence γ_p, the total e^- - h^+ recombination rate γ_r and spin relaxation rate γ_s. The influence of these parameters can be highlighted when rewriting the equations (2.59)-(2.61) in terms of the orthogonal linear components of the electric field: $E_x = \frac{1}{\sqrt{2}}(E_+ + E_-)$, $E_y = \frac{i}{\sqrt{2}}(E_+ - E_-)$. The system becomes [270]:

$$\begin{cases} \dfrac{dE_x}{dt} = -(\kappa+\gamma_a)E_x - i(\omega_0+\gamma_p)E_x + \kappa(1+i\alpha)(NE_x + inE_y) \\ \dfrac{dE_y}{dt} = -(\kappa-\gamma_a)E_y - i(\omega_0-\gamma_p)E_y + \kappa(1+i\alpha)(NE_y + inE_x) \end{cases} \tag{2.63}$$

$$\frac{dN}{dt} = -\gamma_r \left[N\left(1 + |E_x|^2 + |E_x|^2\right) - \mu + in\left(E_y E_x^* - E_x E_y^*\right)\right] \tag{2.64}$$

$$\frac{dn}{dt} = -\gamma_s n - \gamma_r \left[n\left(|E_x|^2 + |E_x|^2\right) + iN\left(E_y E_x^* - E_x E_y^*\right)\right] \tag{2.65}$$

where $\omega_0 = \kappa\alpha$ is a frequency shift and μ is the normalized injection current (μ=1 at threshold). We see from the set of equation (2.63)-(2.65) that the linear birefringence γ_p induce a frequency detuning of $2\gamma_p$ between the $\hat{x}$- and the $\hat{y}$-polarized solutions (with $\omega_{\hat{x}} < \omega_{\hat{y}}$ when $\gamma_p > 0$). The linear dichroism γ_a leads to different thresholds for the two linearly polarized solutions ($\mu_{th}^{\hat{x}} < \mu_{th}^{\hat{y}}$ when $\gamma_a > 0$). Note that the values of linear birefringence and the linear dichroism strongly depend on the VCSEL design. The eigenstates of the system are linearly polarized (rather than circularly or elliptically polarized) because of the cross-saturation preference exerted through the nontrivial value of γ_s [270]. In the absence of saturable dispersion ($\alpha = 0$) and/or birefringence ($\gamma_p = 0$), the dichroism γ_a fully controls the stability of the two modes. In this case, the mode with the higher Gain-to-Loss ratio (lower threshold) is always stable above threshold and the orthogonally polarized mode is always unstable when the solution exists (above a higher threshold value of the current). Then a polarization switch can only occurs for a sign change of γ_a [270].

Basic polarization states:

The rate equations (2.59)-(2.61) admit CW solutions above threshold that corresponds to linearly polarized light and can be generally written as [270]:

$$E_\pm = Q_\pm \cdot exp\left[i(\omega_\pm t \pm \psi) + i\theta\right], \quad N = N_0, \quad n = n_0 \tag{2.66}$$

where θ is the global arbitrary laser phase and ψ the relative phase. Solutions with a well defined polarization are those with a single frequency ($\omega_+ = \omega_-$). Circularly polarized solutions are those in which either $Q_+ = 0$ or $Q_- = 0$. Linearly polarized solutions are those with $Q_+ = Q_-$. For these solutions the angle ψ gives the orientation of the linearly polarized light in the (x,y)-plane. Ellipticaly polarized solutions are those in which the two real amplitudes $Q_\pm$ are nonzero and different. The ellipticity of these solutions is given by $\varepsilon = \frac{Q_+ - Q_-}{Q_+ + Q_-}$. Starting from these expressions for the electric field's circularly polarized components, we are going to distinguish different situation depending on the values of the linear birefringence γ_p and the linear dichroism γ_a [270]. The detailed solutions with the associated electric field projections in the (x,y)-basis can be found in the Appendix 2.

A) **If $\alpha \neq 0$, $\gamma_a \neq 0$ and $\gamma_p \neq 0$:** In the most general case, the system admits two orthogonal linearly polarized solutions along the $\hat{x}$- and the $\hat{y}$-axis. These two states have different amplitudes and different threshold values $\mu_{th} = N_0$ due to the amplitude anisotropy γ_a. This anisotropy also causes that the frequency difference ω_x - ω_y between the two modes does not coincide with the birefringence induced splitting $2\gamma_p$.

B) **If $\alpha \neq 0$ and $\gamma_a = \gamma_p = 0$:** If the VCSEL is perfectly isotropic the solutions (2.66) are linearly polarized with equal frequencies and amplitudes for the two circularly polarized components. Here, the relative phase ψ is arbitrary and fixes the orientation of the linear polarizations in the (x,y)-plane. This unique linearly stable solution is susceptible to orientational diffusion in the (x,y)-plane due to perturbations of the phase ψ. Nevertheless, when $\gamma_s \rightarrow \infty$ ($\tau_s \rightarrow 0$) the mode becomes marginally stable with respect to the amplitudes fluctuations. This means that for a perfectly anisotropic VCSEL a long spin lifetime paradoxally stabilizes the linearly polarized emission and destabilizes circularly polarized or elliptically polarized emission [236, 270].

C) **If $\alpha \neq 0$, $\gamma_a = 0$ and $\gamma_p \neq 0$:** In absence of dichroism the system displays four different steady states solutions (Figure 2.28 (a)). For each of these solutions, the birefringence γ_p breaks the rotational invariance of the polarization vector: the relative phase is no longer arbitrary ($\psi \neq 0$). Two of these solutions are orthogonal and linearly polarized (circularly polarized components with equal amplitudes) along $\hat{x}$- and $\hat{y}$-direction respectively (Figure 2.28 (a) ①-②) while the other two solutions are elliptically polarized (circularly polarized components with unequal amplitudes) (Figure 2.28 (a) ③-④). In the particular case where $\gamma_s = 0$ each elliptically polarized solution becomes circularly polarized light, however these circularly-polarized states are never found to be stable solutions of (2.63)-(2.65) [236].

Stability analysis:

We introduce here the main qualitative conclusion of the analysis conducted by Martin-Regalado *et al.* concerning basic polarization modes stability. For quantitative precisions I invite the reader to refer to their paper [270]. This study describes the growth or decay of small fluctuation around the polarization states and identifies the relevant parameters and mechanisms which control polarization selection and switching. The eigenvalues found in such a linear analysis determine the stability boundaries of the different polarization states:

- The stability of linearly polarized mode can be separated in two independent problems. The first one refers to the total laser intensity fluctuations $I = |E_+|^2 + |E_-|^2$ and the total carrier number N_0. It is independent of the dichroism γ_a, the birefringence γ_p and the spin relaxation rate γ_s in the system. The second problem concerns the polarization dynamics properties and

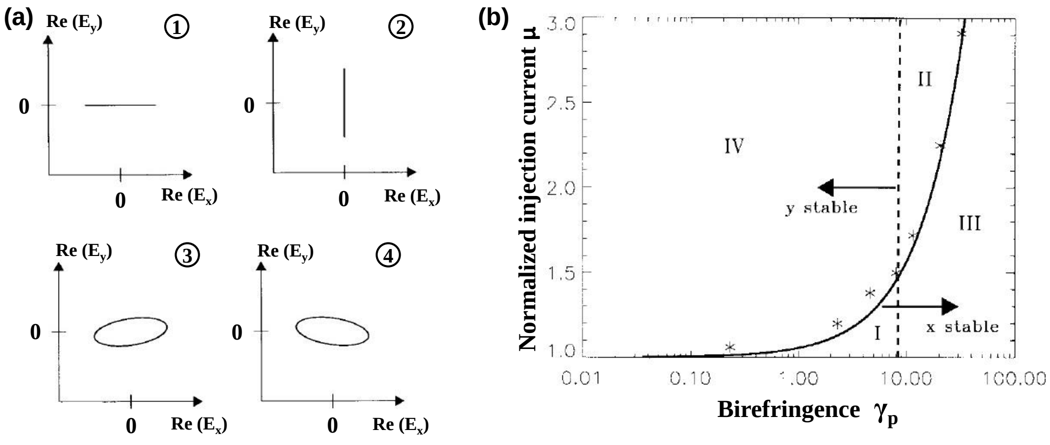

Figure 2.28: (a) Steady-state solutions of (2.63)-(2.65) in the case where $\alpha \neq 0$, $\gamma_a = 0$ **and** $\gamma_p \neq 0$**:** 1. $\hat{x}$-polarized solution, 2. $\hat{y}$-polarized solution and 3-4. elliptically polarized. **(b) Stability diagram for the steady-state solutions:** The $\hat{x}$-polarized state is stable below the continuous line, while the $\hat{y}$-polarized state is stable to the left of the dashed line. The graph is divided into four areas with different stability for the two linearly polarized solutions: in I, both solutions are stable; In II, neither solution are stable; in III, only the $\hat{x}$-polarized solution is stable and in IV, only the $\hat{y}$-polarized solution is stable. Elliptically polarized solutions are stable within the narrow region between the solid line and the stars. The following parameters have been used to perform the simulation: $\kappa = 300$ ns^{-1}, $\gamma_r = 1$ ns^{-1}, $\gamma_s = 50$ ns^{-1} and α $= 3$. Figures reprinted from [270].

is linked to the difference in carrier populations with different spin number n_0. It is also equivalently linked to the coupled fluctuations of the polarization direction ψ, the ellipticity and the carrier populations with different spin number n_0.

- Inspection of the characteristic equation that determines the stability of linearly polarized states reveals the importance of different parameters. For a perfectly isotropic VCSEL ($\gamma_a = \gamma_p = 0$, with $\alpha \neq 0$) there is a vanishing eigenvalue associated with the arbitrary orientation of the linearly polarized state. For an anisotropic VCSEL there is three possible situation depending on the parameters domains in which either only one, both (bistability) or none of the linearly polarized states are stable (Figures 2.28 (b)). When there is no birefringence ($\gamma_p = 0$) only one of the two linearly polarized solutions is stable. In the case where $\alpha = 0$ and $\gamma_a = 0$, the VCSEL is bistable and both polarization modes can coexist. This is still true for reasonably small values of γ_a except for extremely large or small birefringence γ_p. For $\alpha = 0$ and typical values of the other parameters ($\gamma_a, \gamma_p, \gamma_s \neq 0$), whichever state is selected at threshold (lower threshold due to the dichroism γ_a) will always remain stable. A change in the relative stability of the two linearly polarized modes is thus due to the combined effect of birefringence γ_p and saturable dispersion

α. Likewise, in the limit of infinitely fast spin relaxation ($\tau_s = 0$) there is again only bistability. A finite spin relaxation time is a necessary condition for stability changes and polarization switching.

- In the domain of parameters where a linearly polarized mode is stable its optical spectrum shows two qualitatively different regimes. For a symmetricl VCSEL ($\gamma_p = 0$) with small dichroism values ($\gamma_a \approx 0$), two regimes can be distinguished depending on the spin relaxation rate γ_s: 1) a fast spin relaxation regime with exponential fluctuations relaxation and 2) a slow spin relaxation regime exhibiting damped polarization relaxation oscillations [236]. The ellipticity ε and the carrier populations with different spin n_0 oscillate at a frequency comparable to the laser relaxation oscillations frequency. The two regimes are separated by a critical value of the spin relaxation rate γ_s comparable to the frequency of the relaxation oscillations. For a non vanishing birefringence ($\gamma_p \neq 0$), the slow spin relaxation regime is continued into one "polarization relaxation oscillations" persisting far above threshold while the polarization direction fluctuations (fixed by γ_p) relax exponentially. However, close to threshold, in the case of fast spin relaxation, a new regime appears where n_0 relaxes exponentially (characteristic time τ_s) while damped coupled oscillations of the ellipticity ε and the polarization orientation ψ emerge. These oscillations occur at a frequency growing linearly with the threshold distance and are thus different from the relaxation oscillation frequency that evolve as the square root of the threshold distance. Most generally, VCSELs operate in this fast spin relaxation regime but note however that relatively small variations of the injection current and/or spin-flip rate can lead to a switch from a regime to another.

- A better understanding of the spin-dynamics influence on the VCSEL behavior is obtained when considering equations (2.63)-(2.65) in the limit where $n = 0$. In the limit of extremely fast spin relaxation ($\tau_s \rightarrow 0$), there is no preferential stabilization between linearly- or circularly-polarized modes. From a mathematical viewpoint, it can be identified using a 3^{rd}-order Lamb expression obtained from (2.63)-(2.65) by adiabatic elimination of N and n when $lim\ \gamma_s, \gamma_r \rightarrow +\infty$ [270]:

$$\frac{\partial E_\pm}{\partial t} = -(\gamma_a + i\gamma_p)E_\mp \cdot \kappa(1+i\alpha)\left(\mu + \frac{\mu}{\rho}\right)\left[\frac{\mu - 1}{\mu + \frac{\mu}{\rho}} - |E_\pm|^2 - \delta|E_\mp|^2\right]E_\pm \tag{2.67}$$

where $\delta = \frac{\rho-1}{\rho+1}$ defines the coupling parameter with $\rho = \frac{\gamma_s}{\gamma_r}$. Then, in the case of a weak coupling ($\delta < 1$) linearly polarized mode will be dominant, while for a strong coupling ($\delta > 1$) a stable circularly polarized emission is predicted.

Polarization switching:

Polarization switching can occur when one of the two linearly polarized states looses stability. For a fixed value of α the analysis can be conduct for two parameters commonly measured in polarization switching experiments: the injection current μ (or optical injection power density) normalized to the threshold current and the birefringence γ_p. One can note that the intrinsic birefringence is a fixed characteristic of a given VCSEL structure and is independent of the injected current. Nevertheless a pumping induced birefringence also influence the dynamical behavior of the device (Thermal effects). For a constant α, the switching of polarization modes is controlled by the relative values of the birefringence γ_p and the spin-flip rate γ_s through $\gamma_p^{crit} = \frac{\gamma_s}{2\alpha}$. In each case a different polarization state is selected at threshold. In both cases elliptically polarized states are only stable in a narrow range of parameters as intermediate states between stable modes transition:

A) **$\gamma_a > 0$ ($\mu_{th}^x > \mu_{th}^y$):** The gain difference favors the $\hat{y}$-polarized mode at threshold so that the threshold for the $\hat{x}$-polarized mode is higher than for the $\hat{y}$-polarized mode.

- If $\gamma_p < \frac{\gamma_s}{2\alpha}$: For a low birefringence VCSEL, the mode with the lower threshold (here $\hat{y}$-polarized mode) is selected at threshold and remains stable as the pumping power increases.
- If $\gamma_p > \frac{\gamma_s}{2\alpha}$: an abrupt $\hat{y} \rightarrow \hat{x}$ switching occurs when increasing the injected current. The switching occurs by destabilization of the mode with the higher gain-to-loss ratio in favor of the weaker mode. In addition, the switching threshold μ_{sw} linearly depends on the dichroism γ_a:

$$\frac{\mu_{sw}}{\mu_{th}^y} = 1 + \frac{2\left(\gamma_s^2 + 4\gamma_p^2\right)}{\kappa\left(2\alpha\gamma_p - \gamma_s\right)} \frac{\gamma_a}{\gamma_e} \tag{2.68}$$

  When decreasing the pumping power, the reverse switching $\hat{x} \rightarrow \hat{y}$ occurs with a potential hysteresis in the switching threshold.

B) **$\gamma_a < 0$ ($\mu_{th}^x < \mu_{th}^y$):** The gain difference favors the $\hat{x}$-polarized mode at threshold so that the threshold for the $\hat{y}$-polarized mode is higher than for the $\hat{y}$-polarized mode. In this case, stable $\hat{x}$-polarized emission is expected close above threshold for any birefringence value.

- If $\gamma_p < \frac{\gamma_s}{2\alpha}$: $\hat{x} \rightarrow \hat{y}$ polarization switching occurs when the injection current is increased and happens again from the higher gain mode to the lower gain mode with higher threshold. The switching is not abrupt and occurs through one of the two stable elliptically-polarized states with degenerate frequencies. Consequently, elliptically polarized modes appear as intermediate states reached in the destabilization of the linearly polarized solution as the pumping is increased. Hysteresis in the switching current, is also predicted here. The switching threshold is given by:

$$\frac{\mu_{sw}}{\mu_{th}^{x}} = 1 + \frac{\left(\gamma_p^2 + \gamma_a^2\right)}{\kappa\left(2\alpha\gamma_a + \alpha\gamma_p\right) - \gamma_p^2}\frac{\gamma_s}{\gamma_e} \tag{2.69}$$

- If $\gamma_p > \frac{\gamma_s}{2\alpha}$: the $\hat{x}$-polarized mode is selected at threshold and remains stable as the pumping power increases.

The above discussion clearly highlights the role of α, γ_p and γ_s in determining the stability properties of the different polarization states. According to the expressions of the switching thresholds (2.68) and (2.69), one can conclude that the basic mechanisms inducing a polarization switching in a VCSEL structure are: 1) the coupling through spin-flip processes (γ_s) of the two carrier populations with different spin number and 2) the combined effect of birefringence γ_p (which couples the two circularly polarized components of the field) with the dichroism (with associated saturable dispersion α).

Specific case of Optically Pumped VCSEL/VECSEL:

So far we considered V(E)CSEL modeled as a two two-level systems assuming that the two transitions associated with the two spin-orientations are pumped with equal strength. However, optically pumping the VCSEL with an off-resonance field allows to selectively favor one of the two lasing transitions by changing the pump ellipticity. For a non-linearly polarized pumping, a non-zero macroscopic magnetization $m_z \sim n$ is induced by generation of carriers with a preferred spin orientation. Doing so, the influence of the spin dynamics on the device behavior is amplified and spin related effects become more apparent. Optically pumped V(E)CSEL are thus very useful for fundamental studies of polarization selection mechanisms and other more general dynamics properties. Additionally, optical pumping with moderate power densities can avoid to a large extent temperature effects mostly due to the self-heating of the electrical devices. Finally, under optical pumping V(E)CSEL exhibit a more effective coupling between the two lasing transitions associated with right and left circularly polarized light. This property is quite interesting for developing potential application based on self-sustained polarization oscillations.
For a V(E)CSEL operating in the fundamental transverse mode the optical pumping is modelized by simply replacing the electrical pumping variable μ in the rate equation (2.63)-(2.65) by η_+ and η_- such that [279]:

$$\begin{cases} \dfrac{dE_x}{dt} = -(\kappa + \gamma_a)E_x - i(\omega_0 + \gamma_p)E_x + \kappa(1 + i\alpha)(NE_x + inE_y) \\ \dfrac{dE_y}{dt} = -(\kappa - \gamma_a)E_y - i(\omega_0 - \gamma_p)E_y + \kappa(1 + i\alpha)(NE_y + inE_x) \end{cases} \tag{2.70}$$

$$\frac{dN}{dt} = -\gamma_r \left[N\left(1 + |E_x|^2 + |E_x|^2\right) - (\eta_+ + \eta_-) + in\left(E_y E_x^* - E_x E_y^*\right)\right] \tag{2.71}$$

$$\frac{dn}{dt} = -\gamma_s n - \gamma_r \left[(\eta_+ - \eta_-) + n\left(|E_x|^2 + |E_x|^2\right) + iN\left(E_y E_x^* - E_x E_y^*\right)\right] \tag{2.72}$$

where η_+ and η_- are the pumping efficiencies for the HH(-3/2)→CB(-1/2) (E_+) and HH(3/2)→CB(1/2) (E_-) transitions respectively. The pump ellipticity is then given by $P^{opt}_{pump} = \frac{\eta_+ - \eta_-}{\eta_+ + \eta_-}$. As for Spin-LEDs, informations on the carriers and spin dynamics in the structure can then be deducted from studying the output laser light ellipticity as a function of P.

2.2.3.4 Interest, Stakes and Applications

Spin-Lasers provide higher performances as compared to Spin-LEDs in terms of output Degree of Circular Polarization (DoCP) due to the amplification effect induced by the combination of a gain medium and a resonant optical cavity. An output DoCP close to 100% can hence be achieved even by injecting a relatively low polarized spin-current in the active medium. From this viewpoint, the device can be seen as a spin-amplifier [224]. Such Spin-Lasers would provide a number of advantages over conventional VCSELs for future optical communication systems such as telecommunications with enhanced bandwidth, spin driven reconfigurable optical interconnects [31, 32, 33], fast modulation dynamics [34, 35], polarization control [36, 37] as well as higher performances such as laser threshold reduction [37, 38, 39], improved laser intensity, and polarization stability. The ideas emerging from Spin-Lasers and polarization switching may also motivate other device concepts such as, for example, cryptography, coherent detection systems or magneto-optical recording [40]. Since electron spin is intricately linked to photon polarization, control and manipulation of electron spin provides a means for polarization control in a laser [84].

Recent experimental advances in the dynamics operation of Spin-Lasers were also highlighted [234, 35]. In dynamic operation, Spin-Lasers are expected to outperform the conventional counterparts in two key categories: the bandwidth modulation and the frequency chirp [280, 34]. In Spin-Lasers there are two basic methods of modulation: amplitude modulation and polarization modulation. While amplitude modulation modifies the injection intensity, polarization modulation modifies the light polarization at a fixed injection intensity [281]. In both cases, bandwidths (the range where the frequency response is above -3dB) are enhanced with increased polarization (see [34]).

2.2.3.5 State-of-the-art

Optical Spin Injection

The very first demonstration of polarization modulation in VCSEL was achieved by Hallstein *et al.* [282]. The philosophy of the experiment was to applied a strong transverse magnetic field on the structure to modulate the spin orientation of the injected carrier through Larmor precession. The VCSEL was pumped by unpolarized light in a pulsed regime. They observed an output stimulated emission with alternating circular polarization synchronized with the Larmor frequency of the electrons.

Strictly speaking, the first demonstration of spin-injection in a VCSEL using circularly polarized optical pumping was performed by Ando *et al.* reaching a DoCP of 75% at room temperature [36]. This first successful experiment already overpowered the best results obtained with Spin-LEDs up to this day and highlighted the attractiveness of such spin-injected devices for potential applications.

Rudolph *et al.* then focused on another interesting property of spin-injected VCSEL. They observed threshold reduction at both low and room temperature in InGaAs QWs and GaAs QWs structures under circularly polarized optical pumping [228, 38]. They also introduced the first rate equation model describing the carrier-photon dynamics of a Spin-V(E)CSEL (section 2.2.3.2).

Pumping	Active Region	λ emission	Spin Polarization (%) / Temperature (K)	Reference
Pulsed	2× InGaAs QWs	835 nm	N.C./15 K	[282]
Pulsed	GaAs bulk	865 nm	75%/300 K	[36]
Pulsed	2× InGaAs QWs	835 nm	N.C.%/6 K	[228]
Pulsed	3× GaAs QWs	850 nm	N.C.%/294 K	[38]
Pulsed	2× InGaAs QWs	1000 nm	100%/300 K	[41]
Pulsed	5× (110)-InGaAs QWs	865 nm77 K 917 nm300 K	94%/77 K 42%/300 K	[283] [283]
Pulsed	3× (110)-GaAs QWs	855 nm	96%/300 K	[42]
Pulsed	N.C.	853 nm	35%/300 K	[284]
CW	15× GaInNAs QWs	1300 nm	73%/300 K	[43]
CW	12× InGaAs QWs	1000 nm	80%/300 K	[225]
Mixed	3× GaAs QWs	830 nm	100%/300 K	[224]

Table 2.6: Comparison of state-of-the-art optical spin injection in V(E)CSEL with different active mediums and architectures. For each type of pumping, the refrences are historically displayed.

Gerhardt *et al.* confirmed the amplification of the spin-information expected in Spin-VCSEL. They achieved a DoCP of 100% with a carrier spin-polarization of 30% and showed that a carrier spin-polarization of 13% still provide a DoCP of 50%. These results are also in good agreement with the theoretical calculations based on the SFM mentioned in section 2.2.3.2 [41].

More recently, Fujino *et al.* and Iba *et al.* stepped up the performances of Spin-VCSEL using (110)-oriented QWs. In (110)-QWs the Dyakonov-Perel relaxation mechanism is canceled inducing a significantly longer spin life-time compare to the more conventional (100)-QWs. They respectively reached DoCP of 94% at 77K [283] and 96% at 300K [42] under pulsed circularly polarized optical pumping.

Spin injection under mixed electrical/optical pumping has also been demonstrated by Hovel *et al.* with an output DoCP of 100% [224]. The industrial VCSEL was pumped with a fixed unpolarized electrical current corresponding to 80% of the electrical threshold. Then, the control the VCSEL polarization through spin-injection by further adding a CW circularly polarized optical pumping to pass the lasing threshold.

Finally, during this Ph.D we reported the first demonstration of optical spin injection in a Vertical-External-Cavity-Surface-Emitting-Laser reaching a DoCP of 80% at room temperature [225]. Table 2.6 overviews the state-of-the-art of spin injection in V(E)CSEL using circularly-polarized optical pumping.

Electrical Spin Injection

To this day, electrical spin-injection in VCSEL has exclusively been investigated by the group of P. Bhattacharya from the Department of Electrical and Computer Engineering of University of Michigan. Their work regroups a total of 4 published papers on the subject. Different structures with different active mediums and different spin-injectors have been implemented. A maximum DoCP of 15% at 200 K for an applied magnetic field $\vec{B}$ of 2 T was reached using an MnAs Schottky injector on InAs/GaAs QDs [44]. Unfortunately, as the intrinsic magnetization of all the spin-injectors used was in-plane, an applied magnetic field was needed to drag the layer's magnetization out-of-plane and polarized the carriers to fulfill the optical quantum selection rules in the Faraday geometry. As for Spin-LEDs, this stands out as a limitation for potential applications. This problem can be solved by the use of a ferromagnetic spin-injector displaying Perpendicular Magnetic Anisotropy.

Architecturally, despite for the first device [285], the spin-injection is achieved laterally by injection through the n-doped bottom DBR thanks to an annular electrode. Questions rises concerning the conservation of the spin-polarization through this stack of alternating materials over an almost micrometric distance.

Spin Injector DMS|FM	Active Region	λ emission	Spin Polarization (%) /Temperature (K)/$\vec{B}$ (T)	Reference
GaMnAs	5× InGaAs QWs	945 nm	4.6%/80 K/1 T	[285]
Fe	3× InGaAs Qws	948 nm	23%/50 K/2 T	[37]
MnAs	10× (InAs/GaAs QDs)	983 nm	8%/200 K/3 T	[235]
MnAs	InAs/GaAs QDs	983 nm	15%/200 K/2 T	[44]

Table 2.7: Comparison of state-of-the-art electrical spin injection in VCSELs with different active mediums and architectures. The references are historically displayed.

To this day, an efficient electrical spin injection in VCSEL without any applied magnetic field remains to be seen, even at low temperature. This stands out as a tremendous technological challenge involving expertise in semiconductors, optics, spintronics, growth and characterization techniques as well as ferromagnetic thin film engineering. Table 3.7 overviews the state-of-the-art of spin injection in VCSEL using spin-polarized electrical pumping.

Chapter 3

Development and optimization of an ultra-thin $MgO/CoFeB/Ta$ spin-injector with perpendicular magnetization.

Contents

Introduction

Since the discovery of an efficient transfer of a solid-state information stored within ferromagnetic materials into circularly polarized photons emitted by spin-light emitting diode (spin-LED) [29, 197, 286], several advanced semiconductor technologies have been proposed. Potential devices have been anticipated ranging from memory elements with optical readout and optical transport of spin information [287], advanced optical switches [84], circularly polarized single photon emitters for quantum cryptography [288] to chiral analysis [289] and 3-dimensional display screens.

According to the optical selection rules [168, 290], conventional spin-injector with in-plane magnetization [204, 123, 91, 93, 22, 99] cannot satisfy the practical application for quantum well (QW)-based spin-LEDs. Indeed, with these injectors a strong external magnetic field up to a few Tesla is required to rotate the injector's magnetization out-of-plane. Moreover, the efficient injection of spin-polarized electrons from a ferromagnetic (F) contact into a semiconducting heterostructure (SC) is a prerequisite for the realization of functional spin-optoelectronic devices. It has been shown that inserting a thin MgO tunnel barrier in-between F and SC can circumvent the impedance mismatch issue arising when a metals is put in contact with a semiconductors (section 2.1.1.4). The SC/MgO/F architecture has already demonstrated very high spin-injection efficiencies [63]. In particular, MgO/CoFeB injectors exhibited the highest spin-injection yield at room temperature. After deposition on a n-i-p LED structure, an emitted Degree of Circular Polarization (DoCP) of 32% was reached at room temperature. To this day, this value remains the world record for circularly-polarized emission using a Spin-LED device [99].

This third chapter focuses on the development and the optimization of a new ultra-thin MgO/CoFeB/Ta spin-injector exhibiting Perpendicular Magnetic Anisotropy on semiconductor Spin-LED. We detail the device structures and their fabrication by photolithography processing. In the second section we focus on the optimization of the MgO tunnel barrier for maximizing the spin-injection efficiency. The third section is fully devoted the development and the characterization of a MgO(2.5nm)/CoFeB(1.2nm)/Ta(5nm) spin-injector with perpendicular magnetization at remanence. Finally, we conclude on the results and the limits brought to light by this research and further introduce spin-injection in lasers as a potential solution for overcoming the intrinsic limitation of Spin-LED.

3.1 Spin-LEDs structures and Photolithography process

In this short technology-oriented section, we briefly detail the typical Spin-LED structures used during the thesis and their fabrication by photolithography processing.

3.1.1 Spin-LEDs structures

A Spin-LED is a spin-optoelectronic device converting the spin information contained in a population of spin-polarized carriers into circularly-polarized light. In practice it is usually employed as a detection tool for the study of electrical spin-injection in semiconductors as it offers a fairly direct readout of the spin-polarization injected in the device. The detailed operation principal of Spin-LEDs can be find in Chapter 2, section 2.2.1.2.

For this collaborative project, all the semiconductor p-i-n LED heterostructures were grown by Molecular Beam Epitaxy in a dedicated III-V chamber. However, the different MTJ spin-injectors deposited on top of the LED structures were grown either by MBE, Sputtering or hybrid MBE/Sputtering methods depending on the conducted research. In a typical p-i-n structure used, the *p*-doped region exhibit a doping gradient from the p^+-substrate toward the intrinsic active medium. Similarly, in the n-region the layer in contact with the MTJ spin-injector is significantly doped compared to the active medium. The doping profile at the interface spin-injector/semiconductor is tuned to adjust the Fermi level pinning near the tunnel barrier region and optimize the spin-injection efficiency in the LED. The active medium is always composed of one or several undoped quantum wells. Here is an example of LED architecture used during the research: p^+-*GaAs substrate* // 500 nm $p - Al_{0.15}Ga_{0.85}As$ ($p = 1.7 \times 10^{19}\ cm^{-3}$) / 50 nm $p - Al_{0.15}Ga_{0.85}As$ ($p > 1.7 \times 10^{19}\ cm^{-3}$) / 50 nm $undoped - Al_{0.15}Ga_{0.85}As$ / 10 nm $undoped - GaAs\ QW$ / 50 nm $undoped - Al_{0.15}Ga_{0.85}As$ / 50 nm $n - Al_{0.15}Ga_{0.85}As : Si$ ($n = 1 \times 10^{17}\ cm^{-3}$) / 15 nm $n - Al_{0.15}Ga_{0.85}As : Si$ ($n = 2 \times 10^{19}\ cm^{-3}$).

During the research on Spin-LED, several structural parameters have been tuned for detection configuration purposes or to optimize the conversion of the spin-information into circularly-polarized light. Among them, a particular attention was paid to the active medium where the number of QWs has been modified depending on the required output optical power. The nature of the QWs has also been adapt to the thickness and the total absorption of spin-injectors. With ultra-thin lowly absorbent MTJ spin-injector, GaAs QWs were usually employed with a frontside-detection configuration. However, for thick highly absorbent injectors, InGaAs QWs were used to avoid absorption of the emitted light by the injector. Indeed, as InGaAs emits below the gap of GaAs, the GaAs substrate becomes transparent to the emission and a backside-detection configuration can thus be implemented to by-pass light absorption by the injector. For the barrier, a previous optimization

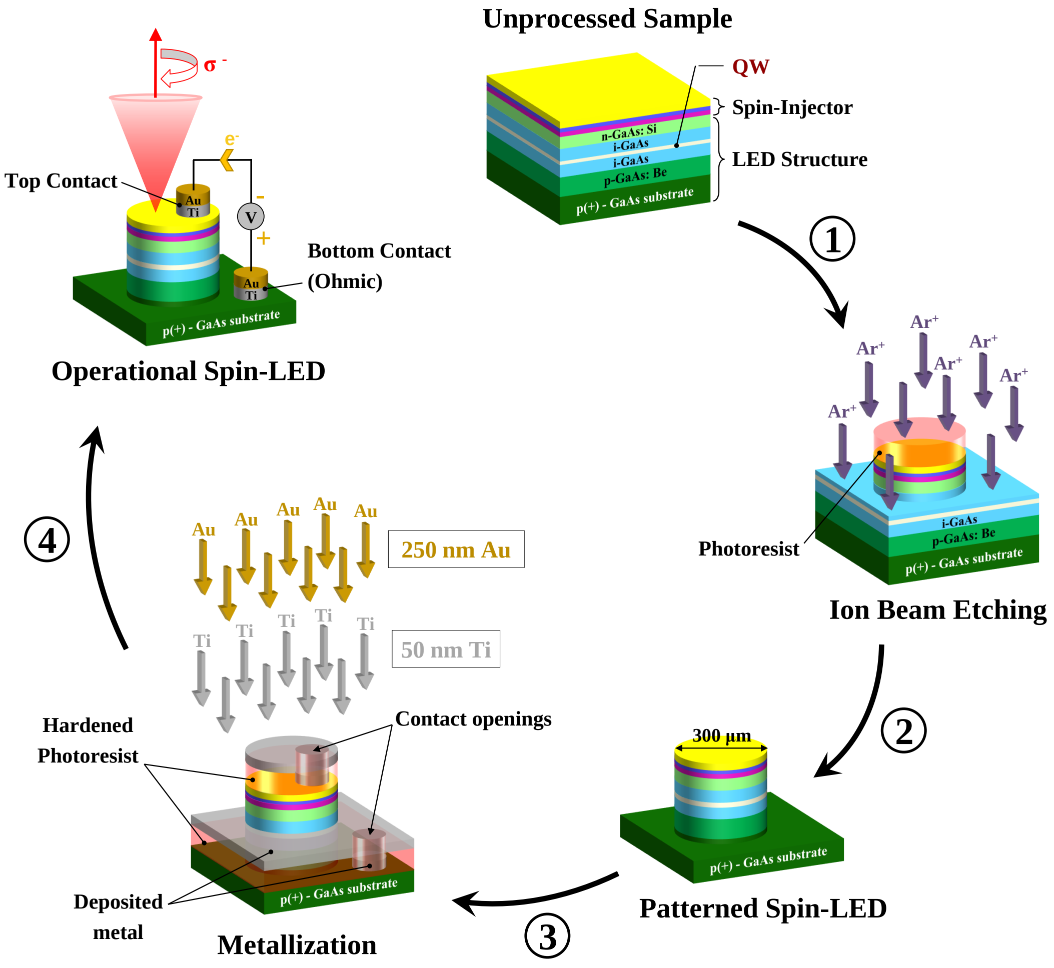

Figure 3.1: Illustration of the fabrication process of the Spin-LED: (1) Spin-coating of 1.2 μm thick SPR700 photoresist and photolithography patterning of the 300 μm diameter junctions. **(2)** O_2-plasma and Acetone/Propanol cleaning of the photoresist hardened by the Ar$^+$-ions bombardment. **(3)** Spin-coating of 1.2 μm thick SPR700 photoresist, photoresist hardening using a Chlorobenzene bath and photolithography patterning of the 110 μm diameter contacts. **(4)** Lift-Off of the photoresist and Acetone/Propanol cleaning of the samples.

study showed that with GaAs QWs, an Al concentration of 15% in the barrier is the best compromise to maximizing the carriers confinement and minimize the strains induced on the active region. Indeed, the barrier heights need to be sufficient to prevent carrier leakage when increasing the measurement temperature.

3.1.2 Sample preparation

In the framework of my Ph.D, I fabricated the Spin-LED structures used as a development tool for the new ultra-thin spin-injector with PMA at remanence. In the three year time lapse, more than 40 different samples were produced to supply the several research angles and optimization studies performed on MTJ spin-injectors. All the devices were prepared using the same micro-pilar photolithography process in the *III-V Lab*'s clean room at *Thales Research Technology.*

The lithography process is based on a classic 2-contacts junction architecture with a top-contact located on the spin-injector and a bottom contact located on the semiconductor substrate. When the junction is reverse biased, the carriers injected through the MTJ spin-injector are being spin-polarized before reaching the LED's active region. Two main stages can be identified in the fabrication process: **(i)** first the patterning of micropillar-shaped LED junctions with a large 300 μm diameter using Ion Beam Etching followed by **(ii)** the deposition of 110 μm diameter (50nm)Ti/(250nm)Au metal contacts using a standard Lift-Off technique. The p-i-n sample is usually IBE-etched down to the bottom p^+-GaAs substrate in order to ensure an ohmic contact between the doped semiconductor and the Ti/Au metals. For the contact, the Au layer is taken thick enough (250 nm) in order to protect the fragile spin-injector during the Au-wire bonding using a bonding-machine. Indeed, even when minimizing the "applied pressure" setting, the bonding-machine is estimated to drill at least over 150 nm in the Au layer. The 40 nm Ti layer is used as an anchor layer for Au. Figure 3.1 illustrates the essential steps of the photolithography fabrication process while the complete clean-room process is detailed step by step in Appendix C.

3.2 Optimization of the MgO Tunnel Barrier: MBE vs. Sputtering growth

MgO/CoFeB/Ta magnetic tunnel spin-injectors deposited on semiconductor (SC) LED structures exhibit two main interfaces: F/MgO and MgO/SC. However, identifying the role and the contribution of each interface in order to reach an optimal electrical spin-injection is still an open question. Additionally, comparably to what is known for the symmetry selection rules driving the tunneling transfer of carriers through MgO-based MTJ [100, 291, 103], the key role of MgO as a relevant spin-filter to enhance the spin-injection efficiency into semiconductor needs to be investigated.

In this section, we propose to pull the blind on these questions by studying MgO barriers grew by two different techniques: Sputtering and Molecular Beam Epitaxy (MBE). This results in different GaAs/MgO and MgO/CoFeB interfaces qualities. It allows us to examine which interface must be optimized in priority to enhance the spin-injection efficiency. CoFeB is a promising candidate to play the role of ferromagnetic injector; after annealing at 350°C, the CoFeB easily forms a bcc grain-to-grain epitaxial crystalline phase on MgO [292]. This improvement by annealing has been particularly observed in MTJ, where a TMR of 600% was measured on CoFeB/MgO/CoFeB junctions [293] as compared to 180% observed on CoFe/MgO/CoFe junctions [103]. The study of the annealing effect on these Spin-LED with MgO/CoFeB spin-injectors was performed by correlating the emitted light DoCP with the CoFeB crystallization state [294, 295]. This method allowed us to examine the key role of interfaces and further determine if the MgO spin filtering effect actually exists in the case of spin-injection into semiconductors. This work has recently been published in the Journal *Applied Physics Letters* [296].

3.2.1 Samples preparation

The p-i-n LED used for the experiments was grown in a dedicated III-V MBE chamber and exhibit the following structure sequence (Figure 3.2): $p-GaAs:Zn$ (001) $substrate$ $(p = 2\times10^{19}\ cm^{-3})$ // 500 $nm\ p-GaAs:Be$ $(p = 2\times10^{19}\ cm^{-3})$ / 200 $nm\ p-GaAs:Be$ $(p = 2\times10^{18}\ cm^{-3})$ / 50 $nm\ undoped-GaAs$ / 10 $nm\ undoped-In_{0.1}Ga_{0.9}As$ / 50 $nm\ undoped-GaAs$ / 50 $nm\ n-GaAs:Si$ $(n = 1\times10^{16}\ cm^{-3})$. The LED surface was passivated with arsenic in the III-V MBE chamber before being transferred through air into a second MBE-Sputtering interconnected system. As a first step, the arsenic capping layer was desorbed at 300°C in the MBE chamber. Two methods were then used to grow the MgO tunneling barrier layer. The first method consisted in growing the MgO layer at 250°C in the MBE chamber after arsenic desorption. With the second method the MgO layer was grown in the Sputtering chamber after transferring the sample from the MBE into the Sputtering system through vacuum. In both cases, the MgO barrier has an identical thickness of 2.5 nm. Finally, a 3 nm CoFeB ferromagnetic contact and 5 nm Ta protection layer were deposited by sputtering on top of the MgO bar-

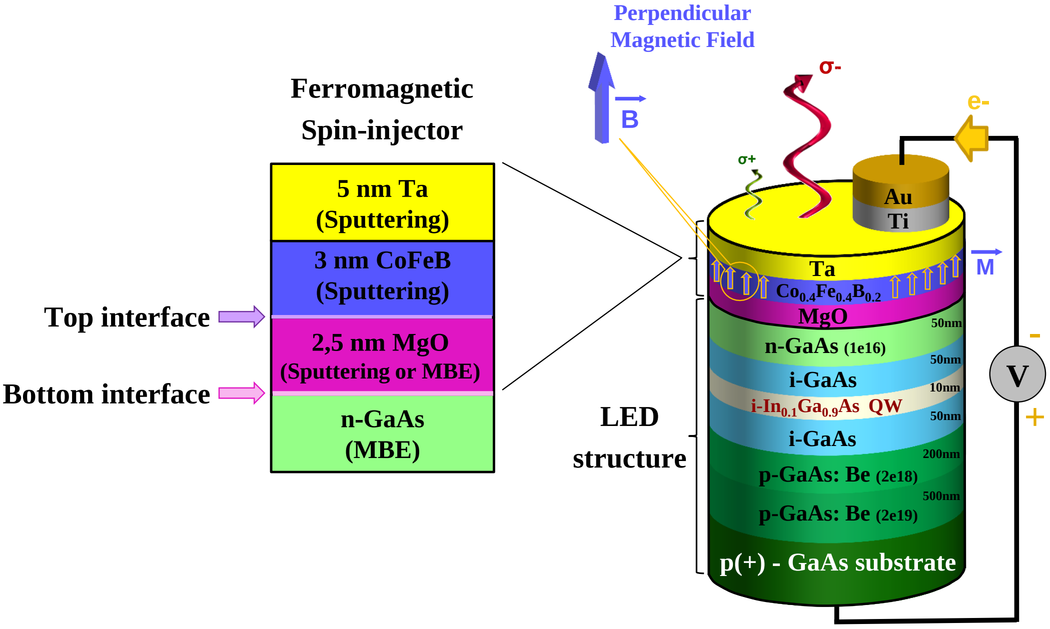

Figure 3.2: Schematic representation of a Spin-LED structure with a single InGaAs/GaAs QW. The MgO/CoFeB/Ta spin-injector deposited on n-GaAs exhibit two interfaces of interest: a top MgO/CoFeB interface and a bottom GaAs/MgO interface. Figure adapted from [296]

rier. Hereafter, we refer to *MBE*- and *Sputtering*-sample to assign the two different Spin-LED carrying MgO barriers prepared by MBE and Sputtering techniques respectively. These two growth techniques produce different qualities of MgO barriers and interfaces (Figure 3.2 "Top and Bottom interface"). These differences allow us to determine which factors are crucial to reach an efficient electrical spin injection. We can operate a direct comparison knowing that all the layers constituting the injectors have the same thicknesses for both kinds of sample. Then, 300 μm diameter circular mesas are processed using conventional UV photolithography and Ion Beam Etching techniques following the process described in the previous section. Finally, the processed wafers were cut into small samples to perform Rapid Thermal Annealing (RTA) at different temperatures (T_a) for one minute. The RTA procedure stands out as a good technic to promote the crystallization of CoFeB [297] while keeping the optical characteristics of the LED almost unchanged.

3.2.2 Impact of annealing on the MgO/CoFeB bi-layer

Electroluminescence measurements:

For the polarization-resolved Electro-Luminescence (EL) measurements, the spin-LED was placed into a Helmholtz-split magnetic coil, providing a maximum magnetic field B of 0.8 T normal to the sample plane. The EL signal was detected in the Faraday geometry. The DoCP of the EL was analyzed through a $\frac{\lambda}{4}$-wave plate combine with a linear analyzer [199]. The DoCP is still defined accordingly to Chapter 2 as $DoCP = \frac{I(\sigma^+)-I(\sigma^-)}{I(\sigma^+)+I(\sigma^-)}$ where $I(\sigma^+)$ and $I(\sigma^-)$ are the intensities of the right and left circularly polarized components of the luminescence, respectively. Insets of Figure 3.3(a) show a typical CW EL spectra from a spin-LED with a sputtered MgO tunnel barrier (T_a=350°C) acquired at 25 K under a bias voltage V_{bias}=2.4 V at B=0 T (top inset) and B=0.8 T (bottom inset). Whereas the EL peak of the heavy-hole exciton (XH) observed at 878 nm does not show any circular polarization at zero magnetic field (top inset), the DoCP reaches 24% ± 1% under B=0.8 T (bottom inset). It was checked that the magnetic circular dichroism contribution is less than 1% at 0.8 T thanks to a control measurement using a linearly polarized He-Ne laser [298]. The measured DoCP increases with the applied longitudinal magnetic field (Figure 3.3(a)) due to the progressive increase of the out-of-plane magnetization's projection (the CoFeB magnetization is in-plane at 0 T). Figure 3.3(b) illustrates a systematic study of the influence of the post-annealing temperature on the DoCP for both kind of Spin-LED. In the case of sputtered tunnel barriers, we observe a clear improvement of the measured EL's DoCP from 13.5% ± 1% before annealing up to 24% ± 1% after annealing at T_a=350°C (optimal). However, the DoCP further decrease when increasing the annealing temperature up to T_a=380°C. This trend is similar for the sample with the MBE-grown MgO tunnel barrier despite a slightly lower optimal DoCP of 20% ± 1% (Inset of Figure 3.3(b)). When varying the annealing temperature, the DoCP behavior is similar to the one observed by Wang *et al.* [108] for spin-LED with MgO/CoFe spin-injectors. Yet the variation in our spin-LED is much more remarkable.

Time resolved photoluminescence measurements:

It is necessary to discriminate if the observed large improvement of the DoCP as a function of annealing temperature displayed in Figure 3.3(b) is due to a real improvement of P_s, or only due to the impact of the annealing process on the QW properties. Therefore, we have performed a systematic measurement of the renormalization factor F as a function of the annealing temperature T_a. To do so, we measured the spin-relaxation time τ_s in the QW and the electron lifetime τ in a bare p-i-n LED sample using Time and polarization Resolved Photo-Luminescence (TRPL).

Indeed, it was already demonstrated in Chapter 2 that the use of Spin-LED as an optical probe to quantify the electrical spin-injection efficiency in GaAs is justified by a quite straightforward relationship between the electron spin-polarization P_s injected in the QW and the measured EL's DoCP so that [299, 198]:

$$DoCP = P_s \times F \qquad with \qquad F = \frac{1}{1+\frac{\tau}{\tau_s}} \tag{3.1}$$

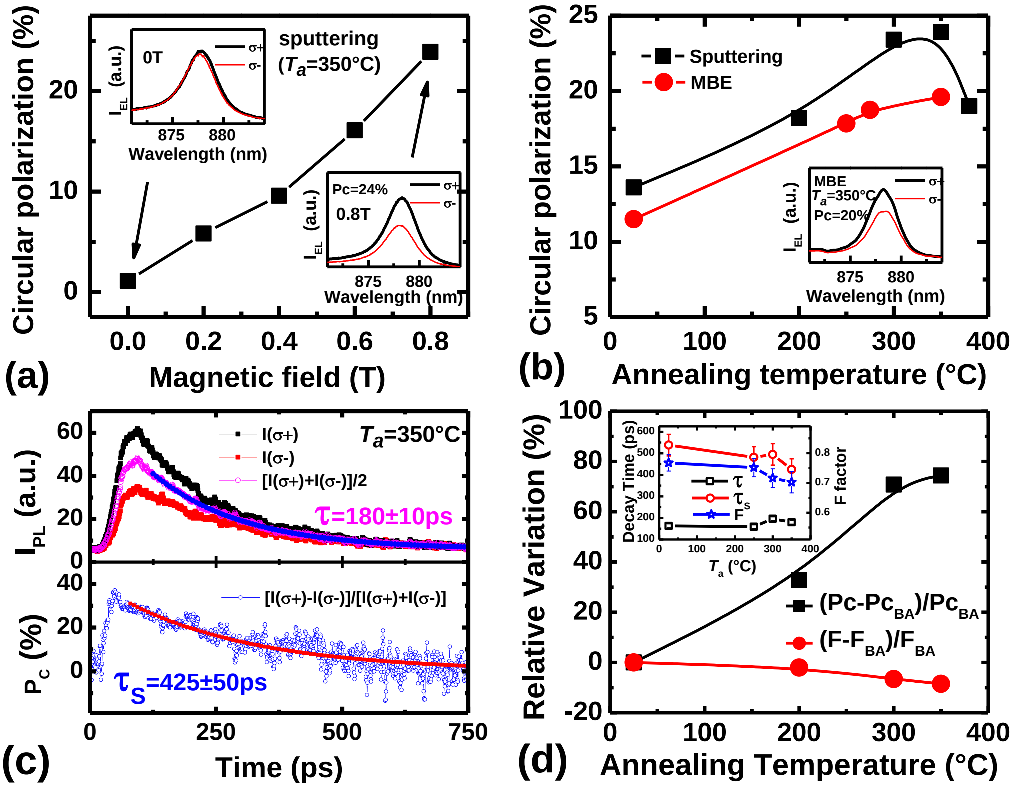

Figure 3.3: **(a)** EL's DoCP as a function of the applied longitudinal magnetic field for the Spin-LED with a sputtered MgO tunnel barrier (T_a=350°C) at T=25 K. EL spectra at zero magnetic field (top inset) and at B=0.8 T (bottom inset) of the $I(\sigma^+)$ (thick black line) and the $I(\sigma^-)$ (thin red line) EL components. **(b)** EL's DoCP as a function of the annealing temperature for sputtering (black squares) and MBE (red circles) grown MgO Spin-LEDs at T=25 K. Inset: EL spectra of a Spin-LED with a MBE grown MgO tunnel barrier (T_a=350°C) at T=25 K and B=0.8 T for $I(\sigma^+)$ (thick black line) and $I(\sigma^-)$ (thin red line) EL components. **(c)** TRPL measurements on a bare p-i-n LED sample (T_a=350°C) at T=25 K. Top: PL intensity components $I(\sigma^+)$ and $I(\sigma^-)$ with respectively σ^+-polarization (black squares) and σ^--polarization (red squares) as a function of time after a 1.5 ps laser (σ^+) pulsed excitation at 780 nm (above GaAs bandgap). The sum of the two intensities components $I_{sum} = I(\sigma^+) + I(\sigma^-)$ is displayed in pink opened circles. The decay is characterized by the electron lifetime τ_s. Bottom: time evolution of the DoCP (noted as P_c) at T=25 K (blue opened circles). The decay is characterized by the electron spin relaxation time τ. **(d)** Relative variation of the EL DoCP (noted as P_c) (black squares) for sputtered samples and of the renormalization factor F (red circles) as a function of T_a. Inset: Electron spin relaxation time τ_s (red open circles), electron lifetime τ (black open squares) and renormalization factor F (blue open stars) as a function of the annealing temperature T_a. Figure reprinted from [296]

For TRPL measurements, a mode-locked Ti:Sapphire laser with a 1.5 ps pulse width was used for the non-resonant circularly-polarized excitation. The PL signals were detected by a 2D synchroscan streak camera, which provides an overall temporal resolution of less than 8 ps and a spectral resolution of approximately 8 meV (5.2 nm). For complementary information, a complete schematic of the TRPL setup can be find in Appendix E (Figure E.1). Figure 3.3(c) exhibit the TRPL measurement of the bare p-i-n LED after annealing at T$_a$=350°C. The electron lifetime τ is extracted from the decay of the $I\left(\sigma^{+}\right)+I\left(\sigma^{-}\right)$ sum and is evaluated around 180±10 ps at $\frac{1}{e}$. In the case of the spin-relaxation time τ_s, the characteristic time is extracted from the decay of the circular polarization and is here evaluated to 425±50 ps at $\frac{1}{e}$. Accordingly, the renormalization factor F is calculated to be 0.7. The variations of τ, τ_s and the associated F-factor as a function of the annealing temperature T_a are summarized in the inset of Figure 3.3(d). In Figure 3.3(d), the DoCP and F-factor variations have been plotted relatively to the before annealing case in order to display a better comparison of the DoCP and F-factor behavior as a function of T_a. For sputtered samples, it clearly shows that the relative improvement of the circular polarization $\frac{DoCP(T_a)-DoCP(BA)}{DoCP(BA)}$ reaches about 80% between $DoCP(BA)$ and $DoCP(T_a = 350°C)$. However, the relative variation of the F-factor $\frac{F(T_a)-F(BA)}{F(BA)}$ is much weaker (less than 10% between $F(BA)$ and $F(T_a = 350°C)$) and is even negative. Consequently, as the F-factor relative variation is smaller and opposite to the DoCP behavior, we can affirm that the large DoCP improvement observed in Figure 3.3(b) is induced by a real upgrade of the spin-injector.

Evolution of the magnetization

For the EL measurement, the maximum magnetic field applicable in the out-of-plane direction is limited to 0.8 T which is not sufficient to fully saturate the magnetization of the CoFeB layer ($B_{sat} = 1.4$ T). To exclude the possibility of DoCP increase due to changes of the saturation field after annealing, we performed Superconducting QUantum Interference Device Magnetometer (SQUID) on the sputtering-MgO sample to measure the CoFeB magnetization in the out-of-plane configuration. Before annealing up to T$_a$=275°C, the evolution of the magnetization is quasi-linear with the magnetic field (B) between -1.3 T to 1.3 T (Figure 3.4(a)). Then the magnetization dependence on the magnetic field becomes non-linear at T$_a$=350°C. One can note that the saturation field measured is 1.3 T when T_a is below 300°C while it reaches 1.75 T for T$_a$=350°C. The DoCP can be extrapolated to saturation by multiplying the DoCP at 0.8 T by the ratio $\frac{M_{sat}}{M(0.8T)}$ based on the results obtained by SQUID. Doing so, the extrapolation leads to a rough estimation of DoCP≈42.0% at saturation and at 25 K for the Spin-LED with sputtered MgO after annealing at T$_a$=350°C. This result confirms the high efficiency of MgO/CoFeB injector. This result is close to the value obtained by Jiang *et al.* with a DoCP=50% at low temperature with AlGaAs//MgO/CoFe injectors which is the best result reported in the literature [99]. It is also larger than the one reported very recently by Li *et al.* with a DoCP=25% using a Schottky barrier as spin-injector [203]. In Figure 3.4(a), the dashed line highlights that the ratio $\frac{M_{sat}}{M(0.8T)}$ does not depend on the annealing temperature. This explains the DoCP variations as function of T_a observed

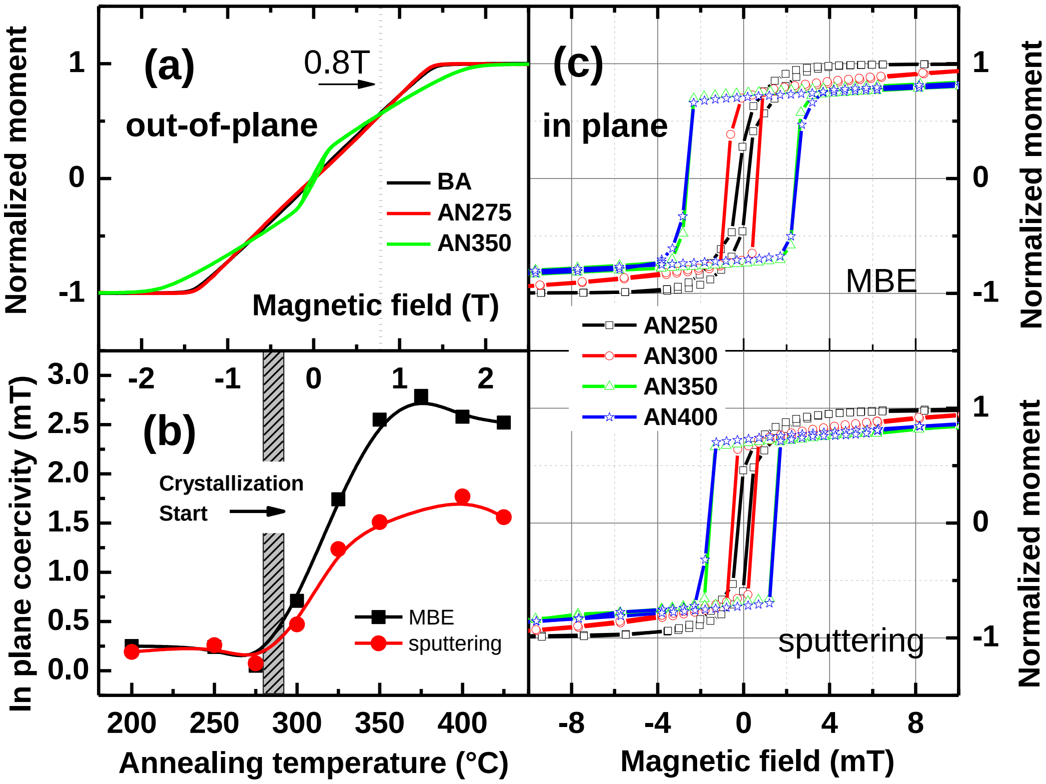

Figure 3.4: SQUID measurement at T=300 K. **(a)** Normalized magnetization as a function of the applied out-of-plane magnetic field for a sputtering Spin-LED before annealing (black line) and annealed at 275°C (red line) and 350°C (green line). **(b)** In-plane coercivity field H_c as a function of the annealing temperature T_a for a Spin-LED with sputtered MgO (red circles) and with MBE grown MgO (black squares). **(c)** Top: In-plane hysteresis loop of a Spin-LED with MBE grown MgO annealed at different temperatures. Bottom: Same measurements for a Spin-LED with a sputtered MgO tunnel barrier. Figure reprinted from [296]

for B=0.8 T (Figure 3.3(b)). The non-linear M-H curve for T$_a$=350°C reflects the crystallization of the CoFeB layer [294].

To further clarify the influence of the annealing temperature on the crystallization of the CoFeB layer, we performed SQUID measurements in an in-plane geometry to check the coercivity H_c of the CoFeB layer. Figure 3.4(c) displays the hysteresis cycles for both type of Spin-LED annealed at different temperatures. Figure 3.4(b) summarized the evolution of H_c as a function of T_a. When T_a is above 300°C, H_c increases for both types of samples witnessing the beginning of the CoFeB crystallization [297]. However, after annealing, the MBE sample has a relatively larger H_c than the sputtering sample which could be related to a different magnetic domain structure in the CoFeB layer (see further). The increase of H_c with T_a saturates around 350°C, noticing a full crystallization of CoFeB layer in good agreement with crystallization temperature reported in the literature [294]. Nevertheless, the EL measurement indicates that the DoCP increases far below 300°C and saturates at 350°C when the crystallization is over. Therefore it is clear that the increase of the DoCP is not due to the crystallization of the whole CoFeB layer.

3.2.3 Role of the GaAs/MgO and MgO/CoFeB interfaces

HRTEM analysis:

We used High-Resolved Transmission Electron Microscopy (HRTEM) to examine the interfacial structures of the injector and push further the understanding of the annealing effect on the DoCP. The good homogeneity of both the sputtering- and MBE-structures annealed at 350°C is checked using low magnification images. The insets of Figure 3.5(d) illustrates the sputtering-sample while the MBE-sample is not shown as it exhibits identical feature. Note also that the MgO thicknesses are identical for the two types of injectors allowing a direct comparison of the measured DoCP emitted by both type of Spin-LED (Figure 3.3(b)).

We start by comparing the TEM images of the MBE-sample before annealing (Figure 3.5(a)) and after annealing at 350°C (Figure 3.5(b)). In both cases the GaAs/MgO interface is sharp. The CoFeB layer is amorphous before annealing and fully crystallized after annealing at 350°C, which further confirms that the increase of H_c measured by SQUID is due to the crystallization of the CoFeB layer. The left inset of Figure 3.5(b) displays the FFT image from the selected zone and shows that the CoFe(B) deposited on MgO exhibits a bcc structure. On the other hand, the right inset of Figure 3.5(b) shows the bright field HR-scanning of the TEM image and allows us to clearly identify the relationship of epitaxial crystalline orientation between GaAs, MgO and CoFe (B has been absorbed by Ta): $GaAs[100](100)//MgO[100](100)//CoFe[110](010)$.

For the MBE-sample, the DoCP clearly increases with T_a (Figure 3.3(b)). In the mean time no change is observed at the GaAs/MgO interface while a drastic change occurs at the MgO/CoFeB interface with evidences of CoFeB crystallization at 350°C. We can then logically affirm that the MgO/CoFeB interface is of central importance for an optimal spin injection. A second observation reinforces this conclusion: when comparing the TEM images for the MBE (Figure 3.5(a)) and Sputtering (Figure 3.5(c)) samples before annealing, a thin amorphous layer (0.4 nm) can be identified at the GaAs/MgO interface of the Sputtering-sample (Figure 3.5(c)). Before annealing, the DoCPs are roughly comparable (Figure 3.3(b)) for both type of samples. However, the GaAs/MgO interface quality is much better by MBE. This reveals the weak influence of the GaAs/MgO interface and highlights the importance of the MgO/CoFeB interface for an efficient electrical spin-injection. Finally, for the Sputtering-samples after annealing at T_a=350°C (Figure 3.5(d)), the complete crystallization of the CoFeB layer is also confirmed by the FFT image (left inset of Figure 3.5(d)) similarly to the MBE sample. We can conjointly point out that the amorphous layer at GaAs/MgO interface is significantly reduced after

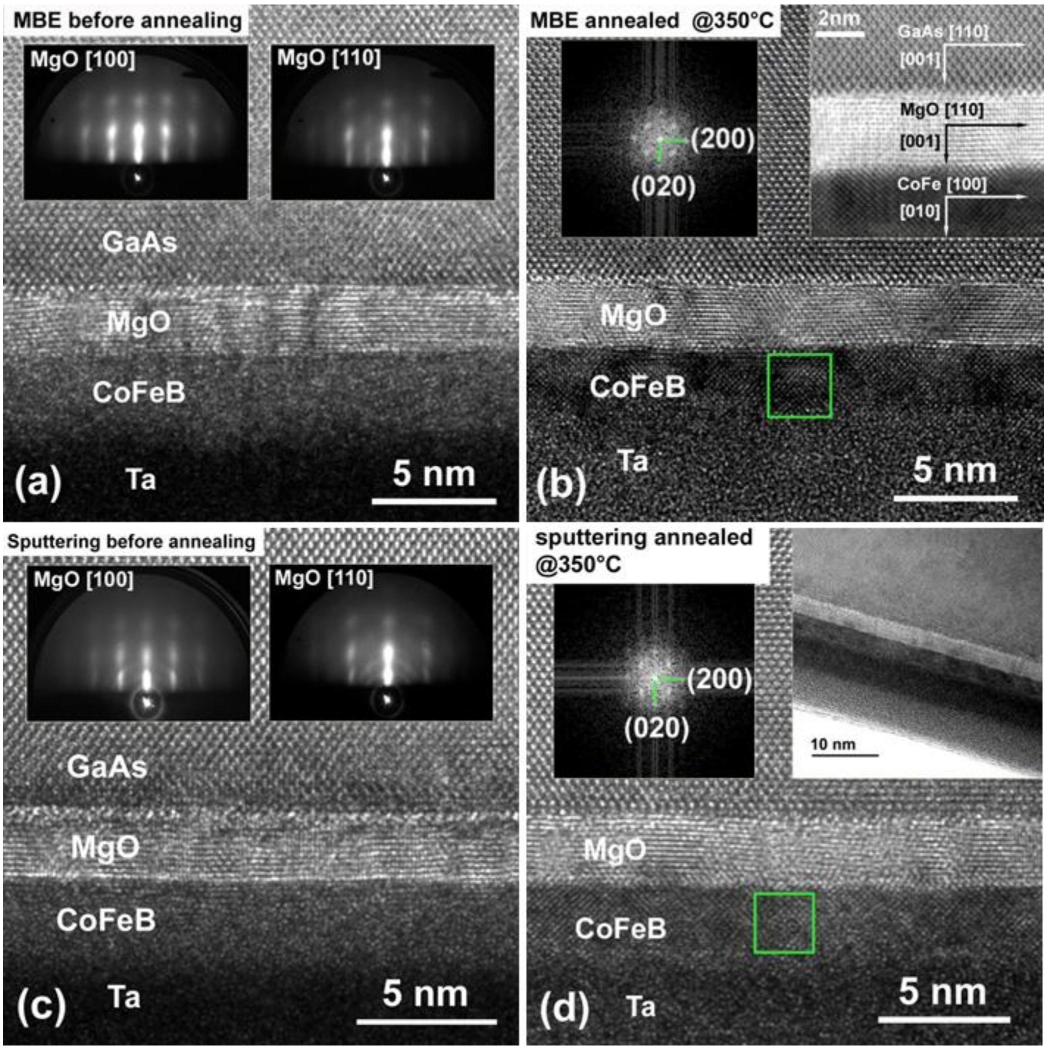

Figure 3.5: HR-TEM images of **(a)** a sample with MBE grown MgO and **(c)** a sample with sputtered MgO, both before annealing. Insets: RHEED patterns on MgO surface from GaAs [100] and [110] azimuths (left and right insets respectively). **(b)** HR-TEM image of the sample with MBE grown MgO after annealing at T_a=350°C. Left inset: FFT pattern on the square zone in CoFeB layer. Right inset: HR-STEM image to show the crystallographic orientation relationship between GaAs, MgO and CoFe. **(d)** HR-TEM image of the sample with sputtered MgO after annealing at T_a=350°C. Left inset: FFT pattern on the square zone in CoFeB layer. Right inset: TEM image with a large scale to show the homogeneity of structures. Figure reprinted from [296]

annealing. The origin of this amorphous layer might be explained by the large kinetic energy of the deposited atoms during the sputtering growth process. The RTA process could then trigger a recrystallized of this thin amorphous layer.

RHEED analysis:

To complete our study, we performed Reflection High Energy Electron Diffraction (RHEED) measurements to check the crystalline structure of MgO surfaces (top interface) prepared by MBE and Sputtering methods. For MBE samples, the RHEED patterns along the GaAs [100] and [110] directions exhibit a mono-crystalline spotty diffraction pattern. This observation further confirms the same in-plane epitaxial relationship (GaAs[100](100)//MgO[100](100)) deduced from the HR-STEM image (insets of Figure 3.5(a)). Oppositely, the polycrystalline rings on the RHEED images of the sputtered MgO surface appear in the two directions indicating a worse crystalline quality (Insets of Figure 3.5(c)). Nevertheless, the fact that the DoCP values are slightly larger for sputtering samples (regardless to the annealing temperature) despite this worse MgO quality indicates that the texture quality of the MgO barrier is not as critical for spin-injection. It has been demonstrated that during an annealing process the Ta layer can absorb B atoms resulting in the crystallization of CoFeB from the MgO/CoFeB interface [300]. For the Sputtering-sample, the polycrystalline MgO grains observed before annealing most certainly induce a high density of grain in the crystallized CoFeB layer after annealing due to the grain to grain epitaxial procedure [292]. The magnetic domain structures related to the grain boundaries [301] could explain the smaller coercivity observed for the Sputtering-samples compared to the MBE-samples in SQUID measurements (Figure 3.4(b)).

Conclusion:

This comparative study on the MgO tunnel barriers highlights that the MgO/CoFeB interface quality seems to be the crucial parameter for an efficient electrical spin-injection in semiconductors. As a large increase of the spin-injection efficiency takes place below annealing at 300°C, i.e. before crystallization of the whole CoFeB layer, we attribute this trend to an improvement of chemical bounds at the MgO/CoFeB interface, as it was also observed for the TMR improvement in MgO MTJs below annealing at 300°C [302]. A below 300°C annealing can move the Co and Fe atoms toward the top of Oxygen atoms at the MgO/CoFeB interface, which not only efficiently enhance the interfacial spin-polarization but also generates an interfacial Perpendicular Magnetization Anisotropy [303].

The other point to address is that, regardless to the annealing temperature, the DoCP of Sputtering-samples with a MgO/CoFeB interface grown in the same chamber without transfer interruptions are always slightly larger than the DoCP of MBE-samples that went through a transfer step during the injectors growth. This directly stands out another proof of the preponderant importance of this MgO/CoFeB interface.

From 300°C to 350°C annealing the DoCP improvement is quite marginal indicating that, in our case, the MgO spin filter effect selecting the Δ_1-symmetry electrons in the CoFe band structure (highest spin-polarization for tunneling) does not play an important role . This could be related to the Ta diffusion toward the MgO/CoFeB interface happening after a high temperature annealing [293, 304]. The decrease of the DoCP after annealing of the sample at T_a=380°C (Figure 3.3(b)) corroborate this hypothesis. Therefore, to enhance the MgO spin filtering effect, a path to explore is the suppression of any Ta diffusion toward the MgO/CoFeB interface (eg. replace with other metals for B absorption).

3.3 Development of an ultra-thin MgO/CoFeB spin-injector with Perpendicular Magnetic Anisotropy

A prerequisite towards optimized device functionalities is to promote a medium with robust perpendicular magnetic anisotropy (PMA) [209] up to room temperature (RT) to be used as a solid-state ferromagnetic (F) injector electrode. Good candidates are systems including alternated planes of 3d/4f Fe/Tb [305, 306], 3d/5d Fe/Pt [307] or Co/Pt [24, 308] and 3d/3d Co/Ni multilayers [309]. However, these systems generally suffer from the requirement of a minimum thickness (generally several units of bilayers). They are grown on a thin oxide layer which is used as a tunneling barrier to circumvent the conductivity mismatch between metal and semiconductor [63]. The large thickness of injector results in a large absorption of light in the near infrared region, e.g. 95% light is absorbed for 40nm Fe/Tb multilayers [305, 306]. Moreover, in the case of Spin-LED, there is also a requirement that the first F atomic plane at the interface must possess a robust spin-polarization for an efficient spin-injection. This condition is hardly attainable due to the chemical inter-diffusion or intermixing in the multilayer systems [308]. Therefore, up to now, the Degree of Circular Polarization (DoCP) of the light emitted by Spin-LED with PMA injectors is still limited at 3-4% at remanence [306, 307, 308].

A series of recent theoretical investigations have proposed that the Fe(Co)/MgO interface itself could provide PMA in the range of magnitude of 1 $mJ.m^{-2}$. Such PMA values are sufficient to reorient the magnetization along the out-of-plane direction [304, 310]. This PMA property has been put forward in the case of CoFeB/MgO/CoFeB p-MTJs grown on SiO_2 substrate used for spin transfer torque (STT) operations in MRAM technologies (STT-MRAM) [220, 311]. These STT devices display high Tunneling Magneto-Resistance (TMR) ratio, good thermal stability together with low switching current density. In the following work, we demonstrate, for the first time, the occurrence of such PMA functionality on semiconducting heterostructures with III-V based Spin-LED by integrating CoFeB/MgO perpendicular spin-injectors. Large values of Electro-Luminescence's DoCP of 20% at 25 K and 8% at 300 K are measured under zero magnetic field. These results constitute the cornerstone for future implementation of electrical control of circularly polarized light via STT in III-V optical devices (LED, Lasers) operating at room temperature. This work has recently been accepted for publication in the Journal *Physical Review B* [312].

3.3.1 Physical origins of Perpendicular Magnetic Anisotropy in ultrathin-ferromagnetic-films

This sub-section discusses the work of Van Vleck 1937 (Awarded Nobel Prize with Mott and Anderson) [313], Néel [314] and Bruno [315, 316] on the magnetic anisotropy. The aim is to provide the reader with a simple tool-box to help him better understand the development and optimization work we performed on MgO/CoFeB/Ta spin-injector with perpendicular magnetic anisotropy.

Definition and macroscopic description:

Ferromagnetic single crystals exhibit intrinsic easy and hard directions of the magnetization, i.e. the energy required to magnetize a crystal directly depends on the direction of the applied field relative to the crystal axes: $\Delta E_M = f\left(\vec{M}_{<xyz>}\right)$. This energy difference ΔE_M represents the magnetic anisotropy of the material.

In ultra-thin magnetic films and multilayers the physical basis that underlies a preferred magnetic moment orientation can be quite different from the factors that account for the easy-axis alignment along a symmetry direction of a bulk material, and the strength can also be markedly different. The prominent presence of symmetry-breaking elements such as planar interfaces and surfaces, which automatically follows the layer's formation in these systems, are the basic ingredients for this behavior. By varying the thicknesses of the individual layers and choosing appropriate materials, it is possible to tailor the magnetic anisotropy. As individual layers in a multilayer stack become thinner, the role of interfaces and surfaces may dominate that of the bulk. This is the case in many magnetic multilayers, where a perpendicular interface contribution to the magnetic anisotropy is capable of rotating the easy magnetization direction from an in-plane orientation to the direction perpendicular to the plane. This phenomenon is usually referred to as Perpendicular Magnetic Anisotropy (PMA) and is particularly important for information storage and retrieval applications [317]. The PMA is a result of a magnetic anisotropy at the interface which considerably differs from the magnetic anisotropy in the bulk.

The (effective) magnetic anisotropy energy K_{eff} (J.m^{-3}) can be phenomenologically separated in a volume contribution K_v (J.m^{-3}) and a contribution from the interfaces K_s (J.m^{-2}). For a magnetic layer of thickness t bounded by two identical interfaces, the effective magnetic anisotropy approximately obeyed the relation [317]:

$$K_{eff} = K_v + \frac{2K_s}{t} \tag{3.2}$$

This relation represents the average magnetic anisotropy energy of the magnetic layer's interface atoms and the bulk atoms. The relation is presented under the convention that $\frac{K_s}{d}$ (d being the thickness of a monolayer) represents the difference between the anisotropy of the interface atoms with respect the bulk atoms. Below a limit thickness $t_\perp = -\frac{2K_s}{K_v}$, the contribution of the interface anisotropy outweighs the volume contribution and drives out-of-plane the magnetization of the thin film. In other words, the systems successfully overcomes the demagnetizing fields appearing when tilting the layer's magnetization out-of-plane.

Microscopic origin of the magnetic anisotropy:

The energy involved in rotating the magnetization from the easy-axis (low energy) toward the hard-axis (high energy) is typically of the order of 10^{-6} to 10^{-3} $eV.at^{-1}$. Thus, this anisotropy energy is a very small correction to the total magnetic energy. Physically, it arises from relativistic corrections of the Hamiltonian which break the rotational invariance with respect to the spin quantification axis: these are the *Exchange Interaction* and the *Spin-Orbit Coupling.*

- The exchange interaction (Heisenberg in 1928) between two electron's spin $\vec{s_1}$ and $\vec{s_2}$ is defined by:

  $$E_{exc} = -J_{exc}\left(\vec{s_1} \cdot \vec{s_2}\right) \tag{3.3}$$

  where J_{exc} represents the exchange energy. Due to its long range character, the contribution of the exchange interaction to the anisotropy generally directly depends on the shape of the specimen. It is of particular importance in thin films, and this interaction is largely responsible for the in-plane magnetization usually observed.

- The Spin-Orbit coupling H_{SO} can be interpreted as the coupling between the spin of the electron and the magnetic field created by its own orbital motion around the nucleus. As the orbital motion itself is directly coupled to the crystal lattice via the electric potential of the ions, this term provides a contribution to the magneto-crystalline anisotropy. If we consider a nucleus with a spherical electric potential, the Spin-Orbit Hamiltonian can be expressed as:

  $$\mathrm{H}_{SO} = \lambda_{SO}\left(\vec{L} \cdot \vec{S}\right) \ (3.4)$$

  where λ_{SO} is the Spin-Orbit constant, $\vec{L} = \sum_i \vec{l_i}$ the angular momentum and $\vec{S} = \sum_i \vec{s_i}$ is the spin angular momentum.

In the absence of Spin-Orbit and exchange interaction, the total energy of the electron-spin system would not depend on the magnetization direction. However, for itinerant materials such as $3d$ transition metals (Fe, Co, Ni), the presence of Spin-Orbit interaction induces a small orbital momentum, which then couples the total magnetic moment $\vec{J} = \vec{L} + \vec{S}$ to the crystal axes. As a direct consequence, the total energy depends on the magnetization orientation relatively to the crystalline axes and thus reflects the crystal symmetries. This is known as the magneto-crystalline contribution to the anisotropy. The lowered symmetry at an interface strongly modifies this contribution as compared to the bulk, yielding as previously mentioned to a so-called interface anisotropy. In short, the microscopic origin of the magneto-crystalline anisotropy in solids is the Spin-Orbit interaction (see van Vleck work [313]). In 1954, Néel extended van Vleck‘s pair interaction model to surfaces and showed that the reduced symmetry at the surface should indeed results in surface magnetic anisotropies strongly differing from the magnetic anisotropy of the bulk atoms [314].

Assuming a bulk sample where magnetostatic effect are absent, the magnetic anisotropy ΔE_M is given by the Spin-Orbit energy ΔE_{SO} [318, 315, 316]:

$$\Delta E_M = \Delta E_{SO} = \langle H_{SO} \rangle_{hard} - \langle H_{SO} \rangle_{easy} = \lambda_{SO} \left[\left\langle \vec{L} \cdot \vec{S} \right\rangle_{hard} - \left\langle \vec{L} \cdot \vec{S} \right\rangle_{easy} \right] \quad (3.5)$$

$\Delta E_M > 0$, it costs energy to rotate the magnetization into the hard direction. This Spin-Orbit anisotropy is directly related to the orbital moment anisotropy by [318, 316, 315]:

$$\Delta E_{SO} = \lambda_{SO} \left[\left\langle \vec{L} \cdot \vec{S} \right\rangle_{hard} - \left\langle \vec{L} \cdot \vec{S} \right\rangle_{easy} \right] = \frac{\lambda_{SO}}{4\mu_B} \left(m_{orb}^{hard} - m_{orb}^{easy} \right) \quad (3.6)$$

where m_{orb}^{hard} and m_{orb}^{easy} are the orbital moments along the hard and easy axis respectively while $\mu_B = \frac{\hbar e}{m}$ is the Bohr magneton. The Bruno model states that the orbital moment is larger along the easy magnetization direction and that the difference between the orbital moments along the easy and hard directions is proportional to the magneto-crystalline anisotropy. Accordingly, in a thin film there is a directional quenching of the atom’s orbital moment by *Ligand Field Effect*: In-plane orbits are quenched $\langle L_z \rangle = 0$ and molecular orbitals are formed $(3d_{x^2-y^2},\ 3d_{xy})$ while out-of-plane orbits are less perturbed. The Spin-Orbit interaction recreates the orbital momentum that was destroyed by the orbital arrangements [318].

Magnetic Anisotropy in 3d transition metals (Fe, Co, Ni):

The primary property of a ferromagnet such as Fe, Co, or Ni is the appearance of a spontaneous magnetization $\vec{M}$ below the Curie temperature T_c ($k_B T_c \approx 0.1$ eV/atom). The mechanism responsible for the appearance of ferromagnetism emerges from the *Pauli Principle* which prevents two electrons of parallel spins to occupy the same orbital state. Accordingly, the effective Coulomb repulsion for a pair of electrons with parallel spins is weaker than for anti-parallel spins.

In $3d$ transition metals (Fe, Co, Ni) the current is essentially carried by the s-electrons (high mobility) while the magnetism moment is carried by the delocalized d-electrons (low mobilities). Accordingly, for these materials the exchange interaction J_{exc} is given by the energy shift between the $3d_{\uparrow}$-band and the $d_{\downarrow}$-band with $J_{exc}^{3d} \approx 1$ eV (Figure 3.6). In these compounds, the total magnetization $\vec{J} = \vec{S} + \vec{L}$ origins at 90% from the spin magnetization $\vec{S}$ (quantum origin) and only at 10% from the orbital moment magnetization $\vec{L}$ (classical orbit). For such compounds the spin magnetization is given by:

$$|\vec{S}| \equiv m \equiv \left(n_{\uparrow}^{3d} - n_{\downarrow}^{3d}\right) \cdot \mu_B \tag{3.7}$$

where $n_{\uparrow}^{3d}$ and $n_{\downarrow}^{3d}$ are the carrier densities in the $3d_{\uparrow}$ and $3d_{\downarrow}$ bands respectively. For example in the case of Fe where $J = 2.22\ \mu_B.at^{-1}$, the spin contribution to the total magnetization is of $S = 2.10\ \mu_B.at^{-1}$ while the orbital contribution is only $L = 0.12\ \mu_B.at^{-1}$.

In magnetic materials, the exchange interaction creates the spin moments and the ligand field generates anisotropic d-orbitals: $3d_{x^2-y^2}$, $3d_{3z^2-r^2}$, $3d_{yz}$, $3d_{xz}$, $3d_{xy}$ (introduced from lowest to highest energy). The Spin-Orbit coupling forms the link between the spin system and the orbital system by creating an orbital moment locked into a particular lattice direction [318]. In $3d$ metals the role of the crystal field is played by the band dispersion W of the levels (5 hybrids d-bands). Its energy ($\Delta E = \frac{W}{n} \approx 1$ eV) is much larger than the SO coupling contribution to the magnetic anisotropy ($\lambda_{SO}^{3d} \approx 50 - 100$ meV) which can be neglected in first approximation. Because of the crystal field, the energy levels no longer correspond to a definite quantum number m_l but rather to hybrids of opposite orbital moments m_l and $-m_l$ in a manner that the net orbital moment of these levels is zero ($\langle L_z \rangle$ quenched at 0). Thus, in absence of Spin-Orbit coupling, the total magnetic moment of $3d$-atoms would purely originate from a spin moment with a gyromagnetic factor $g = \frac{2s_z+l_z}{s_z+l_z} = 2$. In the $3d$ metals, the Spin-Orbit coupling partially remove the quenching of the orbital moment.

As in $3d$ transitions metals the SO coupling λ_{SO} is much smaller than the crystal field splitting (d-Band width) W (≈ 5 eV), a simple model can be developed for the magnetic anisotropy by treating the contribution arising from the Spin-Orbit coupling through the perturbation theory [316]. This perturbation approach is interesting as it provides a simple explanation of the order of magnitude of the magnetic anisotropy without having to explicitly calculate the total system energy as a function of the magnetization direction [316]. As the magnetism of $3d$ metals originates from d-electrons, it is sufficient to consider only the Spin-Orbit interactions for d electrons [315]:

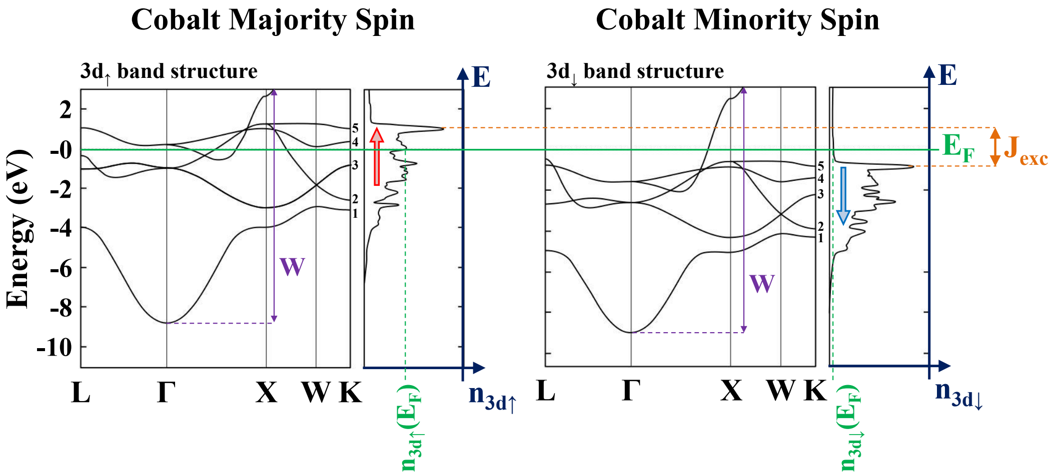

Figure 3.6: Band structure and density of states for the majority (left) and the minority (right) carriers of Cobalt: The band diagrams display the 5 hybrids 3d-bands between the important symmetry points of the Brillouin zone. On the band structure, W represents the band width which plays the role of crystal field in $3d$ metals. On the Density Of States diagram, the shift in energy between the majority and minority spin DOS represents the exchange energy $J_{exc} \approx 1$ eV. The intrinsic magnetism of the material originates from the higher DOS of majority spin compared to minority spin at the Fermi level: $n_{3d\uparrow}(E_F) > n_{3d\downarrow}(E_F)$.

$$H_{SO} = \lambda_{SO}^{3d}\left(\vec{L}\cdot\vec{S}\right) \tag{3.8}$$

where λ_{SO}^{3d} is the Spin-Orbit constant averaged over the d-orbitals. For hcp crystals and ultra-thin films a 2^{nd}-order perturbation calculation is sufficient while for cubic crystals the magnetic anisotropy only appears for a 4^{th}-order perturbation calculation. The change in Spin-Orbit energy at the 2^{nd}-order $\delta H_{SO}^{(2)}$ is calculated for an electron $(\vec{k})$ raised from an occupied state E_{grd} (ground state) into an empty state E_{exc} (excited state) above the Fermi level and without Spin-Flip. From 2^{nd}-order perturbation theory and for a spin direction in the crystal, one can show that the anisotropy K_1^s in a uni-axial system (ultra-thin film) can be approximate by [316]:

$$K_1^s = \left\langle \delta H_{SO}^{(2)} \right\rangle \cong \frac{\lambda_{SO}^2}{W} \tag{3.9}$$

For $3d$ transition metals, this gives $K_1^s = \frac{(75meV)^2}{5eV} = 1$ meV/atom. In the same way, one can estimate the anisotropy of cubic crystals K_1^v from 4^{th}-order perturbation theory [316]:

$$K_1^v = \left\langle \delta H_{SO}^{(4)} \right\rangle \cong \frac{\lambda_{SO}^4}{W^3} \tag{3.10}$$

For $3d$ transition metals, this gives $K_1^v = \frac{(75meV)^4}{(5eV)^3} = 0.3\ \mu\text{eV/atom}$. These rough numerical estimations are of the order of magnitude of the anisotropy found in ultrathin-films and bulk cubic ferromagnets respectively.

It follows from these approached calculations that the cubic anisotropy (bulk) is negligible compared to the surface anisotropy: $K_1^s \gg K_1^v$. Consequently, when a thin-film converges toward a perfect uni-axial system, the contribution of surface atoms anisotropy (Out-of-Plane) becomes preponderant compare to the bulk atoms anisotropy (In-Plane) leading to a change of preferential orientation of the film magnetization. This explains why Perpendicular Magnetic Anisotropy appears in ultra-thin ferromagnetic layers when the dimension of the films are reduced below a limit thickness $t_\perp$.

Beyond the phenomenological approach, many experimental factors such as the roughness, the formation of interface alloys, or the ultrathin-layers patchiness may cause a reduction of the PMA. Hereafter we discuss the experimental development and optimization of an ultra-thin MgO/CoFeB/Ta ferromagnetic spin-injector on GaAs LED. The main goal is to magnetically stabilize the ultra-thin film and reach PMA at magnetic remanence.

3.3.2 Sample preparation and structural characterization

In our experiments, the p-i-n semiconductor structure of the Spin-LED was grown by Molecular Beam Epitaxy (MBE), while the tunnel barrier/ferromagnet contacts were deposited by sputtering. The p-i-n LED device has the following structure sequence: $p - GaAs : Zn$ (001) $substrate$ ($p = 2 \times 10^{19}\ cm^{-3}$) // 500 $nm\ p - GaAs : Be$ ($p = 2 \times 10^{19}\ cm^{-3}$) / 100 $nm\ p - Al_{0.3}Ga_{0.7}As : Be$ ($p = 2 \times 10^{19}\ cm^{-3}$) / 100 $nm\ p - Al_{0.3}Ga_{0.7}As : Be$ ($p = 2 \times 10^{18}\ cm^{-3}$) / 50 $nm\ undoped\ Al_{0.3}Ga_{0.7}As$ / [15 $nm\ undoped{-}GaAs$ / 8 $nm\ undoped{-}In_{0.1}Ga_{0.9}As$]×3 / 15 $nm\ undoped{-}GaAs$ / 5 $nm\ undoped{-}Al_{0.3}Ga_{0.7}As$ / 30 $nm\ undoped{-}GaAs$ / 50 $nm\ n{-}GaAs : Si$ ($n = 1 \times 10^{16}\ cm^{-3}$). The LED surface was passivated with arsenic in the III-V MBE chamber. The intended design of 3×QW for the LED is to obtain stronger electro-luminescence intensity especially at room temperature. Another important reason is that the surface roughness of 3×QW-LED is found to be much better than the single QW-LED, which is also a critical factor to obtain a continuous ultra-thin CoFeB layer. The sample was then transferred through the air into a magnetron sputtering-MBE interconnected system to grow the MgO/CoFeB spin-injector. The arsenic capping layer was firstly desorbed at 300°C by monitoring in-situ Reflection High Energy Electron Diffraction (RHEED) patterns in the MBE chamber, and then the sample was transferred to the sputtering chamber to

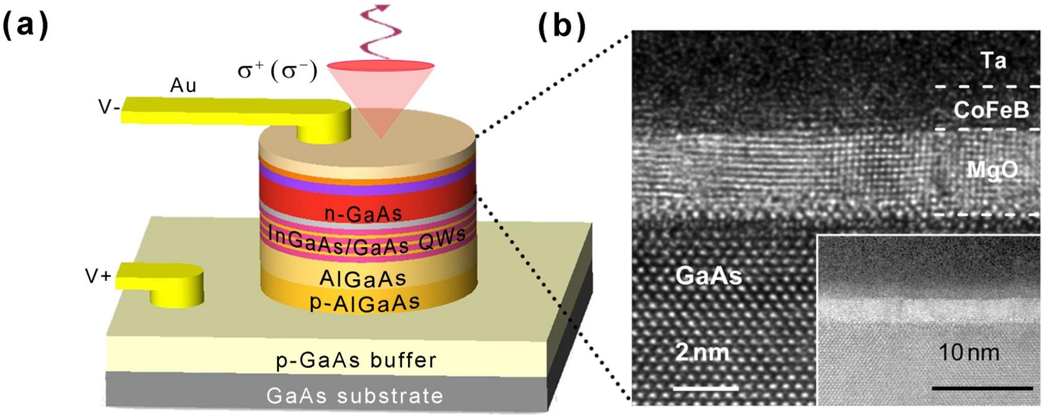

Figure 3.7: **(a)** Schematic representation of the 3 InGaAs/GaAs QW Spin-LED. **(b)** HR-TEM image of the MgO/CoFeB spin-injector with PMA deposited on top of the LED structure. Inset: low magnification image showing an excellent homogeneity and a low roughness of structures. Figure reprinted from [312].

grow the spin-injector. The spin-injector grown at room temperature consists in a 2.5 nm MgO tunnel barrier and a thin $Co_{40}Fe_{40}B_{20}$ ferromagnetic layer (1.1-1.7 nm). Finally, 5 nm Ta was deposited to prevent oxidation. 300 μm diameter circular mesas were then processed using standard UV photolithography and etching techniques. In the end, the processed wafers were cut into small pieces to perform Rapid Temperature Annealing (RTA) at different temperatures for 3 minutes. The RTA procedure is a good way to promote PMA of CoFeB [297] while almost keeping no change to the LED optical characteristics. High-Resolution Transmission Electron Microscopy (HR-TEM) and Scanning Transmission Electron Microscopy (HR-STEM) study were performed by using a JEOL ARM200 cold FEG gun working at 200 kV.

The whole structure of the sample is schematically shown in Figure 3.7(a). The interface of the spin-injector consisting of a 1.2 nm CoFeB layer was annealed at 300°C and then investigated by HR-TEM and HR-STEM. The low magnification HR-TEM image (inset of Figure 3.7(b)) reveals a good homogeneity and a very low roughness of MgO on GaAs. As shown in the HR-STEM images (Figures 3.8(a) and 3.8(b)), the phase distribution at the interface can be directly deduced from the image contrast. From the BF image (Figure 3.8(b)), we can also identify a continuous unltrathin layer of CoFeB but with a rough CoFeB/Ta interface, indicating an intermixing or diffusion of Ta in the CoFeB layer after annealing. The mean thickness of the CoFeB layer was estimated to be 1.2±0.3 nm. Moreover, the red arrow on the Low-Angle Annular Dark-Field (LAADF) image (Figure 3.8(a)) points out the beginning of the crystallization of the CoFeB phase starting from the MgO/CoFeB interface.

3.3.3 Magnetic properties of the spin-injector

To obtain an ultrathin CoFeB layer with PMA on GaAs, we optimized the CoFeB thickness and the annealing temperature (T_a) by SQUID magnetometry measurements. Figure 3.9(a) displays the out-of-plane magnetization vs. external magnetic field (M-H) curves for annealed spin-injectors (T$_a$=250°C) with different CoFeB thicknesses. The saturation field is found to rapidly decrease when reducing the CoFeB thickness. When the thickness is lower than 1.2 nm, CoFeB possesses a remanent out-of-plane magnetization signifying the occurrence of PMA. This behavior can be easily understood from the competition between the bulk in-plane shape anisotropy (K_b) and the interface anisotropy (K_i) scaling with a resulting $\frac{1}{t}$ volume anisotropy. A 0.5 nm thick magnetic dead layer of CoFeB (t_d) is revealed by the analysis of saturation magnetization (M_s) vs. CoFeB thickness and the loss of M_s at smaller thickness (Figure 3.9(b)). This observation is in good agreement with other reported results [297]. This dead layer could be attributed to the intermixing at the top CoFeB/Ta interface during deposition or upon annealing, which is also evidenced from the diffusive interface on the TEM images [319]. The PMA energy density per unit volume (K_{eff}) varies with the effective CoFeB thickness ($t_{eff} = t_{CoFeB} - t_d$) (Figure 3.9(c)). t_{eff} can be obtained from the integrated difference between the out-of-plane and in-plane M-H curves. When $K_{eff} > 0$, the CoFeB is characterized by a perpendicular easy-axis of magnetization. The interface anisotropy K_i can be obtained from the intercept of $K_{eff} \times t_{eff}$ vs. t_{eff} linear fitting. The value found from our results is about 0.63 $mJ.m^{-2}$, which is slightly lower than the value of 1.3 $mJ.m^{-2}$ given by Ikeda *et al.* for metallic MTJ [220].

A precise control over the annealing temperature is also an important factor to obtain a good PMA property. Figure 3.9(d) compares the M-H curves for different T_a in 1.2 nm MgO/CoFeB, with corresponding K_{eff} vs. T_a plotted in Figure 3.9(e). The optimized annealing temperature is found to be around 250°C. Below or above this temperature, the PMA is much reduced and the magnetization rotates back along the in-plane direction. As already investigated theoretically by Yang *et al.*, the PMA is very sensitive to the chemical structure of the MgO/Fe(Co) interface [304]. The improvement of PMA at T_a up to 250°C could be attributed to an optimization of the chemical structure at the MgO/CoFeB interface [302]. When T_a exceeds 250°C, Ta species start to diffuse through the ultra-thin CoFeB layer towards the MgO/CoFeB interface and significantly damage PMA [303]. As our best Electro-Luminescence (EL) results are obtained at low temperature, Figure 3.9(f) shows the in-plane and out-of-plane M-H curves at 30 K for the perpendicular injector with optimized conditions for t_{CoFeB}=1.2 nm and T$_a$=250°C. We can observe a clear perpendicular easy axis with out-of-plane coercivity $\mu_0 H_c$=20 mT and in-plane saturation field $\mu_0 H_k$=150 mT. The effective perpendicular anisotropy energy density K_{eff} is then determined to be 4.6×10^4 $J.m^{-3}$.

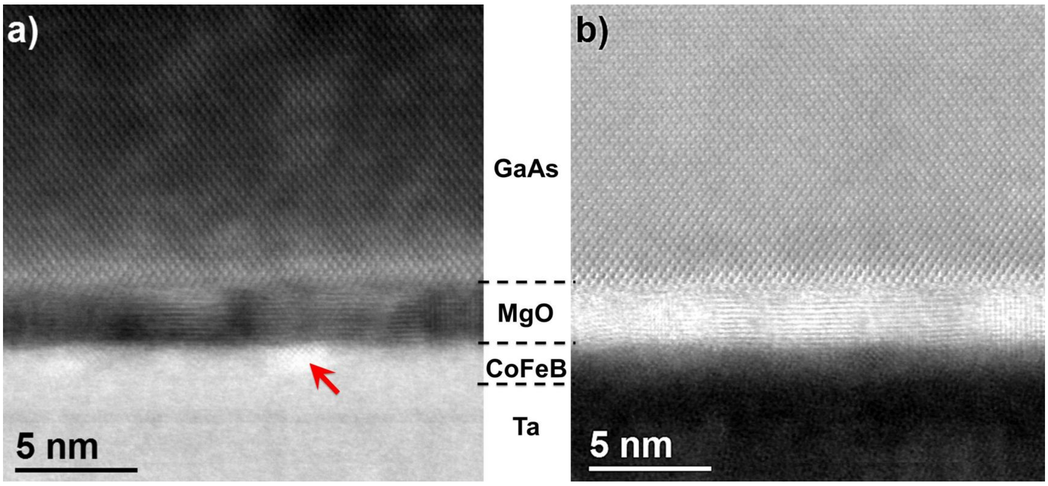

Figure 3.8: HR-STEM images of the MgO/CoFeB/Ta spin-injector on the GaAs Spin-LED: (a) LAADF image and **(b)** BF image. On the LAADF image, the red arrow points out the beginning of the CoFeB crystallization starting from the MgO/CoFeB interface. Figure reprinted from [312].

3.3.4 Perpendicular Magnetic Anisotropy of MgO/CoFeB bi-layer

In order to have a detailed understanding of the origin of perpendicular magnetic anisotropy (PMA), we performed ab initio calculations using Vienna ab initio simulation package (VASP) [320, 321, 322] with the generalized gradient approximation [323] and projector augmented wave potentials [324, 325]. The calculated system is composed of five Fe layers sandwiched between three MgO layers at both sides as shown in Figure 3.14(a) (middle). A 19×19×3K-point mesh was used in our calculations. Calculations were performed in three steps. First, we performed a full structural relaxation in shape and volume until the forces become lower than 0.001 eV^{-1} in order to determine the most stable interfacial geometries. Next, we solved the Kohn-Sham equations, without taking into account the spin-orbit coupling (SO), in order to determine the charge distribution of the system ground state. Finally, we calculated the density of states (DOS), the orbital moment anisotropy ($\Delta\mu$) and the magnetic anisotropy energy (MA) using the corresponding orbital moment and energy of the system for out-of-plane and in-plane magnetization orientation with SO included.

We can explain the origin of PMA in our system in the following pedagogical way. In bulk Fe with bcc structure, the charge distribution in the 3d shell and the resulting average orbital moment are almost isotropic. The orbital moment acquired in the plane of the layer exactly compensates the orbital moment acquired along the out-of-plane direction by equal filling of the corresponding orbitals. This produces zero orbital moment anisotropy ($\Delta\mu$) as shown in Figure 3.14(a) (left) for the bulk Fe3 atom. In contrast to bulk Fe film, the MgO/Fe interface exhibits a strong uni-axial character. The out-of-plane Fe $3d_{z2}$ orbital strongly bonds to the O 2pz orbital and it introduces a significant charge transfer from Fe to O orbitals due to the strong electronegativity of O (Left inset of Figure 3.14(a)). This results in a lack of electrons within the Fe $3d_{z2}$, $3d_{xz}$ and $3d_{yz}$ out-of-plane orbitals compared to the Fe in-plane orbitals ($3d_{x2-y2}$ and $3d_{xy}$). As a consequence, an enhanced out-of-plane orbital moment appears from the uncompensated in-plane orbiting electrons and generates a sizable PMA once the spin-orbit coupling (SO) is introduced. To better understand this simple explanation of PMA origin, we show in Figure 3.14(a) (right) the DOS with spin-orbit coupling of averaged Fe $3d$ out-of-plane ($d_{z2} + d_{xz} + d_{yz}$) and in-plane orbitals ($d_{x2-y2} + d_{xy}$) both at the interface and in the bulk (spin up and down are mixed due to SO). From the integration of the occupied states below Fermi level (E_F), we found a difference of about 3% between respective out-of-plane and in-plane orbitals for Fe atoms bounded to O atoms at the interface (Fe5), while almost no difference appears for Fe in the bulk (Fe3). This gives an unbalanced orbital moment anisotropy ($\Delta\mu \approx 0.0025\mu_b$) associated with the magnetization or spins in the out-of-plane direction for the interfacial atom Fe5 (and Fe1). According to Bruno's model [316], the anisotropy energy (ΔE_{SO}) can be obtained by $\Delta E_{SO} = \lambda_{SO}\frac{\Delta\mu}{4\mu_b}$ considering that the spin moment remains unaffected at the interface, where λ_{SO} is the spin-orbit coupling parameter. The interface anisotropy K_i can then be qualitatively estimated from ΔE_{SO} in the range of 1 mJ.m^{-2}, which is in good agreement with the quantitatively calculated magnetic anisotropy (MA) energy (Figure 3.14(a) (left)).

As we discussed above, the PMA originates from a net uncompensated out-of-plane orbital moment at the MgO/Fe(Co) interface. Such sizable anisotropy of orbital moment is expected to be very sensitive to the interface atomic configuration, bonding and to the chemical ordering. To further check our explanation, we have calculated the DOS, $\Delta\mu$ and MA for over-oxidized (with O atoms inserted at the interfacial magnetic layer) and under-oxidized (Mg-terminated) interfaces as shown in Figure 3.14(b) and 3.14(c), respectively. The details of calculation are available in our previously published work [304]. The calculated averaged DOS represents Fe $3d$ out-of-plane ($d_{z2} + d_{xz} + d_{yz}$) and in-plane orbitals ($d_{x2-y2} + d_{xy}$) for interfacial (Fe5) and bulk iron (Fe3) atoms. One can see that for all cases, the almost equal in-plane and out-of-plane orbital occupation in bulk Fe results in rather small orbital moment anisotropy and magnetic anisotropy energy. However, the situation is quite different at the interface. We have found: (i) a difference of about 3% with higher in-plane orbital occupation for pure Fe interface, a difference of -5% with higher out-of-plane orbital occupation for over-oxidized interface due to a double O-bonding in the plane and (iii) only a difference of 0.5% with higher in-plane orbital occupation for under-oxidized interface. As the PMA originates from the orbital moment anisotropy [316] which is related to the orbital occupation, this results in a strong PMA at the pure Fe interface, a complete loss of PMA for over-oxidized interface, and a much reduced PMA at the under-oxidized interface. This picture is in qualitative agreement with the calculated MA values (total energy difference between in-plane and out-of-plane magnetizations) as shown in Figure 3.14 (left panel).

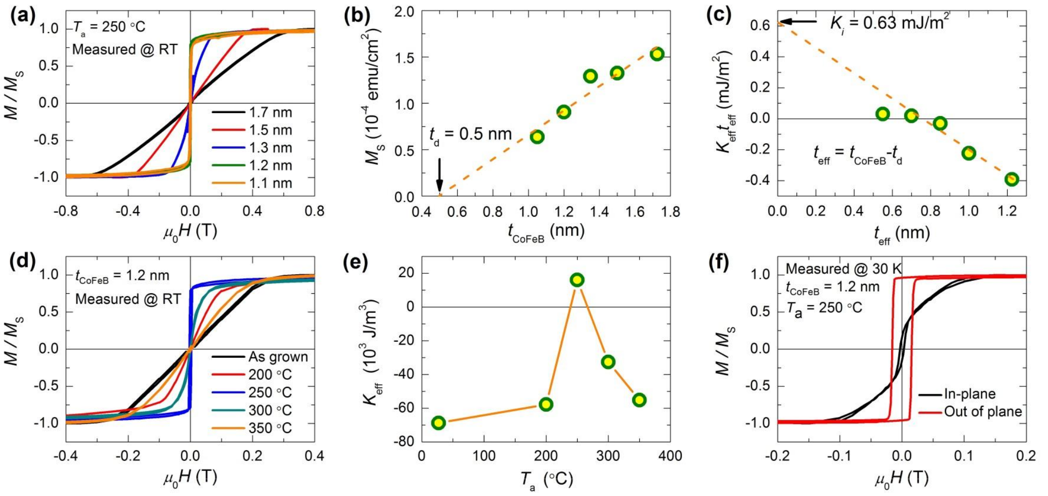

Figure 3.9: **(a)** RT out-of-plane M-H curves of spin-injectors with different CoFeB thicknesses annealed at T_a=250°C. **(b)** Extrapolation of the CoFeB magnetic dead layer t_d from the CoFeB saturation magnetization M_s variations as a function of the CoFeB layer thickness. **(c)** t_{eff} dependence of the $K_{eff} \times t_{eff}$-product. The intersection of the linear extrapolation with the vertical axis gives the value of K_i. **(d)** RT out-of-plane M-H curves before and after annealing of spin-injectors with a 1.2 nm CoFeB layer for different annealing temperature. **(e)** K_{eff} as a function of the annealing temperature. (f) In-plane and out-of-plane M-H curves at 30 K of the spin-injector with a 1.2 nm CoFeB layer annealed at T_a=250°C. Figure reprinted from [312].

Our simple model can explain qualitatively the obtained results. Concerning the over-oxidized MgO/Fe interface, since the bonding mechanism with O species occurs now along both out-of-plane and in-plane directions, the stronger bonding along in-plane direction results in a higher out-of-plane orbital occupation. This completely changes the interface anisotropy and promotes an in-plane magnetization orientation at the interface. On the other hand, for the under-oxidized interface, a lack of bonding with O species makes an almost equivalent orbital occupation for in-plane and out-of-plane orbitals, which also reduces the PMA. Therefore, our simple model from analysis of the anisotropy of orbital charge occupation and the orbital moment anisotropy can well explain the origin of PMA, and can give a very simple and direct image to understand the PMA nature.

3.3.5 Measurements and characterization

Magnetic field dependance:

In the following, we focus on EL measurements of an optimized sample. The polarization-resolved EL measurements have been performed using the same setup than for the previous comparative study on MgO barriers. A typical EL spectrum

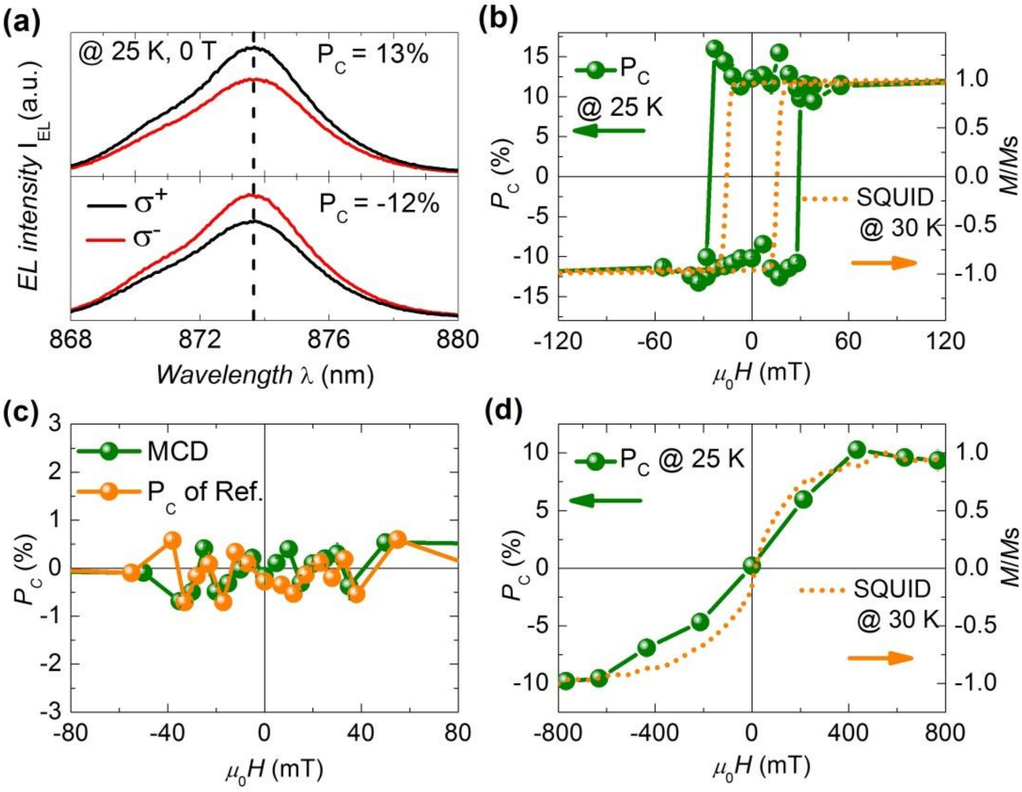

Figure 3.10: **(a)** EL spectra of the σ^+ and σ^- polarizations at 25 K and B=0 T for the sample with optimized PMA conditions when the applied magnetic field is swept from positive to negative values (top) and from negative to positive values (bottom) in the hysteresis loop. **(b,d)** Comparison between the variations of DoCP (noted as P_c) as a function of the applied out-of-plane magnetic field measured at 25K (V_{bias}=2.30 V) for the Spin-LED with a 1.2 nm MgO/CoFeB injector and the corresponding out-of-plane M-H hysteresis loop SQUID measurements at 30 K. **(b)** and **(d)** plots illustrate the cases of an optimized PMA injector and an as-grown injector respectively. **(c)** MCD induced by the ultra-thin CoFeB electrode as a function of the applied magnetic field at 25 K. Measurements were performed by detecting the DoCP of the emitted luminescence (green circles) under linearly polarized excitation of the spin-LED by a He-Ne laser. The orange circles represent the EL's DoCP for a reference sample without CoFeB layer (replaced by a non-magnetic Ta layer) as a function of magnetic field at 25 K. Figure reprinted from [312].

acquired at 25 K under a bias of 2.30 V is shown in the top of Figure 3.10(a) for $\mu_0 H$=0 T. In this spectrum, we can observe a main peak located at about 873 nm corresponding to the heavy exciton line, with a small shoulder at about 870 nm. The multi-peak feature could be attributed to a slight different In concentration between each of the three InGaAs QWs as well as the possible bound exciton at low temperature. One cannot totally exclude a contribution of bound exciton at 25K (it can be ruled out at higher temperature). However, this contribution would only results in

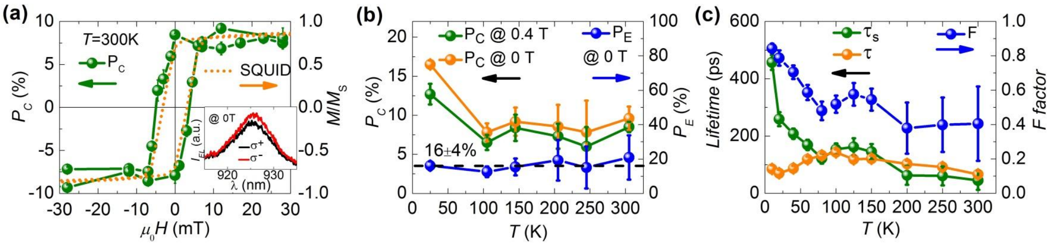

Figure 3.11: **(a)** Comparison between the DoCP variations emitted by a Spin-LED with an optimized PMA injector (noted as P_c) as a function of out-of-plane magnetic field measured at 300 K (V_{bias}=2.30 V) and the out-of-plane M-H hysteresis loop SQUID measurements at 300 K. Inset: EL spectra at 300 K and B=0 T for σ^+ and σ^- polarizations. **(b)** Temperature dependence of the DoCP at 0 T and 0.4 T magnetic field. The temperature dependence of carrier's spin-polarization P_s (noted as P_e) is calculated using the relation $P_s = \frac{P_c}{F}$ from the data at B=0 T. **(c)** Temperature dependence of spin lifetime (τ_s), carrier lifetime (τ) and F-factor extracted from TRPL measurements. Figure reprinted from [312].

an artificial diminution of the EL circular polarization compared to the one of the free exciton line [195, 326]. The striking feature is that we can get a large difference of the EL intensities for right ($I(\sigma^+)$) and left ($I(\sigma^-)$) circularly-polarized components at zero field. The EL DoCP can be determined from the intensity difference of the main peaks for $I(\sigma^+)$ and $I(\sigma^-)$ and is measured to be about 13%. To further confirm that this feature originates from the perpendicular spin-injector, we have measured the variations of DoCP at different magnetic field. As shown in Figure 3.10(b), DoCP exhibits a clear hysteresis loop with almost constant value around 13% at saturation and changing its sign rapidly at $\mu_0 H$=±30 mT. The bottom of Figure 3.10(a) displays the spectrum at $\mu_0 H$=0 T when the field is swept from negative to positive direction. The hysteresis loop of DoCP fairly matches the SQUID hysteresis loop acquired at 30K on an unpatterned sample (Figure 3.10(b)). The difference in the coercivity could be attributed to a slight difference of temperature calibration in the two systems or a small difference of the effective RTA temperature for the two measured samples.

We then performed two complementary measurements to exclude any potential artificial contributions to the measured circular polarization at remanence (zero magnetic field). One is the evaluation of Magnetic Circular Dichroism (MCD) in order to check the differential absorption of respective σ^+- and σ^--polarized light through the ferromagnetic CoFeB layer [306]. With linearly polarized excitation light, we have recorded the MCD signal by Photo-Luminescence (PL) with different magnetic fields. As shown in Figure 3.10(c), the MCD effect from the PMA Spin-LED sample is lower than 1% in all investigated field range. This directly means that the large DoCP is really due to the circularly polarized light emitted from the radiative recombination of the spin-polarized electron with unpolarized holes in the QW. The other measurement is to exclude artificial effects such as Zeeman splitting in the QW [91]. We performed EL characterization of a reference sample without CoFeB layer, which can allow us to verify the origin of this spin-polarized injection of electrons. The reference sample has almost the same structure except that the ultra-thin CoFeB layer is now replaced by a non-magnetic Ta layer in contact with MgO. As shown in Figure 3.10(c), DoCP from the reference sample also shows less than 1% in all investigated field range. This gives a strong argument that the large DoCP we have observed is really due to the spin-polarized electron injected from the ultra-thin CoFeB layer with PMA.

What is then the signature of the polarization-resolved EL for an in-plane magnetization injector such as the as-grown MgO/CoFeB injector? In Figure 3.10(d), we show DoCP vs. field for the same Spin-LED before annealing. As expected, DoCP increases linearly with the field before reaching its saturation value (10%) at about 0.4 T. The variation of DoCP vs. field matches relatively well the corresponding variation of the out-of-plane magnetization. Indeed, in this configuration, DoCP tracks the continuous rotation of magnetization direction from in-plane to out-of-plane, as expected from the optical selection rules in the QW [168].

Temperature dependance:

Another very interesting behavior is that the PMA property of our spin-injector can even persist up to room temperature. The inset of Figure 3.11(a) shows the EL spectra with different circular polarizations at 300 K under zero field. A clear difference of $I(\sigma^+)$ and $I(\sigma^-)$ components allows us to obtain DoCP=8% at RT. The DoCP hysteresis loop is also in good agreement with the RT M-H hysteresis loop (Figure 3.11(a)). Although the out-of-plane coercivity $\mu_0 H_c$ is reduced at about 5 mT, it is sufficient to obtain an almost full remanent magnetization. To further investigate the temperature dependence of the spin-injection efficiency with PMA injectors, we plotted in Figure 3.11(b) the temperature dependence of the DoCP without field and with 0.4 T field which is sufficiently large to insure an out-of-plane magnetization. We observed a non-monotonic variation of the DoCP as a function of T: first a decrease of DoCP, followed by a low varying regime above 100 K. A remarkable feature is the very similar evolution for DoCP at both $\mu_0 H$=0 T and $\mu_0 H$=0.4 T. This behavior confirms that the PMA is strong enough to persist up to room temperature.

The non-monotonic evolution of the DoCP likely reflects physical effects inherent to the semiconductor heterostructures rather than to the property of MgO/CoFeB injector itself. In order to check this assumption, we have performed TRPL measurements on an identical p-i-n LED to extract the spin relaxation time τ_s, as well as the carrier lifetime τ in the structure.

The TRPL measurements were performed using the same mode-locked Ti:Sa laser (1.5 ps pulse width) for the non-resonant circularly-polarized excitation at 1.599 eV (i.e. in the GaAs barrier) on a bare p-i-n LED sample without injector. The PL

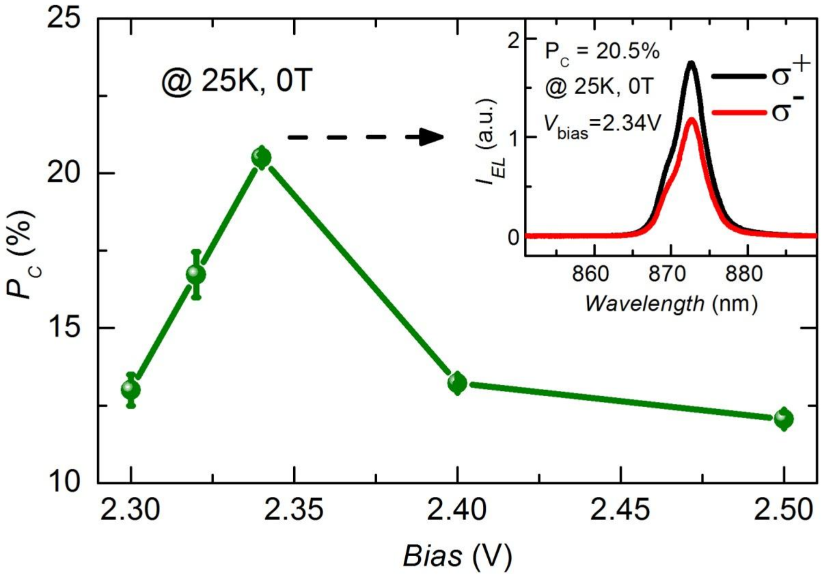

Figure 3.12: DoCP variations as a function of the applied bias for the device with an optimized PMA spin-injector. Inset: EL spectra at 25 K and B=0 T for σ^+- and σ^-- polarizations under an apllied bias of 2.34 V. Figure reprinted from [312].

signals were still detected by a 2D synchroscan streak camera providing an overall temporal resolution of less than 8 ps and a spectral resolution of about 8 meV (5.2 nm) (Schematic Setup in Appendix E, Figure E.1). Figure 3.13(a) shows a typical PL spectra after integration in time domain. Here we cannot distinguish the multi-peak feature as we have observed in EL spectra because the spectral resolution is less good for our PL set-up. With a 50% circularly polarized excitation, we can get a DoCP≈33% for the PL. The electrically injected electrons' spin polarization P_s is almost constant around the maximum of the PL spectra. Then we record the time-resolved information through integrating spectrally around the peak maximum with a window of 4-6 nm depending on the spectral width. In fact, the dynamic parameters (τ and τ_s) do not sensitive to the width of this window. Figure 3.13(b) (left) shows the PL intensity (color code in arbitrary units) as a function of both time and photon wavelength. The white curve represents the PL intensity ($I\left(\sigma^+\right)+I\left(\sigma^-\right)$) as a function of time when the emission is spectrally integrated. The decay time of this PL intensity corresponds to the carrier lifetime τ. As an example shown in Figure 3.13(c), we perform the exponential fitting of the PL dynamic curve to obtain τ to be about 80±15 ps. To extract the spin lifetime τ_s, we have studied time-resolved PL circular polarization DoCP dynamics. Figure 3.13(b) (right) shows DoCP (color code from DoCP=0 to 0.44) as a function of both time and photon wavelength. The white curve represents the DoCP as a function of time. The decay time of this DoCP dynamics which corresponds to the spin relaxation time τ_s can be extracted by exponential fitting of the curve. As an example shown in Figure 3.13(d), the τ_s can be determined to be about 460±30 ps.

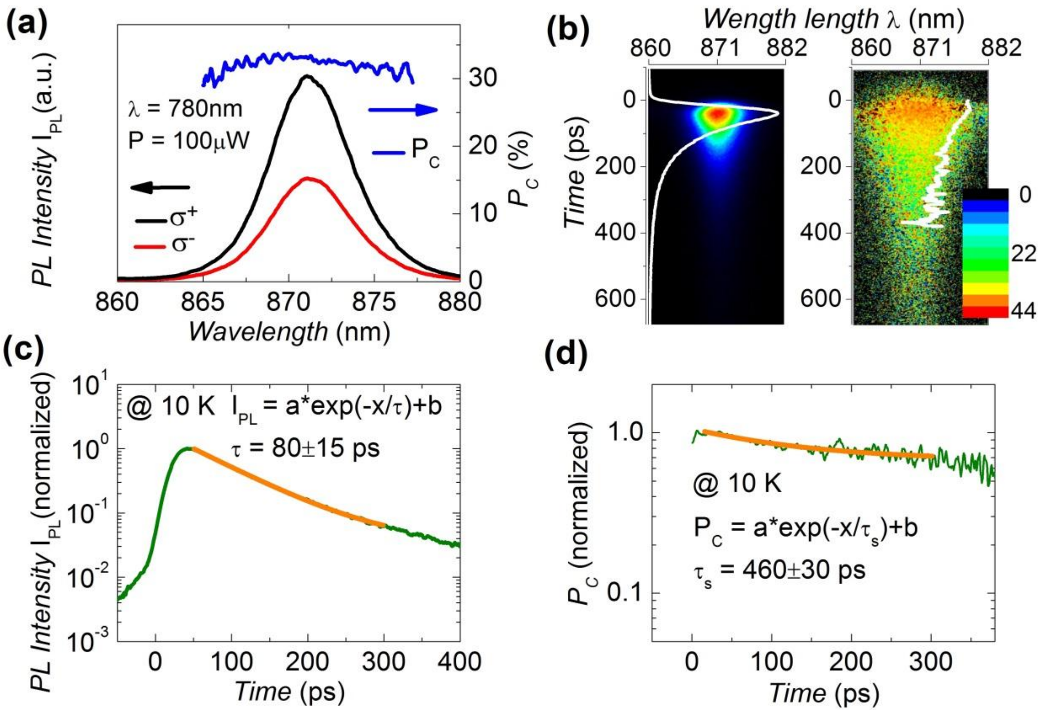

Figure 3.13: **(a)** Typical PL spectra after integration in time domain of the σ^+ and σ^- components. The DoCP (noted as P_c) is deduced from $(I(\sigma^+) - I(\sigma^-))/(I(\sigma^+) + I(\sigma^-))$. **(b)** Left: PL intensity (color code in arbitrary units) as a function of both time and photon wavelength. The white curve represents the PL intensity as a function of time when the emission is spectrally integrated. Right: PL's DoCP (color code from P_c=0 to P_c=0.44) as a function of both time and photon wavelength. The white curve represents the DoCP as a function of time when the emission is spectrally integrated. (c) Determination of the carrier lifetime τ from exponential fitting of the decay time of PL intensity $(I(\sigma^+) + I(\sigma^-))$ dynamics curve. (d) Determination of the spin lifetime τ_s s from exponential fitting of the decay time of P_c dynamics curve. Figure reprinted from [312].

The spin relaxation time τ_s, as well as the carrier lifetime τ, extracted from the TRPL measurements, are presented in Figure 3.11(c). A relatively weak variation of the carrier lifetime τ (of the order of 100 ps) vs. T can be highlighted, whereas a strong thermal variation of the spin lifetime τ_s is evidenced with an initially fast fall-off followed by a smoother decline. The large increase of spin lifetime at low temperature could be attributed to the spatial localization of excitons due to the inhomogeneity of the QW. When the temperature increases, the spin relaxation is then dominated by Dyakonov-Perel (DP) mechanism which gives a small variation of τ_s up to RT. We also plotted in Figure 3.11(c) the temperature dependence of the renormalization factor $F = \frac{1}{1+\frac{\tau}{\tau_s}}$ that links DoCP to the true electrically injected electron spin polarization P_s, according to $DoCP(T) = P_s(T) \times F$. The F factor vs. T behavior mimics the variation of DoCP vs. T, which results in an overall small variation of P_s vs. T. P_s is found to be almost temperature insensitive at about 16±4% (Figure 3.11(b)). This also confirms a thermal stability of our PMA spin-injector with high Curie temperature ferromagnetic layer.

Bias dependance:

Finally, we have measured DoCP as a function of the applied bias at 25 K under zero field. As shown in Figure 3.12, the DoCP is found to be strongly dependent on the bias. Our maximum DoCP at remanence can even reach 20% at the optimal bias of 2.34 V. The corresponding polarization-resolved EL spectra are shown in the inset of Figure 3.12. DoCP decreases below and above this optimized bias. The origin of this behavior is still not completely understood at this step and will require further experiments. One possibility to explain the decrease of DoCP at low bias would be the complex behavior of the ratio $\frac{\tau}{\tau_s}$ as a function of the applied voltage (linked in particular to an increase of the carrier recombination time τ) [204, 209]. The decrease of the DoCP at high bias could also be due to the dependence of $\frac{\tau}{\tau_s}$ as a function of V_{bias}, as well as to the DoCP spin-relaxation mechanism for carriers injected with a large kinetic energy [99]. The best remanent DoCP we obtained is already five times higher than the published results using any other PMA injectors [209, 305, 306, 307, 24, 308]. Although the electrical spin-injection efficiency P_s is still lower than the one obtained for the best in-plane injector [99], which could be linked to some particular effect rising from the ultra-thin CoFeB layer during annealing, we believe that detailed interfacial investigation and optimization of annealing effect could certainly lead to even larger improvement.

Figure 3.14: **(a) Left:** layer-resolved orbital moment anisotropy ($\Delta\mu$) along with the magnetic anisotropy (MA) energy. **Center:** schematics of the calculated crystalline structures. The Fe, Mg, and O atoms are represented by blue, green, and red spheres, respectively. **Right:** DOS with spin-orbit coupling for the averaged Fe3d out-of-plane ($d_{z2} + d_{xz} + d_{yz}$) and in-plane orbitals ($d_{x2-y2} + d_{xy}$) with Fe both at the interface (Fe5) and in the bulk (Fe3). Inset: simple picture showing that the origin of the PMA comes from the hybridization of Fe out-of-plane orbitals ($3d_{z2}$, $3d_{xz}$ and $3d_{yz}$) and O $2pz$ orbitals. This leads to an uncompensated charge occupation in Fe in-plane orbitals ($3d_{x2-y2}$ and $3d_{xy}$) and results in an enhanced out-of-plane orbital moment for the PMA. **(b)** and **(c)** exhibit the same analyze for two other different interface structures with over-oxidized and under-oxidized geometries respectively. Figure reprinted from [312].

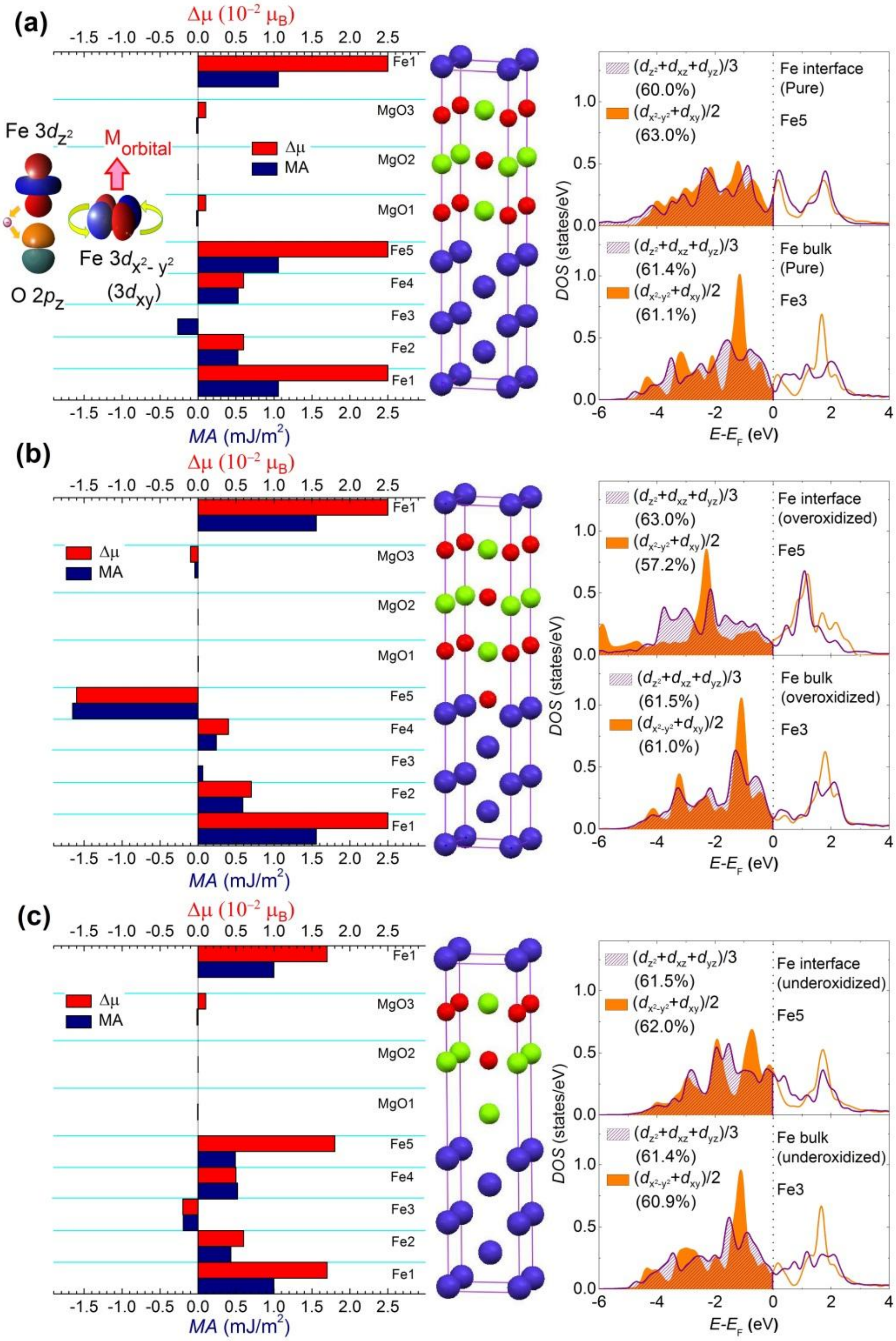
(a)
Δμ (10⁻² μB)
-1.5 -1.0 -0.5 0.0 0.5 1.0 1.5 2.0 2.5
Fe1
MgO3
MgO2
MgO1
Fe5
Fe4
Fe3
Fe2
Fe1
Δμ
MA
Fe 3dz²
M orbital
Fe 3dx²- y² (3dxy)
O 2pz
MA (mJ/m²)
(dz²+dxz+dyz)/3 (60.0%)
(dx²-y²+dxy)/2 (63.0%)
Fe interface (Pure)
Fe5
(dz²+dxz+dyz)/3 (61.4%)
(dx²-y²+dxy)/2 (61.1%)
Fe bulk (Pure)
Fe3
DOS (states/eV)
0.0 0.5 1.0
-6 -4 -2 0 2 4
E-EF (eV)
(b)
Δμ (10⁻² μB)
Δμ
MA
Fe1
MgO3
MgO2
MgO1
Fe5
Fe4
Fe3
Fe2
Fe1
MA (mJ/m²)
(dz²+dxz+dyz)/3 (63.0%)
(dx²-y²+dxy)/2 (57.2%)
Fe interface (overoxidized)
Fe5
(dz²+dxz+dyz)/3 (61.5%)
(dx²-y²+dxy)/2 (61.0%)
Fe bulk (overoxidized)
Fe3
DOS (states/eV)
E-EF (eV)
(c)
Δμ (10⁻² μB)
Δμ
MA
Fe1
MgO3
MgO2
MgO1
Fe5
Fe4
Fe3
Fe2
Fe1
MA (mJ/m²)
(dz²+dxz+dyz)/3 (61.5%)
(dx²-y²+dxy)/2 (62.0%)
Fe interface (underoxidized)
Fe5
(dz²+dxz+dyz)/3 (61.4%)
(dx²-y²+dxy)/2 (60.9%)
Fe bulk (underoxidized)
Fe3
DOS (states/eV)
E-EF (eV)

3.4 Limits and Perspectives

To summarize, in this third chapter, two fundamental studies have been addressed. We first demonstrated an efficient electrical spin-injection from a thin CoFeB ferromagnetic layer into InGaAs/GaAs QW LED through MgO tunnel barriers reaching a DoCP up to $24\pm1\%$ at 0.8 T and at 25 K. An extrapolation to the saturation field would correspond to a DoCP $\approx 42\%$ at the same temperature. The MgO tunnel barriers deposited on the Spin-LED were fabricated using two different growth techniques: Sputtering and MBE. We ran a systematic study to quantify the influence of the post-annealing temperature for both types of samples and observed that: **(i)** a similar increase of the DoCP occurs when increasing the annealing temperature and **(ii)** a comparable optimized spin-injection efficiency for both Sputtering and MBE MgO barriers in the 300-350°C range. As the increase of the DoCP starts far below the crystallization temperature of the whole CoFeB layer, we conclude that the increase of the spin-injection efficiency is mainly due to the improvement of the chemical structure of the MgO/CoFeB interface.

Secondly, we demonstrated the emission a sizable EL's DoCP from a III-V based Spin-LED at zero magnetic field using a ferromagnetic spin-injector with perpendicular magnetization. The structure of the injector consists in an ultra-thin CoFeB ferromagnetic layer (1.2 nm) grown on top of a sputtered MgO tunnel barrier (2.5 nm) and caped with a Ta layer (5 nm). The maximum DoCP measured at zero field is evaluated around 20% at 25K and a value as large as 8% still remains at room temperature. The electrical spin-injection efficiency P_s is found to be almost temperature independent at about $16 \pm 4\%$. In addition, a simple model based on the analysis of the orbital charge occupation and the orbital moment anisotropies is used to explain the origin of the PMA at the MgO/CoFeB interface and gives a pedagogical and direct image to understand the PMA nature. This first demonstration of robust and efficient electrical spin-injection using ultra-thin spin-injectors with perpendicular magnetization at remanence paves the way for future innovative applications. Such revolutionary injectors will enable to implement new room temperature III-V spin-optronic devices based on an all-electrical control of the emitted circularly polarized light using the spin-transfer torque properties of the CoFeB layer. The thinness of such injectors could also enable to implement an electrically spin-injected laser by directly inserting the injector inside the laser cavities, close to the active medium, thanks to the reduced optical absorption.

Nevertheless, despite this great accomplishment, such spin-optoelectronic devices will be competitive for realistic applications only if the device provides a switchable polarization state with an output DoCP of nearly 100% in order for instance to robustly encode a bit of information. Unfortunately, with Spin-LED, the emitted DoCP is intrinsically limited by the nature of the device and the nature of the spin-injector. Indeed, in an ideal system, the maximum emitted DoCP will be at best equal to the spin-polarization degree in the active medium (in case of a perfect conversion of the spin information onto the light polarization). However, given their ferromagnetic nature, such MTJ spin-injectors can only theoretically inject a maximum spin-polarization of 70% in the LED. Consequently, in a perfect device free of any spin relaxation mechanism and with optimal spin-information conversion properties, the maximum emitted DoCP will be around 70% at the very best. Anyhow, experimentally the emitted DoCP will always be inferior to this theoretical value, especially at room temperature. Therefore, solutions need to be found to strive toward realistic and competitive applications.

A first approach would be to enhanced the maximum spin-injection and optimize the LED device by using: **(i)** a spin-injector with a 100% spin-polarization at the Fermi level (DMS, Half-metals) and **(ii)** (110)-oriented QWs to cancel the Dyakonov-Perel relaxation mechanism in the active medium. However, doing so, new issues would arise concerning the thickness and the light absorption by the injector as well as the ability to develop PMA with such materials. Additionally, even if the $\frac{\tau}{\tau_s}$-ratio would greatly increase using (110)-QWs, the spin-relaxation occurring while the electron drifts from the spin-injector toward the active medium will never be completely overcome. The device performances will still be limited by the linear behavior of the LED.

Therefore, a more ambitious and innovative approach is to go toward non-linear systems such as lasers to benefit from an amplified conversion of the injected spin-polarization into circularly-polarized light. During this Ph.D, we initiated original research on spin-injection into Vertical External-Cavity Surface-Emitting Lasers (VECSEL). Ultimately, the philosophy behind this research is to perform a technological transfer of the ultra-thin PMA spin-injector developed on Spin-LED onto a VECSEL. Then, by taking advantage of the non-linear amplification effects, we aim (i) to reach a DoCP≈100% at room temperature and (ii) to develop an all-electrical command to switch between the σ^+ and σ^- polarization states. The next chapter introduces and details the results of this research.

Chapter 4

Spin injection into Vertical External Cavity Surface Emitting Lasers

---

Contents

Introduction

This fourth chapter is fully dedicated to the report of theoretical and experimental advances performed in the field of spin-injection into Vertical External-Cavity Surface Emitting Lasers (VECSEL).

Spin-lasers can provide higher performances as compared to Spin-LED in terms of output Degree of Circular Polarization (DoCP) due to the amplification effects induced by the combination of a gain medium and a resonant optical cavity. An output DoCP close to 100% can hence be achieved even by injecting, electrically or optically, a relatively low spin-polarization in the active medium. From this point of view the such devices can be seen as spin-amplifiers. Vertical External Cavity Surface Emitting Lasers make perfect candidates for a Spin-Laser implementation as their vertical geometry enable to take advantage of optical quantum selection rules in the QW. Furthermore, as there is supposedly no preferential guiding for TE or TM modes like in conventional laser diodes, VECSEL provide a good isotropic emission.

We showed in the state of the art of spin injected VCSEL that so far very few experiments were conducted on electrical spin-injection (section 2.2.5.2). In the very first reported electrically spin-injected VCSEL, the spin-injector was incorporated in the Distributed Bragg Reflector leading to DoCP≈4.6% at 80 K. However, more recent devices developed by Bhattacharya *et al.* involve a lateral spin-injection from an annular electrode through an n-doped DBR. This architecture indubitably demonstrated some brilliant achievements but so far the best result shows an effective spin-injection limited to 23% at 80K and 1T [37]. In this Ph.D we propose to investigate a new paradigm by trying to minimize the distance between the spin-injector and the active medium of the laser.

Our approach is to use Vertical External Cavity Surface Emitting Lasers based on 1/2-VCSEL used in an external cavity configuration. This enables to benefit from an additional degree of freedom provided by the external cavity. Thus, it becomes possible to deposit a spin-injector on top of the structure, close to the QWs, using an architecture similar to Spin-LEDs. The external cavity also offers the possibility to tune the laser parameters without having to change the device, by adjusting the cavity length for example, or even by inserting additional intra-cavity optical components. Additionally, the VECSEL concept is pointed out as a technology

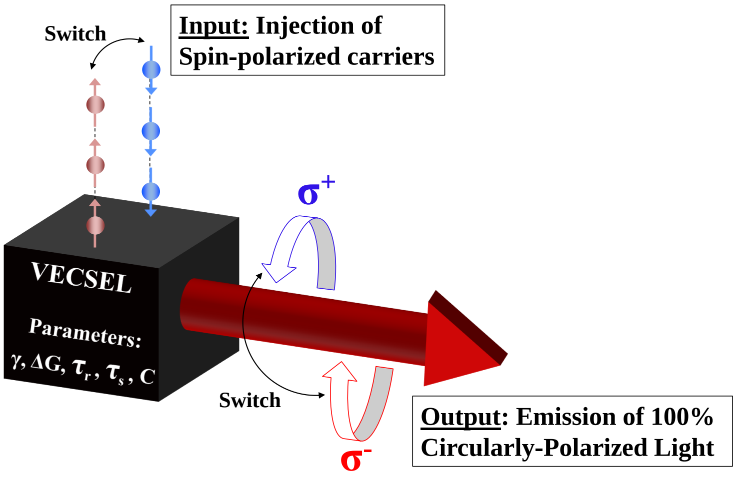

Figure 4.1: Conceptual illustration of the targeted device: The injection of spin-polarized carriers in a VECSEL leads to a control of the emitted light's polarization. The birefringence γ, gain circular dichroism ΔG, spin lifetime τ_s, carrier lifetime τ_r and coupling constant C represent the physical parameter of the system.

of choice for beyond-state-of-the-art laser light sources, demonstrating wavelength flexibility [327], high power [328, 329], high spatial, temporal and polarization coherence [330], in CW or ultra short pulsed operation [46, 329], as well as compacity and functionnalities [331]. It exhibits class-A dynamics, without relaxations oscillations, a low intensity and frequency noise [332, 333].

Ultimately, the targeted device is a VECSEL emitting a 100% right- or left-circularly polarized light at room temperature and which output polarization orientation can be controlled by all-electrical injection of spin-polarized carriers. Figure 4.1 illustrates the operating schematic of the concept. As no investigations had been previously performed on spin-injection in VECSEL, we had to adopt an exploratory approach both for the optical and the electrical pumping. Despite our expertize on Spin-LED, the development of this new Spin-Laser came with great challenges and milestones.

In this fourth chapter, after a general description of VECSELs, we first start by introducing the specific designs and characteristics of the structures used during the project for the experiments on optical and electrical spin-injection. Then we introduce a vectorial model allowing the theoretical understanding of polarization selection in spin-injected VECSEL. The model highlights the importance of the competition between the residual linear birefringence and the circular gain dichroism induced by spin-injection. Accordingly, in the following section, we report the birefringence measurements of a VECSEL design for optical pumping by evaluating the frequency detuning between the two orthogonal TE- and TM-modes. Further, we pursue the investigation by describing the optical spin-injection experiments in VECSEL. The VECSEL behavior and its polarization dynamic under optical spin-injection are discussed using the Lamb model for a Class-A two-mode-operation laser. In this section the VESCEL's spin-amplification behavior is highlighted by comparing the emitted DoCP with the effective spin-polarization in the active medium. In term of spin information conversion efficiency, the study is farther extended to the characterization of the ratio between the carriers spin-lifetime

τ_s and the carriers recombination time τ using Time Resolved Photo-Luminescence measurements. Finally the preliminary results on electrical spin-injection experiment are presented. The possibility of laser operation despite additional losses generated by the deposition of intra-cavity spin-injector on the VECSEL surface are demonstrated. We will also show the successful technological transfer onto electrical VECSEL of the $(2.5nm)MgO/(1.2nm)CoFeB/(5nm)Ta$ spin-injector with perpendicular magnetic anisotropy developed on Spin-LED.

4.1 Description and properties of VECSEL

This chapter aim to introduce and give an overview of Vertical External Cavity Surface Emitting Lasers used during this Ph.D for spin-injection experiments. The operation principals and the potential applications of such devices are detailed in further.

4.1.1 Device

A VECSEL is a semiconductor laser based on a semiconductor gain medium and a laser resonator (Figure 4.2 (a)). The semiconductor device is usually formed of a single DBR and the active region (typically several QW) [334]. The semiconductor structure typically has a total thickness of few micrometers (not including the semiconductor substrate), and is mounted on some kind of heat sink. The laser resonator is completed with an external mirror allowing an external cavity length ranging from few millimeters to some tens of centimeters. The size of laser mode in the semiconductor chip is essentially defined by the external resonator setup. The external resonator adds another degree of freedom. It may be folded using an additional flat or curved mirrors and may contain additional optical elements such as an optical filter for single-frequency operation and/or wavelength tuning, a nonlinear crystal for intracavity frequency doubling, or a saturable absorber for passive mode locking [46]. It is also possible to make a monolithic resonator with a microlens by contacting the gain chip on one side and having an output coupler mirror coating on the other surface [335]. Compared to other types of semiconductor lasers, VECSEL can generate very high optical powers in diffraction-limited beams, i.e., with high beam quality.

4.1.2 Pumping methods

As for monolithic VCSEL, VECSEL can be pumped using optical, electrical or mixed pumping.

Electrical pumping is obviously preferred for applications. Electrically pumped VECSEL usually have a QW-based gain structure but one could imagine using layers of QD as in beyond state-of-the-art optically pumped VECSEL [336, 337]. Architecturally talking, they are commonly injected using an annular electrode similarly to electrically pumped VCSEL. Unfortunately, this technique limits the usable active area and thus the output power. It is indeed difficult to pump large areas uniformly in this way by avoiding a weakly pumped region at the center of the active area [334]. So far the powers achievable with such devices appear to be limited to the order of 1 W [338].

Optical pumping provides an easy way to pump arbitrarily large active areas uniformly. Furthermore, the general design of the structures is usually simplified since doped regions for carrying the current and apertures to direct the current flow are

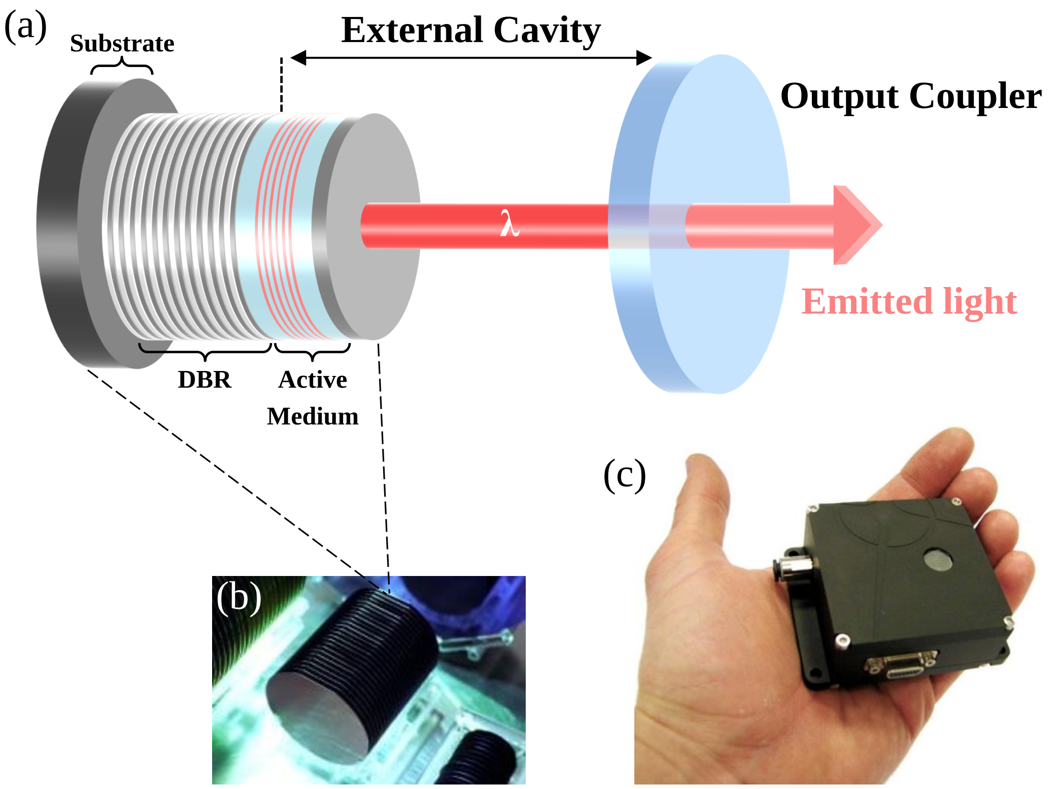

Figure 4.2: **(a) Schematic representation of a VECSEL:** The laser resonator is set by the combination of an in-chip Distributed Bragg Reflector (DBR) and an output mirror. The gain region is typically ensured by a multiple-QW structure. The external laser cavity adds another degree of freedom to the setup. **(b) VECSEL wafers:** illustrating the potentiality for cheap mass production. **(c) InnOptics commercial VECSEL:** a single frequency, low noise and high coherence laser source based on VECSEL technology.

not required. The pump light is typically taken from a high-brightness broad-area laser diode or from a diode bar. Due to the very short absorption length of the semiconductor gain structure, the beam quality of the pump light is not very important. A poor beam quality only requires working with a strongly converging pump beam, which demands more space and may make it more difficult to arrange the intra-cavity elements. In terms of performances, optically pumped VECSEL offer to achieve tens of watts of output power [339, 340]. Only few applications based on optically pumped VECSEL are commercially available. One example, propose by the french company InnOptics, is a single frequency laser source based on VECSEL technology, targeting applications such as scientific instrumentation, seed lasers, LIDAR or gas analysis (Figure 4.2 (c)).

Due to the small thickness of the QW in the gain region of a VECSEL, pump absorption is not particularly efficient if it occurs only in the quantum wells. Therefore, the usual approach is to design the gain structure such that the spacer layers between the QW also absorb pump radiation [334]. The carriers generated in these layers can be efficiently transferred towards the QW, as these have a smaller bandgap than the spacer layers. However, efficient carrier transfer requires that the bandgaps of both materials are sufficiently different, and thus that the pump wavelength is substantially shorter than the laser wavelength. This increases the quantum defect and so the dissipated power. An alternative is in-well pumping, i.e. directly pumping the QW [341]. Efficient pump absorption may then still be achieved by using a multipass pumping scheme, much as in a solid-state thin-disk laser. However, this adds to the complexity of the setup and also introduces more stringent conditions on the optical spectrum of the pump radiation. Therefore, it is not clear whether this approach is sufficiently practical for widespread application.

4.1.3 Temperature control

As opposition with VCSEL, VECSEL can exhibit large beam areas with diameters of hundreds of microns especially under optical pumping. This keeps the optical intensity at a reasonable level, even for high output powers. An issue is the extraction of the dissipated heat. When using a gain structure grown on a wafer (500 μm thickness) and not applying special cooling techniques, the device heats up unless the active area and output power are again fairly limited. If the temperature variations are too important, it can induce a strong misalignment in energy between the gain peak of the QW and the DBR resonance peak limitation and cause a significant diminution of the output power. For moderate power operation, a Peltier cooler with the warm side mounted on a copper piece is generally efficient enough to keep the device at the desired temperature. There are however techniques to achieve highly efficient cooling like for example the use of a specially processed very thin semiconductor structure on an efficient heat sink (by reverse order growth) or by attaching a transparent heat spreader such as diamond, silicon carbide or sapphire to the emitting surface.

4.1.4 Applications

The VECSEL appear to have a huge potential for widespread applications in various areas as they combine wavelength versatility, potential for high output power with a high beam quality and potentially cheap mass production (Figure 4.2 (b)). The device has already been used to demonstrate ultrashort pulses generation with modelocking using semiconductor saturable absorber mirrors (SESAM) [46, 47, 48, 49, 50, 51] as well as intracavity frequency doubling by inserting a nonlinear crystal into the laser resonator which allows the construction of efficient Red, Green and Blue frequency modes. Future realistic applications could include RGB-sources for digital laser projection displays or even intracavity laser absorption spectroscopy.

Thales needs to acquire increasingly sophisticated technologies, particularly in detection, analysis and decision-making technology, in order to design and develop critical information systems. Dual-frequency VECSEL could stand out as innovative solutions in the fields of secure military communications, space systems, air traffic control but also on-board electronics and government information networks. Optically pumped VECSEL could represent an interesting alternative compact source for atomic clocks with Cesium Coherent-Population-Trapping (CPT) and simplify the optical benches by replacing the two independent lasers setup commonly used. They emit two orthogonally-polarized coherent beams with a frequency detuning between the modes that can be precisely adjusted from few MHz to few THz and an intrinsically excellent beating between the two frequencies (typically 10 kHz) [52]. Low noise-level optical sources are also required for applications such as optical-fiber sensing and microwave photonics [53]. A -156 dB/Hz relative intensity noise level as already been demonstrated over a 100 MHz to 18 GHz bandwidth using high-Q external cavity 1/2-VCSEL [333]. This is several orders of magnitude better than the noise level usually observed in VCSEL belonging to the class-B regime. Simultaneous oscillations of two cross-polarized modes have also been demonstrated in a VECSEL by reducing the overlap of the eigen-polarizations in the active medium [342, 343]. The cavity was designed so that the laser operates in the low noise class-A regime while sustaining the oscillations of two modes with frequency-beatnote in the GHz range. Furthermore, the implementation of an Optical-Phase-Locked-Loop showed to drastically improve the spectral purity of the beatnote. The phase noise obtained was then below -110 dBc/Hz from 100 Hz to 100 kHz. These results are close to that required for optical distribution of references, for communication and sensing applications, as well as for navigation.

4.2 Designs and characteristics of the structure

4.2.1 General considerations

The structures are grown on a (001)-GaAs substrate and the bottom Distributed Bragg Reflectors are made of alternative layer of GaAs and AlAs. The active mediums of all the structures are based on strained balanced $In_{22\%}Ga_{78\%}As/GaAs_{95\%}P_{5\%}$ QW developed at the LPN by the team of Dr. Isabelle Sagnes. The use of $GaAs_{95\%}P_{5\%}$ barriers instead of standard GaAs barriers compensate the strain induce by the insertion of 20% of Indium in the GaAs matrix (1% strain over $\approx$ 8 nm). An inclusion of 5% Phosphorous in the GaAs barriers creates a compression of 0.18% over 560 nm and increases the barriers's gap energy from 1.423 eV to 1.488 eV. However, an overly high concentration of Phosphorous (10%) reduces the electron capture efficiency of the QW and affects the device performances. These compensated QW enables to stack more active layers without inducing strains that would lead to dislocations and so reduced carrier lifetimes. The number of QW can change from a VECSEL to another to add more or less gain to the structure.

Structures can be designed to be either resonant or anti-resonant. This characteristic is set regarding the oscillating electric field in the cavity. For a resonant structure the electric field exhibits a maximum of amplitude at the VECSEL surface. Oppositely, in a non-resonant structure, the electric field exhibits an amplitude node at the VECSEL surface. For the project we privileged anti-resonant structures having in mind the deposition of a ferromagnetic spin-injector on top of the VECSEL. Indeed, to minimize the absorption of the electric field by this intra-cavity multilayer, the injector has to be placed on an anti-node of the electric field's amplitude.

A VECSEL structure is always designed to work between a given temperature range of few Kelvins. Indeed to ensure a good laser operation the micro-cavity peak and the QW's Photo-Luminescence (PL) peak need to overlap in λ at the targeted operation temperature. If the micro-cavity and the PL are not well aligned the efficiency of the spontaneous emission's amplification is drastically reduce and can eventually prevent laser operation. The issue emerges from the shift of the QW-PL with the temperature at a rate of 0.35 $nm.K^{-1}$ thus requiring a precisely adjusted design. In case of slight misalignment (few nm), the VECSEL performances can still be optimized using the temperature as a degree of freedom during dynamic operation once the thermal effects are already into play.

When it comes to optical pumping, two type of pumping can be distinguished. A resonant pumping defines a photo-excitation of the carriers triggering a band-to-band transition only in the QW at the Γ-point. In this case the excitation energy of the pump's wavelength is typically resonant with the HH-band to CB transition energy in Γ but below the excitation energy of the rest of the HH-Band and the whole LH-Band. The mechanism is illustrated in figure 4.3 for the case of a left-circularly

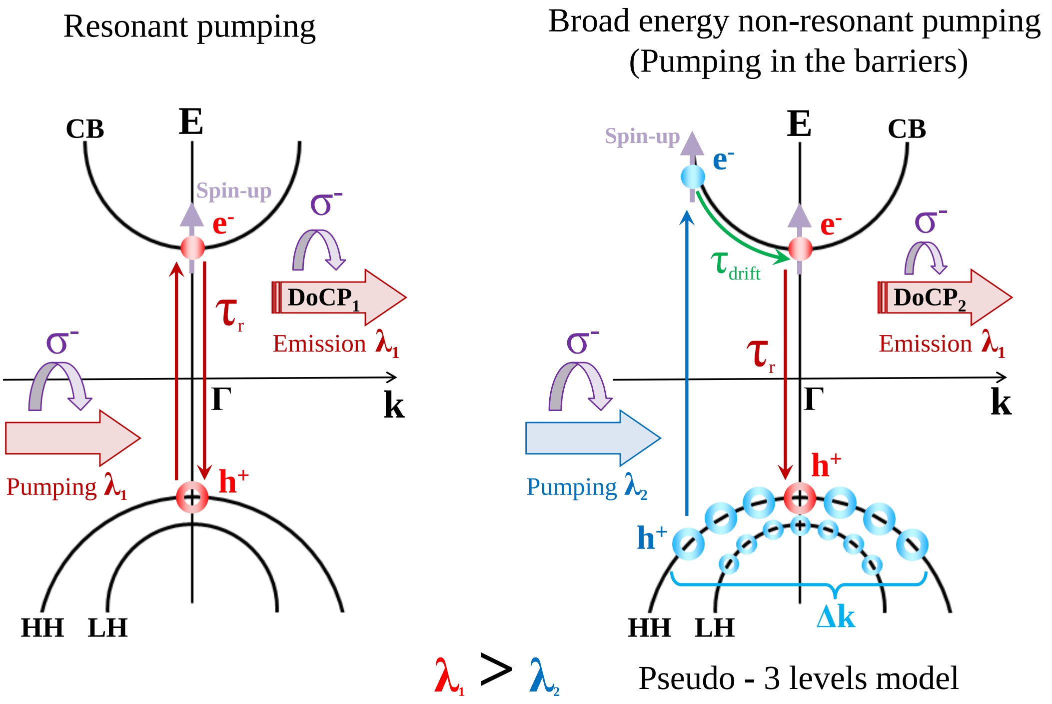

Figure 4.3: Illustrated comparison of both resonant and non-resonant pumping mechanisms.

polarized pumping photo-generating spin-up polarized electron in Γ.
Oppositely, for a non-resonant pumping the excitation energy is above the Γ-transition energy. It generates a carrier excitation over a width Δk in the HH-Band and can even excite carriers from the LH-Band if the pumping energy is high enough. The mechanism can be identify as a pseudo-three levels model for semiconductor lasers: **(i)** Carriers from the HH- and LH- bands are excited high into the CB. **(ii)** A first non-radiative intra-band relaxation toward Γ occurs with a characteristic lifetime τ_{drift} of few ps. This relaxation is accompanied by the emission of phonons. **(iii)** Inter-band radiative transition from the CB to the HH-Band with a characteristic lifetime τ_r (Figure 4.3). A non-resonant pumping significantly increases the density of photo-generated carriers as well as the population inversion and therefore facilitate stimulated emission operation. Pumping in the barriers is also possible by increasing even more the pump energy. In this case the carriers photo-generated in the barriers cascade in the QWs and boost the population inversion. For our optically pumped structures pumping in the barriers is a requirement to reach laser operation regarding to the threshold power. Unfortunately, by exciting carriers from both the HH- and LH- bands, such a non-resonant pumping strongly reduces the efficient carrier spin-polarization in the QW and so the output DoCP of the emitted light.

Both optically and electrically pumped structures were grown during the project.

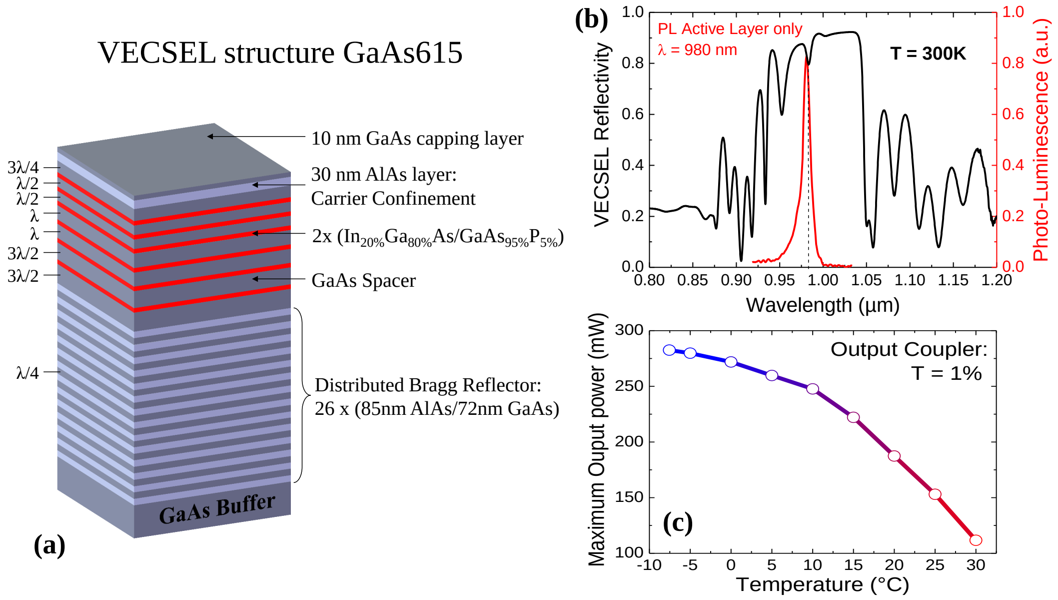

Figure 4.4: Overview of the anti-resonant 1/2-VCSEL structure GaAs615 designed for optical spin-injection: **(a)** Schematic cross sectional view of the VECSEL GaAs615 design for optical pumping. **(b)** FTIR Spectrum (black line) and active medium PL (red line) characterizing the structure at room temperature. The vertical dashed line indicated the calibrated wavelength of the micro-cavity peak. **(c)** Variation of the maximum output optical power as a function of the operation temperature. The VECSEL can decently perform with an output power above 100 mW on a temperature range of 40°C. However the VECSEL performs much better when thermalized around 0°C.

Even though they share the same growth technique and a similar active medium their nature are intrinsically different. Hereafter we detailed the structures and properties of the VECSEL used during the project.

4.2.2 Optically Pumped Structures

From a general viewpoint, as opposition with VECSEL designed for electrical pumping, the optical structures display a 30 nm insulating AlAs layer in-between the surface and the active medium used as a carrier confinement layer (Figure 4.4). Additionally the substrate, the Distributed Bragg Reflector and the QWs spacers are usually undoped as there is no requirement for carrier transportation through the structure. The excited carriers are directly photo-generated in the QW and in the barriers.

One main structure expressively design for the optical pumping at room temperature has been used during this Ph.D thesis: the structure GaAs615. This structure has been used to perform all the optical spin-injection experiment described in further.

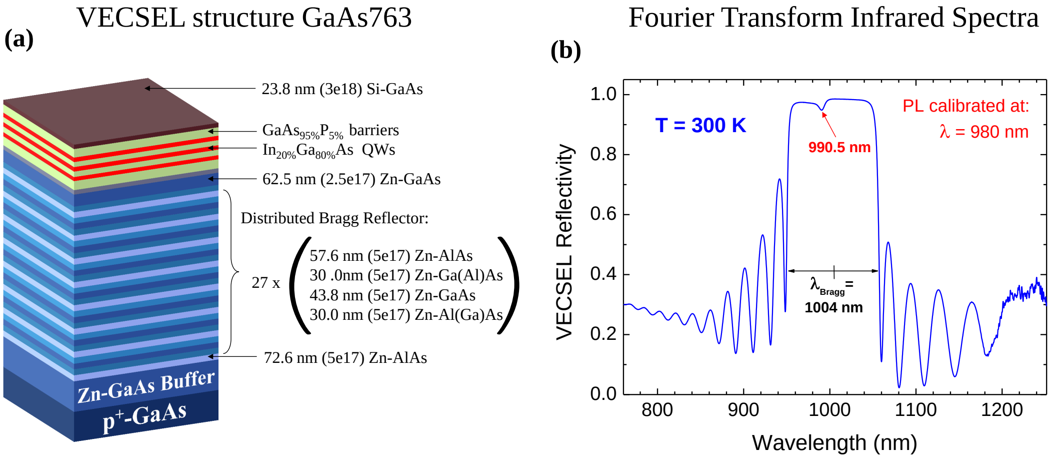

Figure 4.5: Overview of the 1^{st} anti-resonant 1/2-VCSEL structure GaAs763 designed for electrical spin-injection: (a) Schematic cross sectional view of the VECSEL GaAs763. **(b)** FTIR Spectrum characterizing the structure at room temperature. The micro-cavity peak is clamped at 990.5 nm while the QWs PL is still at 980 nm as for the structures design for optical pumping.

It is an intrinsically anti-resonant structure emitting at 1 μm at room temperature. Compared to previous devices, the number of QW was doubled to increase the total gain and enable to tolerate more losses in the cavity. The $\frac{7\lambda}{2}$ - active medium is made of 6 groups of two In$_{22\%}$Ga$_{78\%}$As/GaAs$_{95\%}$P$_{5\%}$ QW each placed in an anti-node of the standing electric field oscillating in the cavity to maximize the energy absorption and boost the stimulated emission regime. Each pairs of QWs is separated by a GaAs spacer which size decreases when getting closer to the surface (Figure 4.4 (a)). The DBR is constituted of 26 pairs of alternating AlAs/GaAs layers. Figure 4.4 (b) presents the Fourier Transform Infrared Reflectivity (FTIR) spectra of the VECSEL with the QW's PL while Figure 4.4 (c) showcases the GaAs615 output power as a function of the operation temperature. The FTIR measurements clearly illustrate the design quality of the structure as the micro-cavity peak and the QWs PL are almost perfectly aligned at room temperature. Then a slight temperature adjustment enables to maximize the overlap between the two peaks and consequently maximize the output power. Another wafer (GaAs630) displaying the exact same architecture than the GaAs615 was grown. This VECSEL was also characterized and exhibited approximately the same performances than the GaAs615. Nevertheless as the GaAs615 output optical power was slightly higher at a given temperature, we chose this structure to perform our experiments.

4.2.3 Electrically Pumped Structures

Two structures design for the electrical pumping were grown during this Ph.D thesis to perform a preparatory work toward electrically spin-injected VECSEL. As opposition with optically pumped structures, a doping of the layers is required

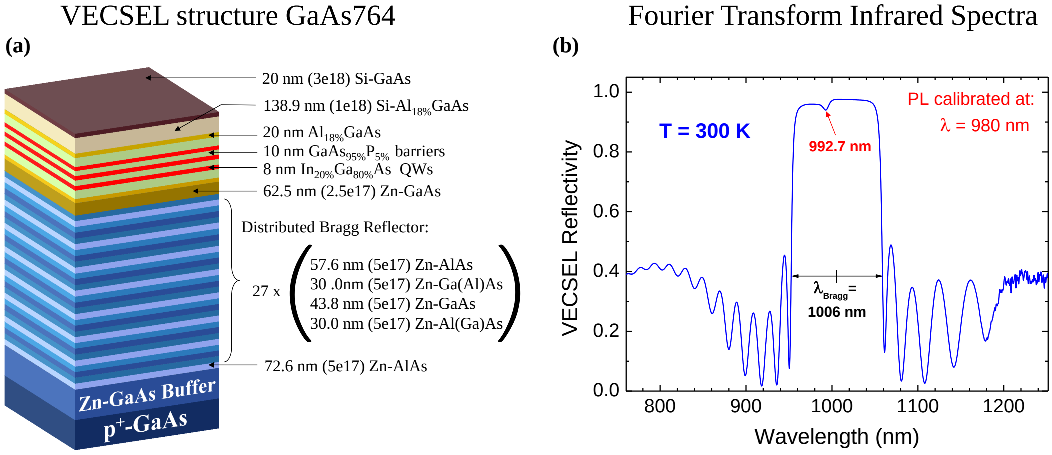

Figure 4.6: Overview of the 2^{nd} anti-resonant 1/2-VCSEL structure GaAs764 designed for electrical spin-injection: (a) Schematic cross sectional view of the VECSEL GaAs764. **(b)** FTIR Spectrum characterizing the structure at room temperature. The micro-cavity peak is clamped at 992.7 nm while the QWs PL is still at 980 nm as for the GaAs763 structure.

to build a n-i-p band structure and ensure a good carrier mobility through the 1/2-VCSEL. The structures are grown on a p^+-GaAs substrate and a Zn-doped GaAs buffer. Both of them exhibit the same DBR made of 27 stack of alternating AlAs/Ga(Al)As/GaAs/Al(Ga)As layers all Zn-doped at 5.0×10^{17} at.cm^{-3} and the same active medium based on three $In_{22\%}Ga_{78\%}As/GaAs_{95\%}P_{5\%}$ QW with a PL at 980 nm at room temperature. The difference between both structures lies in the nature and doping of the layers surrounding the active medium. It is important to point out that both structures have been carefully design to be anti-resonant in order to host a future MTJ spin-injector on the surface in a node of the standing electric field.

- **Room temperature GaAs763:** In this first electrical spin-injection design, the distance between the surface and the active medium has been minimize to benefit as much as possible of the spin diffusion length. The structure is simply capped with a 23.8nm thick Si-GaAs layer directly on top of the active medium (Figure 4.5 (a)). On the p-side, the active medium is separated from the p-doped DBR by a thin intrinsic layer of GaAs stacked on a 62.5 nm Zn-GaAs layer slightly less doped than the DBR (2.5×10^{17} at.cm^{-3}). The FTIR measurements performed on the structure confirmed a micro-cavity peak at 990.5 nm.

- **Room temperature GaAs764:** For this second electrical spin-injection design, a band engineering similar to the one used on Spin-LED was implemented. A thin $Al_{18\%}GaAs$ layer of 20 nm has been added on each side of the active medium. In the n-zone, a 138.9 nm Si-$Al_{18\%}GaAs$ layer significantly increases the distance between the surface and the active medium which could modify the percentage of spin-polarized carrier reaching the QW. The FTIR measurements performed on the structure confirmed a micro-cavity peak at 992.7 nm.

4.3 Vectorial Analysis of spin-injected VECSEL

In this section, we examined the conditions for the control of the electromagnetic field polarization by discussing the competition between the linear birefringence, intrinsic to the 1â2-VCSELs, and the circular gain dichroism originating from the spin-injection.

4.3.1 Influence of birefringence and dichroism on the polarization selection

4.3.1.1 Mathematical formalism

We consider a cold cavity exhibiting a residual phase anisotropy that fixes the polarization states in the cavity. The Jones matrix associated with the phase anisotropy γ can be written as:

$$[J_{\Delta\phi}] = exp\left(-j\frac{2\pi}{\lambda_0}\bar{n}l\right) \cdot \begin{pmatrix} exp(-j\gamma) & 0 \\ 0 & exp(j\gamma) \end{pmatrix} \tag{4.1}$$

where λ_0 is the average laser wavelength, l the cavity optical length and $\bar{n} = \frac{n_e+n_o}{2}$ the average optical index, n_e and n_o being respectively the extraordinary and ordinary optical index of the birefringent component. A reduced expression of the phase anisotropy for a single path in the cavity is given by:

$$\gamma = \frac{\pi}{\lambda_0}\left(n_e - n_o\right) l \tag{4.2}$$

In these conditions, the cold cavity admits two eigen states of the electric field linearly-polarized along the ordinary and extraordinary axis of the residual phase anisotropy.

Here, we are trying to study if a gain circular dichroism generated by spin-injection can trigger a modification of the laser eigen states, and in particular engender circularly-polarized eigen states as previously observed in the litterature [36, 283, 43, 224, 37]. The Jones matrix associated with this gain circular dichoism ΔG induced by a spin population imbalance is:

$$[J_{\Delta G}] = \begin{pmatrix} \bar{G} & -\frac{i}{2}\Delta G \\ \frac{i}{2}\Delta G & \bar{G} \end{pmatrix} \tag{4.3}$$

where $\bar{G} = \frac{G_+ + G_-}{2}$ represents the average gain, G_+ and G_- being the gains seen by the right- and left- circular polarizations respectively. This gain circular dichroism can then be expressed as:

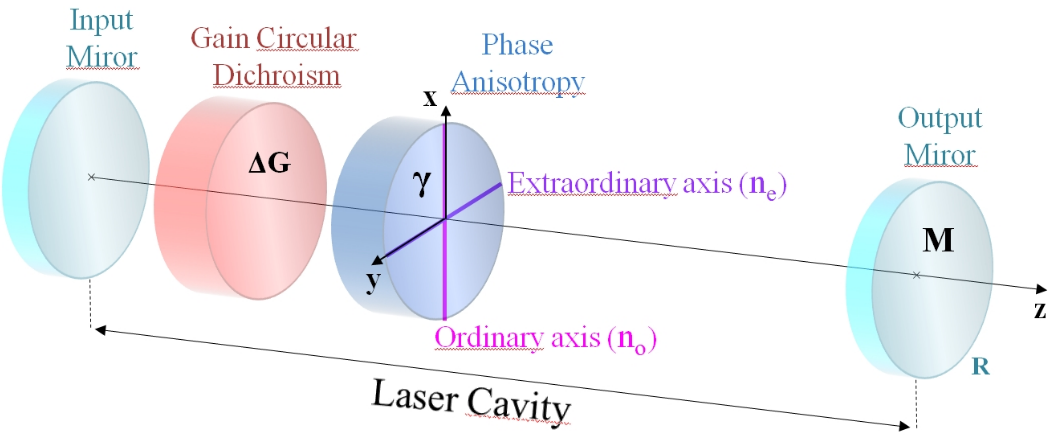

Figure 4.7: Schematic representation of the studied cavity: The residual linear birefringence of the cold cavity induces a phase anisotropy γ. The ordinary (optical indice n_o) and extraordinary (optical indice n_e) axis are oriented along the x- and y-axis respectively. The light propagation occurs along the z-axis. The gain circular dichroism ΔG is induced by optical or electrical spin-injection. We define l as the optical length of the laser cavity and λ_0 as the central laser wave length. The output mirror M has a reflectivity R while the input mirror is considered perfectly reflecting and non-birefringent.

$$\boxed{\Delta G = G_+ - G_-} \tag{4.4}$$

One can note that such a matrix does not introduce any phase anisotropy for the right- and left- circular polarization. However, it introduces a phase term when the incident polarization is linear. This phase term introduces an elliptical polarization component which ellipticity increases with ΔG. In other words, the gain circular dichroism projects the electric field on the orthogonal state.

We assume that the input mirror is perfectly reflecting and does not exhibit any birefringence. It can consequently be neglect in the vectorial model. Note that this hypothesis is not restrictive as it is possible to account for an eventual residual birefringence of the miror in the previously introduced phase anisotropy term $[J_{\Delta\phi}]$. We write the Jones matrix for the output mirror as:

$$[J_M] = \sqrt{R}\begin{pmatrix} 1 & 0 \\ 0 & 1 \end{pmatrix} \tag{4.5}$$

We now assume that the residual birefringence axis are oriented along x and y and we consider z has the light propagation axis (Figure 4.7). We can now express the Jones matrix representing the global spin-injected VECSEL at the output mirror:

$$[J_L] = exp(j\phi) \cdot [J_{\Delta\phi}]\,[J_{\Delta G}]\,[J_{\Delta\phi}]\,[J_M] \tag{4.6}$$

The Jones matrix $[J_L]$ represents the gain for a round-trip in the active medium. The term $exp(j\phi)$ accounts for the accumulated phase during the field propagation in the laser cavity. By developing the expression we find:

$$[J_L] = \sqrt{R}\bar{G} \cdot exp\left(-2jkL_{eff}\right) \cdot \begin{pmatrix} exp(-2j\gamma) & -\frac{i}{2}\Delta G_N \\ \frac{i}{2}\Delta G_N & exp(2j\gamma) \end{pmatrix} \tag{4.7}$$

where $k = \frac{2\pi\nu}{c}$ is the wave number linked to the oscillation frequency and $\Delta G_N = \frac{\Delta G}{\bar{G}}$ is the normalized value of the gain circular dichroism. $L_{eff} = n_{am}e_{am} + \bar{n}l + L$ is the average optical length of the laser cavity with n_{am} and e_{am} standing for the optical index and the thickness of the active medium respectively. L is the cavity length without the active medium and the birefringent component ($L = 0$ for a monolithic VCSEL).

The resonance condition of the electric field $\vec{E}$ for a round-trip in the cavity imposes that:

$$[J_L]\,\vec{E} = \lambda\vec{E} \tag{4.8}$$

where λ are the eigen values. The system admits two eigen states accordingly to the two degrees of freedom of the problem. The diagonalization of $[J_L]$ leads to the identification of the eigen values and polarization eigen states. The equation associated with the eigen value is:

$$\boxed{(\lambda - \cos 2\gamma)^2 = \frac{1}{4}\Delta G_N^2 - \sin^2 2\gamma} \tag{4.9}$$

The resolution of this equation gives access to the oscillation frequencies and the saturated gain:

$$\boxed{\lambda = \frac{1}{\sqrt{R}\bar{G}} \cdot exp\left(-2jkL_{eff}\right)} \tag{4.10}$$

We can now identify from equation (4.9) the different oscillation regimes of the laser.

4.3.1.2 Identification of the oscillation regimes

In this section we study the different oscillation regime of the laser arising from equation (4.9) . Several situation can be identified depending on the relative influence of the linear birefringence γ and the gain circular dichroism ΔG. We start by describing two limit cases where either $\Delta G = 0$ or $\gamma = 0$. Then, we depict the most general case corresponding to our experimental situation where $\Delta G \neq 0$ and $\gamma \neq 0$. The goal here is to theoretically understand the conditions required to make a spin-injected VECSEL oscillate on circularly polarized eigen modes.

A) **Limit cases:**

1. **If there is no gain circular dichroism:** $\Delta G = 0$

   This particular situation corresponds to the case of a spin-unpolarized pumping. Indeed a nonexistent ΔG is directly equivalent to an even population of spin-up and spin-down in the active medium of the laser. in this case, only the residual linear birefringence γ remains. The diagonalization of $[J_L]$ gives two eigen states E_x and E_y linearly-polarized along the ordinary (x-) and extraordinary (y-) axis of the linear birefringence. The equation (4.9) becomes:

   $$\begin{cases} (\lambda - \cos 2\gamma)^2 = \cos^2 2\gamma - 1 \\ \lambda_\pm = exp(\pm 2j\gamma) \end{cases} \tag{4.11}$$

   where $\lambda_\pm$ eigen values verifying the associated equation. As a consequence, the frequency difference between both eigen state is:

   $$\Delta\nu = \nu_y - \nu_x = \frac{c\gamma}{\pi L_{eff}} \tag{4.12}$$

   This situation features the usual behavior of a dual-frequency laser exhibiting two eigen polarization states linearly polarized along the axis of the birefringent crystal. Additionally, the two eigen frequencies are not degenerated and the frequency detuning is directly proportional to the linear birefringence of the crystal.

2. **If there is no linear birefringence:** $\gamma \cong 0$

   This particular situation is quite unlikely to naturally happen and so to be experimentally observe as semiconductor lasers always exhibit a residual component of linear birefringence. Anyway, if this ideal system is pumped with spin-polarized carrier ($\Delta G \neq 0$), the diagonalization of $[J_L]$ leads to:

$$\frac{E_x}{E_y} = \pm i = \exp\left(\pm i\frac{\pi}{2}\right) \tag{4.13}$$

The eigen states are right- and left-circularly polarized. Moreover, as the cavity does not contain any circular birefringent element, both eigen states are degenerate in frequency. In this configuration the equation (4.9) becomes:

$$\begin{cases} (\lambda - 1)^2 = \frac{1}{4}\Delta G_N^2 \\ \lambda_\pm = 1 \pm \frac{1}{2}\Delta G_N \end{cases} \tag{4.14}$$

Both eigen values are real and as their phases are equal to zero both eigen states are degenerate in frequency: $\Delta\nu = 0$. Nevertheless, as these two eigen values do not have the same modules, a gain difference rises between the two eigen states:

$$G_\pm = \frac{1}{\sqrt{R}\left(1 \pm \frac{1}{2}\Delta G_N\right)} \tag{4.15}$$

During laser operation, this means that an eigen state is going to start oscillating before the other one while increasing the pumping. When the pumping power becomes sufficiently high the second eigen state will start oscillating as long as the non-linear coupling constant C remains inferior to 1 (which is the case for our VECSEL: $C \simeq 0.9$). For instance, if $\Delta G_N > 0$ the right-circularly polarized mode will start oscillating first.

Assuming the self-saturation coefficients $\beta_{R(L)}$ and cross-saturation coefficients $\theta_{RL(LR)}$ are identical for both polarization modes ($\beta_R = \beta_L$ and $\theta_{RL} = \theta_{LR}$), similar intensities for both eigen states should be expected far from threshold. Moreover, as the two eigen states are degenerate in frequency, increasing the pumping also induces a polarization transition regime. Close to threshold, the laser is perfectly circularly polarized as only the σ^+-polarized eigen state (lower threshold) is lasing. Rather, far from threshold both σ^+- and σ^--circularly-polarized modes are oscillating with the same intensity in the cavity leading to a linearly-polarized output polarization ($\updownarrow = 50\%\ \sigma^+ + 50\%\ \sigma^-$). In other word the laser DoCP should drastically decrease as soon as the second eigen states start oscillating. This situation precisely fits the experimental observation realized by Iba *et al.* with an optically pumped (110)-VCSEL [42].

B) **General case: $\Delta G \neq 0$ and $\gamma \neq 0$**

This non-trivial situation closely describes an actual experiment of spin-injection in a V(E)CSEL. Both the residual linear birefringence and the gain circular dichroism induced by optical or electrical spin-injection are considered here. To clarify the problem, we further assume that $\Delta G > 0$ and $\gamma > 0$. We remind the expression of the equation associated with the eigen values: $(\lambda - \cos 2\gamma)^2 = \frac{1}{4}\Delta G_N^2 - \sin^2 2\gamma$ (eq. 4.9). Accordingly, three situation must be considered.

1. **The linear birefringence is dominant: $\frac{1}{4}\Delta G_N^2 < \sin^2 2\gamma$**
   In this case, equation (4.9) admits two complex solutions:

$$\lambda_{\pm} = \cos 2\gamma \pm i\sqrt{\sin^2 2\gamma - \frac{1}{4}\Delta G_N^2} \tag{4.16}$$

   The imaginary term straightly causes a frequency degeneracy breaking and each polarization eigen state now has its own eigen frequency. By developing equation (4.9) one can express the frequency detuning between the polarization eigen states:

$$\Delta\nu = \frac{c}{2\pi L_{eff}} \arctan\left(\frac{\sqrt{\sin^2 2\gamma - \frac{1}{4}\Delta G_N^2}}{\cos 2\gamma}\right) \tag{4.17}$$

   Figure 4.8 illustrates the evolution of this frequency detuning as a function of the gain circular dichroism for a fixed birefringence value. When ΔG_N increases the frequency detuning $\Delta\nu$ decreases with a non-linear behavior until a phase lock is triggered for $\frac{1}{4}\Delta G_N^2 = \sin^2 2\gamma$.

   Concerning the evolution of the polarization eigen states, the electric field component verify the following relation:

$$\frac{E_y}{E_x} = -\frac{2\sin 2\gamma}{\Delta G_N}\left(1 \pm \sqrt{1 - \frac{\Delta G_N^2}{4\sin^2 2\gamma}}\right) \tag{4.18}$$

   The system admits two linearly-polarized solution which respective orientations depend on the ratio between the gain circular dichroism and the linear birefringence (figure 4.9 (a)-(b)).

2. **The linear birefringence and the gain circular dichroism are of equal magnitude: $\frac{1}{4}\Delta G_N^2 = \sin^2 2\gamma$**

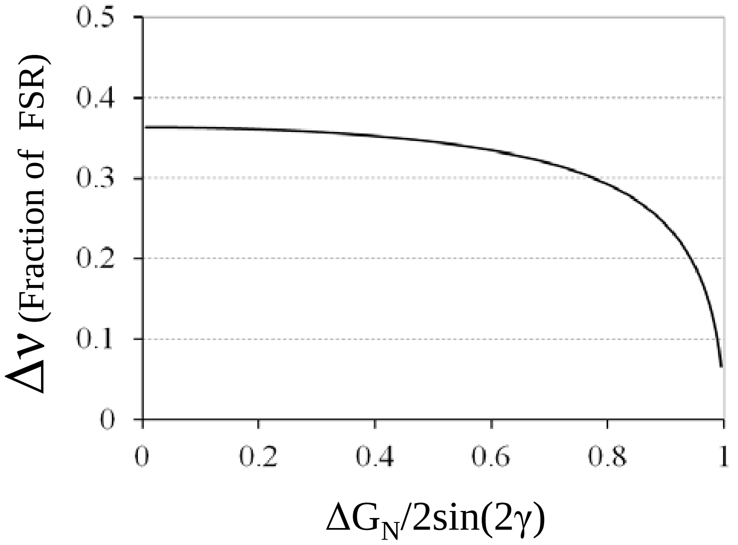

Figure 4.8: Evolution of the frequency detuning between the two polarization eigen states as a function of the ratio between the Gain Circular Dichroism ΔG_N and the linear birefringence γ. Here γ is taken as 1.

In dynamics operation of spin-injected V(E)CSEL, this particular operation regime comes out as a punctual transition phase between two polarization regimes. Both eigen states are linearly-polarized along the same direction and degenerate in frequency. There is no way of distinguishing them and everything happens as if there was only one linearly-polarized eigen state oriented at -45° from the birefringence axis. Equation (4.9) becomes:

$$\begin{cases} (\lambda - \cos 2\gamma)^2 = 0 \\ \lambda_\pm = \cos 2\gamma \end{cases} \tag{4.19}$$

And accordingly to the $\Delta G > 0$ and $\gamma > 0$ hypothesis, the electric field components verify:

$$\frac{E_y}{E_x} = -1 \tag{4.20}$$

Which is well in line with a linear polarization oriented at -45° from the birefringence axis (along x and y). The boundary condition between the B.1 and B.2 situation is correctly verify.

3. **The gain circular dichroism is dominant:** $\frac{1}{4}\Delta G_N^2 > \sin^2 2\gamma$
   In this case, equation (4.9) admits two real solution:

$$\lambda_\pm = \cos 2\gamma \pm \sqrt{\frac{1}{4}\Delta G_N^2 - \sin^2 2\gamma} \tag{4.21}$$

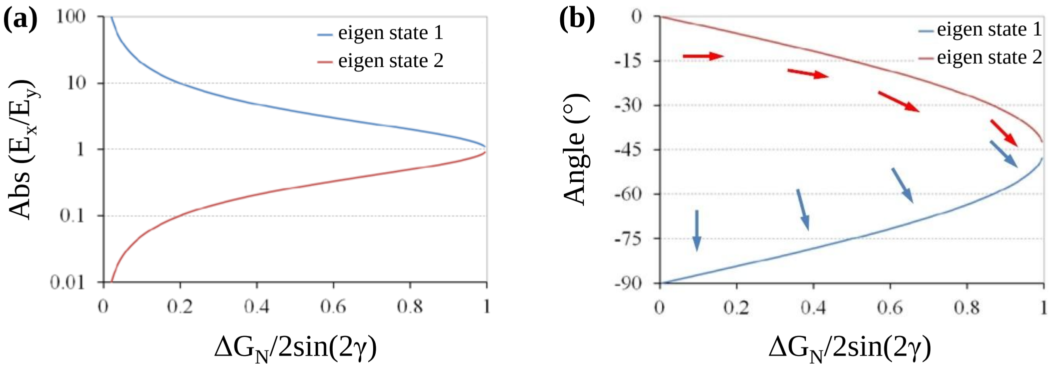

Figure 4.9: Evolution of **(a)** the electric field component and **(b)** the respective orientation of both polarizations eigen states as a function of the ratio between the Gain Circular Dichroism ΔG_N and the linear birefringence γ.

Consequently, the polarization eigen states are degenerated in frequency and the output polarization state of the laser will be determined by their superposition. The apparition order of the polarization modes is directly link to the gain dichroism. We can expect a change in the polarization state of the laser with the pump power and the gain dichroism magnitude. The components of the electric field verify:

$$\frac{E_y}{E_x} = \frac{exp(-2i\gamma) - \lambda_\pm}{\frac{i}{2}\Delta G_N} \tag{4.22}$$

and we can extract the module and the phase in polar coordinates:

$$\begin{cases} \left|\frac{E_x}{E_y}\right| = 1 \\ \Phi_\pm = arg\left(\frac{E_x}{E_y}\right) = \mp \arctan\left(\frac{\Delta G_N^2}{4\sin^2 2\gamma} - 1\right)^{-\frac{1}{2}} \end{cases} \tag{4.23}$$

Consequently, the two allowed eigen states are elliptically polarized. When $\Delta G_N \gg \gamma$ ($\Leftrightarrow \ \gamma \mapsto 0$), the system converges toward the limit case B.2 and both eigen states tend toward one perfectly circular polarization state as $\lim_{\gamma\to 0} \Phi_\pm = \pm\frac{\pi}{2}$. The boundary condition between the B.2 and B.3 situations is correctly verify. The resolution of (4.9) gives access to the gain seen by each eigen state:

$$G_\pm = \frac{1}{\sqrt{R}\left(\cos 2\gamma \pm \sqrt{\frac{\Delta G_N^2}{4} - \sin^2 2\gamma}\right)} \tag{4.24}$$

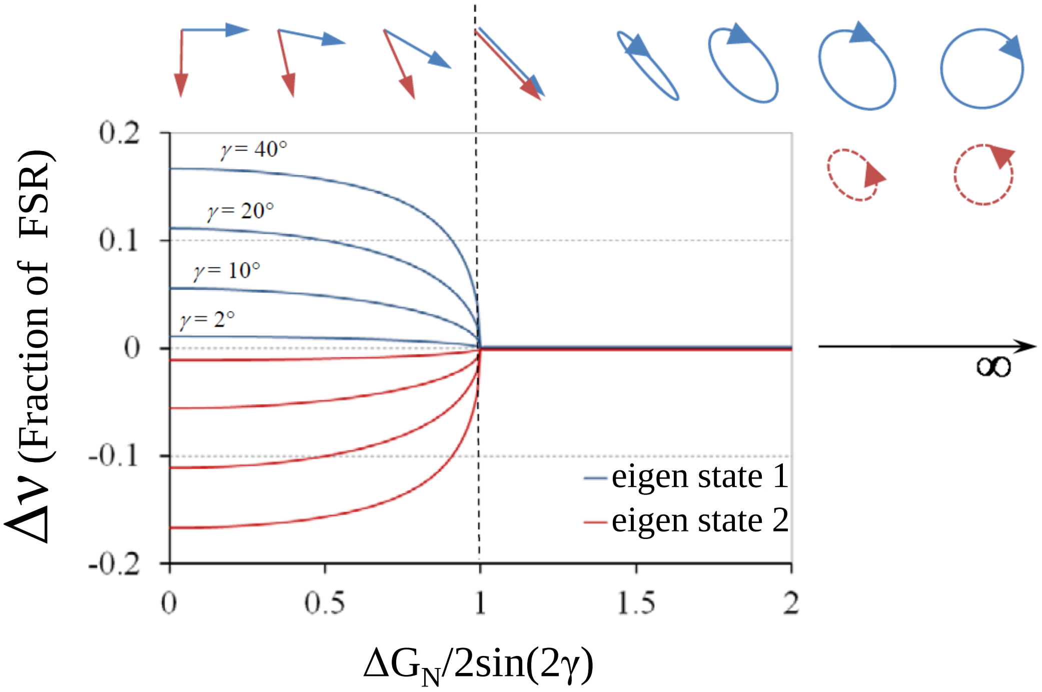

Figure 4.10: Evolution of the frequency detuning and the polarization state of both polarizations eigen states as a function of the ratio between the Gain Circular Dichroism ΔG_N and the linear birefringence γ.

Experimentally, the eigen state with the highest gain will start lasing first. As already discussed, if the non-linear coupling between both eigen state is less than 1 ($C < 1$), the eigen state with less gain will still oscillate far from threshold for a higher pumping rate. The apparition of this second orthogonally polarized eigen state will generate a diminution of the laser DoCP. Finally if $C \geq 1$ only one eigen state will oscillate on the whole pumping range and in this case the DoCP will keep increasing with the pumping power.

4.3.1.3 Synthesis and conclusion

Figure 4.10 summarize the results of the previous section, namely the vectorial behavior of a spin-injected V(E)CSEL with an active medium exhibiting a gain circular dichroism and cavity presenting a residual linear birefringence. Notwithstanding its importance, a linear birefringence is always taking place in a laser mainly due to the residual strain of the material or in the optical element constituting the laser cavity.

We show that when there is no gain circular dichroism (spin-unpolarized pumping), the laser eigen states are both linearly polarized with a frequency detuning proportional phase anisotropy originating from the birefringent element. These two eigen states are orthogonal. Then, when the gain circular dichroism increases, the two eigen states lose their orthogonality and both polarizations tend toward one common direction while staying linearly polarized. The eigen frequencies remains roughly constant. Finally, when the gain circular dichroism becomes sufficient enough, both polarization becomes degenerate and a phase lock occurs in such way that distinguishing the eigen state from one another becomes impossible. They become fully degenerate and combine in one unique linearly polrized state oriented at 45° from the linear birefringence axis.

If the gain circular dichroism keeps increasing, the linear polarization mutate toward an elliptical polarization with the long axis oriented at 45° from the neutral axis of the linear birefringence. Then the ellipticity keeps increasing with the gain circular dichoism until the modes reach a perfectly circular polarization states. It is important to notice that, in the elliptical polarization region, the second orthogonal eigen state can appear. Nevertheless the gain associated with this mode is inferior. If the non-linear Lamb coupling constant C allows the oscillation of both modes ($C < 1$), the laser output DoCP will decrease when the pump power increases.

4.3.2 Preparation of the laser eigen state

We showed in the previous section that the residual linear birefringence in the active medium locks the laser on two linearly-polarized orthogonal eigen states. The laser will consequently naturally oscillate on one of these eigen state or eventually both depending on value of the Lamb non-linear coupling constant. However if the laser is under spin-polarized pumping, the induced gain circular dichroism will break the modes orthogonality. The modes remain linearly polarized as long as the gain circular dichroism does not fully compensate the linear birefringence. In other words, to increase the chance of observing a switch from a circularly-polarized mode to another, there is an interest in preparing the laser to naturally oscillate on circularly polarized eigen modes. To do so, one has to insert in the laser cavity a non-reciprocal material exhibiting Faraday effect as illustrated in figure 4.11. This second section focuses on the modeling of such a system.

4.3.2.1 Intra-cavity Faraday rotator

The Jones matrix associated with a Faraday rotator is defined as:

$$[J_F] = \begin{pmatrix} \cos\theta & -\sin\theta \\ \sin\theta & \cos\theta \end{pmatrix} \tag{4.25}$$

where θ is the rotation angle that the Faraday rotator would induce on a linear polarization. This rotation angle is proportional to the Verdet constant, the Faraday rotator's thickness and to the applied magnetic field. It is interesting to point out that the eigen vectors of such a matrice give two right- and left-circularly polarized eigen polarization states regardless to the value of θ. In practice, this angle is adjusted to $\frac{\pi}{4}$ in optical isolators to provide a total linear polarization rotation of $\frac{\pi}{2}$ over a round trip.

In our case, to ensure that the circular birefringence introduced by the Faraday rotator fully compensates the residual linear birefringence of the active medium, the Faraday effect should be maximized by choosing a rotator displaying a rotation angle $\theta = \frac{\pi}{4}$. The Jones matrix associated with a $\frac{\pi}{4}$-Faraday rotator naturally derives from (4.25):

$$\left[J_F^{\pi/4}\right] = \frac{1}{\sqrt{2}} \begin{pmatrix} 1 & -1 \\ 1 & 1 \end{pmatrix} \tag{4.26}$$

This matrix mixes the linear polarization states originating from the linear birefringence of the active medium.

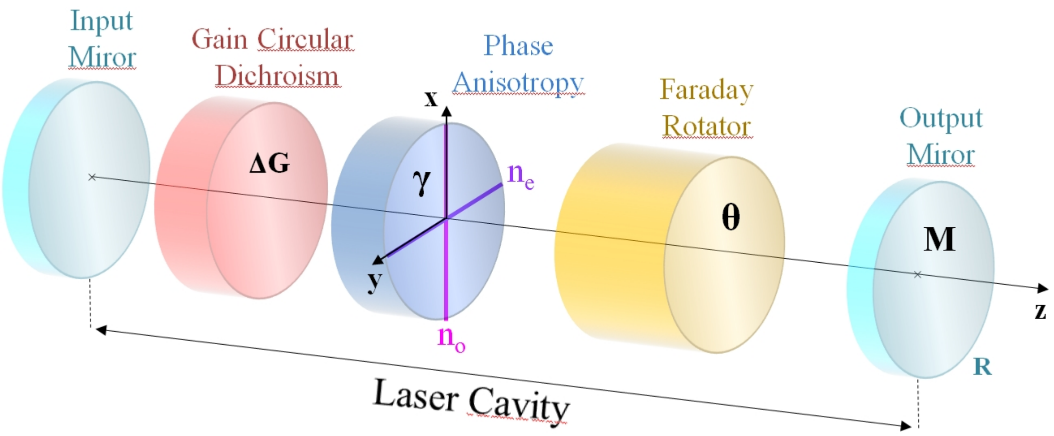

Figure 4.11: Schematic representation of the studied cavity: We considered the same laser cavity exhibiting a residual linear birefringence γ and a gain circular dichroism ΔG. A Faraday rotator F inducing a polarization rotation angle θ is added to the cavity. The circular birefringence generated by the Faraday rotator compensates the linear birefringence of the cold cavity and prepares the laser to oscillate on circularly-polarized eigen modes.

Taking account of the inserted Faraday rotator, the total Jones matrix representing the global spin-injected VECSEL at the output mirror for one light round-trip in the cavity becomes::

$$[J_L] = exp(j\phi) \cdot [J_F]\,[J_{\Delta\phi}]\,[J_{\Delta G}]\,[J_{\Delta\phi}]\,[J_F]\,[J_M] \tag{4.27}$$

where $[J_{\Delta\phi}]$, $[J_{\Delta G}]$ and $[J_M]$ are still respectively the Jones matrix of **(i)** the residual linear birefringence of the active medium given by equation (4.1), **(ii)** the gain circular dichroism induced by spin-polarized pumping of the active medium (eq. 4.3), and **(iii)** of the output mirror given by equation (4.4). In further we keep the same notation of the previous section. We remind that the normalized gain dichroism ΔG_N account for a round-trip in the active medium while the other physical parameters account for a single pass of the optical element in the laser cavity. Furthermore the phase term $exp(j\phi)$, representing the accumulated phase during the electric field propagation in the laser cavity, has to take into account the optical pass in the Faraday rotator so as:

$$\phi = 2k(n_{am}e_{am} + \bar{n}l + n_F e_F + L) = 2kL_{eff} \tag{4.28}$$

with n_F and e_F being the average optical index and the thickness of the Faraday rotator respectively.

The resonance condition of the electric field $\vec{E}$ for a round-trip in the cavity still verifies:

$$[J_L]\,\vec{E} = \lambda\vec{E} \tag{4.29}$$

As in the previous section, the analytic calculation of this matrix and its diagonalization leads to new polarization eigen states of the laser with the associated eigen values. In the particular case of a Faraday rotator with $\theta = \frac{\pi}{4}$ the equations significantly simplify and the equation associated with the eigen values is given by:

$$\boxed{\lambda_{\pm} = (\mp 2 - \Delta G_N)\cdot exp\left(i\frac{\pi}{2}\right) = (2 \pm \Delta G_N)\cdot exp\left(\mp i\frac{\pi}{2}\right)} \tag{4.30}$$

As it was predicted, the residual phase anisotropy γ no longer influences the equation associated with the eigen values and consequently the selection of the eigen polarization states oscillating in the laser.

4.3.2.2 New oscillation regimes

A) **Associated eigen values:**

The situation is similar to the case A.2) where $\gamma \cong 0$ of the previous section. The only difference is that here the system is experimentally observable as it is artificially prepared to imitate such a situation. The amplitude term of equation (4.30) gives the gain seen by each eigen state while the argument provide access to the eigen frequencies:

$$\begin{cases} G_{\pm} = \dfrac{1}{\sqrt{R}\left(1 \pm \frac{1}{2}\Delta G_N\right)} \\ \nu_{\pm} = \left(q \pm \dfrac{1}{4}\right)\dfrac{c}{L_{eff}} \end{cases} \tag{4.31}$$

with $q \in \mathbb{N}$. The frequency difference between both eigen states is given by:

$$\Delta\nu_{\pm} = |\nu_{+} - \nu_{-}| = \frac{c}{4L_{eff}} \tag{4.32}$$

This frequency difference is independent of the residual linear phase anisotropy of the active medium. It is fixed by the Faraday rotator and correspond to exactly half of the laser Free Spectral Range (FSR).

B) **Associated eigen vectors:**

The diagonalization of $[J_L]$ leads to the identification of the laser eigen states. The transverse components of the electric field are expressed as:

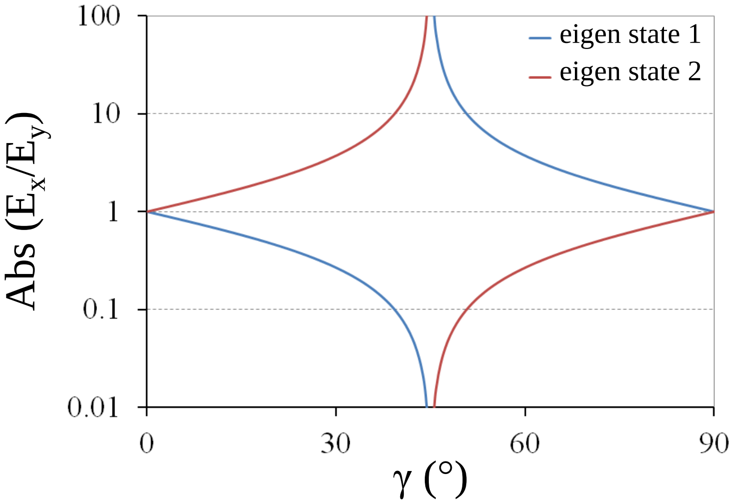

Figure 4.12: Evolution of the transverse components of the electric field as a function of the linear birefringence γ in the active medium.

$$\left.\frac{E_y}{E_x}\right|_{\pm} = -i\tan(2\gamma) \pm i\sqrt{\tan^2(2\gamma)+1} \tag{4.33}$$

This expression highlights how the transverse components of the electric field remains in quadrature (constant $\frac{\pi}{2}$-dephasing) for each eigen states. Furthermore, as the gain circular dichoism does not appear in the equation, the injected electronic spin will not change the laser eigen polarization but can still induce a switch from an eigen state to another. However, as shown by the gain equation (4.31), the gain circular dichroism will favor an eigen state over the other which will preferentially start lasing first because of its lower threshold.

Figure 4.12 illustrates the evolution of the electric field's transverse components for both eigen states as a function of the active medium's linear birefringence. A clear singularity appears for $\gamma = 45°$, when the circular birefringence of the Faraday rotator and the linear birefringence of the active medium perfectly compensate each other. We can distinguish three situations:

1. **If there is no linear birefringence:** $\gamma \mapsto 0°$

   If there is no linear phase anisotropy, the transverse components of the electric field are linked by:

$$\left.\frac{E_y}{E_x}\right|_{\pm} = \pm i \tag{4.34}$$

   The two eigen polarization are respectively right- and left-circularly polarized.

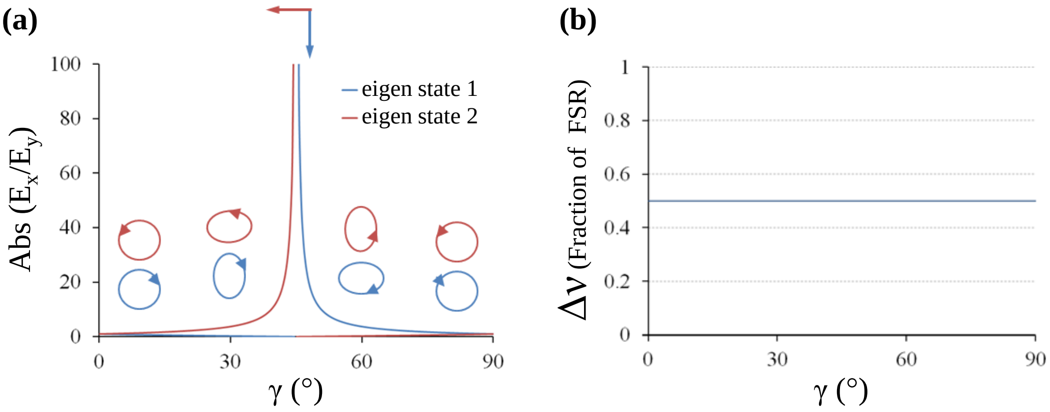

Figure 4.13: (a) Evolution of the electric field transverse components of both polarization eigen states as a function of the linear birefringence γ. (b) Frequency detuning between the two polarization eigen states as a function of the linear birefringence γ.

2. **If $\gamma = 45°$:**

   This scenario is anecdotal and unlikely to happens on real systems as the linear birefringence remains residual. A Taylor expansion around $\gamma = 45°$ enables to identify the eigen states:

   $$\lim_{\gamma\to\frac{\pi}{4}} \frac{E_y}{E_x}\bigg|_{+} = -\infty \qquad\qquad \lim_{\gamma\to\frac{\pi}{4}} \frac{E_y}{E_x}\bigg|_{-} = 0 \tag{4.35}$$

   In this limit case both polarization becomes linear and oriented along the neutral axis of the linear birefringence (x and y)

3. **General case:**

   In this realistic situation, the eigen states are right- and left-elliptically polarized with an ellipticity ranging from perfectly circular (for $\Delta G_N \gg \gamma \;\Leftrightarrow\; \gamma \mapsto 0°$) to linear (for $\gamma = 45°$) (Figure 4.13). The ellipticity of both polarization states decreases when the linear phase anisotropy increases. However, experimentally both polarization states should be almost perfectly circularly-polarized as the linear birefringence remains residual compare to the circular birefringence introduced by the Faraday rotator.

4.3.2.3 Synthesis and conclusion

The insertion of a Faraday rotator in the VECSEL's cavity enables to prepare the laser to oscillate on eigen states conducive to the observation of the influence of spin-injection on the laser polarization. We theoretically showed that such an optical device offers the possibility to mask the impact of the residual linear birefringence of the active medium by conferring to the laser right- and left-circular eigen polarizations. If so, the gain circular dichroism produced by spin injection directly generates a gain disequilibrium between these polarization modes, that can eventually lead to a polarization switch if the non-linear Lamb coupling constant is high enough. In addition, this vectorial model shows that the frequency detuning between the two laser eigen states is equal to half the laser FSR regardless to the linear birefringence value.

4.4 Birefringence measurements

4.4.1 Introduction

We saw in the previous section that the residual linear birefringence γ plays a predominant role in the polarization selection of VECSEL. Accordingly, it is necessary to quantify the birefringence in the structure in order to better understand the relative impact of the birefringence (intrinsic to 1/2-VCSEL) and the gain circular dichroism ΔG_N (from the spin-injection) on the polarization selection. The study of the $\frac{\gamma}{\Delta G_N}$-ratio should enable us to estimate the minimum gain circular dichroism ΔG_N required to take over the control of the modes' polarization. This study has been recently submitted for publication to the journal *Optics Express* [261].

V(E)CSEL provide a relatively good isotropic emission as there is no preferential guiding for TE- or TM- modes like in conventional laser diodes. Nevertheless residual stress [263], lattice strains [251, 344], temperature variations [274, 227], the cavity geometry [265, 244, 345], a high number of strained-balanced QW or even lithography processing of VCSEL can break this in-plane symmetry and give rise to linear birefringence in the structure. In the particular case of $\frac{1}{2}$-VCSEL, the lack of top Distributed Bragg Reflector (DBR) is suspected to increase the lattice strains on the active medium and induce an increase of residual linear birefringence compared to regular VCSEL. For our (100) QW VECSEL, the typical linear polarization axis are along [011] (TM) and $[0\bar{1}1]$ (TE) with a preferential selection for the $[0\bar{1}1]$ direction.

In this section we report birefringence measurements of a VECSEL structure by measuring the frequency detuning between two orthogonal linearly-polarized modes. Previous birefringence estimations based on frequency detuning measurements have been reported in the literature but only for monolithic VCSEL and by performing a direct optical detection [250]. Hendriks *et al.* performed birefringence measurements in the optical domain using a noise-eater to improve the stability of the laser pump combined with a planar Fabry-Perot interferometer. The Fabry-Perot exhibited a free spectral range $FSR \approx 29.3$ GHz, a finesse $F \approx 100$ and accordingly a maximal resolution $R = 293$ MHz $\left(R = \frac{FSR}{F}\right)$. Using this setup they quantified a birefringence $\frac{\gamma'}{2\pi} \approx 2 \times 10^{-4}$ rad in a 3 GaAs-QW monolithic VCSEL. The spectral resolution of such Fabry-Perot interferometers is sufficient to measure the frequency detuning between the TE- and TM- modes of few GHz displayed by monolithic VCSEL (micro-metric cavities). However in the case of VECSEL with long cavities (cm) the frequency detuning is expected as low as few MHz. Consequently the spectral resolution of such Fabry-Perot interferometers is insufficient. To overcome this limitation we transferred the optical frequency detuning between the two TE- and TM- modes into the electrical domain. Then, we performed the frequency detuning measurements using an Electrical Spectrum Analyzer (ESA) near the first adjacent mode where the noise floor is at the shot noise (Figure 4.14).

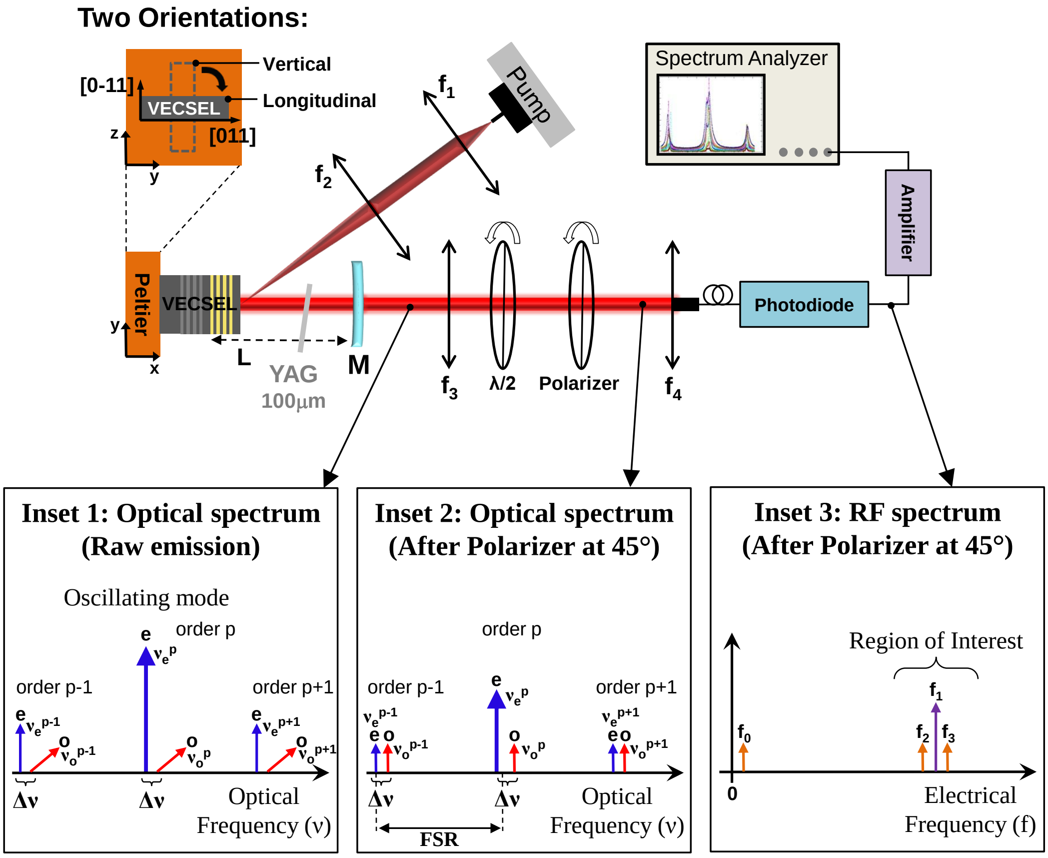

Figure 4.14: Outline schematic illustrating the principle of the experiment: Experimental setup is composed of: $L = 23mm$, $f_1 = 10mm$, $f_2 = 25mm$, $f_3 = 175mm$, $M : (R = 25mm, T = 0.5\%)$. The Insets 1, 2 and 3 illustrate the evolution of the emitted raw optical spectrum (Inset 1) after projection through a 45°-polarizer (Inset 2) and conversion into a RF spectrum by a photodiode (Inset 3). In the optical spectrum, the ordinary and extraordinary polarization are represented in red and blue respectively. In the electrical spectrum, the beating between modes are identified by the frequencies $f_0 = \nu_e^p - \nu_o^p$, $f_1 = \nu_e^p - \nu_e^{p-1}$, $f_2 = \nu_e^p - \nu_o^{p-1}$ and $f_3 = \nu_o^{p+1} - \nu_e^p$. The self-beatings of a mode with itself between different order is represented in purple while the cross-beatings between two different modes is represented in orange (regardeless to the mode orders).

4.4.2 Experimental setup

The experimental setup is described in Figure 4.14. We used an anti-resonant $\frac{1}{2}$-VCSEL (GaAs615) grown by Metal Organic Chemical Vapor Deposition (MOCVD) consisting in a 27.5-period GaAs/AlAs Bragg mirror (99.9% reflectivity). The gain at λ=1 μm is ensured by twelve strained balanced $In_{22\%}Ga_{78\%}As/GaAs_{95\%}P_{5\%}$ QW in a $13\lambda/2$ cavity. The sample consists in a 10×5 mm^2 clived and non-processed piece of raw wafer. The structure is maintained at 282 K with a Peltier thermo-electric cooler throughout the whole experiment. Instead of clamps, the VECSEL is mounted on the Peltier with thermal grease to avoid any parasitic stress on the structure that could bias the measurements. The pumping system consisted in a 808 nm pigtail multimode laser diode delivering up to 2 W and focused on the gain medium to a 100μm spot with a 30 ° incidence angle. The VECSEL is pumped in the continuous regime throughout the experiment. The linear cavity is closed by a 25 mm radius of curvature concave mirrors M with a 0.5% transmission at 1 μm (Figure 4.14). The cavity length was set to 2.3 cm and exhibits a net round-trip losses of 1% giving a photon lifetime of 7.4 ns, which is higher than the carrier lifetime in stimulated emission regime at about twice the threshold (around 1 ns). Such a long cavity implies that the laser is highly multimode longitudinally. We then introduced and carefully adjusted a 100 μm thick Yttrium Aluminum Garnet (YAG) crystal inside the laser cavity to set the laser monomode and focused on the observation of the first adjacent mode to avoid any spectral aliasing. The VECSEL is then oscillating on one linearly-polarized mode and the amplified spontaneous emission of the orthogonal polarization mode is still detectable above the shot-noise. At the output of M the beam is collimated (f_3) and we realize a fiber-coupling with a monomode optical fiber to send the emitted light on a photo-diode. The electrical signal obtained is then amplified using a low noise, high bandwidth amplifier and sent to an ESA. Between the output coupler and the fiber-coupling, we inserted a polarizer to project the orthogonal linear polarizations of the lasing mode and the amplified spontaneous emission on the same optical axis (Figure 4.14 Inset 2). In the electrical domain, we focus on the beatings between these two linearly-polarized modes near the first adjacent mode. On the ESA, the central peak (f_1) corresponds to the self-beating of the lasing mode between adjacent orders while the two smaller satellite peaks (f_2 and f_3) on each side correspond to the cross-beating between the two modes (Figure 4.14 Inset 3).

The birefringence γ' is extracted from the frequency detuning measurements Δf. Δf represents the frequency shift between the central peak f_1 and the satellite peaks f_2 and f_3. By considering that the TE-mode is the mode lasing in the cavity, the central peak f_1 corresponding to the self-beating of the TE-mode while the two satellite peaks f_2 and f_3 on each side correspond to the beating between the TM- and TE-modes (Figure 4.14 Inset 3). In the optical domain, the frequencies ν_{TE}^{p} and ν_{TM}^{q} associated with the TE- and TM-polarization modes at the optical order p and q are respectively given by:

$$\begin{cases} \nu_{TE}^{p} = p \cdot \dfrac{c}{2\left[L+(n_e-1)l\right]} \\ \nu_{TM}^{q} = q \cdot \dfrac{c}{2\left[L+(n_o-1)l\right]} \end{cases} \tag{4.36}$$

where L is the cavity length, c is the celerity of light and l is the thickness of the active medium. n_e and n_o are the optical index seen in the VECSEL along the extraordinary and ordinary polarizations respectively. As the birefringence is

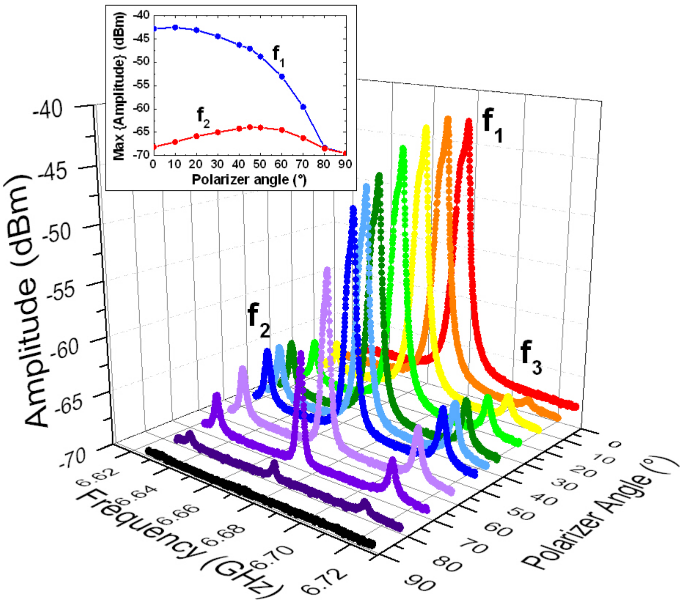

Figure 4.15: Amplitude variations of the projected orthogonal polarization modes as a function of the polarizer angle θ for the VECSEL oriented longitudinally at T=282 K and for a pumping power P_{pump} = 515 mW. The inset presents the variations of the amplitude maximum as a function of the polarizer angle for the frequencies f_1 and f_2.

expected to be relatively small, we assume the relation p=q for the optical orders. After projection of the optical spectrum through a 45°-polarizer, we can show that in the electrical domain the birefringence is linked to the frequency detuning by the relation:

$$\boxed{\frac{\gamma'}{2\pi} = \frac{2L}{c} \cdot \Delta f} \tag{4.37}$$

where $L \approx L_e = L+(n_e-1)l \approx L_o = L+(n_o-1)l$ and c is the light celerity. This relation is established for a round-trip in the cavity. This experimentally measured birefringence γ' and the reduced expression of the linear birefringence γ given for a round-trip in the cavity in the vectorial model (Section 4.3.1.1, Eq. 4.2) are linked by the relation $\gamma' = 4\gamma$. The formal demonstration of the equation (4.37) can be find in the Appendix D. The birefringence measured for the two orthogonal VECSEL orientations [011] and [0$\bar{1}$1] is a combination of the birefringence intrinsic to the VECSEL structure and the birefringence induced by the optical pumping mainly through thermal effect.

The VECSEL is class-A as the photon lifetime in the cavity is higher than the carrier lifetime [333]. In a class-A laser the relaxation oscillations becomes negligible by adiabatic elimination of the population inversion from the laser dynamics. The laser behavior is then exclusively governed by the filtering function of the cold cavity. Thus, one can expect a significant noise reduction compared to monolithic VCSEL [333]. As opposition with previous measurements reported on class-B VCSEL [250], the class-A behavior offer by VECSEL ensure a laser noise limited to the shot-noise limit.

In terms of geometrical convention, we consider that the light emitted by the VECSEL propagates along the x-axis while the linear polarizations associated with the emission evolve in the (y,z)-plane. The long and the short sides of the VECSEL correspond to the [011]- and [0$\bar{1}$1]-crystallographic directions respectively. Accordingly, we define the VECSEL "Longitudinally-oriented" when the long side of the VECSEL ([011]-axis) is parallel the the y-axis and "Vertically-oriented" when the short side of the VECSEL ([0$\bar{1}$1]-axis) is parallel the the y-axis (See Top-Left of Figure 4.14). Finally, we take for notation conventions to identify the frequency in the optical domain as ν and the frequency in the electrical domain as f.

4.4.3 Identification of the two linearly-polarized orthogonal modes

In this preliminary experiment, we demonstrate that the Amplified Spontaneous Emission (ASE) of the TM-mode can be used as a local oscillator to generate beating frequencies in the electrical domain. The study is performed for different polarizer angles θ ranging from 0° to 90°. Figure 4.15 displays the RF power evolution of the beating frequencies. As already emphasized, the measurements are performed near the first adjacent mode where the noise floor is minimum (Figure 4.14, Inset 3). The amplitude for the central beating frequency (f_1) is maximum when the polarizer is aligned with the polarization direction of the lasing mode (reference: 0°) and then progressively decreases until complete extinction at 90°. However for the satellite peaks amplitude, the amount of intensity projected increases from 0° to 45°, where the beating amplitude between the TE- and TM- modes reaches a maximum. Then, by further rotating the polarizer, the measured amplitude of the satellite peaks starts decreasing as the projection of the central mode start to vanish, until complete extinction is reached at 90°. From 0° to 45°, we can clearly see the opposite amplitude evolution of the central peak f_1 and the satellite peaks f_2 and f_3 (Inset Figure 4.15). This behavior confirms that we are indeed detecting a beating between two orthogonal polarization modes. We also conclude from this preliminary experiment that the signal to noise ratio for the central and satellite peaks is maximized by setting the polarizer at 45° from both the TE and TM modes. It is also worthwile to notice that the high finesse external cavity configuration leads to narrow ASE peaks and thus a high discrimination capability of the experiment.

4.4.4 Birefringence measurements

We performed the frequency detuning measurements for two 1/2-VCSEL orientations. We already know that the structure exhibits a dominant polarization mode (TE) along the [0$\bar{1}$1]-direction with an average gain 10% higher than the orthogonal mode (TM) polarized along the [011]-direction. The pump is by default elliptically polarized with the long axis along the y-axis. We first place the 1/2-VCSEL's [0$\bar{1}$1]-direction along the y-axis (1/2-VCSEL oriented Vertically) to strengthen the stabilization of the dominant mode. We start by investigating this stabler situation

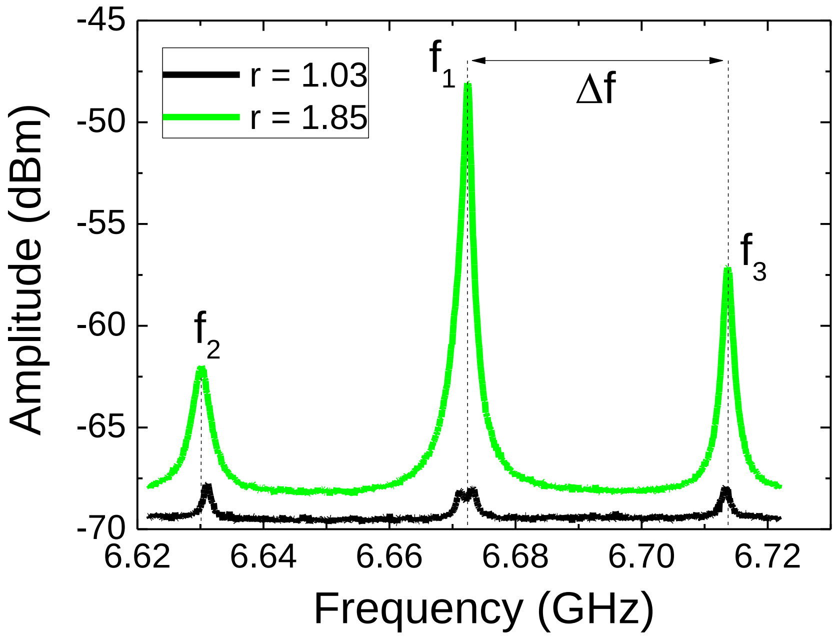

Figure 4.16: Frequency spectra of the monomode emission near the first adjacent mode for the VECSEL oriented vertically for both low (Black) and moderate (Green) pumping power: The central peak f_1 correspond to the self-beating of the lasing TE-mode while the two side peaks f_2 and f_3 both originate from the cross-beating of the TE- and the TM-mode. For this VECSEL's orientation $\Delta f \in [38.08-40.81]$ MHz corresponding to a birefringence $\frac{\gamma'}{2\pi} \in [6.3\times10^{-3}-6.4\times10^{-3}]$ rad. All the measurements were performed at T$=$ 282 K.

before rotating the 1/2-VCSEL in the longitudinal orientation. For both measurements we maximize the signal to noise ratio by setting the polarizer at 45° from the TE- and TM-mode directions. We define the pumping rate as being the ratio between the applied pumping power (P) and the threshold power (P_{th}): $r = \frac{P}{P_{th}}$.

VECSEL oriented vertically:

When the 1/2-VCSEL is oriented vertically, the dominant TE-polarization mode starts lasing at threshold (P$_{th}$ = 295 mW) and prevents the orthogonal TM-mode to oscillate in the cavity due to the gain saturation. Nevertheless, ASE is detectable for the TM-mode. Accordingly, on the electrical spectrum analyzer we detect the intense central peak associated with the beating of the oscillating mode (TE) with the ASE in the first adjacent TE longitudinal mode. Whereas the two satellite peaks correspond to the beating with the TM-modes. When increasing the pumping rate from r = 1.03 to r = 1.85, the amplitude of the three peaks increases (Figure 4.16). We also notice a negligible increase of the frequency detuning Δf between the central and the two satellite peaks due to an increase of the total birefringence in the structure originating from thermal pumping effect. For this range of pumping rate, we measured a frequency detuning Δf included between 38.08 and 40.81 MHz giving an average birefringence value estimated around $\frac{\gamma}{2\pi} = 6.4 \times 10^{-3}$ rad. However closer to threshold, where the thermal birefringence induced by the pump is minimum, $\frac{\gamma}{2\pi}$ is closer to 6.3×10^{-3} rad.

At low pumping rate (r=1.03), the slight splitting of the central peak into two peaks is a signature of residual Coherent Population Oscillation (CPO) effect. This effect induces a non-perfect overlap of the lasing TE-mode with ASE in the longitudinal modes of order p-1 and p+1. As can be noticed, this behavior which is actually due to aliasing effects is not present on the satellite peaks because unlike for TE-TE the TE-TM beating of p-1 and p+1 orders with the lasing mode leads to two different frequencies. Moreover, the CPO splitting effect is not expected to play a role for cross-polarized modes because they do not interfere in the active medium. Consequently, the accuracy of the birefringence measurement is maximized by considering the frequency difference between the two satellite peaks, that is, $2\Delta f$.

VECSEL oriented longitudinally:

When the 1/2-VCSEL is oriented longitudinally, the TM-mode polarized along the [011] direction starts lasing at threshold ($P_{th} = 316$ mW) and the amplified spontaneous of the $[0\bar{1}1]$ orthogonal TE-mode is also observable. On the RF-spectrum we detect the intense central peak this time associated with the beating of the TM oscillating mode and the TM ASE and the two satellite peaks corresponding to the beating between the TM oscillating mode and TE ASE. When increasing the pumping rate from $r = 1.17$ to $r = 1.97$, the amplitude of the three peaks increases (Figure 4.17 (a)). Here, as opposed to the Vertically-oriented case, we also witness a clear increase of the frequency detuning Δf between the central and the two satellite peaks when the pumping power increases: $\Delta f_{r=1.17} < \Delta f_{r=1.97}$. This observation is attributed to an additional birefringence generated by the pump induced thermal strain increasing the total birefringence in the structure. For this range of pumping rate, we measured a frequency detuning Δf included between 33.3 and 40.2 MHz giving an average birefringence value estimated around $\frac{\gamma}{2\pi} = 6.12 \times 10^{-3}$ rad. However closer to threshold, where the thermal birefringence induced by the pump is minimum, $\frac{\gamma}{2\pi}$ is closer to 5.8×10^{-3} rad.

For pumping rates higher than $r = 2.03$, a polarization switch is triggered by the thermal birefringence induced by the optical pumping which favors the stability of the TE-mode in the cavity (Figure 4.17 (b)). This observation is coherent with previous polarization stability experiment performed on monolithic VCSELs [227, 263]. Indeed in our laser system, a polarization bistability regime between the TE- and TM- modes is unlikely to establish due to a non-linear coupling constant C close to unity ($C \approx 0.9$) [343, 225]. By further increasing the pumping power, the detected amplitudes increase until the signal becomes unstable due to the beginning of mode hopping and multimode lasing.

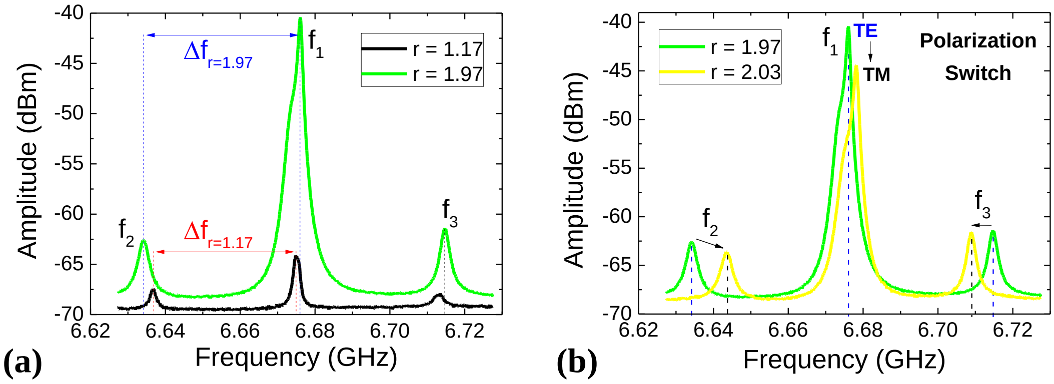

Figure 4.17: Frequency spectra of the monomode emission near the first adjacent mode for the VECSEL oriented longitudinally: (a) Frequency detuning measurement for both low (Black) and moderate (Green) pumping power. For this VECSEL's orientation $\Delta f \in [33.3 - 40.2]$ MHz corresponding to a birefringence $\frac{\gamma'}{2\pi} \in [5.8 \times 10^{-3} - 6.12 \times 10^{-3}]$ rad. **(b)** For pumping rates $r = 2.03$, a polarization switch is triggered by a pump induced birefringence favoring the stability of the TE-mode in the cavity. All the measurements were performed at T=282 K.

4.4.5 Discussion

Comparison analysis:

Figure 4.18 summarizes the birefringence measurements for both the vertical and the longitudinal orientation of the 1/2-VCSEL. It is important to highlight that the total birefringence measured for the two orthogonal VECSEL's orientations [011] and [0$\bar{1}$1] is a combination of: (i) the intrinsic birefringence of the 1/2-VCSEL structure and (ii) the birefringence induced by the optical pumping mainly through thermal effects. The average values of birefringence extracted above threshold are $\frac{\gamma}{2\pi} = 6.12 \times 10^{-3}$ rad and $\frac{\gamma}{2\pi} = 6.4 \times 10^{-3}$ rad for the 1/2-VCSEL oriented longitudinally and vertically respectively. The small difference witnessed between the two orientations can be attributed to the influence of the pump birefringence. The pump polarization is elliptical with the long axis oriented along the y-axis. When the 1/2-VCSEL is oriented vertically (dominant polarization (TM) along y-axis) the thermal birefringence induced by the pump slightly enhances the intrinsic birefringence of the semiconductor structure. Oppositely, when the VECSEL is oriented longitudinally (dominant polarization (TM) perpendicular to y-axis) this thermal birefringence slightly compensates the intrinsic birefringence of the semiconductor structure. Accordingly, we estimate the average birefringence of the VECSEL operating in a laser regime to $\frac{\bar{\gamma}}{2\pi} \approx 6.26 \times 10^{-3}$ rad.

A more accurate value of the intrinsic birefringence is given for low pumping rate where the contribution of the thermally induced birefringence is minimum. Close to threshold, the average values of birefringence extracted are $\frac{\gamma}{2\pi} = 5.8 \times 10^{-3}$ rad

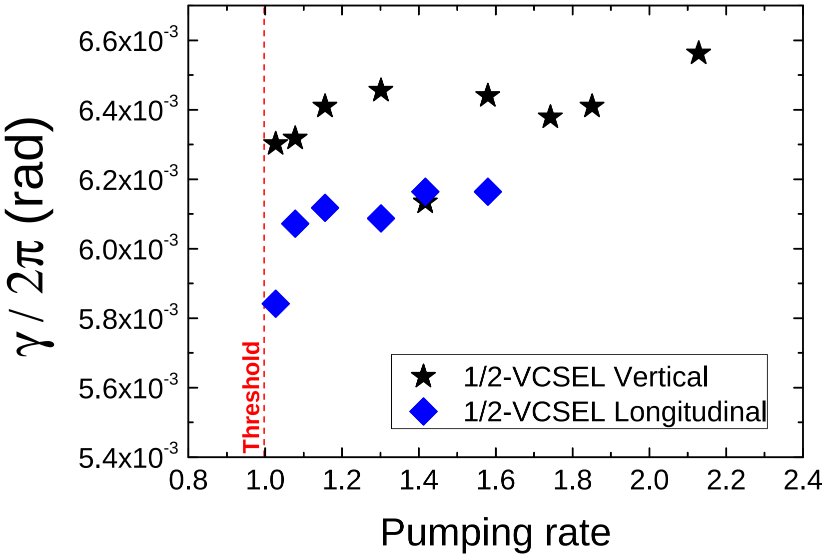

Figure 4.18: Birefringence variations as a function of the pumping rate $r = \frac{P}{P_{th}}$ for the VECSEL oriented longitudinally (blue) and vertically (black) at T= 282K.

and $\frac{\gamma}{2\pi} = 6.3 \times 10^{-3}$ rad for the 1/2-VCSEL oriented longitudinally and vertically respectively. Accordingly, we estimate the average intrinsic birefringence of the 1/2-VCSEL to $\frac{\bar{\gamma}_{int}}{2\pi} \approx 6.05 \times 10^{-3}$ rad.

As anticipated, the birefringence of the $\frac{1}{2}$-VCSEL is more than 30 times higher than the birefringence measured by Hendriks *et al.* in a monolithic 3 GaAs QWs VCSEL $\frac{\bar{\gamma}_{VCSEL}}{2\pi} \approx 2 \times 10^{-4}$ rad [250]. Such high values of residual birefringence compared to regular VCSEL structures are suspected to emerge from the lack of top distributed bragg reflector inducing a symmetry breaking of the crystalline structure close to the active medium (≈ 100-200 nm). This symmetry breaking could increase the lattice strain on the active medium and therefore increase the phase anisotropy between the ordinary (n_o) and extraordinary (n_e) axis leading to an increase of the linear birefringence. Additionally, our active medium is build on twelve strained-balanced QWs (to compare with 3-6 for standard VCSEL [42]). The stacking these InGaAs QWs, each doped with 22% Indium, requires to work with GaAsP barriers doped with 5% Phosphorous to generate a compression factor of 0.18 over 560 nm and balance the strains in the structure. These strain-balanced QWs are also suspected to increase the phase anisotropy in the active medium.

Estimation of the required effective spin-injection:

Thanks to this experimental measurement of γ', we can now estimate the normalized gain circular dichroism ΔG_N required to compensate the residual linear birefringence of the VECSEL structure. In the previously introduced vectorial model (Section 4.3) this equilibrium directly translates to: $\frac{1}{4}\Delta G_N^2 = \sin^2 \frac{\gamma'}{2}$. Using the value

$\frac{\bar{\gamma}'_{exp}}{2\pi} \approx 6.3 \times 10^{-3}$ rad, we calculate that a $\Delta G_N \approx 4\%$ is necessary to compensate the linear birefringence. In other words, as $\Delta G_N = 2\frac{G_+ - G_-}{G_+ + G_-}$ this directly means that one of the circularly-polarized mode needs to exhibit at least 1.04 times more gain than the other circularly-polarized mode: $G_+ = 1.04 \times G_-$ or $G_- = 1.04 \times G_+$. However, one has to keep in mind that this ΔG_N value is just an inferior limit at which the VECSEL is in an artificial isotropic state for the TE- and TM-modes. According to the vectorial model, in this metastable state the TE- and TM-modes are still both linearly polarized and oriented at 45° from the ordinary $[0\bar{1}1]$ and extraordinary [011] axis. To trigger VESCEL oscillations on two elliptically- and further circularly-polarized modes, one would have to increase ΔG_N by boosting the gain differential between the two circularly-polarized modes ($\Delta G = G_+ - G_-$). This mode of operation will be reached by improving the effective spin-injection in the active medium.

Using the same calculation for a regular VCSEL exhibiting a linear birefringence $\frac{\bar{\gamma}'_{VCSEL}}{2\pi} \approx 2 \times 10^{-4}$ rad [250] we find that a normalized gain circular dichroism 8 times inferior $\Delta G_N \approx 0.5\%$ is sufficient to compensate the birefringence in the structure. This can partly explain the impressive values of DoCP already obtained with monolithic VCSEL under optical [36, 41, 283, 42, 43] and electrical [37] spin-injection.

In the next section we are going to experimentally investigate the same GaAs615 VECSEL structure under optical spin-injection. The competition between the residual linear birefringence and the gain circular dichroism is studied by analyzing the light polarization emitted by the VECSEL. Thanks to an original experimental setup, we introduce and highlight the fundamental role of the Lamb non-linear coupling constant C on the polarization selection.

4.5 Optically spin-injected VECSELs

This section presents the experiments and the associated results on optical spin-injection in VECSEL realized during this Ph.D. This work represents a significant portion of the total experimental work developed during the thesis. The study has been successfully published in *Applied Physics Letters* [225].

4.5.1 Linear-Cavity VECSEL

To perform the very first optical spin-injection experiments in VECSEL, we opted for a simple linear cavity in order to minimize the system complexity. The goal here is to see if the output polarization of the VECSEL can be monitored by injection of spin-polarized carriers in the laser active medium through circularly-polarized optical pumping.

4.5.1.1 Experimental Setup

For the experiment (figure 4.19) we used an antiresonant n.i.d VECSEL (GaAs615) grown by Metal Organic Chemical Vapor Deposition (MOCVD) consisting in a 27.5-period GaAs/AlAs Bragg mirror (99.9% reflectivity). The gain at λ=1 μm is ensured by twelve strained balanced $In_{22\%}Ga_{78\%}As/GaAs_{95\%}P_{5\%}$ QW in a $13\lambda/2$ cavity. The structure is mounted on a Peltier thermo-electric cooler with thermal grease and maintained at 285 K throughout the whole experiment. The pumping system consists in a 808 nm pigtail multimode laser diode delivering up to 2 W and focused on the gain medium to a 100 μm spot with a 30° incidence angle. The VECSEL is pumped in the continuous regime throughout the experiment and the laser threshold is measured as being $P_{threshold}$ = 200 mW. The pump light is circularly-polarized after collimation (f_1) using a high power polarizer-cube combined with a $\frac{\lambda}{4}$-wave

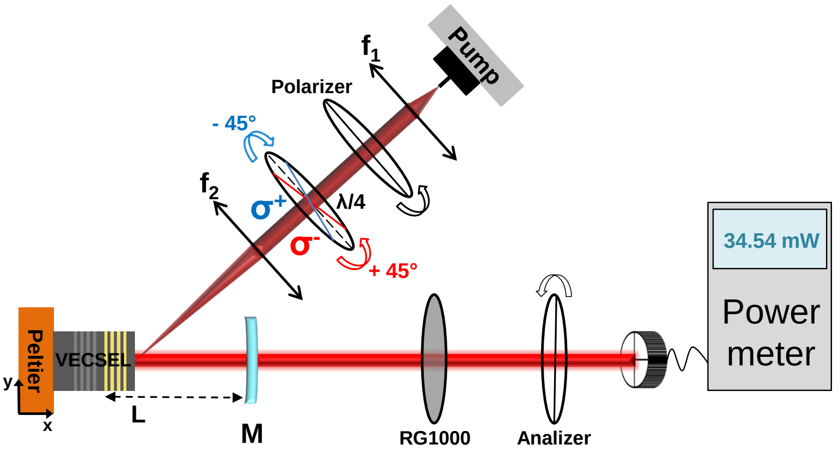

Figure 4.19: Linear-Cavity VECSEL with the associated characterization setup: $f_1 = 10mm$, $f_2 = 50mm$, $M : (R = 50mm, T = 0.5\%)$, $L = 50mm$.

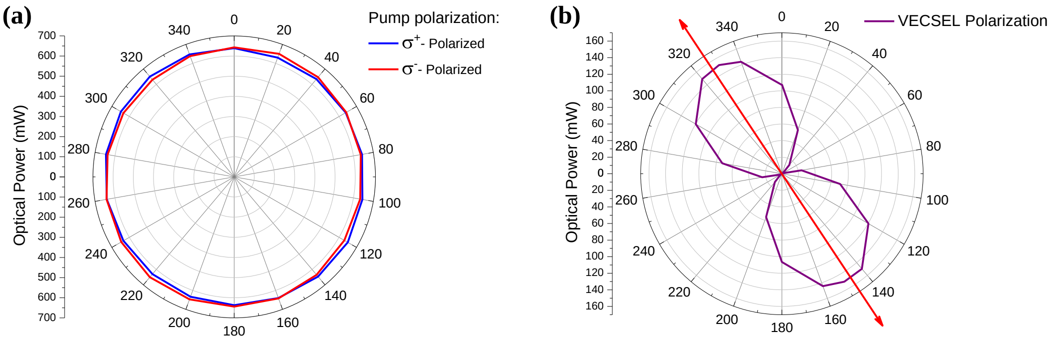

Circular polarizations: **Ɛllipticity ≈ 97%**

Linear polarization: **Ɛllipticity = 0%**

Figure 4.20: Optical power measurements as a function of an analyzer angle: (a) Pump ellipticity for right- and left-circularly polarized pumping. In both cases, the combination of a polarizer and a $\frac{\lambda}{4}$ on the pump setup gives a pump beam almost perfectly circularly-polarized: $\varepsilon \approx 97\%$. **(b)** Despite 97% σ^+- or σ^+-polarized pumping, the output polarization of the VECSEL remains strictly linear $\varepsilon \approx 0\%$.

plate and then focused on the VECSEL surface (f_2). The linear cavity is closed by a 50 mm radius of curvature concave mirrors M with a 0.5% transmission at 1 μm. At the output of M the polarization orientation of the emitted laser light is analyzed using a conventional polarizer. A spectral filter RG1000 cutting frequencies below 1000 nm is introduced in-between the output coupler and the analyzer to clearly separate the laser emission (1000 nm) from any pump reflexion (808 nm).

4.5.1.2 Experimental observations

Despite a 100% right (σ^+) or left (σ^-) circularly-polarized pumping (figure 4.20 (a)) the laser output polarization remains strictly linear (figure 4.20 (b)). This can be explained mainly by the presence of the strong residual linear birefringence γ in the structure conferring to the laser two linearly-polarized orthogonal eigen states. As highlighted in the previous section, such high value of residual linear birefringence compared to regular VCSEL can emerge from the lack of top DBR and the important number of strained-balanced QW thereby increasing the lattice strain on the active medium. For our (100) QW VECSEL, the typical linear polarization axes are along [011] (TM) and [0$\bar{1}$1] (TE). To overcome this problem, it is necessary to insert a non-reciprocal material inside the optical cavity in order to generate an intra-cavity circular birefringence sufficiently high to completely overcome the residual linear birefringence of the 1/2-VCSEL structure. Additionally, pumping with a 30° incidence angle induces a projection of the circularly-polarized pumping light into an elliptically-polarized incident light in the plane of the QW. Consequently, the effective transferable angular momentum from the photons to the QW's carriers required to efficiently generate spin-polarized carriers is significantly reduced and so is the global spin-injection efficiency.

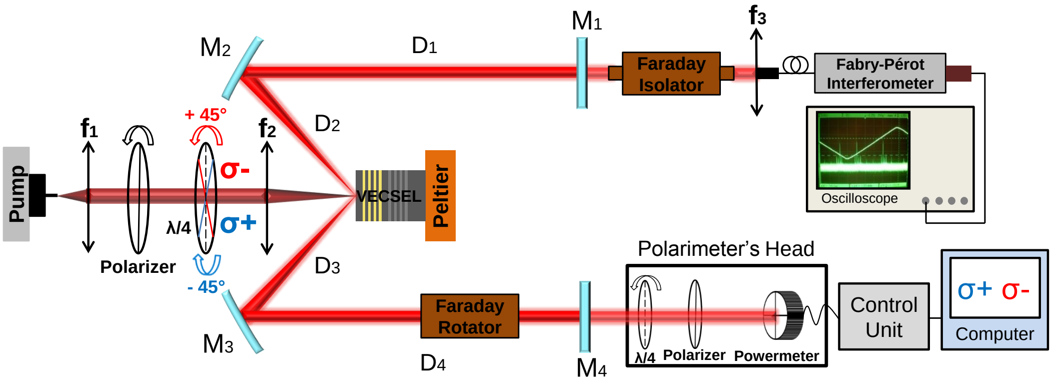

Figure 4.21: New extended M-cavity VECSEL with the associated characterization setup: $f_1 = 10mm$, $f_2 = 25mm$, $M_1 : (Plane, T = 0.5\%)$, $M_2 : (R = 50mm, T = 0.1\%)$, $M_3 : (R = 50mm, T = 0.1\%)$, $M_1 : (Plane, T = 0.1\%)$, $D_1 = 224mm$, $D_2 = 55mm$, $D_3 = 54mm$, $D_4 = 226mm$.

4.5.2 Extended M-Cavity VECSEL

4.5.2.1 Experimental Setup

To artificially introduce a circular birefringence in the cavity and compensate the strong linear birefringence of the structure, we chose to use a 45° Faraday rotator consisting in a Terbium Gallium Garnet (TGG) bar anti-reflection coated at 1μm and placed at the center of a cylindrical magnet. Ideally, the optical component should induce a circular birefringence so important that the linear birefringence γ becomes negligible, making this laser inherently oscillate with respect to a left and/or right circularly polarized light [346]. However, the insertion of such a large optical component (10 cm long) in the laser cavity required to re-think the whole experiment. The new design of the cavity geometry was driven by two main objectives: **(i)** the first one was to maximize the spin-injection efficiency by pumping the VECSEL with a normal incidence to prevent any elliptical projection of the circular polarization and **(ii)** the second point was to prepare the laser to oscillate on two circularly-polarized eigen states by successfully inserting this large intra-cavity Faraday rotator. After reflexions and optical simulations using the software *LaserCalc*, a cavity with an extended M-shaped geometry was chosen for stability, flexibility, adaptability and compactness reasons.

For this new experiment we used the same 12 $\mathrm{In}_{22\%}\mathrm{Ga}_{78\%}\mathrm{As}/\mathrm{GaAs}_{95\%}\mathrm{P}_{5\%}$-QW VECSEL (GaAs615) maintained at 285 K with a Peltier thermo-electric cooler. Figure 4.21 schematized the complete experimental setup. The structure is pumped in a continuous regime throughout the experiment and the laser threshold is measured as being $P_{threshold} = 300$ mW. The pump system consists in the same 808 nm pigtail multimode laser diode delivering up to 2 W and focused on the gain medium to a 100 μm spot with a normal incidence. As previously, the pump light is circularly-polarized after collimation (f_1) using a high power polarizer-cube combined with a

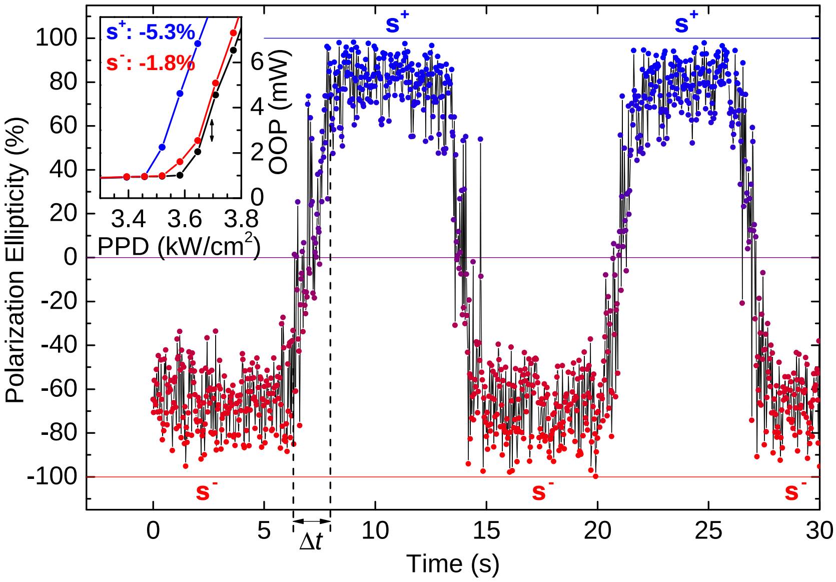

Figure 4.22: Time evolution of the laser output polarization ellipticity when switching the pump polarization from σ^+ to σ^-. The inset presents the evolution at threshold of the Output Optical Power (OOP) as a function of the Pump Power Density (PPD) for different pumping polarization orientations: ↕ linear in black, σ^+ in blue and σ^- in red. The transition time Δt correspond to the time needed to rotate the QWP of the pumping system.

$\frac{\lambda}{4}$-wave plate and then focused on the VECSEL surface (f_2). The optical cavity is composed of five mirrors including the 1/2-VCSEL DBR, two 99.9% reflectivity 50 mm radius of curvature concave mirrors (M_2, M_3) and two plane mirror (M_1, M_4) to close the cavity. We used 99.5% reflectivity for M_1 to facilitate the fiber-coupling with a Fabry-Perot interferometer and 99.9% reflectivity for M_4 to limit the saturation of the polarimeter's head. The angle between M_2 and M_3 was minimized in regard to the limit of the setup and is about 30 °. The distances between the mirrors have been precisely estimated using computer simulations for optimal laser stability.

Finally, the cavity length is 56 cm giving a photon lifetime of 180 ns, which is much higher than the carrier lifetime in stimulated emission regime at about twice the threshold [333] (around 1 ns) ensuring a class-A dynamical behavior for the laser. Such a long cavity also implies that the laser is highly multimode longitudinally. At the output of M_1 we used a Fabry-Perot interferometer to visualize the laser oscillation. The Faraday isolator is used to reduce the laser perturbation by preventing any photon re-injection in the cavity. The laser polarization is analysed at the output of M_4 with a Thorlabs PAX5710 polarimeter combining a rotating 1/4-Wave plate (QWP), a polarizer and a Powermeter. Here, the separation of the laser emission (1000 nm) from pump reflexions (808 nm) is done by choosing the right wavelength calibration (980 nm) in the polarimeter software setups.

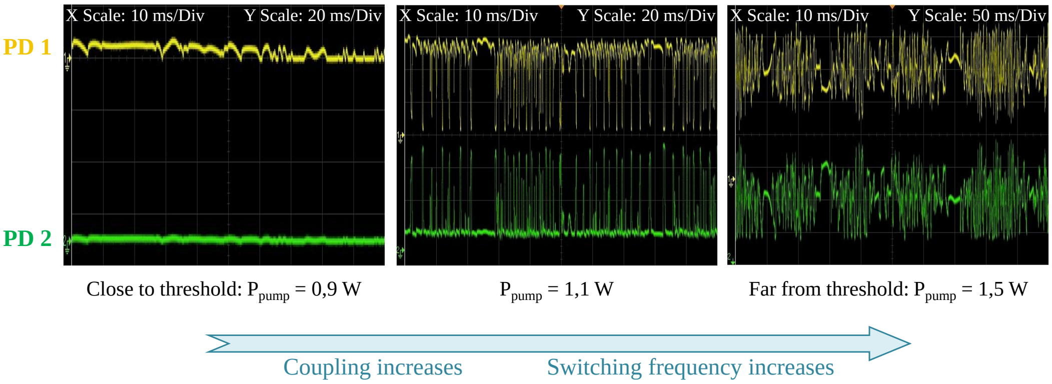

Close to threshold: P_{pump} = 0,9 W

P_{pump} = 1,1 W

Far from threshold: P_{pump} = 1,5 W

Figure 4.23: Evolution of the two circularly polarized orthogonal modes when increasing the pumping power.

4.5.2.2 Experimental observations

This time, when manually switching the pump polarization from right to left circular polarization, we observed a corresponding switch from σ^+ to σ^- of the laser polarization. This witnesses a sufficient spin injection in the active medium of the 1/2-VCSEL (Figure 4.22). Nevertheless, on the other hand, we observed a threshold reduction of few percent when pumping circularly compare to the linearly polarized pumping (Inset Figure 4.22). But, the analytical model and the simulations presented in section 2.2.3.2 clearly highlight that the threshold reduction under spin-injection normalized to the threshold under unpolarized injection J_T is a direct probe of the spin-injection efficiency in the system. Consequently, this weak threshold reduction characterizes a weak effective spin-population difference in the active medium of the laser resulting in a gain dichroism of few percent. The threshold reduction difference between σ^+ and σ^- pumping can be explain by the broken symmetry between the non-saturated gain of the right- (G_R) and left- (G_L) circularly polarized modes due to geometrical consideration. The laser tends to more easily lase on the σ^+ mode as G_R is intrinsically higher than G_L.

We also studied the relative dynamic of both circularly polarized modes as a function of the pump power using a polarization dependent beam splitter, two Photo-Diodes (PD 1 and PD 2) and an oscilloscope. When increasing the pump power, we clearly identified an increase of the coupling between both circularly polarized modes behavior. The oscillation of one circularly polarized mode in the cavity seems to disable the oscillation of the orthogonal mode. Additionally, the switching frequency from a mode to another also increases with the pumping power (Figure 4.23).

4.5.3 Analysis of the physical mechanisms: The Lamb model

The mechanisms inducing this complete polarization switch despite such a small effective spin-injection remain to be understand. We previously showed using a vectorial model (section 4.3.2) that it is possible to prepare the laser's eigen states by inserting a Faraday rotator inside the laser cavity. Doing so, the action of a gain circular dichroism induced by the spin-injection translates into intensity variations of the eigen states or even a complete switch from an eigen state to another. Such a configuration is interesting to probe the impact of the spin injection. Indeed, we show that the insertion of the Faraday rotator mask the effect of the residual linear birefringence in the active medium. Consequently, the gain circular dichroism induced by the spin-injection directly translates into a gain disequilibrium between both eigen state. This disequilibrium, even weak, can trigger a complete switch from an eigen state to the other provided that the non-linear coupling constant is high enough (which is the case in our VECSEL). In other words, it is possible to fabricate a laser source exhibiting a high DoCP and for which the switch from a σ^+-polarized to a σ^--polarized eigen state can be achieve even with a moderate effective spin-injection.

4.5.3.1 Mathematical formalism

To pull the blind on these mechanisms, we turned toward Lamb Model for a class-A, Two-mode operation laser [268]. The laser being class-A, it is possible to adiabatically neglect the population inversion. In this case, the temporal evolution of the two modes intensities can be simply described by two coupled differential equations of the first order [268]:

$$\begin{cases} \dot{I}_R = I_R \left(G_R - \beta_R I_R - \theta_{RL} I_L \right) \\ \\ \dot{I}_L = I_L \left(G_L - \beta_L I_L - \theta_{LR} I_R \right) \end{cases} \tag{4.38}$$

where I_R (respectively I_L) represents the intensity of the right (left) circularly polarized mode and G_R (G_L) is the non-saturated gain of the right (left) circularly polarized mode. β_R (β_L) stands for the self-saturation coefficient of the right (left) circularly-polarized mode while θ_{RL} (θ_{LR}) is the cross-saturation coefficient of the right (left) circularly-polarized mode.

To simplify the problem, we assume that the self-saturation and cross-saturation coefficients for both polarization modes are equals and that the non-saturated gains differ from one another by the gain dichroism induced by the spin-injection $\Delta G = G_R - G_L$. We adopt the following notations: $\beta_R = \beta_L = \beta$, $\theta_{RL} = \theta_{LR} = \theta$, $G_R = \bar{G} + \frac{\Delta G}{2}$ and $G_L = \bar{G} - \frac{\Delta G}{2}$ where $\bar{G} = \frac{G_R + G_L}{2}$ is the average gain. The system of equation (4.38) can then be rewritten in the stationary regime where $\dot{I}_R = 0$ and $\dot{I}_L = 0$:

$$\begin{cases} I_R\left[\left(\bar{G}+\dfrac{\Delta G}{2}\right)-\beta I_R-\theta I_L\right]=0 \\ \\ I_L\left[\left(\bar{G}-\dfrac{\Delta G}{2}\right)-\beta I_L-\theta I_R\right]=0 \end{cases} \tag{4.39}$$

The intensity of the two polarization modes can be extracted from the resolution of this equation system. Three cases can be distinguished:

A) **General case, both eigen states are oscillating $I_R \neq 0$ and $I_G \neq 0$:**

In this case the modes intensities can be expressed as:

$$\begin{cases} I_R=\dfrac{\bar{G}(\beta-\theta)+\frac{\Delta G}{2}(\beta+\theta)}{\beta^2-\theta^2} \\ I_L=\dfrac{\bar{G}(\beta-\theta)-\frac{\Delta G}{2}(\beta+\theta)}{\beta^2-\theta^2} \end{cases} \tag{4.40}$$

The introduction of the Lamb non-linear coupling constant enables to give a physical meaning to these expressions. This constant is a phenomenological parameter formalizing the empirical behavior of laser polarization dynamics [268]:

$$C=\frac{\theta_{RL}\theta_{LR}}{\beta_R\beta_L}\equiv\frac{\theta^2}{\beta^2} \tag{4.41}$$

The modes intensities can be rewritten as a function of C and the normalized gain circular dichroism $\Delta G_N=\frac{\Delta G}{\bar{G}}$:

$$\begin{cases} I_R=\dfrac{\bar{G}}{\beta}\dfrac{(1-\sqrt{C})+\frac{\Delta G_N}{2}(1+\sqrt{C})}{1-C} \\ I_L=\dfrac{\bar{G}}{\beta}\dfrac{(1-\sqrt{C})-\frac{\Delta G_N}{2}(1+\sqrt{C})}{1-C} \end{cases} \tag{4.42}$$

The simultaneous oscillation of both modes is only possible for $C<1$. We can place ourself in this framework as the coupling constant of similar VECSEL has been measured close but inferior to 1: $C\simeq 0.9$ [343]. Additionally simultaneous oscillation regimes have already been observed experimentally. The system of solution (4.42) shows an opposite evolution of the intensities but also that their evolution accelerate when $C\mapsto 1$.

B) **If only the right circularly polarized mode oscillates, $I_R \neq 0$ and $I_G = 0$:**

In this case:

$$\begin{cases} I_R = \dfrac{\bar{G}}{\beta}\left(1 + \dfrac{\Delta G_N}{2}\right) \\ \\ I_L = 0 \end{cases} \tag{4.43}$$

The intensity of the σ^+-polarized mode evolves linearly with the normalized gain circular dichroism ΔG_N and is independent from the non-linear coupling constant

C) **If only the left circularly polarized mode oscillates, $I_R = 0$ and $I_G \neq 0$:**

In this case:

$$\begin{cases} I_R = 0 \\ \\ I_L = \dfrac{\bar{G}}{\beta}\left(1 - \dfrac{\Delta G_N}{2}\right) \end{cases} \tag{4.44}$$

The intensity of the σ^--polarized mode evolves linearly with the normalized gain circular dichroism ΔG_N and is independent from the non-linear coupling constant

4.5.3.2 Synthesis and conclusions

As both modes are oscillating in the cavity, we have to place ourself in the general case A. Figure 4.24 represent the evolution of the two eigenstate intensities as a function of the normalized gain dichroism $\Delta G_N = \frac{\Delta G}{G}$ for different coupling constant. When $C = 0$, the modes intensities evolve independently and are proportional to the gain circular dichroism. When C increases, the oscillation of one mode saturates the gain of the other one leading to a limited range of simultaneous oscillations of the two modes. When C becomes close to 1, as expected in our $\frac{1}{2}$-VCSEL structure where [343] $C \simeq 0.9$, the range of simultaneous oscillations becomes very narrow favoring then an easier switch from an eigenstate to the other one. In this case, a polarization switch can occur even for a very small ΔG. As presented in figure 4.24, for $C = 0.9$, a normalized gain dichroism of about 10% is sufficient to tip over the polarizations. The average gain $\bar{G}$ of such a structure being around 1% [333], a gain circular dichroism of about $\Delta G = 0.1\%$ is sufficient to fully switch the laser

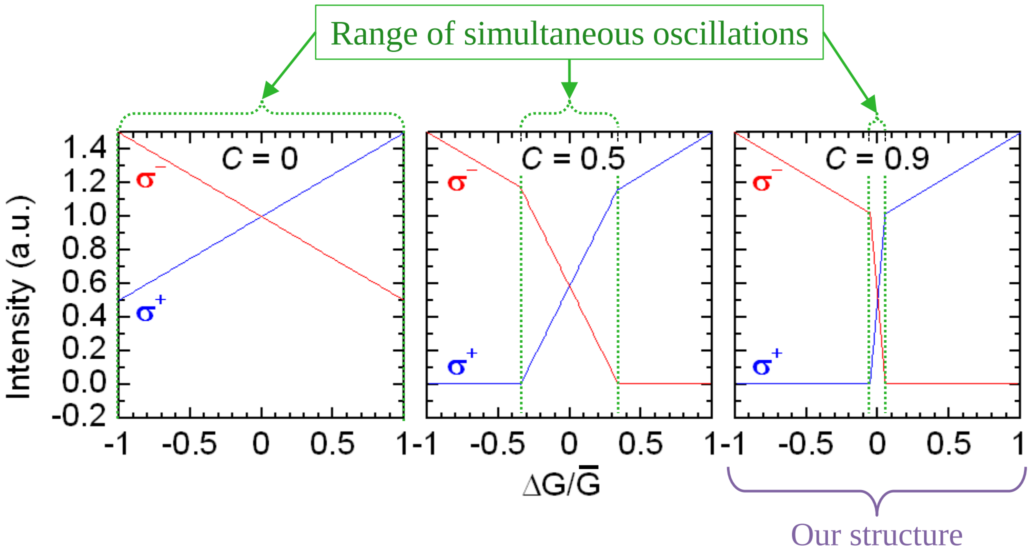

Figure 4.24: Intensities evolution of the two eigen-polarization as a function of the normalized gain dichroism for three values of coupling constant C: 0, 0.5 and 0.9.

polarization thanks to the leverage effect of the non-linear coupling constant.

We can now roughly estimate the effective spin injection in the $\frac{1}{2}$-VCSEL QWs using the measured threshold reduction values (Inset Figure 4.22). Averaging between the threshold reduction for the σ^+- and σ^-- modes enables to minimize the impact of the cavity geometry on the modes selection. Doing so we find an average threshold reduction for the optically spin-injected VECSEL of 3.55%. But we also know from the rates equations simulation performed by Holub & Bhattacharya on GaAs/AlGaAs-MQW VCSEL [84] (section 2.2.3.2) that the limit case of a 100% spin-polarized carriers induces a maximum threshold reduction of 50%. By assuming in first approximation a linear dependence between the injected spin-polarization and the associated threshold reduction, this average threshold reduction of 3.55% observed in our system corresponds to an effective spin-polarization $P_S \approx 7.1\%$ in the VECSEL QW. This value is an order of magnitude greater than the theoretical inferior limit (0.1%) required to trigger a polarization switch. Therefore we understand here how such a moderate effective spin-injection generates a polarization switch from a circular eigen state to another.

In terms of amplification of the spin information, we clearly see that an effective spin-injection $P_S \approx 7.1\%$ leads to the emission of circularly-polarized modes with a DoCP of 80%. This amplification of the spin-information injected in the laser by a factor of 11 can be attributed to the leverage effect of the non-linear coupling constant C. This empirical constant accounts for the gain competition between the laser modes trying to oscillate in the cavity. In our case where $C = 0.9$, the mode selected at threshold will be the one exhibiting the highest gain. Generally, for a mode to be selected at threshold, its associated gain does not need to be extremely high but just higher than those of the other modes.

Finally, we can compare this estimated $P_S \approx 7.1\%$ to the gain circular dichroism ΔG extracted from the previous birefringence measurements of the same $\frac{1}{2}$-VCSEL (GaAs615). We remind that a $\Delta G_N \approx 4\%$ corresponding to a net gain circular dichroism $\Delta G \approx 0.4\%$ (assuming $\bar{G} = 1\%$) was shown to be an inferior limit required to simply compensate the average linear birefringence. For the value $\Delta G \approx 0.4\%$, the VECSEL is set in an artificial isotropic state for the TE- and TM-modes and both modes are supposed to still be linearly-polarized and oriented at 45° from the ordinary $[0\bar{1}1]$ and extraordinary [011] axis (section 4.4). The estimated effective spin-polarization in the VECSEL's QW $P_S \approx 7.1\%$ is greater than this minimum value $\Delta G \approx 0.4\%$ required to compensate the birefringence in the structure. Consequently, this value of P_S should be sufficient to overpower the linear birefringence and set a circularly-polarized emission. However, in the first optical spin-injection experiment (linear cavity, no Faraday rotator) no influence of the spin-injection could be seen on the modes polarization even if the VECSEL was optically spin-injected with an approximately similar efficiency. The same observation was also made in the second experiment after withdrawing the Faraday rotator from the M-Cavity. We conclude that although the effective spin-polarization injected in the VECSEL compensates the linear birefringence, the laser might still be just above the compensation point ($\frac{1}{4}\Delta G_N^2 = \sin^2 \frac{\gamma'}{2}$) and P_S is not high enough to even trigger oscillations on elliptically-polarized modes. This locking of the laser on linearly-polarized modes might also be favored by an additional residual linear birefringence originating from the cold cavity. Indeed, contrary to the short linear cavity used to perform the birefringence measurements, this extended M-cavity is composed of four additional mirrors each of them introducing a residual birefringence. Consequently, we can make the hypothesis that the effective spin-injection required to compensate the total linear birefringence of the M-Cavity VECSEL might be sensibly higher than in the previous birefringence experiment from where the value $\Delta G \approx 0.4\%$ has been extracted. As predicted by the vectorial model (section 4.3.2), the importance of the intra-cavity Faraday rotator is thus clearly highlighted. The emission of circularly-polarized modes with a DoCP of 80% shows how the circular birefringence artificially introduced by the Faraday rotator compensate the intrinsic linear birefringence of the $\frac{1}{2}$-VCSEL and enable us to reveal the influence of the injected spin-polarized carriers on the modes polarization.

One has to note that the DoCP measurement of 80% reported here has been performed on a carefully chosen operating point on the $\frac{1}{2}$-VCSEL surface, for a 100 μm pump spot and for a given pumping power. Just like monolithic VCSELs, $\frac{1}{2}$-VCSELs exhibit local strain variations between different regions of the structure and thus local variation of birefringence γ. As shown by the Spin-Flip Model in the case of two linearly polarized mode (section 2.2.3.3), for a given linewidth enhancement factor α of the semiconductor laser, polarization switching can occur for variation of pumping power and birefringence. One can note that the intrinsic birefringence γ is a fixed characteristic of a given VECSEL structure and is though independent of the optical pumping. Nevertheless, as witnessed during the birefringence measurements (section 4.4), a pump induced birefringence also influences the dynamical behavior of the device (Thermal effects). To summarize, the spin-injected VECSEL is a system highly sensitive to small perturbations. By changing the pump parameters (power and/or spot size), the operating point on the $\frac{1}{2}$-VCSEL surface but also the VECSEL temperature, the measured DoCP would have been either higher or lower. Complementary systematic studies focusing on: **(i)** the influence of the pump parameters and **(ii)** the influence of the external cold-cavity shape would provide interesting additional insights on the VECSEL behavior under spin-injection.

In any case, this experiment highlights the fundamental difference between spin-injection in LED and spin-injection in VECSEL. In this section, we showed how a spin-injection of 7.1% in VECSEL leads to an output DoCP of 80% with a complete polarization switch at room temperature while in a Spin-LED an input P_S of 7.1% would give at best an output DoCP of 7.1%. Once the VECSEL oscillates on a circularly-polarized eigen state, the system has by default a high DoCP. The strong non-linear coupling between the two circularly polarized modes favors the polarization switch despite the generation of a very low net gain circular dichroism in the laser ($\Leftrightarrow$ a very low effective spin injection in the active medium). Consequently, even if the spin-injection mechanism is not highly efficient due to the combination of several spin-relaxation mechanisms, one can still obtain a polarization switch with a high DoCP for both circularly polarized modes at room temperature.

4.6 Discussion on the characteristic lifetimes

A side from the colossal influence of the non-linear amplification effects on the polarization selection of the VECSEL, we still need to understand why an intra-cavity Faraday rotator is required to prepare laser oscillations on circularly polarized eigen mode. Indeed other groups working with monolithic VCSEL successfully reported polarization manipulation using spin injection without any need of a non-reciprocal material in the laser cavity. As discussed in the vectorial model (section 4.3), the influence of the ratio between the linear birefringence and the gain circular dichroism is indisputable but to push further the understanding of the system, one has to pay interest to the ratio between the carrier lifetime τ and the spin lifetime τ_s in the VECSEL. These two parameters fix the average spin population imbalance in the structure and consequently the gain circular dichroism. The importance of the ratio between the carrier lifetime τ and the spin lifetime τ_s in the active medium of spin-optoelectronic devices has already been introduced in the state-of-the-art (section 2.2.1.2). This has been highlighted in the previous chapter during the study focusing on the optimization of the electrical MTJ spin-injector using Spin-LED.

As opposition with Spin-LED where τ_r stays relatively constant as the device only emits in a spontaneous emission regime, the carrier lifetime in VECSEL and in lasers in general, strongly depends on the operation regime. In our VECSEL the carrier lifetime is mainly radiative under the chosen experimental operation conditions. The radiative lifetime of an excited electronic state in the gain medium of the laser is the lifetime which would be obtained if radiative decay via the unavoidable spontaneous emission were the only mechanism for depopulating this state [347]. Depending on the pumping rate η and the operation regime, the radiative lifetime can change by one or sometimes two orders of magnitude. This has a strong impact on the ratio between τ and τ_s and consequently on the laser output DoCP.

4.6.1 Radiative lifetime dynamics in a laser

In a laser the global recombination of the excited carriers can be divided in two categories. The radiative recombination generating spontaneous or stimulated photons depending on the operation regime of the laser and the non-radiative recombination source of phonons and lattice vibrations. In CW pumping and stationary regime, the different types of recombination mechanisms occurring in the laser's active medium are linked by:

$$R = A \cdot N + B \cdot N^2 + C \cdot N^3 \tag{4.45}$$

where R is the total recombination rate and N is the carrier density in the QW. The coefficient A is the trap and surfaces recombination coefficient accounting essentially for recombination on defects (Electrons lifetime on defects: vacancy, impurities,...). B represents the radiative bi-molecular recombination coefficient ($e^- - h^+$) while C is the non-radiative Auger coefficient. The recombination time τ_r can then be derived from (4.45):

$$\tau_r = \frac{1}{A + B \cdot N + C \cdot N^2} \tag{4.46}$$

We also define the radiative quantum yield η_i quantifying the conversion rate of the carrier density into radiative recombination:

$$\eta_i = \frac{BN}{A + B \cdot N + C \cdot N^2} \tag{4.47}$$

Different orders of magnitude for τ_r can then be distinguished depending on the operation regime of the laser:

- **Below threshold, Spontaneous emission regime:** For a low pump density, $N \ll N_{trans}$, where N_{trans} is the carrier density at transparency. This leads to $BN \ll A \implies \eta_i \ll 1$. In the spontaneous emission regime, the average carrier lifetime is completely dominated by spontaneous recombination and one can expect a carriers' non-radiative lifetime of around: $\tau_{non-radiative} \approx$[5-50] ns at room temperature. The non-radiative lifetime is directly proportional to the defect density of the structure. The better the crystalline quality, the longer the non-radiative carrier lifetime will be.

- **Above threshold, Stimulated emission regime (moderate pumping):** When the pump density is above threshold, $N \approx N_{trans}$. At transparency, the Fermi levels start to be tangential to the bands and everything absorbed is re-emitted. This leads to $BN > A \implies \eta_i \mapsto 1$. In the stimulated emission regime the carrier lifetime is drastically reduced and mainly limited by the carrier relaxation time from the pump level to the lasing level $\tau_r \approx 50$ ps, which is much shorter than the spin lifetime at room temperature [228]. In the case of a moderate pumping, when staying close to threshold, the number of electrons lost by Auger recombination remains tolerable and the quantum yield η_i is high enough to ensure laser operation ($B \cdot N > C \cdot N^2$).

- **Above threshold, Auger regime (very high pumping):** In this case most of the excited electrons are lost on non-radiative Auger recombinations: $B \cdot N << C \cdot N^2 \implies \eta_i \mapsto 0$. In this regime the stimulated emission breaks down and the laser stops emitting. However, in the case of V(E)CSEL, the laser usually stops emitting when increasing the pumping several time above threshold as the system faces a thermal roll-over before the Auger regime.

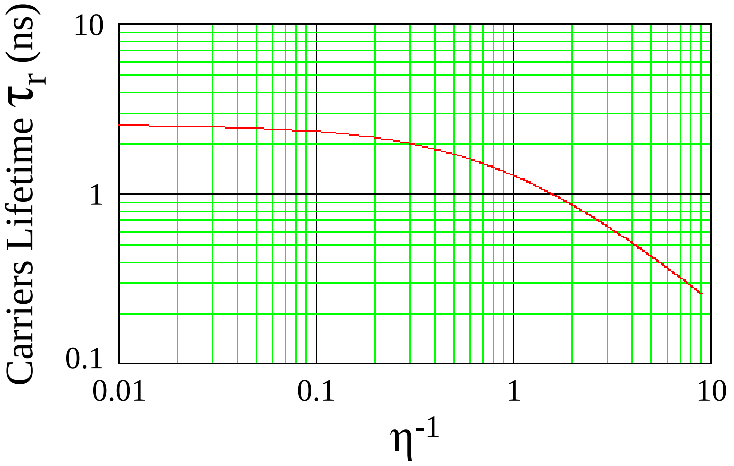

Figure 4.25: Evolution of the carrier lifetime τ_r as a function of the pumping rate η in the stimulated emission regime for the VECSEL GaAs615. $\eta = 1$ defines the threshold.

Figure 4.25 illustrates the variation of the electron lifetime (essentially radiative above threshold) in the QW as a function of the pumping rate for the structure GaAs615 in the stimulated emission regime. $\eta = 1$ defines the threshold. Below threshold in the spontaneous emission regime and close to threshold the carrier lifetime is expected around 2-3 ns. This prediction is coherent with carrier lifetime measured in similar VECSEL that where experimentally estimated around $\tau_{radiative} \approx$[2-3] ns above but close threshold [333]. In these structures the radiative quantum yield is around $\eta_i = 80\%$. When the pumping rate increases, τ_r starts decreasing and a carrier lifetime as low as 200 ps could be expected 8 times above threshold. A spin lifetime of around 10 ps can be reasonably expected in such InGaAs QW at room temperature [348]. Consequently, combined with the non-linear amplification effects, such a spin-lifetime might provide a sufficient gain circular dichroism to compensate the residual linear birefringence of the system and lock the laser on circularly polarized eigen states.

According to the evolution of the carrier lifetime as a function of the pumping rate, the best solution to optimize the $\frac{\tau_r}{\tau_s}$-ratio would intuitively appear to push the pumping several time above threshold. Unfortunately this action would also bring into play spin-depolarizing mechanisms. When increasing the excitation power, electrons with greater wave vector $\vec{k}$ are engaged in the recombination process. Those initially spin-polarized electrons of higher energy $E(\vec{k})$ relax through the Dyakonov-Perel mechanism at a much faster rate. Additionally, in the case of optical pumping important thermal gradients rise in the structure and can potentially have a negative influence on the spin lifetime. It directly causes important lattice vibration and phonon generation in favor of the Elliot-Yafet spin-relaxation mechanism which considerably reduces the spin-lifetime: $\tau_s \cong \tau_{sf}^{EY}(T) \propto \frac{\tau_p(T)}{T^2}$. Additionally, thermal strains on the active medium can potentially increase the effective total birefringence of the structure and compensate the gain circular dichroism generated by spin injection in favor of linearly-polarized eigen modes. As for optical pumping, under high electrical pumping thermal effects could reduce τ_s in the $\frac{1}{2}$-VCSEL's QW through the DP- and EY-mechanism. In short, the situation is non-trivial and a balance has to be found between maximizing the spin lifetime and the minimizing the carrier lifetime. Experimentally, this optimum functioning point is difficult to find in dynamics operation.

With TRPL measurement we measured the carrier lifetime τ_r and the spin lifetime τ_s of our VECSEL structure design for optical pumping. These extracted characteristic lifetime are then compared with state-of-the-art measurements achieved on monolithic Spin-VCSEL.

4.6.2 Time-Resolved Photo-Luminescence measurements

The study of the carrier lifetime τ and the spin lifetime τ_s in the VECSEL is performed by Time Resolved Photo-Luminescence (TRPL) using a pulsed Ti:Sa laser with a pulsed width of 1.5 ps and a repetition rate of 80 MHz, combined with a streak camera (S1-Photocathode) for the detection. The temporal resolution of the streak camera depends on the selected time range. A temporal resolution of 17 ps is chosen for the measurements performed on the VECSEL. The objective is to extract precise measurements of τ and τ_s in order to estimate the effective average percentage of spin polarized electron recombining in the QW.

The measurements on the $\mathrm{In_{20\%}Ga_{80\%}As/GaAs_{95\%}P_{5\%}}$ QW used as the active medium of the VECSEL are performed by varying several experimental parameters such as the excitation energy of the photon (excitation within the barriers or intra-QW), the power regime and the temperature. Measurements were realized at both low (10 K) and room temperature (300K) and for an average excitation power ($P_{Ti:Sa}$) ranging from 1 μW up to 10 mW with a 50 μm-diameter spot. This gives a peak power range between 8 mW and 80 W ($P_{peak} = \frac{P_{Ti:Sa} \times 12ns}{1.5ps}$). Excitation powers are kept relatively low in order to mainly explore the spontaneous regime.

First, *k.p* simulations considering a 8-bands structure (2 CBs - 2 HH-Bands - 2 LH-Bands - 2 Split-Off Bands) in $\mathrm{In_{20\%}Ga_{80\%}As/GaAs_{95\%}P_{5\%}}$ QW were performed using the approximation of infinite thickness barriers to estimate the values of the different optical transitions [349]. Figure 4.26 schematizes the band diagram derives from the simulation. This preliminary step was necessary in order to identify the different excitation energies required to target specific band-to-band transitions and then calibrate the $Ti:Sa$ laser accordingly. Complementary information on the experimental setup, the band-to-band transition energies and the different $Ti:Sa$ wavelengths used to performed the TRPL measurements can be found in Appendix E, Section E.1 and E.2.

The results of the TRPL measurements performed on the GaAs615 VECSEL with $\mathrm{In_{20\%}Ga_{80\%}As/GaAs_{95\%}P_{5\%}}$ QW are display below. Different cases corresponding to different experimental conditions are reported. In every cases, the excitation light emitted by the Ti:Sa laser is circularly polarized (σ_+ or σ_-) and the detection system is configured to detect circularly polarized light. The DoCP of the

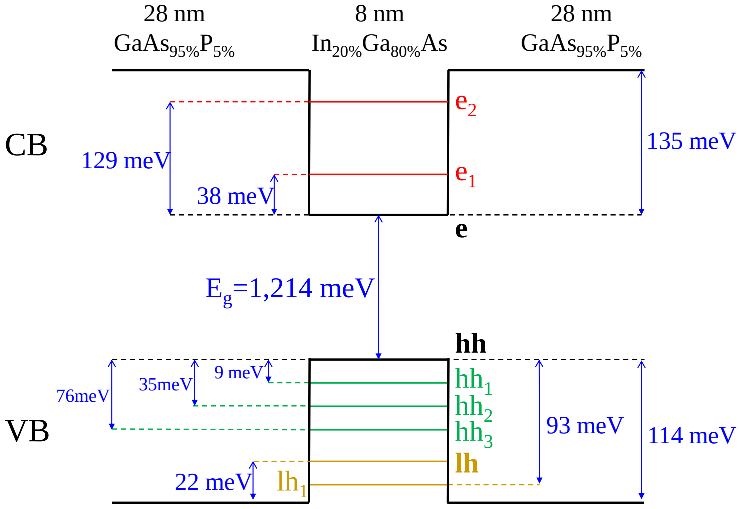

Figure 4.26: Schematic representation of the InGaAs/GaAsP QW band structure with the associated transition energies extracted from $k.p$ simulations in the approximation of infinite thickness barriers [349].

VECSEL emission can then be calculated from the measured I_{σ_+} and I_{σ_-} intensities: $DoCP = \left|\frac{I_{\sigma_+} - I_{\sigma_-}}{I_{\sigma_+} + I_{\sigma_-}}\right|$. A control experiment was primarily performed by exciting the system with linearly-polarized light to ensure that the measurements were not biased. A weak artifact DoCP of -1% was measured witnessing a good alignment of the experimental setup (see Figure 4.27 (b)). Note that in a $\frac{1}{2}$-VCSEL designed for electrical pumping, one has to take into account the internal electric field due to the $p-i-n$ junction. This field can be screened depending on the density of photo-generated carriers and this may have an influence on the characteristic relaxation time. In our case this problem is ruled out as we study a $\frac{1}{2}$-VCSEL designed for optical pumping with no p-i-n junction. For clarity and presentation reasons I personally chose not to include here every graph related to every single measurements. The curious reader is cordially invited to refer to Appendix E, section E.3, for complementary information.

A) Low temperature measurements (10 K):

1. Carrier lifetime measurements:

i. Non-resonant excitation above the GaAsP Barriers:

The excitation energy is chosen above the gaps of GaAs and GaAsP $E_{Ti:Sa} = 1.589$ eV corresponding to a wavelength of $\lambda_{Ti:Sa} = 780$ nm. In these experimental conditions, the measured carrier lifetime τ is in the range of $[410 \pm 20ps - 550 \pm 20ps]$ for the range of excitation power $P_{Ti:Sa}$ comprise between $[1\mu W - 100\mu W]$. We observe a longer rising time for the luminescence in the first pico-seconds when increasing the excitation power. Indeed, the number of carrier generated in the GaAsP barriers increase as well as the average diffusion time toward the QW where radiative recombinations occur.

ii. Intra-QW excitation below $e1 - lh1$ transition energy:

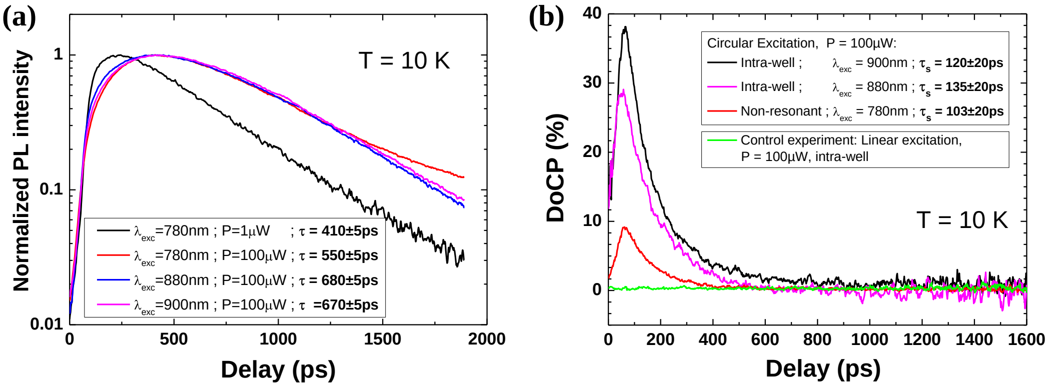

Figure 4.27: Time Resolved Carrier lifetime and Spin lifetime measurements comparison: (a) Carrier lifetime measurements at T=10 K for non-resonant (780 nm) and (880 - 900 nm) intra-well pumping with different excitation powers of the VECSEL structure. **(b)** Spin lifetime measurements at T=10 K for non-resonant (780 nm) and (880 - 900 nm) intra-well pumping under an excitation power of 100 μW. Note that the photo-generated carriers densities are very different in these two modes of excitation due to the strong difference in light absorption. The control experiment under linearly-polarized excitation ensures that the measurements are not biased (DoCP≈0%).

In this case, the excitation energy $E_{Ti:Sa} = 1.424$ eV corresponding to a wavelength of $\lambda_{Ti:Sa} = 870$ nm is chosen to trig an excitation below $e1 - lh1$ transition energy. Therefore the active transitions in this measurements are mainly between the CB and the HH-band (Figure 4.26):

- **When $\lambda_{Ti:Sa}$ is fixed at 870nm:** The carrier lifetime τ varies little with the excitation power when the latter is kept relatively low. When increasing the excitation power from 0.3 mW up to 1 mW, τ only changes by 5 ps which stays in the error bar of the measurement setup giving an estimated carrier lifetime of $\tau = 685 \pm 20$ ps on this power range (see figure E.2 in Appendix E, section E.3). However, when the excitation power increases up to 3 mW and then 10 mW, the carrier lifetime significantly increases as well to $\tau = 875 \pm 20$ ps and $\tau = 900 \pm 20$ ps respectively (figure E.2 in Appendix 5, section E.3).
- **When $P_{Ti:Sa}$ is fixed to 100 μW($\Leftrightarrow P_{peak} = 800$ mW):** Measurements were also performed to evaluate the dependance of the carrier lifetime on the excitation wavelength λ_{exc}. By slightly tuning λ_{exc} from 880 nm ($\Leftrightarrow E_{Ti:Sa} = 1.408$ eV) to 900 nm ($\Leftrightarrow E_{Ti:Sa} = 1.377$ eV), τ was seen to sensibly decrease from 680$\pm$20 ps to 670$\pm$20 ps. This highlight the weak dependance of the carrier lifetime on λ_{exc}, at least for a low excitation power (Figure 4.27 (a)).

Comments: To summarize, whatever the excitation conditions are (intra-QW or non-resonant in the barriers, excitation power range), the carrier lifetime measured at 10 K is below 1 ns in the window $\tau \in [410 - 900]$ ps. Let's note that at low temperature (10 K) the emission is mainly due to the heavy-exciton (bounded $e^- - h^+$ pairs due to the Coulomb interaction) line. However, as the excitation is non-resonant with this line, the luminescence dynamics is controlled by a complex mixing of free electron-Heavy Hole pairs and heavy excitons. The characteristic decay time of the photo-luminescence can be seen in first approximation as an effective electron lifetime.

2. **Spin lifetime measurements:**

   One has to keep in mind that at 10 K we detect the luminescence of the heavy-exciton line. However, as we do not perform strictly resonant excitation of this line, the hole spin relaxation is very fast (few ps). Accordingly, we can consider that the decay of the circular polarization rate is controlled by the electron spin lifetime.

   i. **Non-resonant excitation above the GaAsP Barriers:**
   The excitation energy is chosen above the gaps of GaAs and GaAsP $E_{Ti:Sa} = 1.589$ eV corresponding to a wavelength of $\lambda_{Ti:Sa} = 780$ nm. The DoCP and the spin lifetime are measured for $P_{Ti:Sa} = 100$ μW and we find an initial DoCP $\approx 8.5\%$ with $\tau_s = 105 \pm 15$ ps (Figure 13.3 (b)). For a range of excitation power $P_{Ti:Sa} \in [1\mu W - 100\mu W]$, we find that the initial DoCP and the initial τ_s are decreasing with power and are respectively in the windows $[8.5\% - 17.5\%]$ and $[103 \pm 20ps - 170 \pm 20ps]$.

   ii. **Intra-QWs excitation:**
   Here, the excitation is kept intra-well while slightly tuning the excitation wavelength to evaluate the spin lifetime dependency on λ_{exc}. For these measurements, the excitation power is fixed to $P_{Ti:Sa} = 100$ μW. First, a control experiment was performed by exciting the system with linearly-polarized light and detecting the emitted DoCP to ensure that the measurements were not biased. Doing so, a neglectful artifact DoCP of -1% was identified witnessing a good alignment of the experimental setup (see Figure 4.27 (b)). Then, for an excitation at $\lambda_{Ti:Sa} = 880$ nm ($E_{Ti:Sa} = 1.408$ eV), the recorded initial DoCP reaches approximately 28% with a spin lifetime estimated around $\tau_s = 135 \pm 15$ ps, while for an excitation at $\lambda_{Ti:Sa} = 900$ nm ($E_{Ti:Sa} = 1.377$ eV) the initial DoCP increases up to 38% and the measured spin lifetime decreases down to $\tau_s = 120 \pm 15$ ps (Figure 4.27 (b)). So, for intra-well excitation, the initial DoCP decreases when the energy of photons increases. It can be explained by the mixing between the HH and LH valence bands out of the Γ-point, when $e^- - h^+$ pairs are photo-generated with $\vec{k} \neq \vec{0}$.

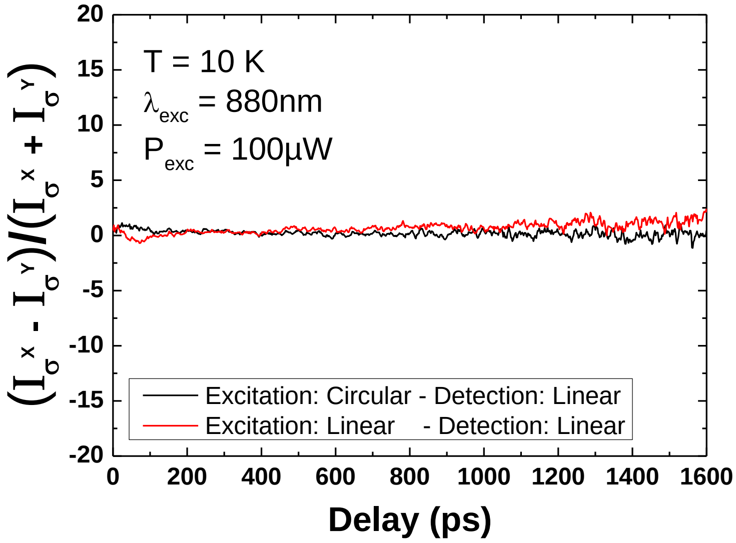

Figure 4.28: Measurements of the linear polarization degree under linearly- and circularly-polarized excitation by detecting linearly-polarized light along the [110] and [$1\bar{1}0$] crystallographic axis.

General comments:

- The measured spin lifetime at 10 K is in the window $[103 - 170]$ ps depending on the excitation conditions (photon energy, excitation power).
- Under non-resonant excitation, the initial DoCP is clearly lower. When electrons are excited in the 28 nm thick GaAsP barriers, which are thick enough to be consider as a bulk like material, the maximum photo-generated spin-polarization achievable is only 50% (and not 100% as the in QW) due to the optical selection rules [168]. Subsequently, when these electrons diffuse from the barrier toward the QW, they induce a decrease of the average spin-polarization in the active medium of the VECSEL and consequently reduce the emitted DoCP. It is important to note that this mechanism is hosted by the VECSEL during laser operation. The broad pumping at 808 nm excite the GaAsP barriers as well as both the $HH - CB$ and $LH - CB$ transitions leading to a maximum achievable spin-polarization of 50% in the QW.
- **Degree of Linear Polarization:** An additional experiment was performed to identify the Degree of Linear polarization $\left(DoLP = \frac{I_{\sigma X} - I_{\sigma Y}}{I_{\sigma X} + I_{\sigma Y}}\right)$ under both linearly- and circularly- polarized excitation. The detection axis X and Y are chosen along crystallographic axis [110] and [$1\bar{1}0$] respectively. The excitation energy is chosen intra-well at $E_{Ti:Sa} = 1.408$ eV corresponding to a wavelength of $\lambda_{Ti:Sa} = 880$ nm and the average excitation power is fixed to $P_{Ti:Sa} = 100\ \mu$W. For both type of excitation, the linear polarized emission was found to be very minor (Figure 4.28). A DoLP of $\approx 0\%$ and $\approx 1.5\%$ were measured under circularly-polarized excitation and linearly-polarized

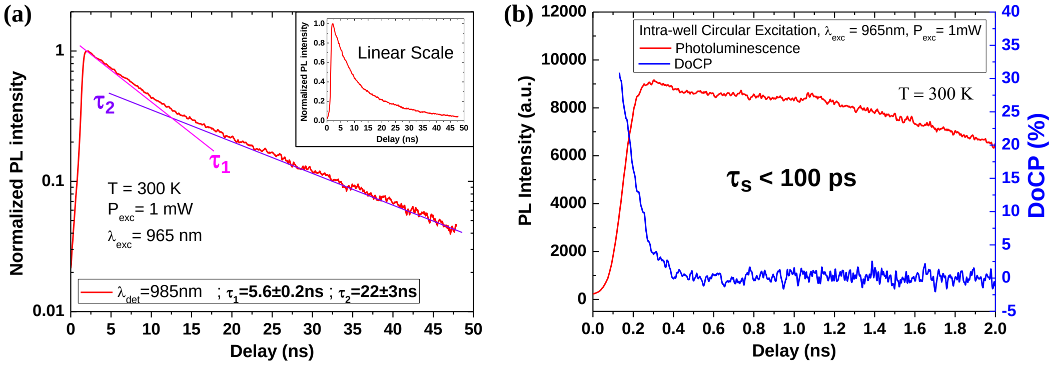

Figure 4.29: Time Resolved Carrier and Spin lifetimes measurements: (a) Carrier lifetime measurement at T=300 K for resonant pumping with an excitation power of 1 mW at 965 nm. The inset shows the same data plotted on a linear scale. **(b)** Polarization dynamics at T=300 K for resonant pumping with an excitation power of 1 mW at 965 nm.

excitation respectively. Unfortunately, as we are not able to excite and detect strictly resonant with the heavy-exciton (XH) due to the use of the streak camera, these experiments do not allow us to conclude that the eigenstates are not linearly polarized and that the linear birefringence of the structure is not due to the QW themself.

B) Room temperature measurements (300 K) under Intra-QW excitation below $e1 - lh1$ transition energy:

The same carrier lifetime measurements were then performed at 300 K for $\lambda_{Ti:Sa}$ = 965 nm. Preliminary runs revealed significantly longer carrier lifetimes compare to the 10 K measurements. Consequently, to avoid issues linked to long relaxation time, the experimental setup had to be modified. A pulse picker was installed on the laser chain in order to bring the repetition rate down to 4 MHz and allow a good evacuation of the excited carriers before any re-excitation. Additionally, a triggering module was mounted on the streak camera. With this setup, the camera's detection is triggered instead of being synchronized with the Ti:Sa emission.

Figure 4.29 (a) shows the PL intensity for an excitation at 965 nm and a detection window centered at 985nm. The measured relaxation of the PL intensity can be modeled by a double exponential with a first short relaxation time τ_1 of ≈5 ns and a second longer relaxation time τ_2 of ≈20 ns. Most of the photons are emitted during the first 10-15 ns. Consequently, the first relaxation time τ_1 gives a better image of the dynamics of the real system and is the one that should be considered when comparing the carrier lifetime to the spin lifetime in CW experiments. Preliminary test to measure circular polarization dynamics seems to indicate that the spin relaxation time is below

100 ps (Figure 4.29 (b)).

4.6.3 Data comparison and partial conclusion

Table 4.1 summarizes the values of τ_r et τ_s extracted from the TRPL measurement with other measurements performed in V(E)CSEL structures with different active medium at various temperatures. To this day, only few formal studies of the spin lifetime in VCSEL have been reported. In general, it is quite challenging to precisely describe the behavior of the characteristic lifetimes as they are strongly dependent on several experimental parameters namely the temperature, the nature of the active medium (doping, number of QWs, QWs width,...) and especially the operation regime.

At 300 K, the carrier lifetime is estimated around $\tau = 5$ ns for an excitation power of $P_{Ti:Sa} = 1$ mW. This measurement is coherent with the value of τ previously reported on similar VECSEL close to threshold using a different experimental approach [333]. The extracted spin lifetime tend to be smaller than the low temperature values reported in the literature for similar active mediums. At 10K, τ_s is of the order of magnitude of ≈ 100 ps for both resonant and non-resonant pumping. At 300K, first measurements seems to indicate that τ_s is below 100 ps. To my knowledge, no spin lifetime measurements has expressly been performed on (100)-QW VCSEL at room temperature. The only room temperature data was disclosed by Fujino *et al.* with a $\tau_s = 440$ ps in (110)-GaAs QW VCSEL [283]. This spin lifetime can not be used for a direct comparison as a [110] growth direction of GaAs cancels the Dyakonov-Perel mechanism and considerably increase the spin relaxation time [193, 350, 351].

Under optical pumping ($\lambda_{exc} = 808$ nm) in real operation conditions, carriers are also excited in GaAsP barriers and GaAs spacers. However, while the GaAsP carriers diffuse and recombine in the QW, the 28 nm thick GaAsP barriers provide a good shielding against the diffusion of GaAs spacers's carriers in the QW. Nevertheless as the QWs absorption is only about 1%, pumping in the barriers is needed to push the VECSEL in the stimulated emission regime.

The main limitation in order to compare the results obtained with our VECSEL under continuous wave excitation at 300 K and by TRPL at 300 K on the $\frac{1}{2}$-VCSEL are: **(i)** the different operation regimes (Stimulates Vs. Spontaneous respectively) and **(ii)** the excitation energy (above the GaAsP barriers Vs. intra-well below $e1 - hh1$ exciton respectively). Complementary measurements will be led at the *LPCNO* to perform TRPL under experimental conditions closer to those used for CW laser operation under optical pumping.

Oestreich *et al.* studied in detail the threshold reduction dependence on the spin relaxation time of an electrically pumped commercial VCSEL (*Infineon Technology*) using simulation based on the analytical model presented in section (2.2.3.2) [232]. For a theoretical 100% spin-injection efficiency, they showed a strong decrease of

Active Medium	Carrier lifetime τ_r	Spin lifetime τ_s	Reference
(100)-GaAs QW	Low pumping rate: $\approx$ ns High pumping rate: 50 ps	100 ps	[228]
(100)-GaAs QW	$\tau_{capture}$=20 ps	-	[84]
InAs/GaAs QD	100 ps @ RT	6 ps @ RT	[235]
(100)-InGaAs QW	$\tau_{capture}$=45 ps	Barriers: 500 ps QWs: 300 ps	[37]
(110)-GaAs QW	420 ps @ 77 K	2.8 ns @ 77 K 440 ps @ RT	[283]
(100)-GaAs QW	40 ps @ RT	230 ps @ 70 K	[283]
(100)-InGaAs QW	$\approx$ ns @ RT		[333]
(100)-InGaAs QW	-	100 ps @ 15 K	[282]
-	-	1-13 ps @ RT	[273]
-	-	10 ps @ RT	[?]
(100)-InGaAs QW (our sample)	10 K, non-resonant, 1 μW, $\lambda_{exc} = 780$ nm $\hookrightarrow \tau_r$=**410 ps**	10 K, non-resonant, 1 μW, $\lambda_{exc} = 780$ nm $\hookrightarrow \tau_s$=**170 ps**	TRPL
	10 K, non-resonant, 100 μW, $\lambda_{exc} = 780$ nm $\hookrightarrow \tau_r$=**550 ps**	10 K, non-resonant, 100 μW, $\lambda_{exc} = 780$ nm $\hookrightarrow \tau_s$=**105 ps**	
	10 K, intra-well, 100 μW, $\lambda_{exc} = 870$ nm $\hookrightarrow \tau_r$=**680 ps**	10 K, intra-well, 100 μW, $\lambda_{exc} = 880$ nm $\hookrightarrow \tau_s$=**135 ps**	
	10 K, intra-well, 10 mW, $\lambda_{exc} = 870$ nm $\hookrightarrow \tau_r$=**900 ps**	-	
	300 K, intra-well 1 mW, $\lambda_{exc} = 965$ nm $\hookrightarrow \tau_r \approx$**5 ns**	300 K, intra-well 1 mW, $\lambda_{exc} = 965$ nm $\hookrightarrow \tau_s <$ **100 ps**	

Table 4.1: Comparison of state-of-the-art carrier lifetime and spin lifetime measurements of V(E)CSEL structures with different active medium at various temperatures.

the laser threshold when τ_s increases from 50 ps to 200 ps and they also compared the room-temperature "spin-performances" of various QW-based active mediums (Figure 4.30). Spin relaxation times of few ps and about 50 ps are typical for undoped InGaAs QW and bulk GaAs, respectively. Consequently, one should not expect a significant threshold reduction of the V(E)CSEL when using these material as an active medium. With the active medium of our $\frac{1}{2}$-VCSEL made of 12 $In_{20\%}Ga_{80\%}As/GaAs_{95\%}P_{5\%}$-QW, we have observed a low threshold reduction of

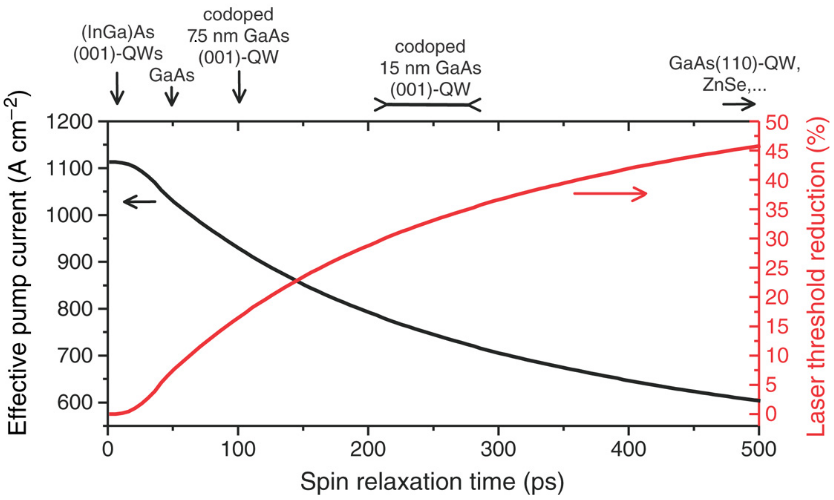

Figure 4.30: Simulation of the threshold evolution of a commercial VCSEL at room temperature: Left axis: Evolution of the laser threshold as a function of the spin relaxation time (Black line). **Right axis:** Percentage of threshold reduction as a function of the spin relaxation time. **Top axis:** Spin relaxation time of several semiconductor systems. The estimated long spin relaxation time for the 15 nm co-doped (001)-GaAs QW has not been experimentally confirmed yet. The experimental parameters used for the simulation can be find in [232]. Figure reprinted from [232]

few percents in agreement with preliminary measurements of τ_s below 100 ps. In 7.5 nm wide co-doped (001)-GaAs QW spin relaxation times of about 100 ps have been measured at room temperature [352]. These relatively long spin relaxation times result from motional narrowing due to fast momentum scattering at the co-doping and should yield a threshold reduction of about 20%. Even longer spin relaxation times of a few hundred ps are expected in wider co-doped (001)-GaAs QW. The relevant Dyakonov-Perel spin relaxation mechanism decreases when quantization energy decreases, leading to a laser threshold reduction of about 40%. As supported by the experimental results of Fujino *et al.* [283], changing the growth direction of GaAs QW from [001] to [110] increases the spin relaxation times up to the nanosecond regime as the Dyakonov-Perel mechanism is canceled for electrons spin-polarized along the growth direction [193]. For such systems the expected threshold reduction approaches the limit value of 50%. A similar reduction is in principle expected for wide band-gap semiconductors like ZnSe with a weak spin-orbit interaction [353].

4.7 Electrically spin-injected VECSELs

In an electrically pumped, commercial monolithic GaAs/AlGaAs-QW VCSEL, the minimum transport time of an electron from the contact to the laser gain medium is estimated around 10 ns [232]. However, the spin relaxation time of the electron in GaAs is about 50 ps at room temperature. Consequently, the spin-polarization in the gain medium of the laser is close to zero. Side contacts are not a practical way to shorten the transport time into the active medium of the laser as typical small-area VCSEL still have diameters exceeding 5 μm. At first sight, one could conclude that metallic spin injectors are not a practical option for a Spin-VCSEL implementation.

Nonetheless, from the electrical injection viewpoint, the use of 1/2-VCSELs offer the unique advantage to deposit a spin-injector on top of the structure as close as possible to the QW. Using this technique maximizes the spin polarization degree reaching the active medium by taking advantage of a spin diffusion length l_{sf} longer than the distance between the injector and the QW. In GaAs, typical l_{sf} values are given around [8] 6 μm at 50 K while in our structure the distance between the spin polarizer and the first QW is about 180 nm. In the active zone, the spin polarization level will then be governed by the ratio between the spin lifetime τ_s and the radiation lifetime τ_r in the QW. Typical values of spin relaxation time are estimated around [354] $\tau_s = 60$ ps at Room Temperature (RT) for GaAs QW while the radiative lifetime for high excitation (gain regime) far from threshold is given around [228] $\tau_r \simeq 100$ ps at RT. The ultimate goal of this work is to study electrically injected Spin-VECSEL. Nevertheless, given the technological challenges, we first started by studying the structure under optical spin-injection. As a first result, we demonstrate laser oscillations under unpolarized optical pumping despite the insertion of a non-transparent ferromagnetic spin-injector in the laser cavity.

4.7.1 Insertion of an Intra-Cavity spin-injector

We validated the concept of electrically spin-injected VECSEL by demonstrating laser oscillations with an optically pumped 1/2-VCSEL incorporating an intra-cavity $(2.6nm)MgO/(1.8nm)Co/(3nm)Pt)$ MTJ ferromagnetic spin-injector with in-plane magnetization (Figure 4.31(b)). Thanks to the oxyde barrier, this type of spin-injector permits to circumvent the impedance mismatch issue [63]. Moreover, the efficiency of this architecture has beforehand been proved with Spin-LED [199]. We used an antiresonant n.i.d 1/2-VCSEL grown by Metal Organic Chemical Vapor Deposition (MOCVD) consisting in a 27.5-period GaAs/AlAs Bragg mirror (99.9% reflectivity). The gain at $\lambda = 1$ μm is ensured by twelve strained balanced $\mathrm{In_{22\%}Ga_{78\%}As/GaAs_{95\%}P_{5\%}}$ QW in a $13\lambda/2$ cavity. The structure is maintained at 279 K with a Peltier thermo-electric cooler. The pumping system consists in a 808 nm pigtail multimode laser diode delivering up to 2 W and focused on the gain medium to a 100 μm spot with a 30° incidence angle. The VECSEL is pumped

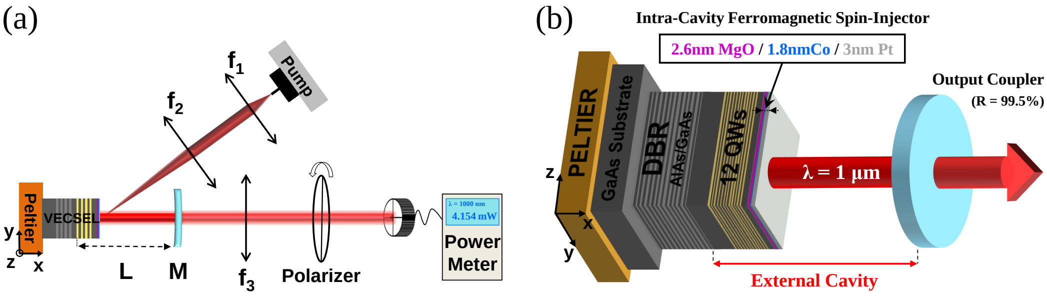

Figure 4.31: **(a) Experimental setup:** We used a linear cavity optically pumped with a 30° angle. The output optical power emitted by the VECSEL is evaluated using a Power-meter. $L = 50mm$, $f_1 = 10mm$, $f_2 = 50mm$, $f_3 = 100mm$, $M : (R = 50mm, T = 0.5\%)$ **(b) Overview of the VECSEL structure:** The $(2.6nm)MgO/(1.8nm)Co/(3nm)Pt$ MTJ ferromagnetic spin-injector is deposited intra-cavity, close to the active medium, on a node of the electromagnetic field.

in the continuous regime throughout the experiment. The linear cavity is closed by a 50 mm radius of curvature concave mirrors with a 0.5% transmission at 1μm (Figure 4.31 (a)). At the output of M the beam is focused on a power-meter (f_3) and a polarizer can be inserted to determine the direction and ellipticity of the light polarization.

This preliminary experiment was challenging given the high absorption of classical MTJ ferromagnetic spin-injector (typically 10% for 5 nm thickness) compared to the low optical gain in 1/2-VCSEL ($\approx 1\%$). At $\lambda = 980$ nm, the MgO layer can be consider transparent ($\alpha_{MgO} = 5.0 \times 10^{-2}$ cm^{-1}) compared to the Co and Pt metallic layers ($\alpha_{Co} = 7.2458 \times 10^5$ cm^{-1} and $\alpha_{Pt} = 7.3254 \times 10^5$ cm^{-1}). To overcome this strong limitation, the semiconductor structure was designed so as to place the spin-injector in one node of the stationary electromagnetic field. This technique enables to minimize the absorption by the ferromagnetic multilayer (FML). The spin-injector is deposited by sputtering on the surface of the anti-resonant MOCVD 1/2-VCSEL (Figure 4.31 (b)). By analyzing the Fourier Transform Infrared Reflectivity spectra (FTIR) of the system DBR+FML, we see that the FML acts as a narrow frequential pass-band filter on the reflectivity (Figure 4.32(b)). The higher threshold for VECSEL+FML witnesses an increase of losses in the cavity that can be attributed to surface defects (Figure 4.32(a)). This encouraging result is a first step toward the realization of an electrically pumped Spin-VECSEL.

4.7.2 Deposition of a spin-injectors with Perpendicular Magnetic Anisotropy on a $\frac{1}{2}$-VCSEL

In the previous section we successfully demonstrated the feasibility of laser operation despite the insertion of a highly absorbent MTJ spin-injector in the laser cavity. However, this previous accomplishment was realized using a ferromagnetic multilayer with a magnetization oriented in the plane of the film. We remind the reader

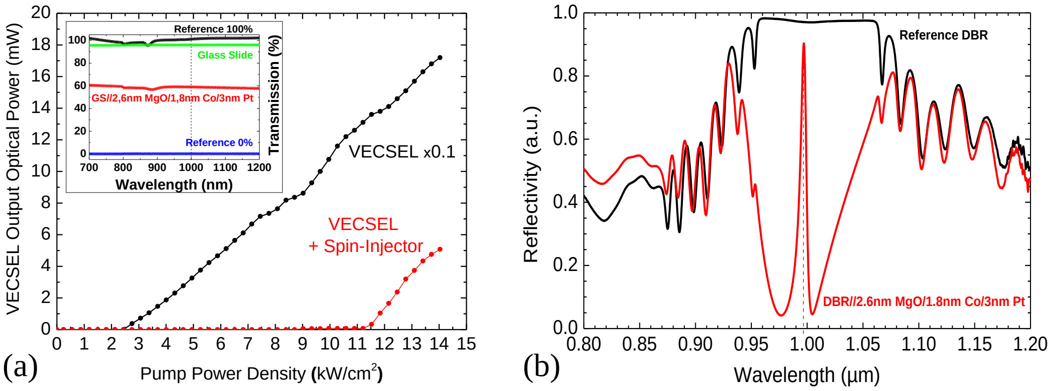

Figure 4.32: (a) **VECSEL output optical power as a function of the pump power density:** The structure with the $(2.6nm)MgO/(1.8nm)Co/(3nm)Pt$ ferromagnetic spin-injector is lasing at 279 K despite the losses introduced in the cavity by the spin-injector. Both measurements have been realized with an output coupler transmission of T=0.5%. The Inset showcases the spin-injector transmission spectra. The absorption at 1 μm is around 40%. **(b)DBR and DBR+Spin-injector measured reflectivities as a function of the wavelength:** the deposition of the FML strongly influence the reflectivity profile of the bottom DBR. By a careful design we managed to keep a high reflectivity close to the QW Photo-Luminescence (PL) at $\lambda = 980nm$. The energy difference between the QW gain peak and the DBR resonance peak ($\lambda = 997nm$) can be minimized by adjusting the VECSEL temperature in order to maximize the output laser power. The shift of the QW PL is about 0.35 nm/K.

that the quantum optical selection rules require an electron's spin-polarization parallel to the quantization axis of the QW constituting the active medium of the laser. This could of course be achieved by applying a magnetic field perpendicularly to the structure in order to drive the spin-injector's magnetization out-of-plane. Unfortunately, when targeting potential applications, avoiding the requirement of an applied magnetic field for operation is non-optional. Consequently, the development of an injector exhibiting Perpendicular Magnetic Anisotropy at remanence and at room temperature on 1/2-VCSEL stood out as the next challenge.

The philosophy of these research was to apply the expertize acquired with the development of PMA spin-injectors on Spin-LED to the deposition of PMA injectors on the surface of anti-resonant $\frac{1}{2}$-VCSEL. However even if the technology transfer could seems trivial at first sight, several verifications and tests needed to be performed in order to validate and confirmed the feasibility. First of all, the growth methods used to grow the LED used for optimization and the $\frac{1}{2}$-VCSEL are different. The LED are grown by MBE while the $\frac{1}{2}$-VCSEL are grown by MOCVD which could lead to different surface natures and surface qualities. Our study on Spin-LED showed that the surface quality and the surface preparation before deposition are decisive parameters for the successful deposition of MTJ spin-injectors with PMA. Therefore, a preliminary verification was to analyze the surface quality of the $\frac{1}{2}$-VCSEL.

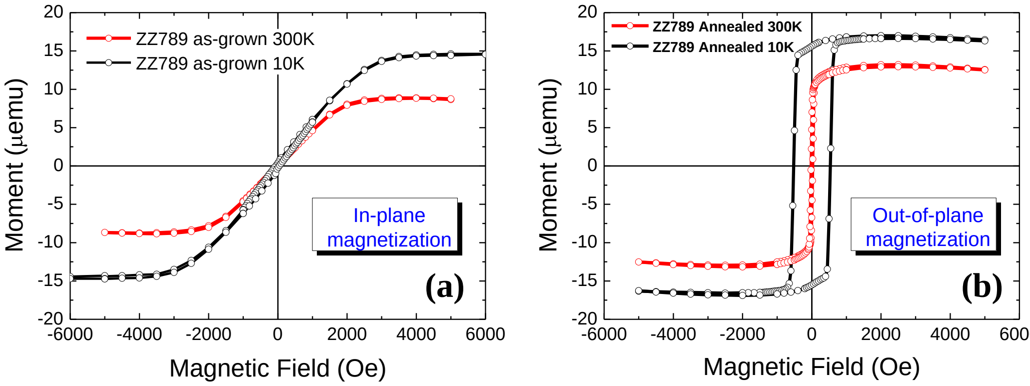

Figure 4.33: Magnetic moment evolution of the system $GaAs763//MgO(2.2nm)/CoFeB(1.2nm)/Ta(5nm)$ as a function of an applied magnetic field at both 10 K and 300 K. **(a)** Before Rapid Thermal Annealing SQUID measurements show an in-plane magnetization. **(b)** After Rapid Thermal Annealing at 300°C for 3 minutes the reconstruction of the CoFeB layer from the MgO/CoFeB interface induces perpendicular magnetic anisotropy in the multilayer and drive the magnetization out-of-plane at magnetic remanence.

MOCVD growth provides high quality surfaces with small roughness. An AFM analyze performed on the surface of the GaAs763 electrical 1/2-VCSEL confirmed a good flatten surface with a measured roughness of 0.259 nm and a step height of 3 Angstroms. The surface quality of MOCVD $\frac{1}{2}$-VCSEL and MBE LED is thus quite comparable, which is in favor of a successful technological transfer of the PMA spin-injector onto the surface of $\frac{1}{2}$-VCSEL.

For preliminary electrical testing we decided to first grow a $MgO(2.2nm)/CoFeB(1.2nm)/Ta(5nm)$ PMA spin-injector on the electrical structure GaAs763 (structure detailed in section 4.2.3) as the distance between the spin-injector and the active medium has been minimized to approximately 30 nm. The choice was to use the simplest design to verify: **(i)** if the structure could lase under electrical pumping, **(ii)** the possibility of laser operation with an intra-cavity ferromagnetic spin-injector under electrical pumping and **(iii)** to study the spin-injection efficiency by analyzing the DoCP of the light polarization. Nevertheless, contrary to the Spin-LED used during the development of this PMA spin-injector, the 1/2-VCSEL required specific surface preparation before deposition. Indeed, all the LED structures were passivated with arsenic after growth inside the III-V MBE chamber. Then, this As cap was desorbed after the LED transfer in the magnetron Sputtering-MBE system used to grow the injector, right before deposition (section 3.2.1). Here however, the 1/2-VCSEL grown by MOCVD are not capped with a protective As layer which leads to a thin surface oxidation due to air exposure. First, the surface of the 1/2-VCSEL was chemically etched with HCl for 1 minute and then cleaned with Propan-2-ol for 1 minute. After chemical surface preparation, the second step of the process consisted in depositing the $MgO(2.2nm)/CoFeB(1.2nm)/Ta(5nm)$ spin-injector using sputtering growth. This MTJ spin-injector is identical to the one developed on Spin-LED. After deposition, SQUID measurements revealed without surprise that the magnetization of the multilayer was in-plane at both 10 K and room temperature (Figure 4.33 (a)). Afterward, a micro-pillar photo-lithography was performed using the same process developed for Spin-LED patterning (section 3.1.2). The $\frac{1}{2}$-VCSEL pillar is 300 μm in diameter and the two (50nm)Pt/(250 nm)Au contacts on the n-doped surface and one on the p-doped 62.5 nm Zn-GaAs (2.5e17) layer respectively are both 110 μm in diameter. To trig a restructuration of the MgO/CoFeB interface and induce a perpendicular magnetic anisotropy in the multilayer, the whole $GaAs763//MgO(2.2nm)/CoFeB(1.2nm)/Ta(5nm)$ structure was annealed using a Rapid Thermal Annealing (RTA) process of 3 minutes at 300°C. Figure 4.33 (b) exhibits the SQUID measurements of the sample after RTA and confirm the out-of-plane magnetization of the spin-injector at remanence at both 10 K and room temperature .

To summarize, we demonstrated both the possibility to insert an intra-cavity spin-injector and to grow a spin-injector with PMA on the surface of a MOCVD $\frac{1}{2}$-VCSEL. Combine together, these two properties are highly encouraging toward the realization of an electrically spin-injected VECSEL operating at magnetic remanence. By bypassing the requirement of an applied magnetic field, one could then envisage to control the VECSEL polarization using a current line to switch the magnetization's orientation of the spin-injector as in MRAM systems.

Chapter 5

Overall Conclusion

Contents

During this Ph.D thesis, we focused on the study of spin-injection into III-V semiconductor based light emitting devices with vertical geometries. This paradigm offers to propagate the information contained in a magnetic bit over really long distances by converting the associated spin-information into circular polarization information carried by the emitted photons using the optical quantum selection rules. We paid a particular attention to Spin-VECSELs exhibiting a tremendous potential for beyond state-of-the-art spin-optoelectronic devices. They offer to combine non-volatile magnetic storage of the information in an ultra-thin ferromagnetic spin-injector with the potentiality of spin-information propagation over macroscopic distances. To develop this ambitious and highly multidisciplinary Ph.D subject we performed various original investigations and experiments in the fields of material science, III-V semiconductor physics, spintronics and photonics.

To replace oneself in the general context, this manuscript was divided into three major chapters. The second chapter of the manuscipt regrouped a state-of-the-art of spin-injection into III-V semiconductors optoelectronics devices and focused on the physical phenomena engaged in the conversion of a spin accumulation into light polarization information. The third chapter was articulated around our experimental work on the development and the optimization on III-V semiconductors LEDs of an ultra-thin $MgO(2.5nm)/CoFeB(1.2nm)/Ta(5nm)$ spin-injector with perpendicular magnetization at magnetic remanence. Finally, the fourth chapter presented our main experimental studies on both optical and electrical spin-injection in Vertical External Cavity Surface Emitting Lasers. Hereinafter, we are going to summarize the main results and conclusions obtained during this thesis but also discuss the short and long term perspectives related to this project.

5.1 Development of a new ultra-thin spin-injector

We used Spin-LED as a research tool for the development and the optimization of an ultra-thin $MgO/CoFeB/Ta$ spin-injector. This revolutionary spin-injector exhibits Perpendicular Magnetic Anisotropy (PMA) at magnetic remanence and at room temperature on III-V compounds. Two main studies have been conducted to successfully achieve this goal.

First, by conducting a comparative study on the optimization of the MgO tunnel barrier using two growth methods (sputtering and MBE), we showed that: **(i)** a similar increase of the emitted DoCP was occurring when the annealing temperature is increased and **(ii)** a comparable improvement of the spin-injection efficiency was observable for both Sputtering and MBE Spin-LED after annealing in the 300-350°C temperature range. As the increase of the Degree of Circular Polarization (DoCP) starts far below the crystallization temperature of the whole CoFeB layer, we concluded that the increase of the spin-injection efficiency is mainly due to the improvement of the top MgO/CoFeB-interface's chemical structure. A DoCP as high as $24 \pm 1\%$ at 0.8 T and at 25 K has been observed. This study highlighted the critical importance of the interface states for the spin-injection spin-injection process.

Secondly, we successfully developed an ultra-thin spin-injector with perpendicular magnetic anisotropy at remanence and at room temperature on GaAs. The structure of the sputtered injector consists in an ultra-thin CoFeB ferromagnetic layer (1.2 nm) on top of a MgO tunnel barrier (2.5 nm) and caped with a Ta layer (5 nm). The injector efficiency was highlighted by the emission at magnetic remanence of a maximum DoCP evaluated around 20% at 25K and a value as large as 8% at room temperature. This room temperature value establishes a new world record for PMA devices operating at magnetic remanence. This first demonstration of robust and efficient electrical spin-injection using ultra-thin spin-injectors with perpendicular magnetization at remanence paves the way for future innovative applications. Such revolutionary injectors will enable to implement new room temperature III-V spin-optronic devices. Since there is no need of applied magnetic field for operation, an all-electrical control of the emitted circularly-polarized light could be implemented using the Spin-Transfer-Torque (STT) properties. Several mechanism could be investigated including STT on TMR junction [355], domain wall propagation [356, 357], SHE- or Rashba-materials [136, 358] as well as All Optical-Helipticity Dependent Switching (AO-HDS) [40, 359]. The thinness of such injectors will also enable to implement an electrically spin-injected VECSEL by directly inserting the injector inside the laser cavitiy, close to the active medium, thanks to the reduced optical absorption.

5.2 Summary on spin-injection into VECSELs

The study of spin-injection in an $In_{22\%}Ga_{78\%}As/GaAs_{95\%}P_{5\%}$ QW - Vertical External Cavity Surface Emitting Lasers constituted the heart of this Ph.D thesis. Both the optical and the electrical injection of spin-polarized carriers have been investigated.

Conclusions on the optical spin-injection:

In the first optical spin-injection experiment, the VECSEL was setup in a linear-cavity geometry and oblically spin-injected with circularly-polarized light. Despite a 100% right (σ^+) or left (σ^-) circularly-polarized pumping the laser output polarization remained strictly linear.

A vectorial model has then been developed to pull the blind on the system dynamics. It brought to our understanding that the polarization selection in spin-injected VECSEL is essentially ruled by the competition between the residual linear birefringence γ in the structure and the Gain Circular Dichroism ΔG induced by the spin-injection. The linear birefringence γ tend to set the laser emission on linearly-polarized modes along the [011]- and [0$\bar{1}$1]-directions while the spin-induced GCD favors oscillations on circularly-polarized modes. Therefore, we concluded from the first experiment that the structure was exhibiting a linear anisotropy high enough to mask any spin-injection effects.

We further investigated more precisely the linear anisotropy and the GCD controlling the polarization selection in the structure. An original experimental setup was developed to quantify the residual linear birefringence in the VECSEL by measuring the frequency detuning between two orthogonal modes linearly-polarized along [011]- and [0$\bar{1}$1]-directions respectively. We measured an average birefringence $\frac{\gamma'_{exp}}{2\pi} \approx 6.3 \times 10^{-3}$ rad for a pump power in the [400-600] mW range ($\gamma' = 4\gamma$). This value is more than 30 times higher than the birefringence measured by Hendriks *et al.* in a monolithic 3-QW VCSEL ($\gamma'_{VCSEL} \approx 2 \times 10^{-4}$ rad) [250]. This increase of birefringence compared to regular VCSEL is suspected to origin from the higher number of strained-balanced QW (12) constituting the active medium but also from the lack of top Distributed Bragg Reflector that could potentially increase the strains on the active medium and the bottom DBR. Such a value of linear birefringence is in agreement with the observations realized during the first optical spin-injection experiments. We then used the vectorial model to estimate that a normalized GCD $\Delta G_N \approx 4\%$ was required to compensate the residual linear birefringence of the 1/2-VCSEL structure. As the average gain of the VECSEL is $\bar{G} \approx 1\%$, this normalized GCD correspond to a net GCD $\Delta G \approx 0.4\%$. For this inferior limit, the VECSEL is in an artificial isotropic state for the TE- and TM- mode. According to the vectorial model, in this metastable state the TE- and TM-modes are still both linearly polarized and oriented at 45° from the ordinary [0$\bar{1}$1] and extraordinary [011] axis. To trigger VESCEL oscillations on two elliptically- and further circularly-polarized modes, one has to further increase ΔG by boosting the gain differential between the two circularly-polarized modes ($G_+ - G_-$). Using the same calculation for a regular VCSEL we found that a GCD of only $\Delta G_N \approx 0.5\%$ is sufficient to compensate the birefringence in such monolithic structures. This partly explains the impressive values of DoCP already obtained with monolithic VCSEL under optical [36, 41, 283, 42, 43] and electrical [37] spin-injection.

Accordingly, we designed a new M-shaped extended cavity having two main objectives in mind. The first one was to maximize the spin-injection efficiency by pumping the VECSEL with a normal incidence to prevent any elliptical projection of the circular polarization. The second point was to prepare the laser to oscillate on two circularly-polarized eigen states by inserting a large intra-cavity Faraday rotator. The role of this non-reciprocal material was to artificially introduce a circular birefringence in the cavity in order to compensate the strong linear birefringence of the structure.

Thanks to this original setup, we further successfully demonstrated an optical spin-injection in the VECSEL structure. We showed a clear control of the light polarization using the spin orientation of the electron despite a weak gain circular dichroism in the active medium. This low effective spin-injection was quantified to $P_S \approx 7.1\%$ by measuring a normalized laser threshold reduction of 3.55% under circularly-polarized pumping. However, despite this low spin-injection efficiency, the output DoCP emitted by the laser was closed to 80% corresponding to a spin-information amplification greater than 1000%. To understand the mechanism behind this experimental observation we turned toward the Lamb Model for a Class-A, Two-mode operation laser. The spin-amplification effect occurs thanks to the leverage effect of the non-linear coupling constant C controlling the lasing modes competition in the VECSEL. In our structure $C \approx 0.9$ meaning that a normalized GCD $\Delta G_N = 10\%$ is sufficient to switch between σ^+ and σ^- polarization modes. Accordingly, as the average gain $\bar{G}$ of our VECSELs is close to 1%, a GCD $\Delta G \approx 0.1\%$ is sufficient to fully switch the laser polarization. Consequently, the estimated 7.1% spin-injection value is an order of magnitude greater than the theoretical inferior limit (0.1%) required to trigger a polarization switch. Conclusively, we understood here how such a moderate effective spin-injection can generated a polarization switch from a circular eigen state to another. When comparing this estimated effective spin-polarization $P_S \approx 7.1\%$ to the GCD $\Delta G \approx 0.4\%$ extracted from the previous birefringence measurements of the same $\frac{1}{2}$-VCSEL, we see that P_S is four times greater than this minimum ΔG value required to compensate the birefringence in the structure. Consequently, the GCD should be sufficient to overpower the linear birefringence and set a circularly-polarized emission. However, in the first optical spin-injection experiment no influence of the spin-injection could be seen on the modes polarization even if the VECSEL was optically spin-injected with an approximately similar efficiency. The same observation was also made in the second experiment after withdrawing the Faraday rotator from the M-Cavity. We concluded that although the effective spin-polarization injected in the VECSEL might compensate the linear birefringence, the laser is probably still just above the compensation point ($\frac{1}{4}\Delta G_N^2 = \sin^2\frac{\gamma'}{2}$) and P_S is not high enough to even trigger oscillations on elliptically-polarized modes. This locking of the laser on linearly-polarized modes might also be favored by an additional residual linear birefringence originating from the cold cavity. Indeed, contrary to the short linear cavity used to perform the birefringence measurements, this extended M-cavity is composed of four additional mirrors each of them introducing a residual birefringence. Consequently, we made the hypothesis that the effective spin-injection required to compensate the total linear birefringence of the M-Cavity VECSEL might be sensibly higher than in the previous birefringence experiment from where the value $\Delta G \approx 0.4\%$ has been extracted. As predicted by the vectorial model, the importance of the intra-cavity Faraday rotator has thus clearly be highlighted experimentally. The emission of circularly-polarized modes with a DoCP of 80% shows how the circular birefringence artificially introduced by the Faraday rotator compensate the intrinsic linear birefringence of the $\frac{1}{2}$-VCSEL and enable us to reveal the influence of the injected spin-polarized carriers on the modes polarization.

Auxiliary to the importance of the spin-population imbalance, the gain circular dichroism value induced by spin-injection is highly dependent on the ratio between the carrier lifetime τ and the spin lifetime τ_s in the VECSEL's active medium. Consequently, we investigated the $\frac{\tau}{\tau_s}$-ratio by performing Time Resolved Photo-Luminescence measurements on the structure to evaluate these characteristic lifetimes. At 300 K, the carrier lifetime is estimated around $\tau = 5$ ns for an excitation power of $P_{Ti:Sa} = 1$ mW. This measurement is coherent with the value of τ previously reported on similar VECSEL close to threshold using a different experimental approach [333]. The extracted spin lifetime tend to be smaller than the low temperature values reported in the literature for similar active mediums. At 10K, τ_s is of the order of magnitude of ≈ 100 ps for both resonant and non-resonant pumping. At 300K, first measurements seems to indicate that τ_s is below 100 ps.

Conclusions on the electrical spin-injection:

From the electrical injection viewpoint, the use of $\frac{1}{2}$-VCSEL offer the unique advantage to deposit an intra-cavity spin-injector on top of the structure as close as possible to the QW. Using this technique maximizes the spin polarization degree reaching the active medium by taking advantage of a spin diffusion length l_{sf} longer than the distance between the injector and the QW. As a first result, we demonstrate laser oscillations under unpolarized optical pumping despite the insertion of a non-transparent ferromagnetic spin-injector in the laser cavity. To overcome the strong absorption induced by the $MgO(2.6nm)/Co(1.8nm)/Pt(3nm)$ multilayer, the semiconductor structure was designed so as to place the spin-injector, in one node of the stationary electromagnetic field on the surface of the anti-resonant VECSEL. The Fourier Transform Infrared Reflectivity spectra highlighted that the spin-injector acts like a narrow frequential pass-band filter for the structure reflectivity. An increase of the laser threshold was also witnessed due to the additional losses introduced in the cavity by the MTJ spin-injector.

Following, the very first VECSEL dedicated to pure electrical spin-injection were designed and grown by MOCVD. We further successfully performed a technological transfer of the $MgO(2.5nm)/CoFeB(1.2nm)/Ta(5nm)$ PMA spin-injector developed on Spin-LED onto the surface of an antiresonant $\frac{1}{2}$-VCSEL designed for electrical pumping. For preliminary electrical testing we decided to first grow the PMA injector on the structure exhibiting the shortest distance between the injector and the active medium (30 nm). After chemical surface preparation, sputtering deposition of $MgO(2.5nm)/CoFeB(1.2nm)/Ta(5nm)$, photo-lithography processing and a 3 minutes Rapid Thermal Annealing at 300°C, the injector showed to exhibit PMA at room temperature. This achievement is highly encouraging toward the realization of an electrically spin-injected VECSEL operating at magnetic remanence. As for Spin-LED, bypassing the requirement of an applied magnetic field opens the door for an all-electrically driven Spin-VECSEL with an output polarization controlled by spin-transfer torque of the CoFeB layer.

5.3 Perspectives, challenges and future applications

The pioneer research initiated during this Ph.D thesis on spin-injection in Vertical External Cavity Surface Emitting Lasers already brought to light really interesting and encouraging results. Such devices are expected to outperform their conventional counterpart in the departments of laser threshold reduction [37, 38, 39], improved laser intensity, and polarization stability. They also exhibit a tremendous potential for future optical communication systems such as telecommunications with enhanced bandwidth, spin driven reconfigurable optical interconnects [31, 32, 33], fast modulation dynamics [34, 35], polarization control [36, 37] and very low noise operation [333]. The ideas emerging from Spin-Lasers and polarization switching may also motivate other device concepts like spin-amplifiers, cryptography, coherent detection systems or magneto-optical recording [40]. With the challenges emerging from such a plethora of innovative concepts, further research will be carried out on Spin-VECSEL. Several experiments are already planned out to improve our understanding of this spin-optoelectronic device.

Optical spin-injection:

Low temperature measurements will be conducted on a VECSEL structure specially designed for low temperature operation. The global GaAs633 architecture is similar to the one of the GaAs615 except for the $\frac{7\lambda}{2}$ - active medium. The gain is still ensure by 6 pairs of InGaAs/GaAsP but the In/Ga- and Ga/P-ratios have been modified to display a room temperature emission at 1037 nm and a low temperature emission at 980 nm. The voluntary shift of 57 nm between the micro-cavity peak and the QWs PL has been introduced to compensate the PL's temperature deviation of 0.35 nm.K^{-1} (Figure 5.1). The experimental setup is already operational and is composed of an *attoCUBE* dry He-cryocooler (attoDRY1000). The cryostat offers a maximum refrigeration temperature of 4 K thanks to a Gifford-McMahon compression/decompression cycle. A vertically-mounted superconducting magnet also offers

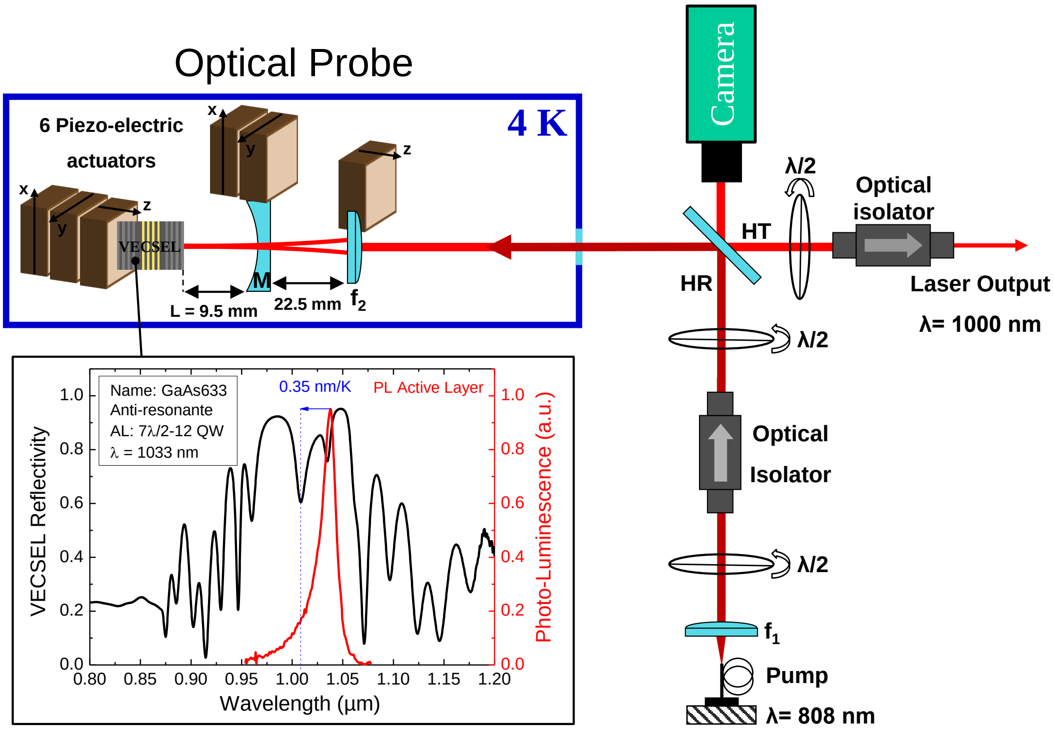

Figure 5.1: Illustration of the low temperature optical bench especially designed for optical spin-injection in VECSELs: The $\frac{1}{2}$-VCSEL is mounted at on a support at the bottom of the probe on 3 piezoelectric actuators (x-axis, y-axis, z-axis). The positioning of the output coupler (M) can also be control thanks to a (x-axis, y-axis)-piezo stack. Finally the focus of the pump beam is adjusted with the focus lens f_2 mounted on a z-axis piezo. The camera is added as an adjustment tool for the laser optimization by imaging the pump beam and its reflection by M on the $\frac{1}{2}$-VCSEL surface. The graph exhibits the FTIR Spectrum (black line) and the active medium PL (red line) characterizing the structure at room temperature. The vertical dashed blue line indicated the calibrated wavelength of the micro-cavity peak.

to apply a magnetic field up to 9 T. The VECSEL will be mounted on a specially design optical probe with 6-piezoelectric actuators among which 3 are dedicated to the VECSEL positioning (x-axis, y-axis, z-axis), 2 to the output coupler (M) positioning (x-axis, y-axis) and 1 to the adjustment of a focalization lens f_2 (z-axis) (Figure 5.1). As the spin lifetime is expected to be longer at low temperature, we aim to examine if the $\frac{\tau}{\tau_s}$-ratio can increase sufficiently enough to boost the gain circular dichroism compared to the residual birefringence and accordingly see if the VECSEL can reach an emitted DoCP of 100% without having to introduce a Faraday rotator in the cavity.

In terms of characteristic lifetimes of the $In_{22\%}Ga_{78\%}As/GaAs_{95\%}P_{5\%}$ QW, the main limitation in order to compare our results obtained on our VECSEL under Continuous Wave (CW) excitation at 300 K and by TRPL at 300 K on the $\frac{1}{2}$-VCSEL are:

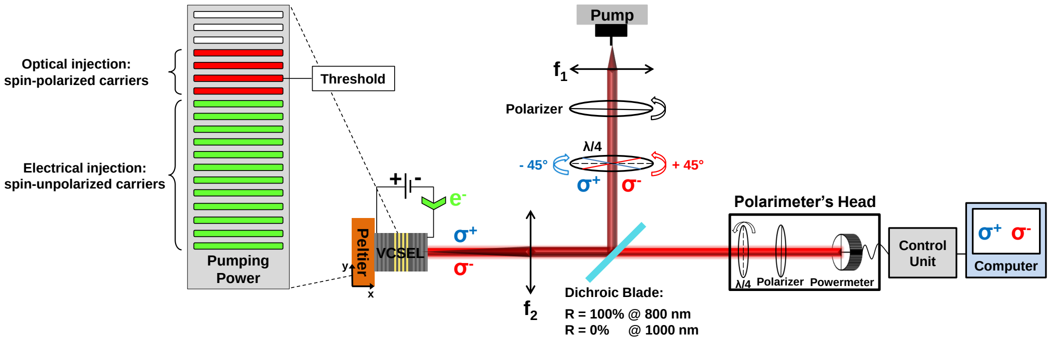

Figure 5.2: Experimental setup envisaged for the mix electrical/optical pumping of V(E)CSEL: The VCSEL is pumped both electrically and optically with circularly polarized light at 808 nm using a laser diode. The setup is articulated around a dichroic blade conserving the light polarization which is transparent for the laser emission (R=0% at 1000 nm) and perfectly reflective for the pump beam (R=100% at 800 nm). The pumping power gauge illustrates the combined pumping of electrically injected spin-unpolarized carriers (green) and optically injected spin-polarized carriers (red). The polarization emitted by the V(E)CSEL is analyzed using a polarimeter.

(i) the different operation regimes (Stimulated Vs. Spontaneous respectively) and **(ii)** the excitation energy (above the GaAsP barriers Vs. intra-well below $e1 - hh1$ exciton respectively). Accordingly, complementary measurements will be led at the $LPCNO$ to perform TRPL under experimental conditions closer to the used for CW laser operation under optical pumping.

Electrical spin-injection:

The very first electrical spin-injection will be performed on the patterned structure capped with a perpendicular spin-injector. A first step would consist in characterizing the junction through I-V measurements and evaluate the critical current as well as the breakdown voltage of the MgO barrier. Further, the structure will be mounted in a linear cavity setup in order to see if a stimulated emission regime can be achieve under electrical pumping despite the intra-cavity ultra-thin $MgO(2.5nm)/CoFeB(1.2nm)/Ta(5nm)$ injector.

Hybrid Optical/electrical pumping:

The investigation of an industrial monolithic VCSEL under mixed optical/electrical pumping is already planned. This experience, already realized by Hovel *et al.* [224], consists in manipulating the polarization of the electrically pumped VECSEL by optical spin-injection. During the experiment, the VCSEL will be electrically pumped up to 80-90% of its threshold with spin-unpolarized carriers while additional spin-polarized carriers are spin-injected though circularly-polarized pumping. The goal is to see if a perturbative injection of spin-polarized carriers can set the laser polarization on circularly-polarized mode. The envisaged experimental setup is detailed in figure 5.2. This experiment will stand as a preliminary examination to align and optimize the experimental setup before performing the same experiment using our VECSEL structures designed for electrical pumping.

Spin-information propagation over very long distances:

Finally, combined with the new research field of all-optical magnetization switching, Spin-lasers could become the missing conceptual link toward an all-spintronics based circuit logic. Indeed, in the future, it could be envisage to transfer spin-information over kilometric distances by propagating it in optical fibers after encoding on the light polarization.
Magnetization reversal using circularly polarized light provides a way to control magnetization without any external magnetic field and has the potential to revolutionize magnetic data storage [40, 359]. The low power manipulation of magnetization, preferably at ultra-short timescales, has become a fundamental challenge with implications for future magnetic information memory and storage technologies. The All Optical-Helipticity Dependent Switching (AO-HDS) occurs through transfer of angular momentum from incident circularly-polarized photons to a multilayer magnetization. In short, it can be seen as the reverse mechanism to the one converting spin-information into light polarization information in Spin-lasers. AO-HDS can be observed not only in selected rare earth-transition metal (RE-TM) alloy films but also in a much broader variety of materials, including RE-TM alloys, multilayers and heterostructures. It has recently been demonstrate that $(Co/Pt)_{\times 3}$ and RE-free Co-Ir-based synthetic ferrimagnetic heterostructures designed to mimic the magnetic properties of RE-TM alloys also exhibit AO-HDS [40]. The discovery of AO-HDS in RE-free TM-based heterostructures can enable breakthroughs for numerous applications because it exploits materials that are used in magnetic data storage, memories and logic technologies.

The communication process for the propagation of spin-information over very long distances would break down into four essential steps (Figure 5.3):

1. Conversion of the magnetic bit information encode on an ultra-thin ferromagnetic layer into circularly-polarized light using an electrically spin-injected VECSEL.
2. Fiber coupling of the VECSEL with an optical fiber conserving the light polarization information.
3. Propagation of the 100% σ^+- or σ^--polarized light in the optical fiber toward the terminal device (High density magnetic recording media, Magnetic electrode of a spin-transistor,...).
4. At the optical fiber output, the preserved spin-information contained in the circular-polarization is re-encoded onto a magnetic media through All-Optical Helipticity Dependent Switching.

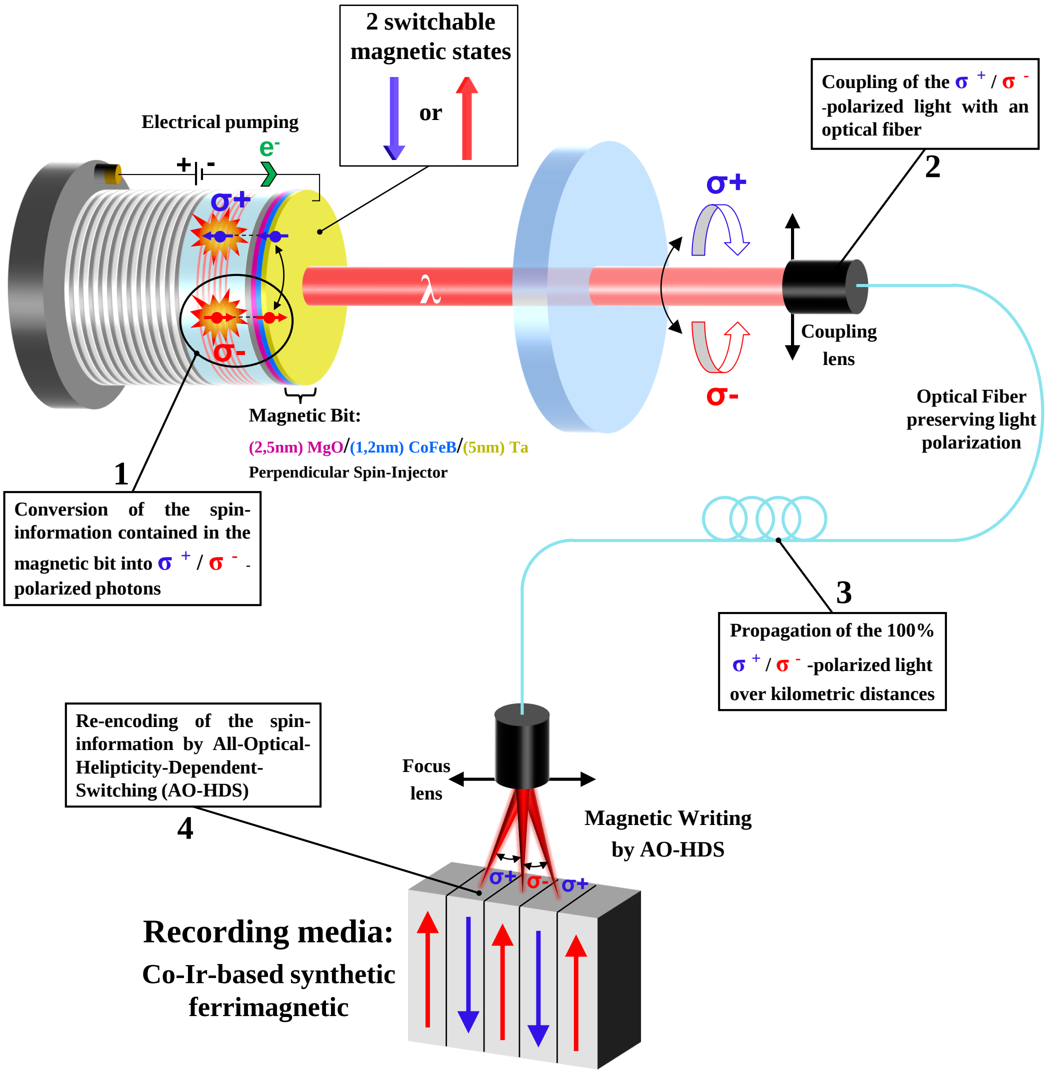

Figure 5.3: Illustration of a new paradigm for spin-information propagation over very long distances.

This concept offers the possibility to transfer safely and at light-speed the spin-information over kilometric distances between two spintronic-based terminals for example. Additionally, this method of communication would provide several advantages linked to the intrinsic operation mode of Spin-V(E)CSEL such as **(i)** good performances thanks to the reduced laser threshold [37, 38, 39] and **(ii)** highly efficient dynamics operation [234, 35] with enhanced bandwidth communication [34], lower frequency chirp but also fast modulation dynamic [280, 34].

I hope that the research efforts provided during this Ph.D successfully illustrated that spintronic with semiconductors still have many opportunities to offer for a next generation of innovative concepts and devices. I have no doubt that such attractive beyond state-of-the-art applications will stimulate an important research effort in a near future. To this day, ideas of innovative applications using Spin-Lasers are just emerging and such devices, borned from the fusion of Spintronics and Semiconductor-Photonics, just revealed an infinitesimal part of their capabilities.

Appendix A

Complementary calculation related to spin-injection into semiconductors

Contents

A.1 Formal demonstration of the General Boltzmann equation

The semi-classical treatment of the electronic transport starts by considering an electron gas described as a wave packet Φ and defined in the direct space by the position $\vec{r}$. The application of an electric field induces a shift of all carriers in the phases space while at the same time the random collisions tend to bring back the electrons toward their equilibrium distribution. Hence, the carriers distribution function $f(\vec{k},\vec{r},t)$ fully characterize the system evolution. It is defined so as $f(\vec{k},\vec{r},t)d\vec{k}d\vec{r}/(4\pi^3)$ represents the number of electrons in the considered band contained in the infinitesimal phase space element $d\vec{k}d\vec{r}$ at time t. Here, we are going to identify the nature of this function by studying the dynamical equilibrium between the carriers acceleration in the electric field and their diffusion by the crystalline network [360].

The localized Gaussian wave function representing the electron gas is defined by:

$$\Phi_{\vec{k}} = \sum_{\vec{k}} u_{\vec{k}} \cdot exp\left(i\vec{k} \cdot \left[\vec{r} - \frac{1}{\hbar}\frac{dE(\vec{k})}{d\vec{k}}t \right] \right) \cdot exp\big(- \alpha[\vec{k} - \vec{k_0}]\big)^2 \qquad \text{(A.1)}$$

where $u_{\vec{k}}$ is the base vector, $E(\vec{k})$ is the electric field, $\vec{k_0}$ is the wave vector corresponding the rest system without any applied electric field and α is a positive integer characterizing the shape of the wave packet envelope.

One must also take into account the carrier scattering probability by the crystalline network $W_{\vec{k}\vec{k'}}$. The probability of an electron to scatter from an initial state $\Phi_{\vec{k}}$ to a final state $\psi_{\vec{k'}}$ is given by Fermi golden rule:

$$W_{\vec{k}\vec{k'}} = \frac{2\pi}{\hbar} \left| \left\langle \Psi_{\vec{k'}} \right| V(\vec{r}) \left| \Phi_{\vec{k}} \right\rangle \right|^2 N(E_F) \tag{A.2}$$

where $V(\vec{r})$ is the perturbation Hamiltonian materializing the applied electric potential and $N(E_F)$ is the final Density Of State (DOS) at the Fermi level.

Thanks to the carrier scattering probability it is now possible to write the transport equation. The temporal evolution of the distribution function is equal to the collision integral calculated by summing the scattering probabilities over k:

$$\frac{df}{dt} = \left.\frac{\partial f}{\partial t}\right|_{\text{scattering}} \Longleftrightarrow \frac{\partial f}{\partial t} + \left.\frac{\partial f}{\partial \vec{r}} \cdot \frac{\partial \vec{r}}{\partial t}\right|_{\text{diffusion}} + \left.\frac{\partial f}{\partial \vec{k}} \cdot \frac{\partial \vec{k}}{\partial t}\right|_{\text{drift}} = \left.\frac{\partial f}{\partial t}\right|_{\text{scattering}} \tag{A.3}$$

where:

- The diffusion term take into account the speed of the electronic wave packet $\vec{v}(\vec{k})$:

$$\frac{\partial \vec{r}}{\partial t} = \vec{v}(\vec{k}) = \frac{1}{\hbar} \frac{dE(\vec{k})}{d\vec{k}} \tag{A.4}$$

- The drift component describes the global motion induced by the different in-system forces. In the approximation of the free electron gas the drifting force is generated by the applied electromagnetic field $\vec{F} = \hbar \frac{\partial \vec{k}}{\partial t} = -e\left[\vec{E} + \vec{v}(\vec{k}) \times \vec{H}\right]$. Hence:

$$\left.\frac{\partial f}{\partial \vec{k}} \cdot \frac{\partial \vec{k}}{\partial t}\right|_{\text{drift}} = -\frac{e}{\hbar}\left[\vec{E} + \vec{v}(\vec{k}) \times \vec{H}\right] \frac{\partial f}{\partial \vec{k}} \tag{A.5}$$

- The scattering term represents the collision integral. Physically, it corresponds to the total rate at which the distribution function is changing due to collisions. We can notice that as the electrons can scatter into ($W_{\vec{k}'\vec{k}}$) or outo ($W_{\vec{k}\vec{k}'}$) the considered $d\vec{k}$ element, the collision integral correspond to the sum of $(\partial f(\vec{k})/\partial t)_{in}$ and $(\partial f(\vec{k})/\partial t)_{out}$. In the relaxation-time approximation, it can be expressed as follow [360]:

$$\left.\frac{\partial f(\vec{k})}{\partial t}\right|_{\text{scattering}} = -\frac{f(\vec{k}) - f^0(\vec{k})}{\tau(\vec{k})} \tag{A.6}$$

  where $f^0(\vec{k})$ is the non-perturbed Fermi-Dirac distribution function and $\tau(\vec{k})$ is the characteristic scattering time define such as $dt/\tau(\vec{k})$ is the probability for an electron to experience a collision in the infinitesimal time interval dt.

The equation (A.3) can then be rewritten by taking into account these developments:

$$\boxed{\frac{\partial f}{\partial t} + \vec{v}\frac{\partial f}{\partial \vec{r}} - \frac{e}{\hbar}\left[\vec{E} + \vec{v} \times \vec{H}\right]\frac{\partial f}{\partial \vec{k}} = -\frac{f - f^0}{\tau}} \tag{A.7}$$

This fundamental equation is the general Boltzmann equation describing the electronic transport.

Comments:

- ▶ If quantum interferences become dominants it is necessary to add a quantum correction term in order to take into account the weak localization effects, the electron-electron interactions, etc... [361].
- ▶ The previously developed Boltzmann model is valid for a diffusive system. In case of a ballistic electrons regime, a formalism based on non-equilibrium Green functions should be preferentially considered to study the electronic transport in a conductive system.
- ▶ Equation (A.7)stays valid under two conditions. Firstly, the wave packet width in the phase space needs to be negligible compare to the 1st Brillouin-zone: $\Delta\vec{k} \ll a$. Secondly, the electron mean free path must stay greater than the De Broglie wavelength associated to the wave packet: $\lambda > \lambda_\Phi$

A.2 Valet-Fert Model: Expressions of the electrochemical potentials and the associated currents

For a F/N bilayer system, the general solutions of the electrochemical potentials and the associated currents obtained from the Valet-Fert theory are given by:

For a ferromagnetic layer numerated (n) with "up" magnetization:

$$\Delta\mu_F^{(n)}(z) = K_2^{(n)F} \cdot exp\left(\frac{z}{l_{sf}^F}\right) + K_3^{(n)F} \cdot exp\left(-\frac{z}{l_{sf}^F}\right) \tag{A.8}$$

$$\begin{cases} \bar{\mu}_+^{(n)F}(z) = e\rho_F^*(1-\beta^2)Jz + K_1^{(n)} + (1+\beta)\left[\Delta\mu_F^{(n)}\right] \\ \bar{\mu}_-^{(n)F}(z) = e\rho_F^*(1-\beta^2)Jz + K_1^{(n)} - (1-\beta)\left[\Delta\mu_F^{(n)}\right] \end{cases} \tag{A.9}$$

$$\begin{cases} J_+^{(n)F}(z) = (1-\beta)\dfrac{J}{2} + \dfrac{1}{2er_F}\left[K_2^{(n)F} \cdot exp\left(\dfrac{z}{l_{sf}^F}\right) - K_3^{(n)F} \cdot exp\left(-\dfrac{z}{l_{sf}^F}\right)\right] \\ J_-^{(n)F}(z) = (1+\beta)\dfrac{J}{2} - \dfrac{1}{2er_F}\left[K_2^{(n)F} \cdot exp\left(\dfrac{z}{l_{sf}^F}\right) - K_3^{(n)F} \cdot exp\left(-\dfrac{z}{l_{sf}^F}\right)\right] \end{cases} \tag{A.10}$$

For a F layer with "down" magnetization, one has to interchange the positive and negative index to get the related expressions.

In the same way, for a non-magnetic layer numerated (n+1):

$$\Delta\mu_N^{(n+1)}(z) = K_2^{(n+1)N} \cdot exp\left(\frac{z}{l_{sf}^N}\right) + K_3^{(n+1)N} \cdot exp\left(-\frac{z}{l_{sf}^N}\right) \tag{A.11}$$

$$\begin{cases} \bar{\mu}_+^{(n+1)N}(z) = e\rho_N^*Jz + K_1^{(n+1)} + \left[\Delta\mu_N^{(n+1)}\right] \\ \bar{\mu}_-^{(n+1)N}(z) = e\rho_N^*Jz + K_1^{(n+1)} - \left[\Delta\mu_N^{(n+1)}\right] \end{cases} \tag{A.12}$$

$$\begin{cases} J_+^{(n+1)N}(z) = \dfrac{J}{2} + \dfrac{1}{2er_F}\left[K_2^{(n)N} \cdot exp\left(\dfrac{z}{l_{sf}^F}\right) - K_3^{(n)N} \cdot exp\left(-\dfrac{z}{l_{sf}^F}\right)\right] \\ J_-^{(n+1)N}(z) = \dfrac{J}{2} - \dfrac{1}{2er_F}\left[K_2^{(n)N} \cdot exp\left(\dfrac{z}{l_{sf}^F}\right) - K_3^{(n)N} \cdot exp\left(-\dfrac{z}{l_{sf}^F}\right)\right] \end{cases} \tag{A.13}$$

The integration constants $K_i^{(n)F}$ and $K_i^{(n+1)N}$ can be determined by taking into account the boundary conditions (2.12) at each interfaces.

A.3 Valet-Jaffrès Model: Expressions of the electrochemical potentials and the associated currents

For a F/SC bilayer system, the general solutions of the electrochemical potentials and the associated currents obtained from the Fert-Jaffrès theory are given by:

For the ferromagnetic layer with "up" magnetization:

$$\Delta\mu_F(z) = K_2^F \cdot exp\left(\frac{z}{l_{sf}^F}\right) \tag{A.14}$$

$$\begin{cases} \bar{\mu}_+^F(z) = e\rho_F^*(1-\beta^2)Jz + K_1 + (1+\beta)K_2^F \cdot exp\left(\frac{z}{l_{sf}^F}\right) \\ \bar{\mu}_-^F(z) = e\rho_F^*(1-\beta^2)Jz + K_1 - (1-\beta)K_2^F \cdot exp\left(\frac{z}{l_{sf}^F}\right) \end{cases} \tag{A.15}$$

$$\begin{cases} J_+^F(z) = (1-\beta)\frac{J}{2} + \frac{1}{2er_F}K_2^F \cdot exp\left(\frac{z}{l_{sf}^F}\right) \\ J_-^F(z) = (1+\beta)\frac{J}{2} - \frac{1}{2er_F}K_2^F \cdot exp\left(\frac{z}{l_{sf}^F}\right) \end{cases} \tag{A.16}$$

For a F layer with "down" magnetization, one has to interchange the positive and negative index to get the related expressions.

For the semiconductor:

$$\Delta\mu_{SC}(z) = K_3^{SC} \cdot exp\left(-\frac{z}{l_{sf}^{SC}}\right) \tag{A.17}$$

$$\begin{cases} \bar{\mu}_+^{SC}(z) = e\rho_{SC}^*Jz + K_1 + K_3^{SC} \cdot exp\left(-\frac{z}{l_{sf}^{SC}}\right) \\ \bar{\mu}_-^{SC}(z) = e\rho_{SC}^*Jz + K_1 - K_3^{SC} \cdot exp\left(-\frac{z}{l_{sf}^{SC}}\right) \end{cases} \tag{A.18}$$

$$\begin{cases} J_+^{SC}(z) = \frac{J}{2} - \frac{1}{2er_{SC}}K_3^{SC} \cdot exp\left(-\frac{z}{l_{sf}^{SC}}\right) \\ J_-^{SC}(z) = \frac{J}{2} + \frac{1}{2er_{SC}}K_3^{SC} \cdot exp\left(-\frac{z}{l_{sf}^{SC}}\right) \end{cases} \tag{A.19}$$

Here again, the integration constants K_i^F and K_i^{SC} can be determined using the boundary conditions (2.12).

Appendix B

Spin Flip Model - Single mode emission: Basic polarization states

For a VCSEL operating in a single mode emission, the detailed solutions extracted from the SFM and the associated electric field projections in the (x,y)-basis are given by:

A) **If $\alpha \neq 0$, $\gamma_a \neq 0$ and $\gamma_p \neq 0$:**

In the most general case, the system admits two linearly polarized solutions:

- For the $\hat{x}$-polarized solution is given by:

$$\begin{cases} Q_{\pm}^2 = \dfrac{1}{2}\dfrac{\mu - N_0}{N_0}, \qquad \psi = 0, \\ \omega_{\pm} = \omega_x = -\gamma_p + \gamma_a \alpha, \\ N_0 = 1 + \dfrac{\gamma_a}{\kappa}, \qquad n_0 = 0, \end{cases} \tag{B.1}$$

  Which leads by projection of the circularly polarized field (E_+,E_-) on the (x,y)-basis to:

$$\begin{cases} E_x = \sqrt{\dfrac{\kappa(\mu+1)+\gamma_a}{\kappa+\gamma_a}} \cdot exp\left[i\left(-\gamma_p + \gamma_a \alpha\right)t + i\theta\right] \\ E_y = 0 \end{cases} \tag{B.2}$$

- The $\hat{y}$-polarized solution is given by:

$$\begin{cases} Q_{\pm}^2 = \dfrac{1}{2}\dfrac{\mu - N_0}{N_0}, \qquad \psi = \dfrac{\pi}{2}, \\ \omega_{\pm} = \omega_y = \gamma_p - \gamma_a \alpha, \\ N_0 = 1 - \dfrac{\gamma_a}{\kappa}, \qquad n_0 = 0, \end{cases} \tag{B.3}$$

Which leads by projection of the circularly polarized field (E_+,E_-) on the (x,y)-basis to:

$$\begin{cases} E_x = 0 \\ E_y = \sqrt{\dfrac{\kappa(\mu+1)+\gamma_a}{\kappa+\gamma_a}} \cdot exp\left[-i\left(-\gamma_p+\gamma_a\alpha\right)t+i\theta\right] \end{cases} \tag{B.4}$$

B) **If $\alpha \neq 0$ and $\gamma_a = \gamma_p = 0$:**

If the VCSEL is perfectly isotropic the system admits a unique linearly polarized solution given by:

$$\begin{cases} Q_\pm^2 = \dfrac{1}{2}(\mu-1), \psi \neq 0 \\ \omega_\pm = 0, \\ N_0 = 1, \quad n_0 = 0, \end{cases} \tag{B.5}$$

Which leads by projection of the linearly polarized field (E_+,E_-) on the (x,y)-basis to:

$$\begin{cases} E_x = \sqrt{\mu-1} cos\psi \\ E_y = \sqrt{\mu-1} sin\psi \end{cases} \tag{B.6}$$

C) **If $\alpha \neq 0$, $\gamma_a = 0$ and $\gamma_p \neq 0$:**

In this case the system admits two linearly- and two elliptically-polarized solution:

- The $\hat{x}$-polarized solution (Figure 2.28 (a) ①) is given by:

$$\begin{cases} Q_\pm^2 = \dfrac{1}{2}(\mu-1), \quad \psi = 0, \\ \omega_\pm = -\gamma_p, \\ N_0 = 1, \quad n_0 = 0, \end{cases} \tag{B.7}$$

Which leads in the (x,y)-basis to:

$$\begin{cases} E_x = \sqrt{\mu - 1} exp\left(-i\gamma_p t\right) \\ E_y = 0 \end{cases} \tag{B.8}$$

- The $\hat{y}$-polarized solution (Figure 2.28 (a) ②) is given by:

$$\begin{cases} Q_{\pm}^2 = \frac{1}{2}(\mu - 1), & \psi = \frac{\pi}{2}, \\ & \omega_{\pm} = \gamma_p, \\ N_0 = 1, & n_0 = 0, \end{cases} \tag{B.9}$$

  Which leads in the (x,y)-basis to:

$$\begin{cases} E_x = 0 \\ E_y = \sqrt{\mu - 1} exp\left(i\gamma_p t\right) \end{cases} \tag{B.10}$$

- The two elliptically polarized solutions (Figure 2.28 (a) ③-④) are given by:

$$\begin{cases} Q_{\pm}^2 = \frac{1}{2}(\mu - N_0)\left(1 \mp \frac{N_0 - 1}{n_0}\right), \\ \omega_{\pm} = \kappa\alpha \frac{(N_0 - 1)^2 - n_0^2}{N_0 - 1}, \\ tan(2\psi) = \frac{1}{\alpha}\frac{N_0 - 1}{n_0}, \end{cases} \tag{B.11}$$

  The two solutions are then discriminated by the two values of the population difference between the sublevels with opposite value of the spin n_0:

$$n_0^2 = \frac{(\mu - N_0)(N_0 - 1) N_0}{\frac{\gamma_s}{\gamma_r} + \mu - N_0}, \qquad N_0 > 1 \tag{B.12}$$

These two elliptically polarized solutions exhibit the same frequencies but different elliptical polarization orientation and different rotation senses (Figure 2.28 (a) ③-④). Elliptically polarized states have been experimentally observed for VCSEL operation under applied longitudinal magnetic fields with very small remnant ellipticity at zero field [273, 362].

In the particular case where $\gamma_s = 0$ each elliptically polarized solution becomes circularly polarized light. In this case [270]:

$$N_0 = \frac{\mu + \frac{\gamma_s}{\gamma_r}}{1 + \frac{\gamma_s}{\gamma_r}}, \qquad n_0 = \pm(N_0 - 1) \tag{B.13}$$

where $n_0 > 0$ and $n_0 < 0$ correspond the left and right circularly polarized modes respectively. Nevertheless, these circularly polarized states are never found to be stable solutions of (3.63)-(3.65) [236]. These situation corresponds to the previous case B) where for a perfectly isotropic VCSEL ($\gamma_a = \gamma_p = 0$) linearly polarized states exist with an arbitrary orientation . Birefringence alone (γ_p) is able to fix the direction of polarization selecting two preferred values of ψ which can be identified with the $\hat{x}$ and $\hat{y}$ linearly polarized states.

APPENDIX C

Micro-pillar photolithography process

This section details the photolithography process used to pattern all the Spin-LED and the Spin-VECSEL designed for electrical injection. The architecture consists in a 2-contacts pillar-shaped diode junction:

1. **Patterning of the 300 μm pillar-shaped diodes by Ion Beam Etching:**
   (a) Sample bonding on a Silicon Wafer using red *sticky wax* on a 110°C plate. Use toothpick to gently press the sample onto the wafer and remove any potential air bubbles.
   (b) Spin-coating of the Photo-resist:
      - Primer *HDMS*: 4 kRPM, 30s
      - Photo-resist *SPR 700 1.2 μm*: 4kRPM, 30s
      - Soft bake: 110°C for 1 min
   (c) UV-Exposure on *Karl SUSS MA100* Mask-aligner: 5s at 18 mW.cm^{-2} in soft contact mode.
   (d) Photo-resist development using *MF319*:
      - 35-40s in *MF319* (First 10s steady + 25-30s slow rotation)
      - 2 min in running H_2O DI
   (e) Ion Beam Etching in *IBE-Plassys*: 350eV - 80mA, etching control via SIMS
   (f) O_2-Plasma cleaning:
      - O_2-Plasma: 400W for 5 min
      - Rinse: Acetone/Propanol
   (g) Control: Optical microscope
   (h) Remove sample from Silicon wafer with a toothpick on a 110°C plate.
   (i) Sample cleaning:
      - Hot Trichloroethylene or Toluene (140°C)
      - Cold Trichloroethylene or Toluene
      - Rinse: Acetone/Propanol

2. **110 μm top and bottom contact deposition by Lift-Off:**
    (a) Sample bonding on a Silicon Wafer using *Crystalbond 555* on a 60°C plate. Use toothpick to gently press the sample onto the wafer and remove any potential air bubbles.
    (b) Spin-coating of the Photo-resist:
        - Primer *HDMS*: 4 kRPM, 30s
        - Photo-resist *SPR 700 1.2 μm*: 4kRPM, 30s
        - Soft bake: 110°C for 1 min
    (c) Remove sample from Silicon wafer with a toothpick on a 60°C plate and rinse 2 min in running H_2O DI
    (d) Photo-resist hardening:
        - Chlorobenzene for 10 min
        - Dry with N_2
        - Hard bake: 110°C for 1 min
    (e) Sample bonding on a Silicon Wafer using red *sticky wax* on a 110°C plate. Use toothpick to gently press the sample onto the wafer and remove any potential air bubbles.
    (f) UV-Exposure on *Karl SUSS MA100* Mask-aligner: 10s at 18 mW.cm^{-2} in soft contact mode.
    (g) Photo-resist development using *MF319*:
        - 1min30s in *MF319* (First 10s steady + 1min20s slow rotation every 20s)
        - 2 min in running H_2O DI
    (h) Metallic contacts deposition (Ask the Thales technological platform):
        - Plasma Etching: 200V â 110mA for 1 min
        - (50nm) *Ti* / (250nm) *Au* by side evaporation
    (i) Lift-Off:
        - Minimum 1H in Acetone
        - Acetone gun $\mapsto$ LIFT
        - Rinse: Spray Acetone/Propanol
    (j) Control: Optical microscope
    (k) Remove sample from Silicon wafer with a toothpick on a 110°C plate.
    (l) Sample cleaning:
        - Hot Trichloroethylene or Toluene (140°C)
        - Cold Trichloroethylene or Toluene
        - Rinse: Acetone/Propanol

APPENDIX D

Formal demonstration of the relation between frequency detuning and birefringence

---

In this appendix, we aim at giving the relationship between the frequency detuning between the TE- and TM-modes emitted by a laser and the intrinsic birefringence of 1/2-VCSEL. We choose for notation conventions to identify the frequency in the optical domain as ν and the frequency in the electrical domain as f. We consider the general case of a VECSEL emitting on the TE-mode linearly-polarized along the extraordinary-axis while the spontaneous emission of TM-mode linearly-polarized along the ordinary-axis is amplified by the cavity but still below threshold (Figure D.1 (a)).

We define L as the cavity length, c the celerity of light, l the thickness of the active medium while n_e and n_o are the refractive indexes seen in the 1/2-VCSEL by the extraordinary and ordinary polarizations respectively. Accordingly, the optical frequencies associated with the extraordinary and ordinary polarization modes at the order p and q are respectively given by:

$$\begin{cases} \nu_{TE}^{p} = p \cdot \dfrac{c}{2\left[L + (n_e - 1)l\right]} \\ \nu_{TM}^{q} = q \cdot \dfrac{c}{2\left[L + (n_o - 1)l\right]} \end{cases} \tag{D.1}$$

However, as the birefringence is expected to be relatively small, the order p and q are equals. Hence, the system of equations becomes:

$$\begin{cases} \nu_{TE}^{p} = p \cdot \dfrac{c}{2\left[L + (n_e - 1)l\right]} \\ \nu_{TM}^{p} = p \cdot \dfrac{c}{2\left[L + (n_o - 1)l\right]} \end{cases} \tag{D.2}$$

After projection of the two ordinary and extraordinary optical spectra on the same polarization axis (Figure D.1 (b)), we focus on the associated RF spectrum (Figure D.1 (c)). In the electrical domain, the corresponding spectrum displays

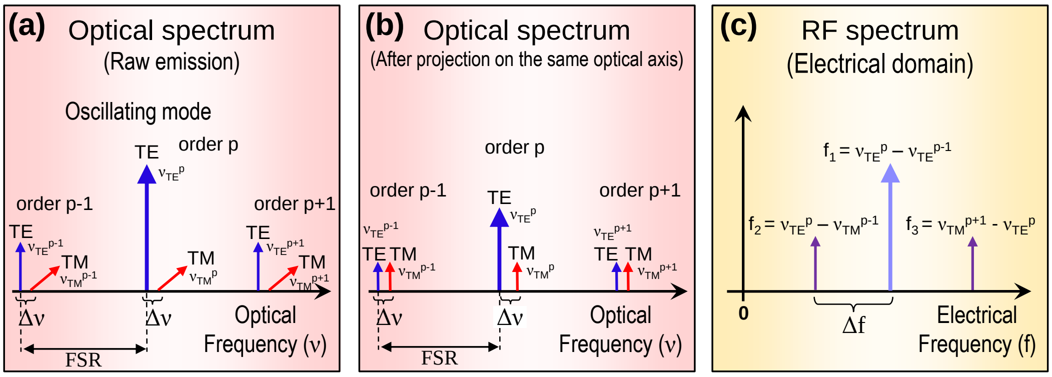

Figure D.1: Optical and electrical mode spectra: (a) Optical spectrum emitted by the laser. For a given mode, the frequency detuning between two adjacent orders is equal to the Free Spectral Range (FSR) of the cavity. (b) Corresponding optical spectrum after projection on the same polarization axis using a polarizer. (c) Associated electrical spetrum after quadratic detection by a photodiode of the projected optical spectrum at 45°.

beating frequencies between the different optical modes. On figure D.1 (c): (i) the central peak (light blue) corresponds to the beating frequency f_1 between the lasing TE-mode at the order p (optical frequency ν_{TE}^{p}) and the Amplified Spontaneous Emission (ASE) of the TE-mode at the order p+1 (optical frequency ν_{TE}^{p+1}). (ii) On the other hand, the satellite peak f_2 (purple) corresponds to the beating frequency between the lasing TE-mode at the order p (optical frequency ν_{TE}^{p}) and the ASE of the TM-mode at the order p-1 (optical frequency ν_{TM}^{p-1}). Similarly, the satellite peak f_3 (purple) corresponds to the beating frequencies between the lasing TE-mode at the order p (optical frequency ν_{TE}^{p}) and the ASE of the TM-mode at the order p+1 (optical frequency ν_{TM}^{p+1}). Obviously, the beating between the lasing TE-mode and the nonlasing TM-modes at the order p is also present in the low frequency part of the spectrum. However, we do not rely on this peak for our measurements because it suffers from pump to laser noise transfer as well as from CPO effects that cannot be neglected for beatnotes below 1 GHz. The above different frequencies read:

$$\begin{cases} f_1 = \nu_{TE}^{p} - \nu_{TE}^{p-1} = \dfrac{c}{2L_e} \\ f_2 = \nu_{TE}^{p} - \nu_{TM}^{p-1} = \dfrac{pc}{2}\left(\dfrac{1}{L_e} - \dfrac{1}{L_o}\right) + \dfrac{c}{2L_o} \\ f_3 = \nu_{TM}^{p+1} - \nu_{TE}^{p} = \dfrac{pc}{2}\left(\dfrac{1}{L_o} - \dfrac{1}{L_e}\right) + \dfrac{c}{2L_e} \end{cases} \tag{D.3}$$

where $L_e = L + (n_e - 1)l$ and $L_o = L + (n_o - 1)l$ are the optical lengths seen by the modes polarized along the extraordinary (TE) and the ordinary (TM) axis respectively. Using (D.3), we further calculate the frequency detunings $f_1 - f_2$ and

$f_3 - f_1$ between the central peak (f_1) and the left (f_2) and right (f_3) satellite peaks respectively (Figure D.1 (c)):

$$\begin{cases} f_1 - f_2 = \dfrac{c}{2}(1-p)\left(\dfrac{1}{L_e} - \dfrac{1}{L_o}\right) \\ f_3 - f_1 = \dfrac{c}{2}(1+p)\left(\dfrac{1}{L_o} - \dfrac{1}{L_e}\right) \end{cases} \tag{D.4}$$

Finally, the birefringence $\Delta n = n_e - n_o$ can be extracted from (D.4):

$$\Delta f = \frac{(f_1 - f_2) + (f_3 - f_1)}{2} = \frac{pc}{2L_o}\frac{l\Delta n}{L_e} = \nu_o \frac{l\Delta n}{L_e} \tag{D.5}$$

Then the dephasing $\Delta\varphi$ associated with the birefringence Δn can be expressed for a round-trip as:

$$\Delta\varphi = \frac{2\pi}{\lambda} 2l\Delta n \tag{D.6}$$

Finally, the expression (D.6) can be rewritten as follow using the relation of equation (D.5):

$$\boxed{\frac{\Delta\varphi}{2\pi} = \frac{\gamma'}{2\pi} = \frac{2L}{c}\Delta f} \tag{D.7}$$

where $L \approx L_e \approx L_o$. This relation is established for a round-trip in the cavity.

APPENDIX E

Complementary information on TRPL measurements

E.1 Experimental setup

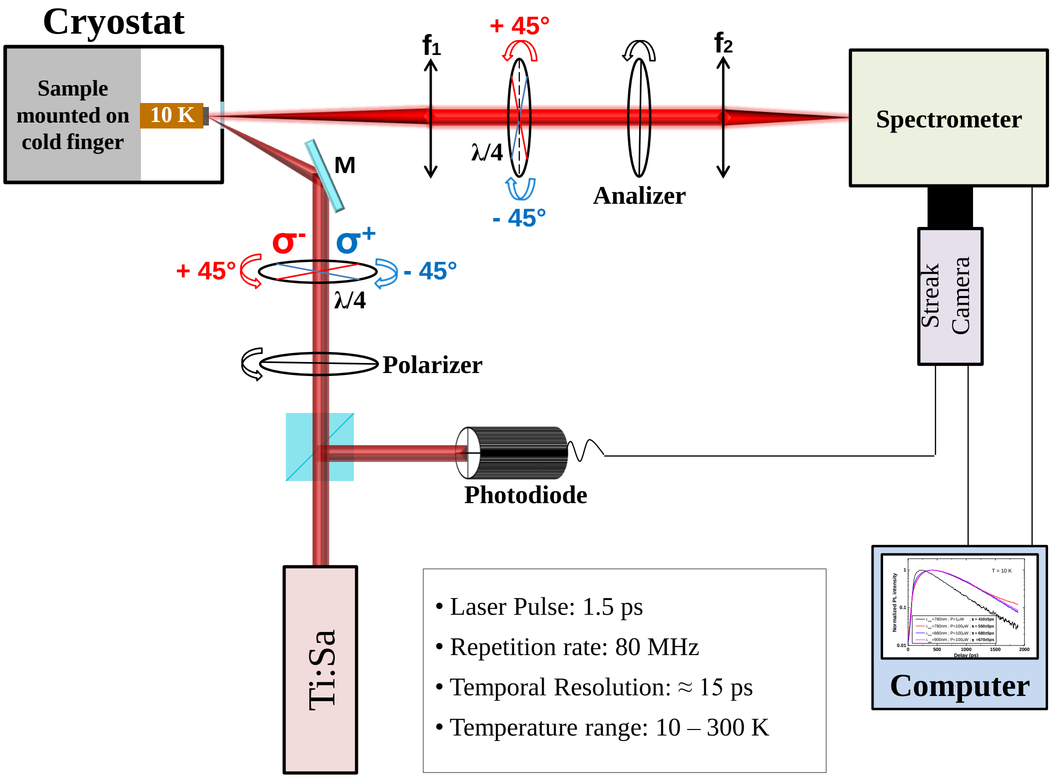

Figure E.1: Schematic of the experimental setup used to performed the Time Resolved Photo-Luminescence measurements on Spin-LED and Spin-VECSEL.

E.2 Band-to-band transitions and excitation energies of the InGaAs/GaAsP $\frac{1}{2}$-VCSEL

Temperature	Transition	Energy (eV)	Wavelength λ (nm)
300 K	$e_1 - hh_1$	1.261	982.9
	$e_2 - hh_2$	1.378	899
	$e_1 - lh_1$	1.345	921.5
	Gap $In_{20\%}Ga_{80\%}As$	1.214	1021
	Gap $GaAs$	1.423	871
	Gap $GaAs_{95\%}P_{5\%}$	1.463	847
10 K	$e_1 - hh_1$	1.357	913
	$e_2 - hh_2$	1.474	841
	$e_1 - lh_1$	1.441	860
	Gap $In_{20\%}Ga_{80\%}As$	1.310	946
	Gap $GaAs$	1.519	816
	Gap $GaAs_{95\%}P_{5\%}$	1.559	795

Table E.1: Band-to-band transition energies derived from $k.p$ simulations of $\mathrm{In_{20\%}Ga_{80\%}As/GaAs_{95\%}P_{5\%}}$ QW used as the active medium of the GaAs615 VESCEL. From 300 K to 10 K the energy gap shift of $\mathrm{In_{20\%}Ga_{80\%}As}$ and $\mathrm{GaAs_{95\%}P_{5\%}}$ has been estimated to be approximately the same than the shift of the GaAs's gap: 95.9 meV.

Temperature	Excitation Wavelength (nm)	Corresponding Energy (eV)	Comments
300 K	769	1.612	Above $GaAs$ and $GaAsP$
	808	1.534	Above $GaAs$ and $GaAsP$
	845	1.466	Above $GaAs$ and $GaAsP$
	879	1.410	Under $GaAs$ and $GaAsP$ but above $e_1 - hh_1$, $e_2 - hh_2$ and $e_1 - lh_1$
10 K	769	1.612	Above $GaAs$ and $GaAsP$
	845	1.466	Under $GaAs$ and $GaAsP$ but above $e_1 - hh_1$, $e_2 - hh_2$ and $e_1 - lh_1$

Table E.2: Excitation energies of the Ti:Sa laser used to perform the TRPL measurements at both low and room temperature.

E.3 Complementary TRPL measurements of the InGaAs/GaAsP GaAs615 $\frac{1}{2}$-VCSEL

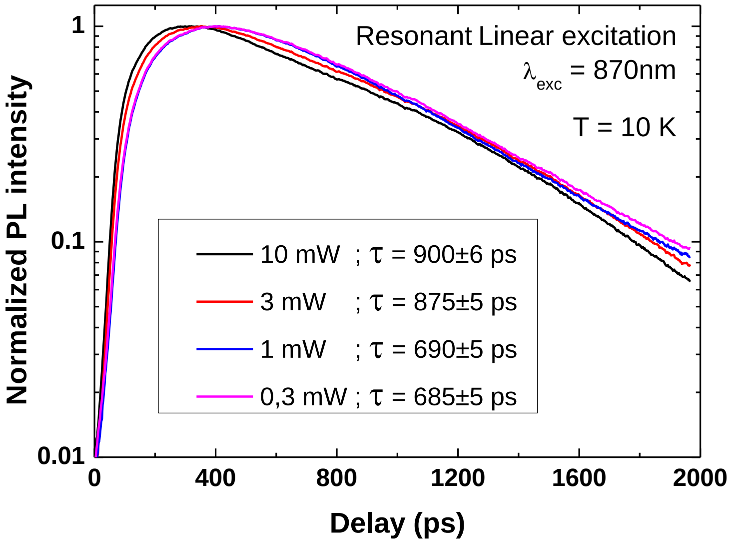

Figure E.2: Carrier lifetime measurements at T=10 K for a resonant (870 nm) and linearly-polarized pumping under variable excitation power ranging from 0.3 mW to 10 mW.

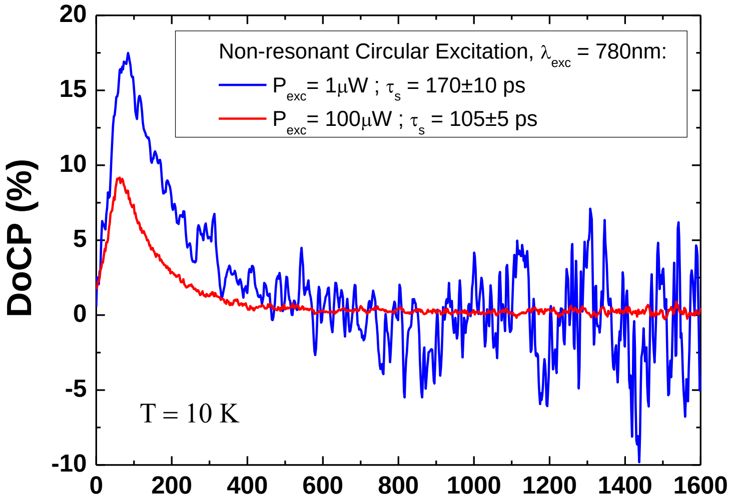

Figure E.3: **Time Resolved Spin lifetime measurements:** Comparison of Spin lifetime measurements at T=10 K under non-resonant pumping at 780 nm for two excitation power of 1 μW and 100 μW.

Appendix F

List of Publications

- **"Accurate measurement of the residual birefringence in VECSEL: Towards understanding of the polarization behavior under spin-polarized pumping"**
  J. Frougier, G. Baili, I. Sagnes, D. Dolfi, J. M. George and M. Alouini
  Optics Express **Submitted** (2014)

- **"Large and robust electrical spin injection into GaAs at zero magnetic field using an ultrathin CoFeB/MgO injector"**
  S. Liang, T. Zhang, P. Barate, **J. Frougier**, M. Vidal, P. Renucci, B. Xu, H. Jaffres, J. M. George, X. Devaux, M. Hehn, X. Marie, S. Mangin, H. Yang, A. Hallal, M. Chshiev, T. Amand, H. Liu, D. Liu, X. Han, Z. Wang and Y. Lu
  Physical Review B **90**, 085390 (2014)

- **"Electrical spin injection into InGaAs/GaAs quantum wells: A comparison between MgO tunnel barriers grown by sputtering and molecular beam epitaxy methods"**
  P. Barate, S. Liang, T. T. Zhang, **J. Frougier**, M. Vidal, P. Renucci, X. Devaux, B. Xu, H. Jaffres, J. M. George, X. Marie, M. Hehn, S. Mangin, Y. Zhen, T. Amand, B. Tao, X. Han, Z. Wang and Y. Lu
  Applied Physics Letters **105**, 012404 (2014)

- **"Control of light polarization using optically spin-injected vertical external cavity surface emitting lasers"**
  J. Frougier, G. Baili, M. Alouini, I. Sagnes, H. Jaffres, A. Garnache, C. Deranlot, D. Dolfi and J. M. George
  Applied Physics Letters **103**, 252402 (2013)

- **"Spin Injection at Remanence into III-V Spin Light Emitting Diodes using (Co/Pt) Ferromagnetic Injectors"**
  J. Zarpellon, H. Jaffres, **J. Frougier**, C. Deranlot, J. M. George, D. H. Mosca, A. Lemaitre, F. Freimuth, Quang Ha Duong, P. Renucci and X. Marie
  Physical Review B **86**, 205314 (2012)

Appendix G
List of Conferences

- **Invited Speaker:**
  - 08/17/2014: **"Control of light polarization using spin-injected opto-electronic devices with vertical geometries"**
    J. Frougier, T. T. Zhang, S. Liang, P. Barate, P. Renucci, X. Marie, G. Baili, M. Alouini, I. Sagnes, A. Garnache, H. Jaffres, Y. Lu and J. M. George
    SPIE-Spintronics VII, San Diego, USA
  - 10/18/2012: **"Towards Control of Light Polarization using electron spin in Half-VCSEL"**
    J. Frougier, G. Baili, M. Alouini, I. Sagnes, H. Jaffres, A. Garnache, D. Dolfi and J. M. George
    First VeCSEL Workshop, Montpellier, FRANCE

- **Oral Communications:**
  - 11/04/2013: **"Electrical Spin-Injection enhancement in III-V Spin-LEDs: Towards control of light polarization using spin-injected Lasers"**
    J. Frougier, T. T. Zhang, S. Liang, P. Barate, P. Renucci, X. Marie, G. Baili, M. Alouini, I. Sagnes, A. Garnache, H. Jaffres, Y. Lu and J. M. George
    MMM Conference, Denver, USA
  - 10/15/2013: **"Control of light polarization using spin-injected VECSELs"**
    J. Frougier, G. Baili, M. Alouini, I. Sagnes, H. Jaffres, A. Garnache, D. Dolfi and J. M. George
    Second VeCSEL Workshop, Montpellier, FRANCE

- **Seminars:**
  - 15/01/2015: **"Towards Spin-LED and Spin-VECSEL operation at magnetic remanence"**
    J. Frougier, G. Baili, M. Alouini, I. Sagnes, H. Jaffres, A. Garnache, D. Dolfi and J. M. George
    Institut National des Sciences Appliquées, Toulouse, FRANCE
  - 09/01/2015: **"Towards Spin-LED and Spin-VECSEL operation at magnetic remanence"**
    J. Frougier, G. Baili, M. Alouini, I. Sagnes, H. Jaffres, A. Garnache, D. Dolfi and J. M. George
    University of Alabama at Birmingham, Birmingham, Alabama, USA
  - 05/01/2015: **"Towards Spin-LED and Spin-VECSEL operation at magnetic remanence"**
    J. Frougier, G. Baili, M. Alouini, I. Sagnes, H. Jaffres, A. Garnache, D. Dolfi and J. M. George
    The Pennsylvania State University, State College, Pennsylvania, USA
  - 02/21/2013: **"Towards Control of Light Polarization using electron spin in Half-VCSELs"**
    J. Frougier, G. Baili, M. Alouini, I. Sagnes, H. Jaffres, A. Garnache, D. Dolfi and J. M. George
    Institut d'Électronique Fondamentale, Montpellier, FRANCE
  - 01/17/2013: **"Towards Control of Light Polarization using electron spin in Half-VCSELs"**
    J. Frougier, G. Baili, M. Alouini, I. Sagnes, H. Jaffres, A. Garnache, D. Dolfi and J. M. George
    Unité Mixte de Physique CNRS-Thales, Palaiseau, FRANCE

- **Poster Communications:**
  - 07/29/2013: **"Towards control of light polarization using spin-injected VECSELs"**
    J. Frougier, G. Baili, M. Alouini, I. Sagnes, H. Jaffres, A. Garnache, D. Dolfi and J. M. George
    Spintech VII, Chicago, USA
  - 03/19/2013: **"Contrôle de la Polarisation Lumineuse d'un LASER par injection de porteurs polarisées en spin"**
    J. Frougier, G. Baili, M. Alouini, I. Sagnes, H. Jaffres, A. Garnache, D. Dolfi and J. M. George
    XV Colloque Louis Néel, Tours, FRANCE

Bibliography

[1] M. N. Baibich et al., Physical Review Letters **61**, 2472 (1988). (Cited on pages 1 and 11.)

[2] G. Binasch, P. Grunberg, F. Saurenbach, and W. Zinn, Physical Review B **39**, 4828 (1989). (Cited on pages 1 and 11.)

[3] M. Julliere, Physics Letters A **54**, 225 (1975). (Cited on pages 1 and 11.)

[4] J. S. Moodera, L. R. Kinder, T. M. Wong, and R. Meservey, Physical Review Letters **74**, 3273 (1995). (Cited on pages 1 and 11.)

[5] S. Yuasa, A. Fukushima, H. Kubota, Y. Suzuki, and K. Ando, Applied Physics Letters **89**, 042505 (2006). (Cited on page 1.)

[6] W. H. Rippard, M. R. Pufall, S. Kaka, S. E. Russek, and T. J. Silva, Physical Review Letters **92**, 027201 (2004). (Cited on page 1.)

[7] T. Yang, T. Kimura, and Y. Otani, Nature Physics **4**, 851 (2008). (Cited on pages 1 and 38.)

[8] X. Lou et al., Nature Physics **3**, 197 (2007). (Cited on pages 1, 38 and 198.)

[9] B. Dlubak et al., Nature Physics **8**, 557 (2012). (Cited on pages 1 and 22.)

[10] M. H. D. Guimaraes et al., Nano Letters **12**, 3512 (2012). (Cited on page 1.)

[11] L. E. Hueso et al., Nature **445**, 410 (2007). (Cited on pages 1 and 22.)

[12] Z. H. Xiong, D. Wu, Z. Valy Vardeny, and J. Shi, Nature **427**, 821 (2004). (Cited on page 1.)

[13] T. S. Santos et al., Physical Review Letters **98**, 016601 (2007). (Cited on page 1.)

[14] C. Barraud et al., Nature Physics **6**, 615 (2010). (Cited on page 1.)

[15] S. A. Wolf, Science **294**, 1488 (2001). (Cited on pages 1, 2 and 3.)

[16] J. F. Gregg, Nature Materials **6**, 798 (2007). (Cited on page 2.)

[17] S. Datta and B. Das, Applied Physics Letters **56**, 665 (1990). (Cited on page 2.)

[18] J. C. R. Sanchez et al., Nature Communications **4** (2013). (Cited on page 2.)

[19] C. M. Jaworski et al., Nature Materials **9**, 898 (2010). (Cited on pages 2 and 40.)

[20] K. C. Hall and M. E. Flatte, Applied Physics Letters **88**, 162503 (2006). (Cited on page 2.)

[21] S. Murakami, N. Nagaosa, and S.-C. Zhang, Science **301**, 1348 (2003), PMID: 12907808. (Cited on page 2.)

[22] B. T. Jonker, G. Kioseoglou, A. T. Hanbicki, C. H. Li, and P. E. Thompson, Nature Physics **3**, 542 (2007). (Cited on pages 3 and 98.)

[23] O. M. J. van't Erve et al., Applied Physics Letters **91**, 212109 (2007). (Cited on page 3.)

[24] L. Grenet et al., Applied Physics Letters **94**, 032502 (2009). (Cited on pages 3, 112 and 129.)

[25] S. P. Dash, S. Sharma, R. S. Patel, M. P. de Jong, and R. Jansen, Nature **462**, 491 (2009). (Cited on pages 3 and 38.)

[26] C. H. Li et al., Applied Physics Letters **91**, 262504 (2007). (Cited on page 3.)

[27] C. H. Li, O. M. J. van't Erve, and B. T. Jonker, Nature Communications **2**, 245 (2011). (Cited on page 3.)

[28] Tomoyasu Taniyama, Eiji Wada, Mitsuru Itoh, and Masahito Yamaguchi, NPG Asia Materials **3**, 65 (2011). (Cited on page 3.)

[29] R. Fiederling et al., Nature **402**, 787 (1999). (Cited on pages 4, 53, 66, 67, 68 and 97.)

[30] S. A. Crooker, D. D. Awschalom, J. J. Baumberg, F. Flack, and N. Samarth, Physical Review B **56**, 7574 (1997). (Cited on pages 4 and 58.)

[31] H. Dery, Y. Song, P. Li, and I. Zutic, Applied Physics Letters **99**, 082502 (2011). (Cited on pages 4, 93 and 208.)

[32] D. Miller, Proceedings of the IEEE **97**, 1166 (2009). (Cited on pages 4, 93 and 208.)

[33] B. Ciftcioglu et al., Optics Express **20**, 4331 (2012). (Cited on pages 4, 93 and 208.)

[34] J. Lee, W. Falls, R. Oszwaldowski, and I. Zutic, Applied Physics Letters **97**, 041116 (2010). (Cited on pages 4, 72, 75, 76, 93, 208 and 212.)

[35] N. C. Gerhardt et al., Applied Physics Letters **99**, 151107 (2011). (Cited on pages 4, 76, 93, 208 and 212.)

[36] H. Ando, T. Sogawa, and H. Gotoh, Applied Physics Letters **73**, 566 (1998). (Cited on pages 4, 93, 94, 149, 174, 206 and 208.)

[37] M. Holub, J. Shin, D. Saha, and P. Bhattacharya, Physical Review Letters **98**, 146603 (2007). (Cited on pages 4, 75, 76, 93, 96, 136, 149, 174, 196, 206, 208 and 212.)

[38] J. Rudolph, S. Dohrmann, D. Hagele, M. Oestreich, and W. Stolz, Applied Physics Letters **87**, 241117 (2005). (Cited on pages 4, 76, 77, 93, 94, 208 and 212.)

[39] C. Gothgen, R. Oszwaldowski, A. Petrou, and I. Zutic, Applied Physics Letters **93**, 042513 (2008). (Cited on pages 4, 72, 75, 76, 77, 93, 208 and 212.)

[40] S. Mangin et al., Nature Materials **13**, 286 (2014). (Cited on pages 4, 93, 204, 208 and 211.)

[41] N. Gerhardt et al., Electronics Letters **42**, 88 (2006). (Cited on pages 4, 94, 95, 174 and 206.)

[42] S. Iba, S. Koh, K. Ikeda, and H. Kawaguchi, Applied Physics Letters **98**, 081113 (2011). (Cited on pages 4, 94, 95, 153, 173, 174 and 206.)

[43] K. Schires et al., Optics Express **20**, 3550 (2012). (Cited on pages 4, 94, 149, 174 and 206.)

[44] D. Basu, D. Saha, and P. Bhattacharya, Physical Review Letters **102**, 093904 (2009). (Cited on pages 4, 76, 95 and 96.)

[45] J. Sinova and I. Zutic, Nature Materials **11**, 368 (2012). (Cited on page 5.)

[46] S. Hoogland et al., IEEE Photonics Technology Letters **12**, 1135 (2000). (Cited on pages 6, 137, 139 and 141.)

[47] D. Lorenser et al., IEEE Journal of Quantum Electronics **42**, 838 (2006). (Cited on pages 6 and 141.)

[48] R. Haring et al., IEEE Journal of Quantum Electronics **38**, 1268 (2002). (Cited on pages 6 and 141.)

[49] A. Garnache et al., Applied Physics Letters **80**, 3892 (2002). (Cited on pages 6 and 141.)

[50] P. Klopp, F. Saas, M. Zorn, M. Weyers, and U. Griebner, Optics Express **16**, 5770 (2008). (Cited on pages 6 and 141.)

[51] D. Maas et al., Applied Physics B **88**, 493 (2007). (Cited on pages 6 and 141.)

[52] F. Camargo et al., Two-cross-polarized-frequency VECSEL at 852nm for CPT-based cs clocks, in *Advanced Solid-State Lasers Congress*, edited by G. Huber and Moulton, OSA Technical Digest (online), page JTh2A.20, Optical Society of America, 2013. (Cited on pages 6 and 142.)

[53] T. E. Darcie, A. Stohr, and P. K. L. Yu, Lightwave Technology, Journal of **26**, 2336 (2008). (Cited on pages 6 and 142.)

[54] N. F. Mott, Proceedings of the Royal Society of London. Series A - Mathematical and Physical Sciences **153**, 699 (1936). (Cited on page 11.)

[55] N. F. Mott, Proceedings of the Royal Society of London. Series A - Mathematical and Physical Sciences **156**, 368 (1936). (Cited on page 11.)

[56] A. Fert and I. A. Campbell, Physical Review Letters **21**, 1190 (1968). (Cited on page 11.)

[57] C. Chappert, A. Fert, and F. N. Van Dau, Nature Materials **6**, 813 (2007). (Cited on pages 12, 16 and 21.)

[58] A. G. Aronov and G. E. Pikus, Sov. Phys. Semicond. **10**, 698 (1976). (Cited on pages 11 and 17.)

[59] M. Johnson and R. H. Silsbee, Physical Review Letters **55**, 1790 (1985). (Cited on page 11.)

[60] B. Dieny et al., Physical Review B **43**, 1297 (1991). (Cited on page 12.)

[61] Forbes, Declining growth projections for hard disk drive industry in 2013, 2014. (Cited on page 12.)

[62] T. Valet and A. Fert, Physical Review B **48**, 7099 (1993). (Cited on pages 13, 17, 18 and 19.)

[63] A. Fert and H. Jaffres, Physical Review B **64**, 184420 (2001). (Cited on pages 13, 20, 21, 98, 112 and 198.)

[64] P. C. van Son, H. van Kempen, and P. Wyder, Physical Review Letters **58**, 2271 (1987). (Cited on pages 14 and 18.)

[65] M. Johnson and R. H. Silsbee, Physical Review Letters **60**, 377 (1988). (Cited on pages 14 and 18.)

[66] R. Magno and J. H. Pifer, Physical Review B **10**, 3727 (1974). (Cited on page 17.)

[67] J. Peiro, *Phénomène d'injection et de décohérence de spin dans des structures semiconductrices*, PhD thesis, Unité-Mixte de Physique CNRS-Thales - Université Parsi-Sud, 2012. (Cited on pages 20, 28, 51 and 53.)

[68] Z. G. Yu and M. E. Flatté, Physical Review B **66**, 201202 (2002). (Cited on page 21.)

[69] A. M. Bratkovsky and V. V. Osipov, Journal of Applied Physics **96**, 4525 (2004). (Cited on page 21.)

[70] W. Y. Lee et al., Journal of Applied Physics **85**, 6682 (1999). (Cited on page 21.)

[71] P. R. Hammar, B. R. Bennett, M. J. Yang, and M. Johnson, Physical Review Letters **83**, 203 (1999). (Cited on page 21.)

[72] G. Schmidt, D. Ferrand, L. W. Molenkamp, A. T. Filip, and B. J. van Wees, Physical Review B **62**, R4790 (2000). (Cited on pages 21, 25 and 31.)

[73] E. I. Rashba, Physical Review B **62**, R16267 (2000). (Cited on page 21.)

[74] H. Jaffrès, Physical Review B **82** (2010). (Cited on page 22.)

[75] J. M. Kikkawa and D. D. Awschalom, Physical Review Letters **80**, 4313 (1998). (Cited on pages 25 and 85.)

[76] D. Hagele, M. Oestreich, W. W. Ruhle, N. Nestle, and K. Eberl, Applied Physics Letters **73**, 1580 (1998). (Cited on page 25.)

[77] W. Park et al., Physical Review B **62**, 1178 (2000). (Cited on page 27.)

[78] I. Zutic and H. Dery, Nature Materials **10**, 647 (2011). (Cited on page 29.)

[79] J. D. Albrecht and D. L. Smith, Physical Review B **66**, 113303 (2002). (Cited on pages 29 and 33.)

[80] P. M. Tedrow and R. Meservey, Physical Review Letters **26**, 192 (1971). (Cited on page 29.)

[81] J. F. Gregg, I. Petej, E. Jouguelet, and C. Dennis, Journal of Physics D: Applied Physics **35**, R121 (2002). (Cited on pages 30, 32, 34 and 35.)

[82] N. C. Gerhardt and M. R. Hofmann, Advances in Optical Technologies **2012** (2012). (Cited on page 30.)

[83] J. S. Moodera and G. Mathon, Journal of Magnetism and Magnetic Materials **200**, 248 (1999). (Cited on page 30.)

[84] M. Holub and P. Bhattacharya, Journal of Physics D: Applied Physics **40**, R179 (2007). (Cited on pages 31, 37, 46, 47, 49, 54, 55, 56, 59, 60, 61, 62, 63, 64, 68, 72, 74, 77, 78, 93, 98, 183 and 196.)

[85] I. I. Mazin, Physical Review Letters **83**, 1427 (1999). (Cited on page 31.)

[86] B. Jonker, A. Hanbicki, D. Pierce, and M. Stiles, Journal of Magnetism and Magnetic Materials **277**, 24 (2004). (Cited on page 31.)

[87] C. H. Li et al., Applied Physics Letters **85**, 1544 (2004). (Cited on page 31.)

[88] P. Van Dorpe, W. Van Roy, V. F. Motsny, G. Borghs, and J. De Boeck, Journal of Vacuum Science & Technology A: Vacuum, Surfaces, and Films **22**, 1862 (2004). (Cited on pages 31, 32 and 68.)

[89] W. Van Roy, P. Van Dorpe, J. De Boeck, and G. Borghs, Materials Science and Engineering: B **126**, 155 (2006). (Cited on pages 32 and 37.)

[90] T. B. P. Hyperphysics, http://hyperphysics.phy-astr.gsu.edu/hbase/quantum/barr.html, 2013. (Cited on page 32.)

[91] H. J. Zhu et al., Physical Review Letters **87**, 016601 (2001). (Cited on pages 32, 98 and 126.)

[92] A. T. Hanbicki et al., Applied Physics Letters **82**, 4092 (2003). (Cited on pages 32, 36 and 53.)

[93] A. T. Hanbicki, B. T. Jonker, G. Itskos, G. Kioseoglou, and A. Petrou, Applied Physics Letters **80**, 1240 (2002). (Cited on pages 32, 48, 67, 68 and 98.)

[94] J. Strand, B. D. Schultz, A. F. Isakovic, C. J. Palmstrom, and P. A. Crowell, Physical Review Letters **91**, 036602 (2003). (Cited on page 32.)

[95] S. F. Alvarado and P. Renaud, Physical Review Letters **68**, 1387 (1992). (Cited on page 34.)

[96] W. Van Roy, P. Van Dorpe, R. Vanheertum, P. Vandormael, and G. Borghs, IEEE Transactions on Electron Devices **54**, 933 (2007). (Cited on page 34.)

[97] L. Lombez et al., Applied Physics Letters **90**, 081111 (2007). (Cited on pages 27 and 34.)

[98] V. F. Motsnyi et al., Physical Review B **68**, 245319 (2003). (Cited on pages 34, 36, 53, 62 and 68.)

[99] X. Jiang et al., Physical Review Letters **94**, 056601 (2005). (Cited on pages 27, 34, 36, 53, 67, 68, 98, 106 and 129.)

[100] W. Butler, X.-G. Zhang, T. Schulthess, and J. MacLaren, Physical Review B **63** (2001). (Cited on pages 27, 34, 36 and 102.)

[101] J. Mathon and A. Umerski, Physical Review B **63** (2001). (Cited on pages 34 and 36.)

[102] X.-G. Zhang and W. Butler, Physical Review B **70** (2004). (Cited on page 34.)

[103] S. S. P. Parkin et al., Nature Materials **3**, 862 (2004). (Cited on pages 27, 34 and 102.)

[104] P. Mavropoulos, N. Papanikolaou, and P. H. Dederichs, Physical Review Letters **85**, 1088 (2000). (Cited on page 34.)

[105] J. M. D. Teresa et al., Science **286**, 507 (1999), PMID: 10521341. (Cited on page 35.)

[106] J. S. Moodera et al., Physical Review Letters **83**, 3029 (1999). (Cited on page 35.)

[107] O. M. J. van't Erve et al., Applied Physics Letters **84**, 4334 (2004). (Cited on page 36.)

[108] R. Wang et al., Applied Physics Letters **86**, 052901 (2005). (Cited on pages 36 and 104.)

[109] V. F. Motsnyi et al., Applied Physics Letters **81**, 265 (2002). (Cited on pages 36, 62 and 68.)

[110] H. Ohno et al., Applied Physics Letters **69**, 363 (1996). (Cited on page 37.)

[111] T. Dietl, H. Ohno, F. Matsukura, J. Cibert, and D. Ferrand, Science **287**, 1019 (2000), PMID: 10669409. (Cited on page 37.)

[112] M. Kohda, Y. Ohno, K. Takamura, F. Matsukura, and H. Ohno, Japanese Journal of Applied Physics **40**, L1274 (2001). (Cited on pages 37 and 68.)

[113] P. Van Dorpe et al., Applied Physics Letters **84**, 3495 (2004). (Cited on pages 37 and 68.)

[114] J. K. Furdyna, Journal of Applied Physics **64**, R29 (1988). (Cited on page 37.)

[115] R. A. de Groot, F. M. Mueller, P. G. v. Engen, and K. H. J. Buschow, Physical Review Letters **50**, 2024 (1983). (Cited on page 37.)

[116] J. Kubler, A. R. William, and C. B. Sommers, Physical Review B **28**, 1745 (1983). (Cited on page 37.)

[117] T. Graf, C. Felser, and S. S. Parkin, Progress in Solid State Chemistry **39**, 1 (2011). (Cited on pages 37 and 38.)

[118] A. Yanase and K. Siratori, Journal of the Physical Society of Japan **53**, 312 (1984). (Cited on page 37.)

[119] T. Ambrose, J. J. Krebs, and G. A. Prinz, Applied Physics Letters **76**, 3280 (2000). (Cited on page 38.)

[120] A. Hirohata et al., Journal of Applied Physics **97**, 103714 (2005). (Cited on page 38.)

[121] M. C. Hickey et al., Applied Physics Letters **86**, 252106 (2005). (Cited on pages 38 and 68.)

[122] S. Picozzi, A. Continenza, and A. Freeman, Journal of Physics and Chemistry of Solids **64**, 1697 (2003), 13th International Conference on Ternary and Multinary Compounds. (Cited on page 38.)

[123] X. Y. Dong et al., Applied Physics Letters **86**, 102107 (2005). (Cited on pages 38, 68 and 98.)

[124] K. Ando et al., Nature Materials **10**, 655 (2011). (Cited on pages 38, 42 and 43.)

[125] F. J. Jedema, A. T. Filip, and B. J. van Wees, Nature **410**, 345 (2001). (Cited on page 38.)

[126] S. O. Valenzuela and M. Tinkham, Nature **442**, 176 (2006). (Cited on pages 38 and 39.)

[127] M. V. Costache, M. Sladkov, S. M. Watts, C. H. van der Wal, and B. J. van Wees, Physical Review Letters **97**, 216603 (2006). (Cited on pages 38 and 42.)

[128] K. Uchida et al., Nature **455**, 778 (2008). (Cited on pages 38 and 40.)

[129] M. I. Dyakonov and V. I. Perel, JETP Letters **13**, 467 (1971). (Cited on page 38.)

[130] P. Laczkoski, *Spin currents and spin Hall effect in lateral nano-structures*, PhD thesis, Laboratoire Nanostructure et Magnétisme - Université de Grenoble. (Cited on pages 38 and 39.)

[131] M. Dyakonov and V. Perel, Physics Letters A **35**, 459 (1971). (Cited on page 39.)

[132] J. E. Hirsch, Physical Review Letters **83**, 1834 (1999). (Cited on page 39.)

[133] M. I. Dyakonov, Physical Review Letters **99**, 126601 (2007). (Cited on page 39.)

[134] Y. K. Kato, R. C. Myers, A. C. Gossard, and D. D. Awschalom, Science **306**, 1910 (2004), PMID: 15539563. (Cited on page 39.)

[135] T. Jungwirth, J. Wunderlich, and K. Olejnik, Nature Materials **11**, 382 (2012). (Cited on page 39.)

[136] L. Liu et al., Science **336**, 555 (2012), PMID: 22556245. (Cited on pages 39 and 204.)

[137] L. Liu, T. Moriyama, D. C. Ralph, and R. A. Buhrman, Physical Review Letters **106**, 036601 (2011). (Cited on pages 39 and 43.)

[138] J. Wunderlich et al., Science **330**, 1801 (2010), PMID: 21205664. (Cited on page 39.)

[139] G. E. W. Bauer, E. Saitoh, and B. J. van Wees, Nature Materials **11**, 391 (2012). (Cited on pages 39 and 40.)

[140] E. Saitoh, M. Ueda, H. Miyajima, and G. Tatara, Applied Physics Letters **88**, 182509 (2006). (Cited on page 39.)

[141] T. Kimura, Y. Otani, T. Sato, S. Takahashi, and S. Maekawa, Physical Review Letters **98**, 156601 (2007). (Cited on page 39.)

[142] M. Johnson and R. H. Silsbee, Physical Review B **35**, 4959 (1987). (Cited on page 40.)

[143] C. M. Jaworski, R. C. Myers, E. Johnston-Halperin, and J. P. Heremans, Nature **487**, 210 (2012). (Cited on page 40.)

[144] A. Slachter, F. L. Bakker, J.-P. Adam, and B. J. van Wees, Nature Physics **6**, 879 (2010). (Cited on pages 40 and 41.)

[145] C. M. Jaworski et al., Physical Review Letters **106**, 186601 (2011). (Cited on page 40.)

[146] H. Adachi et al., Applied Physics Letters **97**, 252506 (2010). (Cited on page 40.)

[147] H. Adachi, J.-i. Ohe, S. Takahashi, and S. Maekawa, Physical Review B **83**, 094410 (2011). (Cited on page 40.)

[148] L. Gravier, S. Serrano-Guisan, F. Reuse, and J.-P. Ansermet, Physical Review B **73**, 052410 (2006). (Cited on page 40.)

[149] M. Hatami, G. E. W. Bauer, Q. Zhang, and P. J. Kelly, Physical Review B **79**, 174426 (2009). (Cited on page 40.)

[150] Y. Takezoe, K. Hosono, A. Takeuchi, and G. Tatara, Physical Review B **82**, 094451 (2010). (Cited on page 40.)

[151] K. Uchida et al., Nature Materials **9**, 894 (2010). (Cited on page 40.)

[152] S. Bosu et al., Physical Review B **83**, 224401 (2011). (Cited on page 40.)

[153] A. B. Cahaya, O. A. Tretiakov, and G. E. W. Bauer, Applied Physics Letters **104**, 042402 (2014). (Cited on page 40.)

[154] N. Mojumder, D. Abraham, K. Roy, and D. Worledge, IEEE Transactions on Magnetics **48**, 2016 (2012). (Cited on page 40.)

[155] T. T. Heikkila and Y. Tserkovnyak, Nature **487**, 180 (2012). (Cited on page 41.)

[156] J.-C. Le Breton, S. Sharma, H. Saito, S. Yuasa, and R. Jansen, Nature **475**, 82 (2011). (Cited on page 41.)

[157] J. Flipse, F. L. Bakker, A. Slachter, F. K. Dejene, and B. J. v. Wees, Nature Nanotechnology **7**, 166 (2012). (Cited on page 41.)

[158] M. Walter et al., Nature Materials **10**, 742 (2011). (Cited on page 41.)

[159] Y. Tserkovnyak, A. Brataas, and G. E. W. Bauer, Physical Review Letters **88**, 117601 (2002). (Cited on page 42.)

[160] A. Brataas, Y. Tserkovnyak, G. E. W. Bauer, and B. I. Halperin, Physical Review B **66**, 060404 (2002). (Cited on page 42.)

[161] X. Wang, G. E. W. Bauer, B. J. van Wees, A. Brataas, and Y. Tserkovnyak, Physical Review Letters **97**, 216602 (2006). (Cited on page 42.)

[162] I. Zutic, J. Fabian, and S. Das Sarma, Reviews of Modern Physics **76**, 323 (2004). (Cited on pages 43 and 76.)

[163] K. Ando et al., Journal of Applied Physics **109**, 103913 (2011). (Cited on page 43.)

[164] O. Mosendz et al., Physical Review B **82**, 214403 (2010). (Cited on page 43.)

[165] H. Nakayama et al., Physical Review B **85**, 144408 (2012). (Cited on page 43.)

[166] J.-C. Rojas-SÃ¡nchez, Physical Review Letters **112** (2014). (Cited on page 43.)

[167] M. I. Dyakonov and V. I. Perel, JETP Letters **33**, 1053 (1971). (Cited on page 44.)

[168] F. Meier and B. Zakharchenya, *Optical Orientation*, volume Modern Problems in Condensed Matter Sciences, Vol. 8, Elsevier Science Ltd, 1984. (Cited on pages 45, 80, 98, 126 and 193.)

[169] S. M. V.A. and T. A.N., Soviet Physics-Solid State **25**, 3537 (1984). (Cited on page 45.)

[170] R. I. Dzhioev et al., Physical Review B **66**, 245204 (2002). (Cited on page 45.)

[171] J. N. Chazalviel, Physical Review B **11**, 1555 (1975). (Cited on page 46.)

[172] A. A. G. Bir and G. Pikus, JETP Letters **69**, 1382 (1975). (Cited on page 46.)

[173] A. W. Overhauser, Physical Review **89**, 689 (1953). (Cited on page 47.)

[174] X. Lou et al., Physical Review Letters **96**, 176603 (2006). (Cited on page 47.)

[175] R. J. Epstein et al., Physical Review B **68**, 041305 (2003). (Cited on page 47.)

[176] R. K. Kawakami et al., Science **294**, 131 (2001), PMID: 11588255. (Cited on page 47.)

[177] J. Wagner, H. Schneider, D. Richards, A. Fischer, and K. Ploog, Physical Review B **47**, 4786 (1993). (Cited on page 47.)

[178] H. Gotoh et al., Journal of Applied Physics **87**, 3394 (2000). (Cited on page 47.)

[179] A. Malinowski et al., Physical Review B **62**, 13034 (2000). (Cited on pages 47 and 48.)

[180] A. Tackeuchi, Y. Nishikawa, and O. Wada, Applied Physics Letters **68**, 797 (1996). (Cited on page 48.)

[181] C. H. Li et al., Applied Physics Letters **86**, 132503 (2005). (Cited on pages 48 and 68.)

[182] A. M. Tyryshkin, S. A. Lyon, A. V. Astashkin, and A. M. Raitsimring, Physical Review B **68**, 193207 (2003). (Cited on page 48.)

[183] M. Rohlfing, Physical Review B **48**, 17791 (1993). (Cited on page 51.)

[184] B. T. Jonker et al., Physical Review B **62**, 8180 (2000). (Cited on page 53.)

[185] A. Kastler, Journal de Physique et le Radium **11**, 255 (1950). (Cited on page 56.)

[186] A. Kastler, Proceedings of the Physical Society. Section A **67**, 853 (1954). (Cited on page 56.)

[187] A. KASTLER, Journal of the Optical Society of America **47**, 460 (1957). (Cited on page 56.)

[188] G. Lampel, Physical Review Letters **20**, 491 (1968). (Cited on page 57.)

[189] D. K. Young, E. Johnston-Halperin, D. D. Awschalom, Y. Ohno, and H. Ohno, Applied Physics Letters **80**, 1598 (2002). (Cited on page 59.)

[190] O. M. J. van't Erve, G. Kioseoglou, A. T. Hanbicki, C. H. Li, and B. T. Jonker, Applied Physics Letters **89**, 072505 (2006). (Cited on pages 60 and 68.)

[191] M. Agrawal and G. S. Solomon, Applied Physics Letters **85**, 1820 (2004). (Cited on page 61.)

[192] W. Wang, Physical Review B **74** (2006). (Cited on page 61.)

[193] Y. Ohno, R. Terauchi, T. Adachi, F. Matsukura, and H. Ohno, Physical Review Letters **83**, 4196 (1999). (Cited on pages 61, 195 and 197.)

[194] P. V. Dorpe et al., Japanese Journal of Applied Physics **42**, L502 (2003). (Cited on pages 62 and 68.)

[195] B. T. Jonker et al., Applied Physics Letters **79**, 3098 (2001). (Cited on pages 64, 68 and 125.)

[196] E. H. C. Parker, *The Technology and Physics of Molecular Beam Epitaxy*, volume pp.98, Springer, 1985. (Cited on page 64.)

[197] Y. Ohno et al., Nature **402**, 790 (1999). (Cited on pages 67, 68 and 97.)

[198] G. Salis et al., Applied Physics Letters **87**, 262503 (2005). (Cited on pages 67, 68 and 104.)

[199] Y. Lu et al., Applied Physics Letters **93**, 152102 (2008). (Cited on pages 68, 104 and 198.)

[200] T. Manago and H. Akinaga, Applied Physics Letters **81**, 694 (2002). (Cited on page 68.)

[201] N. Nishizawa, K. Nishibayashi, and H. Munekata, Applied Physics Letters **104**, 111102 (2014). (Cited on page 68.)

[202] H. Saito et al., Applied Physics Letters **96**, 012501 (2010). (Cited on page 68.)

[203] C. H. Li et al., Applied Physics Letters **103**, 212403 (2013). (Cited on pages 68 and 106.)

[204] C. Adelmann, Physical Review B **71** (2005). (Cited on pages 98 and 129.)

[205] G. Itskos et al., Applied Physics Letters **88**, 022113 (2006). (Cited on page 68.)

[206] A. Kawaharazuka et al., Applied Physics Letters **85**, 3492 (2004). (Cited on page 68.)

[207] M. Ramsteiner, Physical Review B **66** (2002). (Cited on page 68.)

[208] E. D. Fraser et al., Applied Physics Letters **97**, 041103 (2010). (Cited on page 68.)

[209] C. Adelmann et al., Applied Physics Letters **89**, 112511 (2006). (Cited on pages 68, 69, 112 and 129.)

[210] N. C. Gerhardt et al., Journal of Applied Physics **99**, 073907 (2006). (Cited on page 68.)

[211] S. Hovel et al., Applied Physics Letters **93**, 021117 (2008). (Cited on pages 68, 69, 112, 125 and 129.)

[212] S. Ghosh and P. Bhattacharya, Applied Physics Letters **80**, 658 (2002). (Cited on page 68.)

[213] Y. Chye, Physical Review B **66** (2002). (Cited on page 68.)

[214] E. Johnston-Halperin, Physical Review B **65** (2002). (Cited on page 68.)

[215] J. Seufert, Physical Review B **69** (2004). (Cited on page 68.)

[216] W. Loffler et al., Applied Physics Letters **88**, 062105 (2006). (Cited on page 68.)

[217] G. Kioseoglou et al., Nature Materials **3**, 799 (2004). (Cited on page 68.)

[218] M. Tanaka et al., Applied Physics Letters **62**, 1565 (1993). (Cited on page 67.)

[219] F. Richomme, Physical Review B **64** (2001). (Cited on page 67.)

[220] S. Ikeda et al., Nature Materials **9**, 721 (2010). (Cited on pages 67, 112 and 120.)

[221] T. Fordos, K. Postava, H. Jaffres, and J. Pistora, Journal of Optics **16**, 065008 (2014). (Cited on page 69.)

[222] H. Soda, K. ichi Iga, C. Kitahara, and Y. Suematsu, Japanese Journal of Applied Physics **18**, 2329 (1979). (Cited on page 71.)

[223] K. Iga, Japanese Journal of Applied Physics **47**, 1 (2008). (Cited on page 71.)

[224] S. Hovel et al., Applied Physics Letters **92**, 041118 (2008). (Cited on pages 71, 93, 94, 95, 149 and 210.)

[225] J. Frougier et al., Applied Physics Letters **103**, 252402 (2013). (Cited on pages 72, 94, 95, 171 and 175.)

[226] C. Chang-Hasnain, J. Harbison, L. Florez, and N. Stoffel, Electronics Letters **27**, 163 (1991). (Cited on pages 72 and 79.)

[227] K. D. Choquette, D. A. Richie, and R. E. Leibenguth, Applied Physics Letters **64**, 2062 (1994). (Cited on pages 72, 79, 165 and 171.)

[228] J. Rudolph, D. Hagele, H. M. Gibbs, G. Khitrova, and M. Oestreich, Applied Physics Letters **82**, 4516 (2003). (Cited on pages 72, 75, 76, 77, 94, 187, 196 and 198.)

[229] R. Oszwaldowski, Physical Review B **82** (2010). (Cited on pages 72 and 75.)

[230] J. Lee, R. Oszwaldowski, C. Gothgen, and I. Zutic, Physical Review B **85**, 045314 (2012). (Cited on pages 73, 74, 75 and 76.)

[231] I. Vurgaftman, M. Holub, B. T. Jonker, and J. R. Meyer, Applied Physics Letters **93**, 031102 (2008). (Cited on page 75.)

[232] M. Oestreich, J. Rudolph, R. Winkler, and D. Hagele, Superlattices and Microstructures **37**, 306 (2005), Spintronics: Spin Injection, Transport, and Manipulation. (Cited on pages 75, 195, 197 and 198.)

[233] M. Holub and B. T. Jonker, Physical Review B **83**, 125309 (2011). (Cited on page 75.)

[234] D. Saha, D. Basu, and P. Bhattacharya, Physical Review B **82**, 205309 (2010). (Cited on pages 75, 76, 93 and 212.)

[235] D. Basu et al., Applied Physics Letters **92**, 091119 (2008). (Cited on pages 76, 96 and 196.)

[236] M. San Miguel, Q. Feng, and J. V. Moloney, Physical Review A **52**, 1728 (1995). (Cited on pages 76, 78, 80, 81, 83, 84, 88, 90 and 224.)

[237] A. Fiore and A. Markus, IEEE Journal of Quantum Electronics **43**, 287 (2007). (Cited on page 76.)

[238] H. D. Summers and P. Rees, Journal of Applied Physics **101**, 073106 (2007). (Cited on page 76.)

[239] D. Alexandropoulos and M. Adams, IEEE Journal of Quantum Electronics **45**, 744 (2009). (Cited on page 76.)

[240] M. Y. Li et al., Applied Physics Letters **97**, 191114 (2010). (Cited on page 76.)

[241] H. Dery and G. Eisenstein, IEEE Journal of Quantum Electronics **40**, 1398 (2004). (Cited on page 76.)

[242] J. Huang and L. W. Casperson, Optical and Quantum Electronics **25**, 369 (1993). (Cited on page 77.)

[243] R. Nagarajan, M. Ishikawa, T. Fukushima, R. S. Geels, and J. Bowers, IEEE Journal of Quantum Electronics **28**, 1990 (1992). (Cited on page 77.)

[244] J.-H. Ser, Y.-G. Ju, J.-H. Shin, and Y. H. Lee, Applied Physics Letters **66**, 2769 (1995). (Cited on pages 78 and 165.)

[245] T. Mukaihara et al., IEEE Journal of Selected Topics in Quantum Electronics **1**, 667 (1995). (Cited on page 78.)

[246] A. Chavez-Pirson, H. Ando, H. Saito, and H. Kanbe, Applied Physics Letters **62**, 3082 (1993). (Cited on pages 78 and 82.)

[247] D. Sun, E. Towe, P. Ostdiek, J. Grantham, and G. Vansuch, IEEE Journal of Selected Topics in Quantum Electronics **1**, 674 (1995). (Cited on page 78.)

[248] Y. Nishikawa, A. Tackeuchi, S. Nakamura, S. Muto, and N. Yokoyama, Applied Physics Letters **66**, 839 (1995). (Cited on page 78.)

[249] H. Kawaguchi, IEEE Journal of Selected Topics in Quantum Electronics **3**, 1254 (1997). (Cited on page 78.)

[250] R. F. M. Hendriks et al., Applied Physics Letters **71**, 2599 (1997). (Cited on pages 79, 165, 168, 173, 174 and 205.)

[251] A. K. Jansen van Doorn, M. P. van Exter, and J. P. Woerdman, Applied Physics Letters **69**, 3635 (1996). (Cited on pages 79 and 165.)

[252] Z. G. Pan et al., Applied Physics Letters **63**, 2999 (1993). (Cited on page 79.)

[253] H. Li, T. L. Lucas, J. G. McInerney, and R. A. Morgan, Chaos, Solitons Fractals **4**, 1619 (1994), Special Issue: Nonlinear Optical Structures, Patterns, Chaos. (Cited on page 79.)

[254] C. Henry, IEEE Journal of Quantum Electronics **18**, 259 (1982). (Cited on pages 80 and 86.)

[255] M. Osinski and J. Buus, IEEE Journal of Quantum Electronics **23**, 9 (1987). (Cited on page 80.)

[256] R. Ferreira, Physical Review B **43**, 9687 (1991). (Cited on page 80.)

[257] M. Maialle, Physical Review B **47**, 15776 (1993). (Cited on page 80.)

[258] T. Uenoyama, Physical Review B **42**, 7114 (1990). (Cited on page 80.)

[259] T. Damen, Physical Review Letters **67**, 3432 (1991). (Cited on pages 80 and 84.)

[260] W. van Haeringen, Physical Review **158**, 256 (1967). (Cited on page 82.)

[261] J. Frougier, G. Baili, I. Sagnes, D. Dolfi, J. M. George and M. Alouini Optics Express **Submitted** (2014). (Cited on page 165.)

[262] T. Ohtoshi, T. Kuroda, A. Niwa, and S. Tsuji, Applied Physics Letters **65**, 1886 (1994). (Cited on page 82.)

[263] K. Choquette, R. Schneider, K. L. Lear, and R. Leibenguth, IEEE Journal of Selected Topics in Quantum Electronics **1**, 661 (1995). (Cited on pages 82, 165 and 171.)

[264] J.-P. Zhang, IEEE Journal of Quantum Electronics **31**, 2127 (1995). (Cited on page 82.)

[265] K. Choquette and R. Leibenguth, IEEE Photonics Technology Letters **6**, 40 (1994). (Cited on pages 82 and 165.)

[266] T. Mukaihara, F. Koyama, and K. Iga, IEEE Photonics Technology Letters **5**, 133 (1993). (Cited on page 82.)

[267] A. Gahl, S. Balle, and M. S. Miguel, Quantum and Semiclassical Optics: Journal of the European Optical Society Part B **10**, L1 (1998). (Cited on pages 82 and 86.)

[268] M. O. S. M. Sargent III and J. W. E. Lamb, *Laser Physics*, volume Chap. 9, pp. 120-127, Addison-Wesley, fifth edition, 1974. (Cited on pages 82, 180 and 181.)

[269] S. Bar-Ad, Physical Review Letters **68**, 349 (1992). (Cited on page 84.)

[270] J. Martin-Regalado, F. Prati, M. San Miguel, and N. B. Abraham, IEEE Journal of Quantum Electronics **33**, 765 (1997). (Cited on pages 85, 86, 87, 88, 89, 90 and 223.)

[271] S. De, V. Potapchuk, and F. Bretenaker, arXiv:1311.4657 (2013). (Cited on page 85.)

[272] C. Serrat, Physical Review A **53**, R3731 (1996). (Cited on page 86.)

[273] A. J. van Doorn, M. van Exter, M. Travagnin, and J. Woerdman, Optics Communications **133**, 252 (1997). (Cited on pages 86, 196 and 223.)

[274] J. MartiÌn-Regalado, J. L. A. Chilla, J. J. Rocca, and P. Brusenbach, Applied Physics Letters **70**, 3350 (1997). (Cited on pages 86 and 165.)

[275] J. Martin-Regalado, *Polarization Properties of Vertical Cavity Surface Emitting Lasers (http://www.imedea.uib.es/PhysDept/publicationsDB)*, PhD thesis, Universitat Illes Balears, Palma de Mallorca, Spain. (Cited on page 86.)

[276] M. van Exter, Physical Review Letters **80**, 4875 (1998). (Cited on page 86.)

[277] H. van der Lem and D. Lenstra, Optics Letters **22**, 1698 (1997). (Cited on page 86.)

[278] M. van Exter, Physical Review A **57**, 2080 (1998). (Cited on page 86.)

[279] A. Gahl, S. Balle, and M. San Miguel, IEEE Journal of Quantum Electronics **35**, 342 (1999). (Cited on page 92.)

[280] G. Boeris, J. Lee, K. Vyborny, and I. Zutic, Applied Physics Letters **100**, 121111 (2012). (Cited on pages 93 and 212.)

[281] J. Lee and I. Zutic, SPIE Newsroom (2012). (Cited on page 93.)

[282] S. Hallstein et al., Physical Review B **56**, R7076 (1997). (Cited on pages 94 and 196.)

[283] H. Fujino, S. Koh, S. Iba, T. Fujimoto, and H. Kawaguchi, Applied Physics Letters **94**, 131108 (2009). (Cited on pages 94, 95, 149, 174, 195, 196, 197 and 206.)

[284] H. Hopfner, M. Lindemann, N. C. Gerhardt, and M. R. Hofmann, Applied Physics Letters **104**, 022409 (2014). (Cited on page 94.)

[285] M. Holub, J. Shin, S. Chakrabarti, and P. Bhattacharya, Applied Physics Letters **87**, 091108 (2005). (Cited on pages 95 and 96.)

[286] T. D. Nguyen, E. Ehrenfreund, and Z. V. Vardeny, Science **337**, 204 (2012), PMID: 22798608. (Cited on page 97.)

[287] R. Farshchi, M. Ramsteiner, J. Herfort, A. Tahraoui, and H. T. Grahn, Applied Physics Letters **98**, 162508 (2011). (Cited on page 98.)

[288] P. Asshoff, A. Merz, H. Kalt, and M. Hetterich, Applied Physics Letters **98**, 112106 (2011). (Cited on page 98.)

[289] J. Xu, A. Lakhtakia, J. Liou, A. Chen, and I. J. Hodgkinson, Optics Communications **264**, 235 (2006). (Cited on page 98.)

[290] M. I. Dyakonov, *Spin Physics in Semiconductors*, Springer, 1st ed. softcover of orig. ed. 2008 edition, 2008. (Cited on page 98.)

[291] S. Yuasa, T. Nagahama, A. Fukushima, Y. Suzuki, and K. Ando, Nature Materials **3**, 868 (2004). (Cited on page 102.)

[292] Y. S. Choi, K. Tsunekawa, Y. Nagamine, and D. Djayaprawira, Journal of Applied Physics **101**, 013907 (2007). (Cited on pages 102 and 110.)

[293] S. Ikeda et al., Applied Physics Letters **93**, 082508 (2008). (Cited on pages 102 and 111.)

[294] D. D. Djayaprawira et al., Applied Physics Letters **86**, 092502 (2005). (Cited on pages 102 and 107.)

[295] S. Yuasa, Y. Suzuki, T. Katayama, and K. Ando, Applied Physics Letters **87**, 242503 (2005). (Cited on page 102.)

[296] P. Barate et al., Applied Physics Letters **105**, 012404 (2014). (Cited on pages 102, 103, 105, 107 and 109.)

[297] W.-G. Wang et al., Applied Physics Letters **99**, 102502 (2011). (Cited on pages 103, 107, 119 and 120.)

[298] W. R. Mason, *A Practical Guide to Magnetic Circular Dichroism Spectroscopy*, John Wiley Sons, Inc., 2007. (Cited on page 104.)

[299] B. L. Liu et al., physica status solidi (c) **1**, 475-478 (2004). (Cited on page 104.)

[300] T. Miyajima et al., Applied Physics Letters **94**, 122501 (2009). (Cited on page 110.)

[301] M. Yamanouchi et al., IEEE Magnetics Letters **2**, 3000304 (2011). (Cited on page 110.)

[302] Y. Jang et al., Applied Physics Letters **91**, 102104 (2007). (Cited on pages 110 and 120.)

[303] H. Meng, W. H. Lum, R. Sbiaa, S. Y. H. Lua, and H. K. Tan, Journal of Applied Physics **110**, 033904 (2011). (Cited on pages 110 and 120.)

[304] H. X. Yang, Physical Review B **84** (2011). (Cited on pages 111, 112, 120 and 122.)

[305] N. C. Gerhardt et al., Applied Physics Letters **87**, 032502 (2005). (Cited on pages 112 and 129.)

[306] S. Hovel et al., Applied Physics Letters **93**, 021117 (2008). (Cited on pages 68, 69, 112, 125 and 129.)

[307] A. Sinsarp, T. Manago, F. Takano, and H. Akinaga, Journal of Superconductivity and Novel Magnetism **20**, 405 (2007). (Cited on pages 112 and 129.)

[308] J. Zarpellon et al., Physical Review B **86**, 205314 (2012). (Cited on pages 112 and 129.)

[309] S. Girod et al., Applied Physics Letters **94**, 262504 (2009). (Cited on page 112.)

[310] K. Khoo, Physical Review B **87** (2013). (Cited on page 112.)

[311] D. C. Worledge et al., Applied Physics Letters **98**, 022501 (2011). (Cited on page 112.)

[312] S. Liang et al., Physical Review B **90**, 085390 (2014). (Cited on pages 69, 112, 119, 121, 123, 124, 125, 127, 128 and 130.)

[313] J. van Vleck, Physical Review **52**, 1178 (1937). (Cited on pages 112 and 115.)

[314] L. Néel, Journal de Physique et le Radium **15**, 225 (1954). (Cited on pages 112 and 115.)

[315] P. Bruno, *Physical origins and theoretical models of magnetic anisotropy*, volume Magnetismus von Festkorpern und grenzflachen, Chap. 24, 1993. (Cited on pages 112, 115 and 116.)

[316] P. Bruno, Physical Review B **39**, 865 (1989). (Cited on pages 112, 115, 116, 117 and 122.)

[317] M. T. Johnson, P. J. H. Bloemen, F. J. A. d. Broeder, and J. J. d. Vries, Reports on Progress in Physics **59**, 1409 (1996). (Cited on page 113.)

[318] J. Stohr and H. C. Siegmann, *Magnetism: From Fundamentals to Nanoscale Dynamics*, volume Chap. 7, pp. 294-310, Springer, 2006. (Cited on pages 115 and 116.)

[319] T. Zhu et al., Applied Physics Letters **100**, 202406 (2012). (Cited on page 120.)

[320] G. Kresse, Physical Review B **47**, 558 (1993). (Cited on page 121.)

[321] G. Kresse and J. Furthmuller, Computational Materials Science **6**, 15 (1996). (Cited on page 121.)

[322] G. Kresse, Physical Review B **54**, 11169 (1996). (Cited on page 121.)

[323] Y. Wang, Physical Review B **44**, 13298 (1991). (Cited on page 121.)

[324] P. Blochl, Physical Review B **50**, 17953 (1994). (Cited on page 121.)

[325] G. Kresse, Physical Review B **59**, 1758 (1999). (Cited on page 121.)

[326] R. Mallory, Physical Review B **73** (2006). (Cited on page 125.)

[327] L. Fan et al., Applied Physics Letters **88**, 021105 (2006). (Cited on page 137.)

[328] J. E. Hastie et al., Optics Express **13**, 77 (2005). (Cited on page 137.)

[329] W. J. Alford, T. D. Raymond, and A. A. Allerman, Journal of the Optical Society of America B **19**, 663 (2002). (Cited on page 137.)

[330] A. Laurain, M. Myara, G. Beaudoin, I. Sagnes, and A. Garnache, Optics Express **18**, 14627 (2010). (Cited on page 137.)

[331] S. Cho et al., IEEE Photonics Technology Letters **19**, 1325 (2007). (Cited on page 137.)

[332] G. Baili, M. Alouini, C. Moronvalle, D. Dolfi, and F. Bretenaker, Optics Letters **31**, 62 (2006). (Cited on page 137.)

[333] G. Baili et al., Optics Letters **32**, 650 (2007). (Cited on pages 137, 142, 168, 178, 182, 188, 195, 196, 207 and 208.)

[334] R. Photonics, Vertical external-cavity surface-emitting lasers, 2014. (Cited on pages 139 and 141.)

[335] N. Laurand et al., Optics Express **15**, 9341 (2007). (Cited on page 139.)

[336] New high for quantum dot VECSELs, Electronics Letters **46**, 807 (2010). (Cited on page 139.)

[337] A. Albrecht et al., Electronics Letters **46**, 856 (2010). (Cited on page 139.)

[338] J. G. McInerney et al., Novel 980-nm and 490-nm light sources using vertical-cavity lasers with extended coupled cavities, volume 4994, pages 21–31, 2003. (Cited on page 139.)

[339] J. L. A. Chilla et al., High-power optically pumped semiconductor lasers, volume 5332, pages 143–150, 2004. (Cited on page 140.)

[340] A. Chernikov et al., IEEE Journal of Selected Topics in Quantum Electronics **17**, 1772 (2011). (Cited on page 140.)

[341] S.-S. Beyertt et al., IEEE Journal of Quantum Electronics **41**, 1439 (2005). (Cited on page 141.)

[342] G. Baili et al., Optics Letters **34**, 3421 (2009). (Cited on page 142.)

[343] V. Pal et al., Optics Express **18**, 5008 (2010). (Cited on pages 142, 171, 181 and 182.)

[344] A. K. Jansen van Doorn, M. P. van Exter, and J. P. Woerdman, Applied Physics Letters **69**, 1041 (1996). (Cited on page 165.)

[345] T. Yoshikawa et al., Applied Physics Letters **66**, 908 (1995). (Cited on page 165.)

[346] M. Vallet et al., Applied Physics Letters **74**, 3266 (1999). (Cited on page 177.)

[347] R. Photonics, Radiative lifetime, 2014. (Cited on page 186.)

[348] A. Tackeuchi, O. Wada, and Y. Nishikawa, Applied Physics Letters **70**, 1131 (1997). (Cited on page 188.)

[349] X. Marie, (2014). (Cited on pages 189 and 190.)

[350] K. Morita et al., Applied Physics Letters **87**, 171905 (2005). (Cited on page 195.)

[351] L. Schreiber et al., physica status solidi (b) **244**, 2960-2970 (2007). (Cited on page 195.)

[352] R. Terauchi et al., Japanese Journal of Applied Physics **38**, 2549 (1999). (Cited on page 197.)

[353] M. Oestreich et al., Semiconductor Science and Technology **17**, 285 (2002). (Cited on page 197.)

[354] Y. Ohno, R. Terauchi, T. Adachi, F. Matsukura, and H. Ohno, Physica E: Low-dimensional Systems and Nanostructures **6**, 817 (2000). (Cited on page 198.)

[355] D. Ralph and M. Stiles, Journal of Magnetism and Magnetic Materials **320**, 1190 (2008). (Cited on page 204.)

[356] S. S. P. Parkin, M. Hayashi, and L. Thomas, Science **320**, 190 (2008), PMID: 18403702. (Cited on page 204.)

[357] M. Klaui et al., Applied Physics Letters **83**, 105 (2003). (Cited on page 204.)

[358] I. Mihai Miron et al., Nature Materials **9**, 230 (2010). (Cited on page 204.)

[359] S. Alebrand et al., Applied Physics Letters **101**, 162408 (2012). (Cited on pages 204 and 211.)

[360] N. W. Ashcroft and N. D. Mermin, *Solid State Physics*, 1976. (Cited on pages 215 and 217.)

[361] J. M. Monsterleet, B. Capoen, and G. Biskupski, Journal of Physics: Condensed Matter **9**, 8657 (1997). (Cited on page 217.)

[362] M. P. Van Exter, A. K. J. van Doorn, R. F. M. Hendriks, and J. P. Woerdman, *Transverse anisotropy and mode structure in VCSELs*, pages 202–212, 1996. (Cited on page 223.)

Toward Spin-LEDs and Spin-VECSELs operation at magnetic remanence

Abstract: This Ph.D Thesis proposes to explore a new paradigm of spin-information propagation over very long distances after encoding on coherent light polarization. The main objective of this manuscript is to provide a detailed study of spin-injection into III-V semiconductor based opto-electronic devices with vertical geometries.
To achieve this goal, we focus on the study of optical and electrical spin-injection in III-V semiconductor based Light Emitting Diodes (LED) and Vertical External Cavity Surface Emitting Lasers (VECSEL). Our investigations and results are presented on three main axis.
A first chapter regroups a state-of-the-art of spin-injection into semiconductors opto-electronic devices and focuses on the physical phenomena engaged in the conversion of a spin accumulation into light polarization information. A discussion on spin-injection and spin-transport into III-V semiconductor structures is followed by a more device-oriented review on spin-injection in LED and VCSEL.
A second chapter is articulated around our experimental work on the development and the optimization on III-V semiconductors LEDs of an ultra-thin MgO/CoFeB/Ta spin-injector with perpendicular magnetization at magnetic remanence. We focus on the optimization of the MgO tunnel barrier for maximizing the spin-injection efficiency and then further detail the development and the characterization of the spin-injector with perpendicular magnetization at remanence.
Finally, a third chapter contains the main work of this Ph.D thesis. It is fully dedicated to our experimental research on spin-injection in Vertical External Cavity Surface Emitting Laser structures. A vectorial model allowing the theoretical understanding of polarization selection in spin-injected VECSEL is first introduced. Next, we report the birefringence measurement of a VECSEL designed for optical pumping using an original frequency detuning measurement between the two orthogonal TE- and TM-modes in the electrical domain. Afterward, our observations and results on optical spin injection in VECSEL are displayed, analyzed and commented. The study is farther extended to the measurement of the system's characteristic lifetimes using Time Resolved Photo-Luminescence in order to evaluate the spin-information conversion efficiency. Finally the preliminary results on electrical spin-injection experiment are presented.

Keywords: III-V Semiconductors, Spin-injection, Spin-optronics, Spin-LED, Spin-VECSEL

Résumé: Cette thèse de doctorat propose d'explorer un nouveau paradigme de propagation de l'information de spin sur de très longues distances après encodage sur la polarisation de lumière cohérente. L'objectif principal de ce manuscrit est de fournir une étude détaillée de l'injection de spin dans des composants optoélectroniques III-V à géométrie verticale.

Pour atteindre cet objectif, nous nous concentrons sur l'étude de l'injection optique et électrique de spin dans des structures "Light Emitting Diodes" (LED) et des structures "Vertical External Cavity Surface Emitting Lasers" (VECSEL) à base de semiconducteurs III-V. Nos investigations et résultats sont présentés suivant trois axes majeurs.

Un premier chapitre regroupe un état de l'art sur l'injection de spin dans les composants optoélectroniques III-V et se concentre sur les phénomènes physiques engagés dans la conversion d'une accumulation de spin en information de polarisation lumineuse. Une discussion sur l'injection et le transport de spin dans des structures semi-conductrices est suivie par une analyse orientée-composant sur l'injection de spin dans les LEDs et les VCSELs.

Un second chapitre s'articule autour de notre travail expérimental sur le développement et l'optimisation sur LEDs III-V d'un injecteur de spin $MgO/CoFeB/Ta$ ultra-fin présentant une aimantation perpendiculaire à la rémanence magnétique. Nous nous focalisons en premier lieu sur l'optimisation de la barrière tunnel MgO pour maximiser l'injection de spin et détaillons par la suite le développement et la caractérisation de cet injecteur de spin possédant une aimantation perpendiculaire à la rémanence magnétique.

Un troisième chapitre contient le travail principal de cette thèse de doctorat. Elle est entièrement consacrée à notre recherche expérimentale sur l'injection de spin dans les structures "Vertical External Cavity Surface Emitting Lasers". Nous commençons par introduire un model vectoriel permettant la compréhension théorique de la sélection de polarisation dans les structures VECSEL injectées en spin. Nous rapportons ensuite la mesure de biréfringence d'une structure VECSEL designée pour le pompage optique en utilisant une technique expérimentale originale basée sur le mesure du décalage en fréquence dans le domaine électrique entre les deux modes de polarisation orthogonaux TE et TM. Ultérieurement, nos observations et résultats sur l'injection optique de spin dans les VECSEL sont détaillés, analysés et commentés. L'étude est étendue à l'estimation des temps de vie caractéristiques du système par mesures de Photoluminescence résolues en temps afin d'évaluer l'efficacité de conversion de l'information de spin. Pour finir, les résultats préliminaires sur l'injection électrique de spin dans les VECSEL sont présentés.

Mots-clés: Semiconducteurs III-V, Injection de spin, Spin-optoéléctronique, Spin-LED, Spin-VECSEL
